Using self-organizing maps to investigate abrupt reductions in Arctic sea ice extent: An application to winter and summer pan-Arctic daily sea level pressure data

by

©Adrienne Kaul

A Thesis submitted to the School of Graduate Studies in partial fulfillment of the requirements for the degree of

Master of Science

Department of Environmental Science, Faculty of Science

Memorial University of Newfoundland

2016

St. John's Newfoundland

Abstract

Self-Organizing maps (SOMs) have been used to explore potential connections between atmospheric circulation over the Arctic (in the form of sea level pressure patterns and teleconnection indices) and sea ice loss. Extended periods of abrupt loss (rapid ice loss events, or RILEs) have been studied, along with high ice loss years (with instantaneous ice loss years >0.45 million km^2). The bulk of the Thesis focuses on ice loss in 21st century projections from general circulation models (GCMs), with complimentary analysis of the observational record as represented by the NCEP/NCAR reanalysis. In addition to examining the frequency of specific weather systems (e.g. Icelandic lows, Beaufort Highs etc.), a SOM-based analogue of traditional teleconnection analysis was applied, which emphasizes impacts on the Arctic and allows for asymmetry between the positive and negative phases of a teleconnection. Results show no simple connection between sea level pressure patterns and RILEs, either in winter or summer analyses; although statistically significant circulation anomalies were identified for individual events, no common potential cause emerged. Results from composites of large ice loss years show fewer significant anomalies than found in RILE periods, but the sign of anomalies is more consistent. This suggests atmospheric drivers of ice loss are better demonstrated over short time scales (a year) rather than longer periods (years to decades). Identified circulation anomalies reflect increased winds along the transpolar drift, and these broadly resemble previously proposed ice

loss mechanisms associated with the North Atlantic Oscillation, Arctic Oscillation, and Arctic Rapid Change pattern.

Acknowledgements

I would like to express my sincere gratitude to my advisor Dr. Joel Finnis for the continuous support of my Masters study, for his patience and willingness to share his immense knowledge. His guidance helped me in all the time of research and writing of this thesis.

Thanks to my husband, family and friends for providing me with support and continuous encouragement over the years. This accomplishment would not have been possible without them.

Thanks to God for his mercy and grace, and for the gift of completing this project.

I wish to thank and acknowledge the organizations from which data for this project was obtained free of charge:

- We acknowledge the Program for Climate Model Diagnosis and Intercomparison (PCMDI) and the WCRP's Working Group on Coupled Modelliing (WGCM) for their roles in making available the WCRP CMIP3 multi-model dataset. Support of this dataset is provided by the Office of Science, U.S. Department of Energy

- NCAR NCEP Reanalysis data used in this experiment was provided by the NOAA/OAR/ESRL PSD, Boulder, Colorado, USA, from their Web site at `http://www.esrl.noaa.gov/psd/`. Model runs for the NCAR CCSM3 mod-

els was sourced from the University Corporation for Atmospheric Research (UCAR). © 2002 University Corporation for Atmospheric Research. All Rights Reserved.

I also thank the following organizations for the use of their free software:

- The NCAR Command Language (Version 6.0.0)[Software].(2012). Boulder, Colorado: UCAR/NCAR/CISL/VETS. http://dx.doi.org/10.5065/D6WD3XH5.
- The Climate Data Operators (CDO). (Version 1.5.2)[Software].(2011). Climate Data Operators Max-Planck-Institut fur Meteorologie 2006-2011. https://code.zmaw.de/projects/cdo/
- SOM_PAK: The Self-Organizing Map Program Package (Version 3.1)[Software].(1996). Espoo, Finland: Helsinki University of Technology, Laboratory of Computer and Information Science. Teuvo Kohonen, Jussi Hynninen, Jari Kangas, and Jorma Laaksonen.

Finally, thanks to Memorial University and the Natural Science and Engineering Research Council for funding the work on this project.

Adrienne Kaul

Table of Contents

List of Tables

List of Figures

Chapter 1

Introduction

The Arctic Ocean is mostly land enclosed, limiting exchanges with the Atlantic and Pacific Oceans (see Figure 1.1). Although the Arctic Ocean is defined differently by various researchers and Arctic stakeholders, it is commonly considered to connected to the Atlantic through Fram Strait (between Greenland and Svalbard), Nares Strait (between Ellesmere Island and Greenland), and the entry to the Barents Sea (rougly between Svalbard and Norway); it connects to Pacific Ocean only through the Bering Strait (Russia to Alaska). These few and narrow passages trap sea ice and limit the import of warmer water into the Arctic Ocean. This definition of the Arctic Ocean has a surface area of 9.4×10^6 km^2 with the majority of its surface area lying north of the Arctic Circle.

Few aspects of observed climate change have received as much scientific and popular attention as the steady retreat of sea ice in the Arctic Ocean. In addition to providing a dramatic visual example of climate change impacts, the rapid pace of Arctic ice loss has prompted concerns that model projections may be underestimating the impact of greenhouse gas emissions on the climate system. Recent years have seen minimum annual ice extent records broken repeatedly (e.g. Stroeve et al. (2012a)), and

a number of pronounced single-year losses have been recorded. The most prominent of these single-year drops occurred in 2007, when mean September extent dropped by roughly 1.6 million km^2 (~27% loss) relative to the previous September and 1.3 million km^2 (~23% loss) relative to the previous record minima set in 2005. Although the 2007 decrease was unprecedented in the observational record (Stroeve et al. 2008), this event shared broad similarities with abrupt ice declines identified in general circulation model projections of the 21st century (Holland et al. 2006). Together, the rapid observed and simulated declines have furthered concerns that the Arctic may either be approaching or have already passed a "tipping point" (Lindsay et al. 2005; Winton 2006; Eisenman et al. 2009; Tietsche et al. 2011), beyond which the Arctic climate system may change rapidly and irreversibly (Serreze et al. 2011a).

The drivers behind periods of accelerated sea ice loss, whether in observations or model simulations, remain uncertain. Holland et al. (2006) identified thermodynamic factors (related to anomalies in the sea ice heat budget) rather than dynamic factors (related to the movement of ice out of the Arctic) as the likely dominant drivers of simulated rapid ice loss events. By contrast, observational studies suggest the accelerating loss over the past decade is the result of a combination of factors, including natural fluctuations in air temperatures, atmospheric and oceanic circulation, and shifts in the surface energy budget arising from increased greenhouse gas concentrations (Stroeve et al. 2012b). Atmospheric circulation has been connected to dynamic ice loss over extended periods (Maslanik et al. 2007; Rigor et al. 2002) and to both thermodynamic (Devasthale et al. 2013) and dynamic ice loss during years of peak loss (Wang et al. 2009a). Atmospheric anomalies are particularly attractive as an explanation for these peak loss years, as the atmosphere's relatively high variability more closely resembles the increasing variability in ice extents, while other aspects of the climate system (e.g. ocean circulation) typically vary more slowly.

Although there is considerable evidence suggesting atmosphere/ice interactions are important to ongoing ice loss, it has proven difficult to identify robust relationships between established modes of large-scale atmospheric variability (or teleconnections) and the retreat of sea ice. In some cases the strength of the proposed relationship varies with time (Overland et al. 2005), while others are tenuously based on a few extreme events (L'Heureux et al. 2008; Wang et al. 2009a). This difficulty may be partially related to reliance on teleconnection patterns defined with only atmospheric data, limitations of the linear statistical methods used to define some patterns, and the fact that these patterns may not adequately represent high frequency or regional variability. Resulting atmospheric patterns a) are not optimized for sea ice applications, b) may not capture important nonlinear ice/atmosphere interactions, c) obscure the influence of high frequency atmospheric variability (i.e. weather) and d) may mask important regional influences. Similarly, efforts to assess similarities between observed and simulated abrupt ice loss are complicated by uncertainties in teleconnection/sea ice relationships, as well as differences between the spatial structure and temporal variability of simulated and observed teleconnection patterns (eg. Finnis et al. (2012)).

The current work presents analyses of observed and simulated ice loss using an alternative framework for atmospheric analysis. Based on the self-organizing map (SOM) methodology, the approach reinterprets circulation anomalies in the context of a synoptic climatology of daily sea level pressure patterns. This approach eases intercomparison of data sets (e.g. different models and observations), while emphasizing variations in daily weather patterns rather than the long-term averages typically examined. As a result, the work presents an alternative and complimentary analysis to prior ice loss studies, with greater emphasis on high frequency atmospheric variability. The current chapter provides background on Arctic ice cover, and atmospheric

circulation. Subsequent chapters outline SOM methodology and it's application to the current work, before proceeding to analyses of the observational record and simulated ice loss. Later chapters present an intercomparison of recent observations and simulated RILEs.

1.1 Sea Ice Geography & Climatology

In many ways, a persistent sea ice cover is a defining characteristic of the Arctic environment. Until recently, the majority of the Arctic Ocean was covered year-round by sea ice that had survived one or more melt seasons, thickened by slow accretion of frozen ocean water during the winter, refreezing of snowmelt at the surface, and rafting during collisions as individual floes move in response to winds and ocean currents. This multi-year ice is considerably thicker, fresher, and more resistant to melting than ice that has yet to survive a melt season (first-year ice). This multi-year cover is promoted by i) cold Arctic temperatures, ii) low surface salinities in the Arctic Ocean, iii) a water mass structure that limits ocean mixing, and iv) limited pathways through which ice can exit the Arctic (Serreze et al. 2005). By contrast, ice cover in the unbounded Antarctic Circumpolar Ocean is largely first-year. Arctic ice extent naturally varies through the year, reaching an annual maxima at the end of the winter (in March; an average of 15 x 10^6 km^2) and an annual minima at the end of the summer (in September; an average of 8 x 10^6 km^2) (Serreze et al. 2005).

The presence of ice exerts a strong influence on various aspects of the climate system, including the radiation, heat, and moisture budgets. With an albedo considerably lower than the underlying ocean surface, sea ice acts to reduce surface absorption of incoming solar radiation during the summer. As an effective barrier to ocean/atmosphere exchange of heat and moisture, it's presence limits ocean cooling in the cold

season and warming in the warm season. In this way, a persistent ice cover promotes cooler, drier conditions than would otherwise occur (Fletcher 1965). The sensitivty of the climate system has been the subject of research for some time. Budyko (1962) predicted that a small change in the sea ice albedo could cause the disappearance of the sea ice within a few years. Work by Fletcher (1965) further suggested the removal of Arctic sea ice would lead to much warmer coastal Arctic temperatures in winter but only slightly warmer temperatures in the summer due to the ocean's heat storing capacity. More recently, sea ice loss has been identified as a key factor in the amplification of anthropogenic warming under enhanced greenhouse conditions (Holland et al. 2003; Lawrence et al. 2008) and a potential driver of abrupt Arctic climate shifts (Lindsay et al. 2005; Livina et al. 2012; Serreze et al. 2011a).

Recent observations indicate the Arctic ice cover is undergoing rapid change. Declines in ice extent have become evident in every month of the year, with the greatest decreases occuring in September (12.4% per decade for the period of 1979-2010) (Stroeve et al. 2012a). Reductions in ice coverage and thickness have also been observed in studies using data from submarine transects of the Arctic. Prior to 1997 over 90% of the area surveyed by submarines was ice covered in summer but this coverage gradually decreased in the early 2000's and was followed by an abrupt drop to 55% in Summer 2007 (Kwok et al. 2009b). The thickness of sea ice was also found to have decreased, -0.17 metres per year between 2003 and 2008 (Kwok et al. 2009a). With large volumes of multi-year ice being replaced with thinner first-year ice, it has been suggested that the Arctic could become seasonally ice free during the 21st century (Stroeve et al. 2012a).

Climate model projections mirror the observed sea ice decline, with multi-model ensembles showing almost universal ice decline when forced with realistic emissions scenarios (Stroeve et al. 2007). Model simulations prepared for recent iterations of

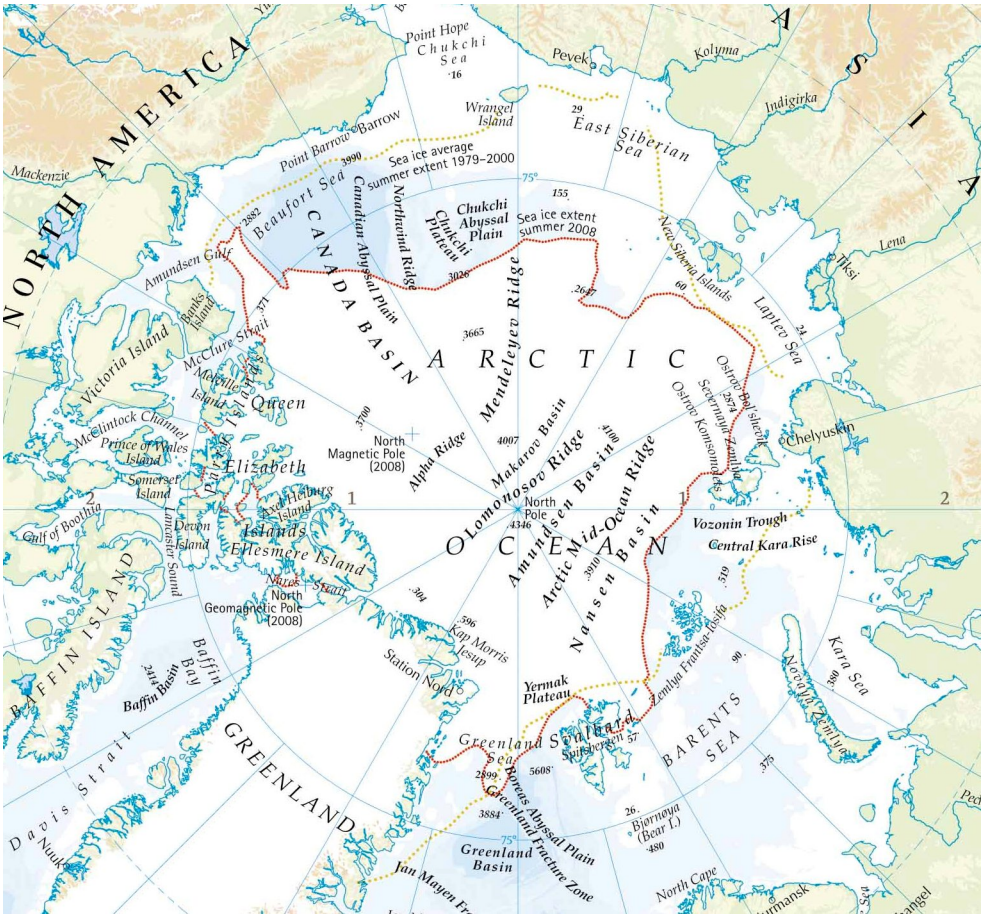

Figure 1.1: Map of the Arctic. Lennox, Jethro. (2008, October 15) "Times mapping of Arctic Sea Ice extent redrawn".retrieved from http://www.timesatlas.com/.

the Coupled Model Intercomparison Project (CMIP), organized through the Program for Climate Model Diagnostic and Inter-comparison (PCMDI) (Meehl et al. 2007)) forced with emission scenarios provided in the Special Report on Emmission Scenarios (SRES) (Nakicenovic et al. 2000) generally converge toward a seasonally ice free Arctic Ocean by the year 2100 (Zhang et al. 2005; Stroeve et al. 2012a), with at least half of models showing ice-free late summer conditions by the end of the 21st century (Arzel et al. 2006).

The SRES emissions scenarios were developed to encompass a range of demographic, economic and technological driving forces of future greenhouse gas and sul-

phur emissions. Each of the scenarios present different storylines for the future. A1B shows a future with rapid economic growth and a peak in global population by the middle of the 21st century and declining thereafter. In this future there is a rapid introduction of new and more efficient technologies with energy produced from a balance of sources. In A1B atmospheric carbon dioxide concentrations reach 532 ppm by the middle of the 21st century and climb to 717 ppm by 2100. In the A2 scenario human population increases continually throughout the century and technological changes are slower than in other scenarios. Atmospheric carbon dioxide concentrations climb to 532 ppm by mid-century and 856 ppm at the end of the century. B2 shows a future world with an emphasis on local solutions to problems of economic, social and environmental sustainability. The population continually increases throughout the century slower though slower than A2. There is more diverse technological change than A1B. Atmospheric carbon dioxide concentrations are 478 ppm in 2050 and 621 ppm in 2100.(Griggs et al. 2002).

Multi-model simulated anomalies in sea ice extent for the 21st century show largest reductions in SRES (Nakicenovic et al. 2000) A1B and A2 compared to B1 (Zhang et al. 2005). Models forced with these scenarios have average sea ice reduction rates of $-3.54 \pm 1.66 \times 10^5$ km^2 per decade and $-4.08 \pm 1.33 \times 10^5$ km^2 per decade for SRES A1B and A2 respectively (Zhang et al. 2005). Comparable changes were observed in the more recent CMIP5 results (Stroeve et al. 2012a), using updated emissions scenarios. Roughly a third of the total ice area reduction in the 21st century is projected to occur in the last 20 years of the century (Zhang et al. 2005). Both emissions scenarios lead to a decrease in area covered by multi-year ice and an increase in area covered by first year ice (Zhang et al. 2005).

An analysis of 21st century runs from six PCMDI models found that ice declines become increasingly apparent after a threshold annual sea ice coverage of 4.6 million

km^2 is reached. Once this threshold has been passed, models further reduce coverage to 1.0 million km^2 within an average of 32 years. This has been interpreted by some as an indication that sea ice may be nearing a 'tipping point', or a minimum annual extent below which a perrenial ice cover cannot be maintained (Wang et al. 2009b). It has further been suggested that the Arctic may have already passed such a tipping (Lindsay et al. 2005), although this hypothesis remains contested (Eisenman et al. 2009; Tietsche et al. 2011).

Several models also demonstrate periods of accelerated ice loss embedded within the broader ice declines (Stroeve et al. 2012a; Holland et al. 2006). In an analysis of ensemble projections from the Community Climate System Model version 3 (CCSM3), Holland et al. (2006) defined a rapid ice loss event (RILE) as a period in which the derivative of the the five year running mean September ice extent falls below -0.5 million km^2 per year for at least one year; any surrounding years with loss rates exceeding 0.15 million km^2 per year are included as part of the event. Using this semi-objective definition, RILEs were identified in eight of eight CCSM3 ensemble members conducted using the A1B emissions scenario (Holland et al. 2008). RILEs were also identified in CCSM3 ensemble members using the emissions scenarios, A2 and B1. Subsequent analysis of other climate models revealed similar abrupt ice events in several other PCMDI models (Holland et al. 2006). The duration of identified RILEs range from four to ten years in CCSM3 projections and three to eight years in other climate models (Holland et al. 2006). RILEs have also been connected to increased rates of land (terresrial) warming in the western Arctic, with 3.5 times greater terrestrial warming during RILEs than the overall 21^{st} century trend with greatest warming rates occuring in autumn. Additional climate model experiments suggest accelerated terrestrial warming is a consequence of the ice loss resulting from an RILE, rather than an additional phenomenon driven by a common cause (Lawrence

et al. 2008).

The current record minimum was set in 2012 at 3.41 million square kilometers (*Arctic sea ice extent settles at record seasonal minimum* 2016). The previous record extent set in September, 2007 at 4.28 million square kilometres (Stroeve et al. 2008). The minimum extent in 2007 is below the critical extent of 4.6 million km^2 described by Wang et al. (2009b) to initiate a rapid decline of ice in model simulations. The September, 2007 ice extent was 50% lower than average extents between 1950 and 1970 and significantly lower than the previous minimum set in September, 2005 (5.56 million km^2) and September, 2002 (5.96 million km^2). The four minimum extents set to date in the 21^{st} century support model findings of ice declines in the 21^{st} century and support the plausibility that a seasonally ice free Arctic will be reached this century.

1.2 Arctic Ocean

The Arctic Ocean contains, on average, the freshest sea water of all major ocean bodies; although waters in the North Pacific are less saline, the Pacific as whole remains more saline. The salinity of the Beaufort Sea is 28 practical salinity units (psu) and near the North Pole the salinity is 31 psu, based on data from transects of the USS Pargo in 1993 (Morison et al. 1998). The Arctic Ocean vertical structure is composed of four primary water masses: fresh cold surface mixed layer (0-50m), the cold halocline layer (50-200m) (Treshnikov et al. 1972; Coachman et al. 1974), warm salty Atlantic water (200-900m), and cold salty bottom water below 900 m (Coachman et al. 1974). The cold halocline layer is characterized by near-constant temperature, close to the freezing point, while salinity increases with depth. This layer is present in most regions of the Arctic Ocean. The cold halocline layer has

a stable density gradient that separates the fresh cold surface mixed layer and the warm salty Atlantic water layer; this acts to insulate the large sub-surface store of sensible heat located in the warm salty Atlantic water from the surface ice cover and the overlying atmosphere (Aagaard et al. 1981). Water salinity in the Arctic Ocean rapidly increases with depth near the top of the warm Atlantic water layer (between 200 to 300m), becoming a constant 34.5 to 35 psu at approximately 400 m (Steele et al. 1998).

The Arctic Ocean is comprised of two major basins: the Eurasian Basin, with a maximum dept of 4500m, and the Canadian Basin, with a maximum depth of 3800m. These two basins account for slightly less than half of the Arctic Ocean area, with 53% of the Arctic Ocean situated over large, shallow shelves and seas. These shallow regions include the Barents Sea (depth of 200-300 m), the Kara Sea (depth of 50-100 m), the Laptev Sea (depth less than 50 m), the East Siberian Sea (mostly less than 50 m) and the Chukchi Sea (depth of 50-100 m) and the narrow shallow continental shelves of North America and Greenland (Rudels et al. 2009).

Water enters the Arctic through the Bering Strait, by the Norwegian Costal Current, by the West Spitzbergen Current and through the Barents Sea Figure 1.2. Water entering the Arctic Ocean through the Bering Strait is relatively fresh compared to the Arctic Ocean. This is caused by freshwater inputs from river run-off and high rates of precipitation into the North Pacific Ocean relative to the Atlantic Ocean. Water and ice exits the Arctic via the Fram Strait, and the Canadian Arctic Archipelago (predominantly Nares Strait).

Work by Treshnikov et al. (1985) and Aagaard et al. (1989) aimed to quantify inflows of freshwater to the Arctic Ocean.Treshnikov et al. (1985) found the total amount of freshwater supplied by rivers to the Arctic Ocean is 3300 km^3/yr. Aagaard et al. (1989) estimated quantities of freshwater supplied to the surface mixed layer

by rivers were as follows: the MacKenzie (340 km^3/yr), Ob (530 km^3/yr), Yenisei (603 km^3/yr) and Lena (520km^3/yr) and influx of low salinity waters from the Pacific to the Arctic Ocean through the Bering Strait supply an equivalent 1670 km^3/yr of freshwater. The net import of freshwater into the Arctic Ocean was estimated to be 890 km^3/yr or a depth of 9 cm over the whole Arctic Ocean (Aagaard et al. 1989). More recent estimates by Serreze et al. (2006) found a volume of 8500 km^3 of freshwater enters the Arctic basin each year with 84,000 km^3 of freshwater resident in the Arctic basin. Transport of freshwater into the Arctic Ocean was found to be dominated by river discharge (38%), inflow through the Bering Strait (30%), and net precipitation over the Arctic (24%) (Serreze et al. 2006). Freshwater export from the Arctic Basin was found to be dominated by liquid transport through the Canadian Arctic Archipelago (35%) and transport of both liquid (26%) and sea ice (25%) through the Fram Strait (Serreze et al. 2006). It is important to note that Serreze et al. (2006) emphasize the high uncertainty in available estimates, but still were able to give mean estimates that close the budget. The Fram Strait is the only deep water connection between the Arctic and the Atlantic Ocean and it has been estimated that 90% of sea ice export from the Arctic flows through the Fram Strait with the remaining 10% exiting through the Canadian Arctic Archipelago (Vinje et al. 1998).

1.3 Ice Circulation

Aside from land fast ice, which grows out towards the open sea from a fixed connection to the shore, sea ice is constantly in motion. There are four principle forces which determine sea ice motion: wind, ocean currents, Coriolis force and internal ice stress. Internal ice stress is the most variable factor in sea ice movement, and depends largely

on ice compactness. When the sea ice is loosely compacted (e.g. as is often the case in summer) it can freely move in response to other forcing. When ice is compact the internal ice stress increases and its response to other forces varies. When wind is blowing compact ice towards the shore little ice movement should be expected due to limited space for the ice to move and increased internal ice stress. However, if the wind is blowing from shore towards the open ocean significant ice motion can occur, as the internal ice stress is reduced. Treshnikov et al. (1982) found that 50% of the long-term (several months) average ice motion is related to the geostrophic wind and the other 50% is tied to the mean ocean circulation. On shorter time scales geostrophic wind was found to account for over 70% of the ice velocity in the central Arctic Ocean with the influence of wind on ice motion decreasing within 400 km of the Coast (Treshnikov et al. 1982). Geostrophic wind is the theoretical wind balance between horizontal components of the pressure gradient force and the coriolis force; it blows parallel to pressure isobars. This implies that much of sea ice motion can be inferred from sea level pressure (SLP) data; mean SLP over the Arctic is shown in Figure 1.3. Key features include climatological anticyclones near the Beaufort, Chuckchi, and East Siberian Sea inferring large-scale clockwise winds in the region, and a strong pressure gradient across the Fram Strait, promoting northerly winds out of the Arctic towards the North Atlantic.

Treshnikov et al. (1982) found that on average, the ice moves 8 degrees to the right of the geostrophic wind direction and at scale factor of 0.008 to the wind speed. In summer the mean drift scale factor increases to 0.011 and at an angle of five degrees to the right of the geostrophic wind. In winter the ice drifts at an angle of 18 degrees to the right of the geostrophic wind and at scale factor of 0.007 to the wind speed. The long term motion of sea ice was found to move with a mean speed of 0.02 m/s (Treshnikov et al. 1982).

The general patterns of sea ice movement have been identified from observing the coordinates of North Pole (NP) research stations established on sea ice, the network of buoys in the Arctic Ocean released and maintained by the International Arctic Buoy Program (IABP) and from satellite measurements of sea ice motion. The majority of ice circulation can be described by two features: the Beaufort Gyre and Transpolar Drift, seen in Figure 1.2. The Beaufort Gyre is a clockwise circulation of ice and water in the Beaufort Sea and the Central Arctic Ocean region. The Transpolar Drift is the linear movement of ice from the Laptev Sea across the pole and into the North Atlantic via the Fram Strait. However, there is seasonal and annual variance in the characteristic ice drift. Serreze et al. (1989) found that although the annual mean of a seven year period studied had clockwise motion of ice in the Canada Basin, periods of anti-clockwise movement often occurred. These reversals were found to occur in late summer to early autumn, last up to 30 days, and have been linked to increased cyclonic activity over the region (Serreze et al. 1989).

Ice drift and wind stress have increased since the 1950s in both winter and summer seasons (Hakkinen et al. 2008). It has been suggested that the cause of the positive trend is increased Arctic storm activity over the Transpolar Drift Stream (TDS), due to movement of storm tracks towards higher latitudes (Hakkinen et al. 2008). However Rampal et al. (2009) suggested that the increase in drift speed is due to thinner ice with reduced mechanical strength leading to lower internal ice stress. Spreen et al. (2011) recognized the importance of both effects on increased ice speed over the period of 1992-2009; whereas Kwok et al. (2009b) found that sea ice drift exhibits a large inter-annual variability which cannot be explained by ice thickness.

Vihma et al. (2012) found that the annual movement of ice in the circumpolar, eastern Arctic, and the Fram strait was best explained by the pressure difference across the meridians 270° E and 90° E at the latitudes of 80°, 82° or 84° North. The suggested

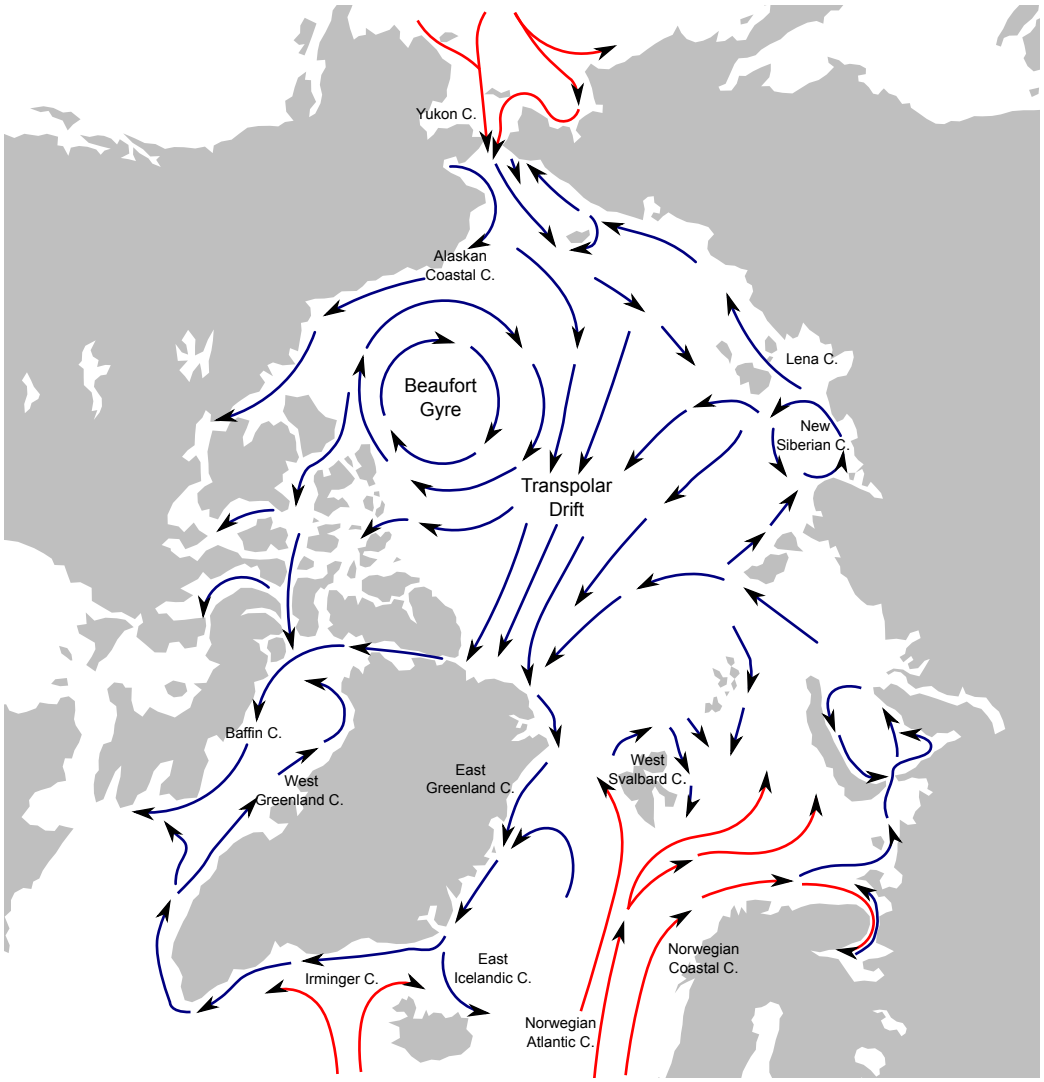

Figure 1.2: Prevailing upper Arctic ocean main currents and drifts.

reason for this relationship is that this pressure distribution produces geostrophic winds across the Fram Strait, flushing ice towards the open North Atlantic. Because internal ice stress is reduced when ice is pushed in the direction of open water, the ability of winds to move ice across the strait are enhanced by reduced internal stress. Enhanced ice melt would also occur as ice moves southward through the strait, further reducing the internal ice stress.

Sea ice movement may play a role in September sea ice extent as Ogi et al. (2007) found that winter and summer wind forcing accounts for up to 50% of the variance in September Arctic sea ice extent from one year to the next, through ice movement within the Arctic Basin and ice export. Meridional wind anomalies to the north and east of Greenland were correlated with September sea ice extent; this may be due to the importance of wind in ice export through the Fram Strait, similar to the findings of Vihma et al. (2012). Ogi et al. (2007) found that anti-cyclonic wind anomalies over the Beaufort Sea during summer favor low September sea ice extents, thought to be due to strengthening of the Transpolar Drift Stream. However, heat advection into the Arctic is associated with winds and it is possible that circulation associated with increased anti-cyclonic winds and increased meridional winds to the North and east of Greenland are associated with increased heat transport into the Arctic region.

1.4 Arctic Circulation

The connection between atmospheric circulation and sea ice variability has been extensively studied, due to its influence on ice movement, cloud cover and heat transport. The ocean and the atmosphere both transport heat from the lower latitudes to the poles, balancing energy imbalances. However, the atmosphere plays a larger role in

heat transport than the Ocean, accounting for 78% of meridional heat transport in the Arctic and 92% in the Antarctic (Trenberth et al. 2001). The overall annual Arctic circulation is shown in Figure 1.3. This image captures key elements of near-surface climatological circulation, including prominent low pressure cells in the North Atlantic (the Icelandic Low) and the North Pacific (the Aleutian Low), and a weak high pressure cell near the Beaufort and Chukchi seas (the Beaufort High). This last feature connects high pressures over Eurasia (the Siberian High) and central Canada. A final high pressure cell can be be seen over Greenland; this feature is largely an artifact of sea level pressure estimation over this high altitude region. The following section further describes these key features of near-surface Arctic ciruclation, and their seasonal variability.

1.4.1 Winter Circulation

Winter Arctic circulation is dominated by three semi-permanent features or centers of action: the Icelandic Low, the Aleutian Low and the Siberian High; these features become particularly strong in the cold season, resulting in very strong climatological pressure gradients. Average winter circulation is shown in Figure 1.4.

In the Arctic, the Icelandic low is the location of the highest frequency and strongest cyclones (Serreze et al. 1993). Cyclones which pass near Iceland often subsequently pass deep into the Arctic, following the North Atlantic storm track. The location of second greatest cyclone frequency is near the Aleutian Islands (Serreze et al. 1993). The Icelandic and Aleutian lows are both semi-permanent atmospheric features due to their positions downstream of major mid-tropospheric stationary troughs, caused by the diversion of the jet stream around orographic boundaries (Greenland and the Rocky Mountains) and differential surface heating between continents and oceans.

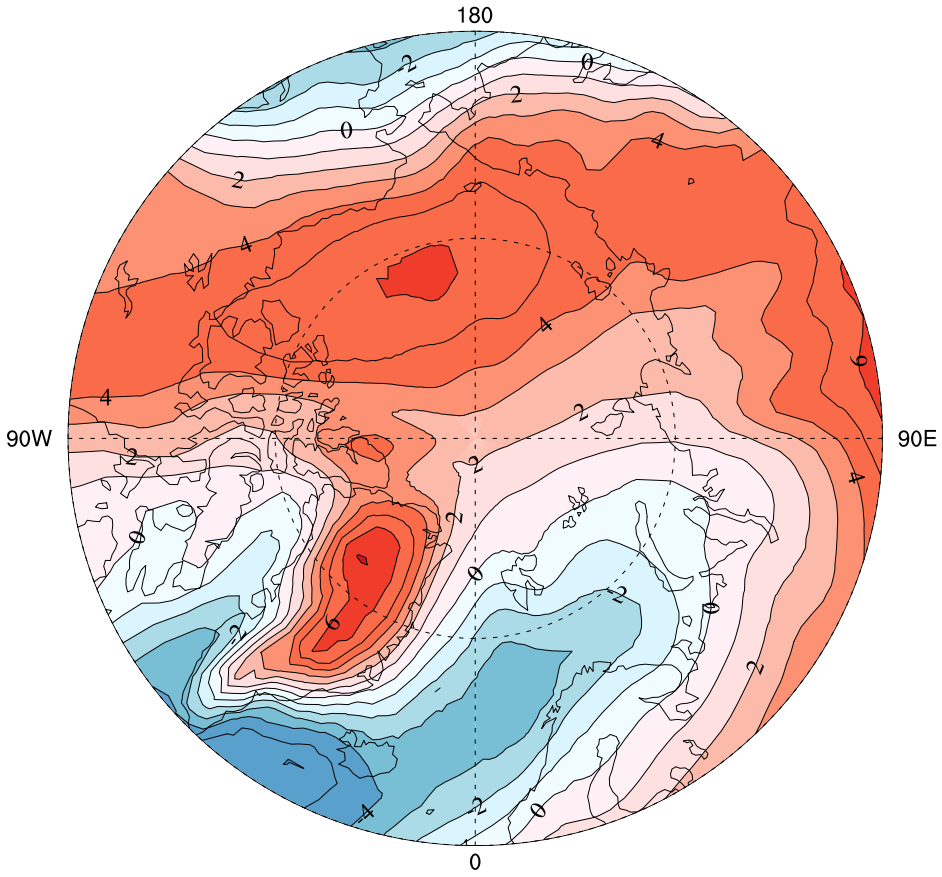

Figure 1.3: Annual average atmospheric sea level pressure anomalies of the Arctic 1961-2010 from monthly NCEP/NCAR reanalysis data. Contour labels show sea level pressure anomalies in kPa.

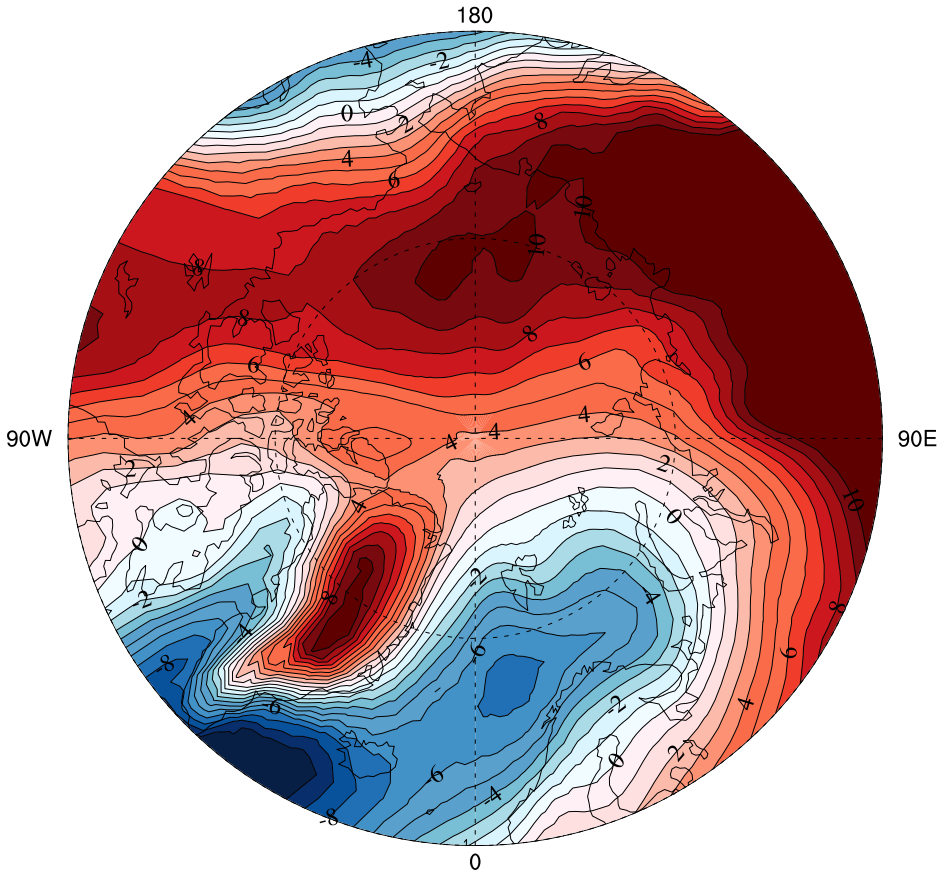

Figure 1.4: Winter (DJF) average sea level pressure anomalies for the period 1961-2010 from NCEP/NCAR monthly data. Contour labels sea level pressure anomalies in kPa.

The Siberian region has the strongest and highest frequency of anti-cyclones in winter. The Siberian High is the strongest semi-permanent anti-cyclone in the Northern hemisphere. Its strength is attributed to radiative heat loss over the snow covered Siberian land surface (Keegan 1958). High frequencies of anti-cyclones also occur over Alaska/Yukon and Western Siberia (Serreze et al. 1993). Winter anti-cyclones over the Central Arctic Ocean and Alaska/Yukon tend to be associated with a region of high pressure caused by the diversion of air around the Rocky Mountains, called the North American Ridge. Anti-cyclones are also common over Greenland, but tend to be weaker and occur less frequently than anti-cyclones in other dominant regions of the Arctic (Serreze et al. 1993). Anti-cyclones over Greenland should be viewed with some suspicion, as they may be partially an artifact of interpolating pressure measurements from observations at altitude to sea level for analysis; this can result in erroneously high sea level pressure values (Keegan 1958; Putnins 1970).

1.4.2 Summer Circulation

Peak cyclone activity is associated with the zone of maximum baroclinicity, which moves northward in summer, due to temperature differentials caused by unequal heating between the ice covered Arctic Ocean and the snow-free land surface. This northward shift coincides with a peak in Arctic cyclone and anti-cyclone frequency in summer, but systems are generally weaker in summer than in winter (Serreze et al. 1993) due to a smaller atmospheric temperature gradients. Cyclones in summer are more widely distributed over the Arctic basin with increased activity over the Alaska/Yukon region, western Eurasia, and Siberia (Serreze et al. 1988). The location of the highest cyclone frequency is at 85 degrees latitude, near the dateline (Serreze and Barrett, 2007). This peak is associated with an influx of lows generated over the Eurasian continent, and cyclogenesis over the Arctic Ocean and Ural trough

(Serreze et al. 2008). The Ural trough is a semi permanent trough in the mid to upper troposphere, associated with the north/south oriented Ural Mountains in western Eurasia. The mean summer circulation for the Arctic is shown in Figure 1.5.

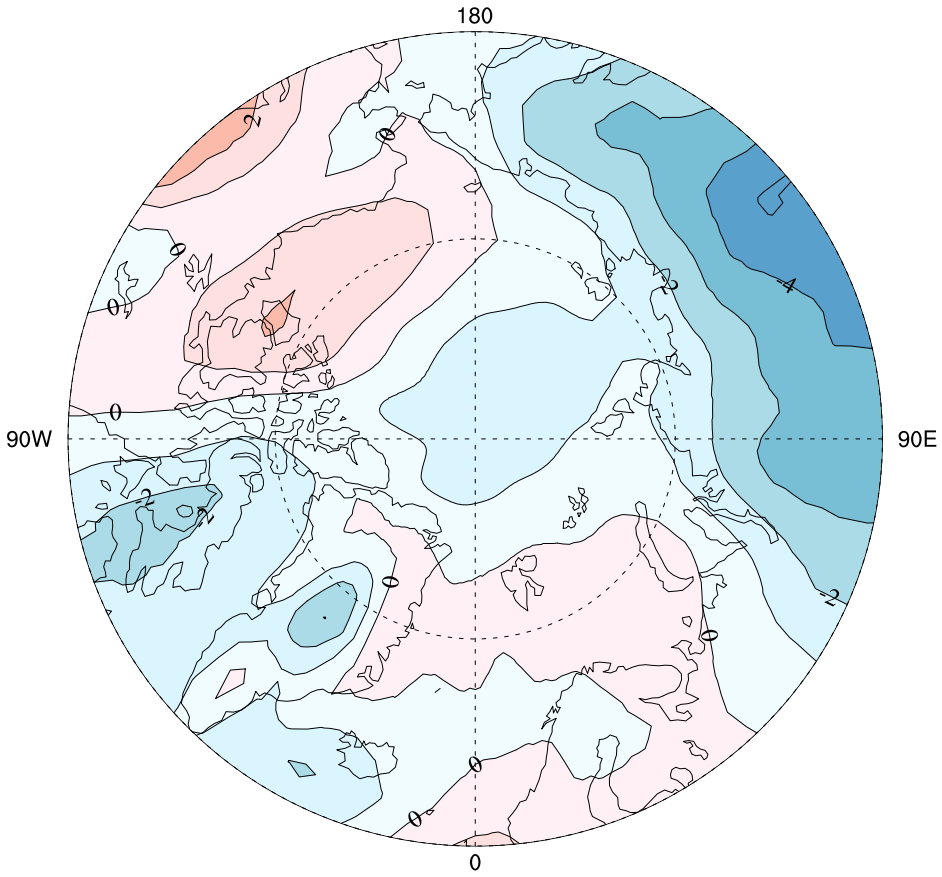

Figure 1.5: Summer (JJA) average sea level pressure anomalies over the Arctic from monthly NCEP/NCAR reanalysis sea level pressure for the period of 1961-2010. Contour labels show sea level pressure anomalies in kPa.

In the summer months, the Siberian and Alaska/Yukon highs largely disappear as anti-cyclonic activity shifts towards the Kara, Laptev, East Siberian, and Beaufort seas (Serreze et al. 1993). The strongest summer anti-cyclones are typically found over the Beaufort Sea (Serreze et al. 1993), corresponding to the semi-permanent feature the Beaufort High.

1.4.3 Beaufort High

The Beaufort High appears as a closed anti-cyclone in the long-term sea level pressure data averaged over spring months (Serreze et al. 2011b). In winter the Beaufort High appears as a weak connection between the Siberian High and the Alaska/Yukon ridge. In summer the Beaufort High is associated with an amplified North American ridge at the 500 hPa level, with a surface manifestation as a weak anticyclone near Victoria and Banks islands and the eastern Beaufort Sea. The Aleutian Low in the North Pacific tends to be deeper than normal when there is a strong Beaufort High. A strong Beaufort High in the summer is also associated with the positive phase of the Pacific North America (PNA) and, to a weaker extent, the positive phase of the Arctic Dipole Anomaly (DA) (Serreze et al. 2011b).

In all seasons but autumn, a strong Beaufort High is associated with positive lower-troposphere temperature anomalies covering much of the Arctic Ocean; especially pronounced in spring (Serreze et al. 2011b). The Beaufort High also causes prevailing anti-cyclonic surface winds over the Beaufort Sea region throughout the year (Serreze et al. 2011b), which act to reinforce ice circulaiton within the Beaufort Gyre. By contrast, increases in cyclone activity over the central Arctic Ocean can lead to temporary reversals of the mean clockwise ice motion in the Beaufort Gyre (Serreze et al. 1988), releasing ice to the Transpolar Drift and enhancing ice transport from the western arctic and out the Fram Strait.

1.5 Teleconnection Patterns and Ice Decline

Teleconnection patterns are persistent and recurring large-scale climate anomalies or preferred modes of lower frequency atmospheric variability. Phases of teleconnection patterns typically last for several weeks to several months, but may persist for years or

decades. Many tele-connection patterns reflect large scale changes in stationary waves in the upper troposphere, and consequently reflect changes in jet stream position. Resulting changes in storm tracks lead to quasi-predictable shifts in temperature and rainfall. Various tele-connection patterns have been connected to sea ice variability: the Pacific North America (PNA), the North Atlantic Oscillation (NAO) (Walker et al. 1932; vanLoon et al. 1978), the Arctic Oscillation (AO) (Thompson et al. 1998), the Dipole Anomaly (DA) (Wu et al. 2006), and the more recently described Arctic Rapid change Pattern (ARP) (Zhang et al. 2008) and Central Arctic Index(CAI) (Vihma et al. 2012). The following sections describe the physical structure of the teleconnection patterns and their connection to sea ice.

1.5.1 Pacific North American Pattern

The PNA involves changes in atmospheric pressure between centers near Hawaii, the Aleutian region, the leeward side of the Rocky Mountains (North American Ridge) and (to a lesser extent) the Gulf Coast Region of the south-eastern United States (Wallace et al. 1981). In the positive phase of the PNA, there is a deepening of low pressure systems over the Aleutian region and the south-eastern United States, a strengthening of the North American Ridge, and an increase in anti-cyclonic circulation over Hawaii. The positive phase of the pattern is tied to an increase in the intensity of the Beaufort High, as the Beaufort High is connected to the North American Ridge. The negative phase of the PNA has a weaker than normal North American Ridge and the strength of the Aleutian low also weakens. There is a reduced pressure gradient between the two circulation centers resulting in reduced storm activity around the Aleutian low and the North Pacific Region (Wallace and Gutzler, 1981). One approximation of the negative and positive phases of the PNA is shown in Figure 1.6.

The extreme September 2007 sea ice minima was accompanied by an unusual

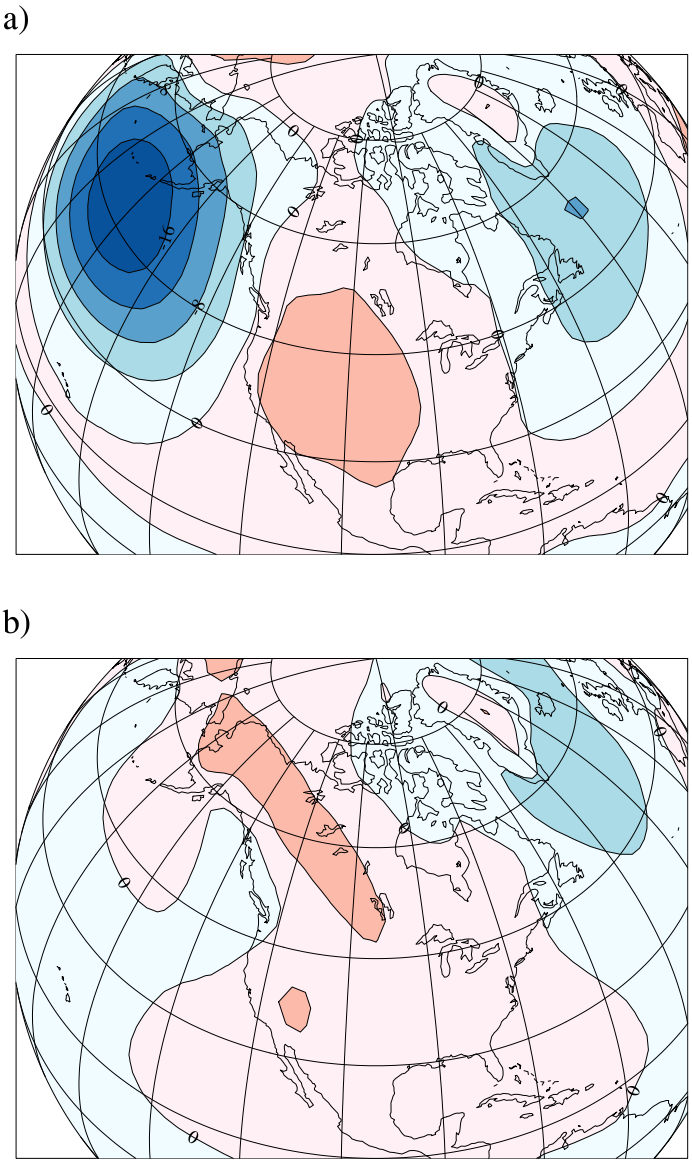

Figure 1.6: PNA positive phase and negative phases created by averaging monthly winter (DJF) sea level pressure observations from the NCEP/NCAR for identified high (+1 STD) and low (-1 STD) index months found in data from national weather service climate prediction center. Contour labels show sea level pressure anomalies in kPa.

summer circulation pattern apparently related to the PNA (L'Heureux et al. 2008). July, August and September had unusually clear skies accompanied by a ridge of higher-than-average atmospheric pressure over the central Arctic region, leading to reduced cloud cover and increased incident short-wave radiation at the surface (L'Heureux et al. 2008). Enhanced anti-cyclonic surface flow, in the Beaufort region favors cross-Arctic sea ice transport away from the western and central Arctic basins (Ogi et al. 2007; Maslanik et al. 2007). The PNA index in summer 2007 for the year was found to be 3 standard deviations above the 1950-2007 mean, and was associated with a strong anomalous anti-cyclone over the region of greatest ice loss between Beaufort and Siberia (L'Heureux et al. 2008).

1.5.2 North Atlantic Oscillation

The NAO describes the oscillation of atmospheric mass between the sub-arctic and sub-tropical Atlantic. The positive phase of the NAO reflects a strengthening of both the Icelandic Low and the Azores High, and the negative phase represents a weakening of both features. The positive and negative phases of the index are not spatially symmetric as the positive phase reflects an eastward displacement of the centers of action relative to the negative phase (Cassou et al. 2004); this is evident in the phases of the NAO shown in Figure 1.7.

The NAO index has been connected to sea ice variability, with the positive phase historically associated with less sea ice and the negative phase with increased ice extent (Deser et al. 2000; Omstedt et al. 2001; Hu et al. 2002). Deser et al. (2000) found that when sea level pressure and temperature fields were connected to the leading mode of ice variability, for the months January to March (1958-1997), the feature resembled the positive phase of the NAO. The first principal component of sea ice variability and the NAO index was found to have a correlation of 0.63 for the period examined.

a)

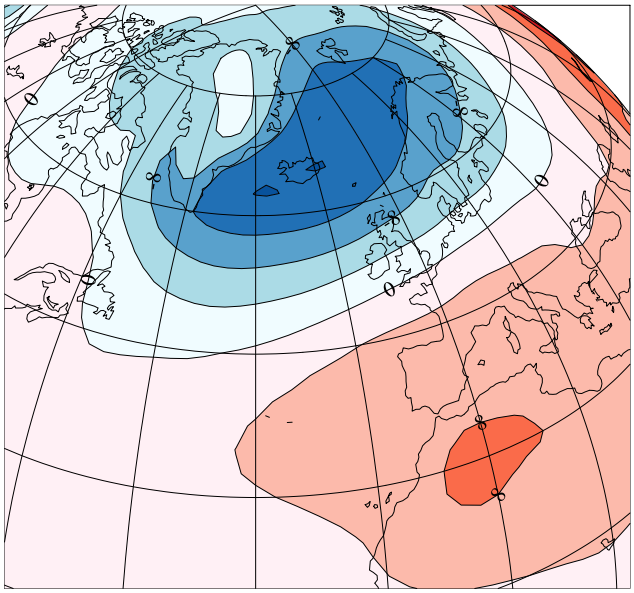

b)

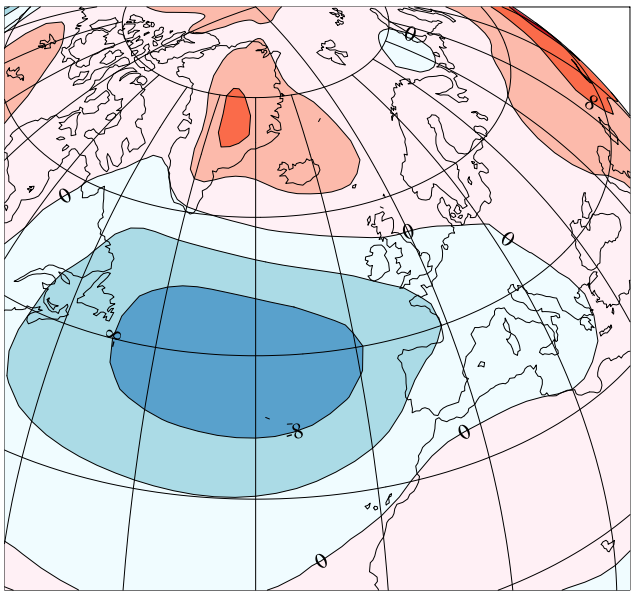

Figure 1.7: NAO a) positive and b) negative phases created by averaging the monthly sea level pressure fields from NCEP/NCAR reanalysisfor identified low (-1 STD) and high months (+1 STD) for winter (DJF) months from the period National Weather Center Climate Prediction Center. Contour labels show sea level pressure anomalies in kPa.

Deser et al. (2000), demonstrating that a negative NAO is associated with positive ice anomalies. The time series of the principal component of sea ice cover and the NAO are similarly correlated, but individual winters were found to be considerably different and unrelated; in some years the NAO was extremely high but the ice principal component was normal (Deser et al. 2000). Deser et al. (2000) suggested that an index like the NAO is a useful indicator of large-scale atmospheric circulation but may be an inadequate measure from which to infer details of atmospheric forcing relevant to ice variability. Deser et al. (2000) also found that large heat flux perturbations were also associated with changes in sea ice cover. This suggests that atmospheric circulation may be sensitive to sea ice variability in the Atlantic sector, particularly in the active storm track region east of Greenland. The winter storm track roughly reflects the position of the sea ice boundary, the 60% ice concentration isopleths (Deser et al. 2000). In the composite of low ice years, the ice edge east of Greenland was retracted poleward and the storm track expanded northwestward into the Greenland Sea relative to the high ice composite; it therefore remained unclear whether the NAO index drives ice variability or ice variability changes the polarity of the NAO (Deser et al. 2000).

NAO positive years have been found to have 50 cm thinner winter ice than NAO negative years in the Eurasian Coastal region (Hu et al. 2002). Thinner winter ice in NAO positive years combined with strengthened southerlies is thought to promote earlier ice break-up, which results in increased sea ice export out of the Arctic through the Fram Strait (Hu et al. 2002). A study by Kwok et al. (1999) found that ice export in the 1980s and 1990s through the Fram Strait has a 0.86 correlation with the NAO. Similarly, Hilmer et al. (2000) found a 0.7 correlation between ice volume flux out of the Fram Strait and the NAO index, indicating that a positive NAO may lead to enhanced ice export out of the Arctic. Strongly positive winter and spring NAO

indices may have also facilitated summer sea ice extent reductions observed during the 1980s and 1990s, as high ice exports in winter reduce ice compactness which leads to enhanced oceanic solar radiation absorption enhancing the summer melting process (Hu et al. 2002).

1.5.3 Arctic Oscillation

The Arctic Oscillation (AO) describes a hemispheric fluctuation of atmospheric mass between the sub-tropics and high latitudes (Thompson and Wallace, 1998), which is most apparent in winter. The AO is the first empirical orthogonal function of northern hemisphere sea level pressure, explaining 61% of the total variability (Wu et al. 2006).

The original definition of the AO has a prominent center of action in the Arctic region centered near Iceland and the Greenland-Iceland-Norwegian sea, with opposing, weaker centers of action in the North Atlantic and North Pacific; if pressures are low (high) over the Arctic, they are high (low) over the North Atlantic and North Pacific (Thompson et al. 1998). One representation of the Arctic Oscillation phases are shown in Figure 1.8.

Thompson et al. (1998) interpret the winter AO as the surface signature of modulations in the strength of the circumpolar stratospheric vortex. Winter stratospheric circulation is typically zonally symmetric, while the troposphere adopts a wavier pattern due to flow disturbance from orography and land-sea distribution. The structure of the AO resembles the stratospheric vortex (Gillett et al. 2003; Thompson et al. 2000), although the dynamic mechanism connecting the AO to the stratospheric vortex remains uncertain. The AO also appears to vary in response to surface forcings such as sea surface temperatures.

Variations in the strength of the AO can be interpreted as an exchange of atmospheric mass between the Arctic and mid-latitudes. The positive phase of the AO

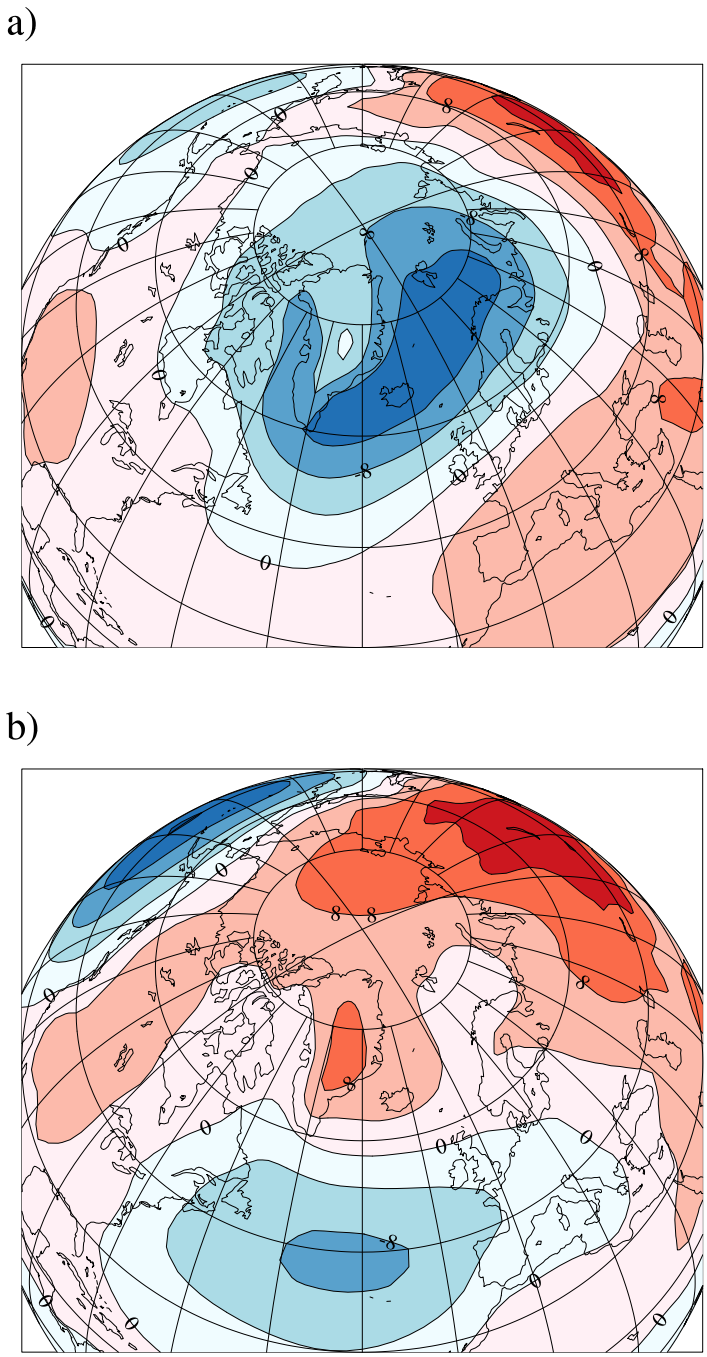

Figure 1.8: AO a) positive and b) negative phases created by averaging monthly sea level pressure field from NCEP/NCAR reanalysis for high (+1 STD) and low (-1 STD) index months in winter (DJF) identified for the period 1961-2010 from the National Weather Service Climate Prediction Center index time series. Contour labels show sea level pressure anomalies in kPa.

regime has less atmospheric mass in the arctic, which may reflect an increase in cyclone activity in the form of more intense storms or a higher frequency of cyclones. In the negative phase of the AO atmospheric mass moves into the Arctic from the lower latitudes, reflecting a decrease in cyclone activity, an increase in anti-cyclones, or a latitudinal shift in the climatological storm track.

The NAO and AO teleconnection patterns are closely related; this is likely a result of the greatest circulation connection between the Arctic and mid-latitudes occurring in the Atlantic region (Ambaum et al. 2001). The similarity of the patterns is supported by the time series of the AO and NAO being nearly indistinguishable from one another with a correlation of 0.95 in monthly data (Ambaum et al. 2001). Both indices also have a similar impact on sea ice variability.

Strong positive AO indexes occurred in the late 1980s and early 1990s accompanied by reductions in ice extent (Rigor et al. 2002). This shift was associated with stratospheric cooling, possibly due to ozone depletion and/or the build up of greenhouse gases leading to a stronger stratospheric vortex. The NAO phase was also positive between the late 1980s and early 1990s when ice reduction occurred, partially explained by the NAO favouring a stronger poleward flux of relatively warm ocean waters that inhibit ice formation (Dickson et al. 2000).

The positive phase of the AO is associated with lower pressure over the Arctic region, higher than normal temperatures over the United States and Northern Eurasia, positive ice anomalies in the western Atlantic and eastern Pacific, and negative ice anomalies in the eastern Atlantic and western Pacific (Deser et al. 2008), similar to the NAO (Dickson et al. 2000). The AO was been found to be the tele-connection pattern that explains the highest portion of sea ice concentration variability for the period of 1979-2006, with a correlation of 0.39 for September sea ice concentration and a correlation of 0.51 for March (Stroeve et al. 2008). The positive phase of the

AO is thought to produce winds favorable to enhancing the rate of ice transport out of the Arctic through the Fram Strait (Rigor et al. 2002) and has also been found to be the most important predictor of sea ice movement within the Canadian Basin in winter (Vihma et al. 2012).

Reduction in sea ice concentration between 1979 and 1993 were consistent with frequent AO positive atmospheric forcing. However, between 1993 and 2007 winter sea ice concentration trends were negative nearly everywhere, including declines in ice concentration in the western Atlantic (Labrador Sea) and the eastern Pacific (Bering Sea). These reductions coincided with the negative phase of the AO which is inconsistent with the theory that a positive AO is driving ice loss (Deser et al. 2008). This decoupling of the AO and sea ice concentration since the mid 1990s has been referred to the Arctic Paradox (Overland et al. 2005), and has raised concerns that Arctic sea ice has passed a critical threshold, where atmospheric circulation may no longer be the dominant driver of sea ice trends and variability (Lindsay et al. 2005). Rigor et al. (2004) presented a theory that the highly positive phase of the AO in the early 1990s led to the export of thick multi-year ice from the Beaufort region leaving thinner, younger ice which is more vulnerable to melt. Others have pointed to other atmospheric circulation regimes as being more important drivers of ice loss, and that links to the AO were overestimated in prior analyses (Maslanik et al. 2007; Wu et al. 2006).

1.5.4 The Dipole Anomaly

The Dipole Anomaly (DA) is the second leading Empirical Orthogonal Function (EOF) of monthly mean sea level pressure (SLP) in the Northern Hemisphere; in the cold season (October-March) it accounts for 13% of the total variance (Wu et al. 2006). The centers of action of the Dipole Anomaly are located between the Kara Sea and the

Laptev Sea and in the Canadian Arctic Archipelago and Greenland region, extending south eastward to the Nordic seas. The Dipole Anomaly is in its positive phase with negative sea level pressure anomalies between the Kara and Laptev seas and positive anomalies over the Canadian Arctic Archipelago extending south-eastward to Greenland, and it's negative phase is associated with positive anomalies over the Kara and Laptev seas and negative anomalies over the Canadian Arctic Archipelago (Wu et al. 2006). The positive phase of the DA is associated with northerly winds across the Fram Strait, increasing ice transport out of the Arctic. The positive phase of the Dipole Anomaly is also associated with a weakened Beaufort gyre which promotes ice dispersion out of the Beaufort Gyre (Wu et al. 2006). Increased ice transport via the Transpolar Drift and out of the Fram Strait is tied to increases in winds aligning with the Transpolar Drift Stream (Wang et al. 2009a).

The dipole anomaly was in positive phase in 2007, 2005, 2002, 1998 and 1995 when record low summer sea ice extents were reached (Wang et al. 2009a). In summer 2007, the DA was thought to enhance the ocean heat flux into the Arctic through the Bering strait, leading to accelerated ice melt (Wang et al. 2009a).

It has been suggested that the DA has greater influence on winter sea ice export out of the central Arctic and through the Fram Strait than the AO (Wu et al. 2006). However, the DA explains only 13% of the sea level pressure variability accounting for very little variance in comparison to the AO, which explains 61% (Wu et al. 2006) and, as the second EOF of SLP, the degree to which the DA reflects meaningful changes in atmospheric circulation patterns is uncertain.

1.5.5 Central Arctic Index

The Central Arctic Index (CAI) has been proposed as a better measure of potential ice export through the Fram Strait. Vihma et al. (2012) found that the CAI was the

most important factor in predicting mean ice velocity in the circumpolar arctic and was generally a better predictor than the Dipole Anomaly (DA). This may be due to the DA centers of action being non-static, allowing them to shift to different locations in the Arctic which may lead to unfavourable winds for ice export out of the Arctic Vihma et al. (2012).

The CAI is calculated as the difference in sea level pressure across the Transpolar Drift Stream, which is aligned with the Fram Strait, between the meridians 270° E and 90° E at 80° N, 82° N and 84° N latitude Vihma et al. (2012). It can be considered a regional (rather than large-scale) measure of wind forcing at the major site of ice export, complementary to the AO/NAO and DA. The majority of ice and water leaving the arctic basin have been found to exit through the Fram Strait (Aagaard et al. 1989) making the CAI a useful tool in predicting when atmospheric forcing is conducive to large volumes of ice export.

1.5.6 Arctic Rapid Change Pattern

The Arctic Rapid Change Pattern (ARP) (Zhang et al. 2008) is a tele-connection pattern with centers of action over the Eurasian Arctic and the North Pacific. The negative phase has anomalously low pressure in the North Pacific region and anomalously high pressure on the Eurasian coast. In the positive phase of the ARP there is higher pressure over the North Pacific center of action and lower pressure over the Eurasian coast. The negative phase of the pattern is thought to strengthen the poleward heat transport by enhancing transport of warmer North Atlantic water into the Arctic Ocean and the Barents Sea. The positive phase of the pattern gives favourable wind anomalies to advect ice out of the Arctic via the Fram Strait (Zhang et al. 2008). Zhang et al. (2008) proposed the pattern as a favourable alternative to the NAO structure when examining short time periods, and described the new pattern

as a northeastward shift of the NAO's Icelandic center of action. A representation of the ARP, based on composite analysis, is given in Figure 9.

The period of 2001 to 2006 was dominated by a negative ARP, which is theorized to have enhanced heat transport to the Arctic, suppressing sea ice growth and reducing multi-year ice production. In fall 2006, the ARP transitioned from it's negative to positive phase; this change persisted until summer 2007 (Zhang et al. 2008). It has been suggested that wind forcing associated with this shift caused advection of ice out of the Arctic and the movement of ice into ocean regions previously warmed by the negative phase of the pattern. The positive phase of the ARP is also thought to be associated with the high pressure anomalies in the Beaufort region which led to clear skies over the Beaufort region and initiated ice-albedo feedback in 2007 (Zhang et al. 2008).

1.6 Proposed Drivers of Observed Ice Loss

Research has been conducted into the relationship between reductions in sea ice extent and factors other than atmospheric circulation; these include: ice albedo feedback, prior ice thinning, critical ice thickness, cloud cover and surface air temperatures. These mechanisms will be discussed in the following sections.

1.6.1 Prior Ice Thinning

Rigor et al. (2004) found that the age of sea-ice explains more than half of the variance in summer sea-ice extent. Younger ice in the Beaufort Sea was theorized to re-circulate to the Alaskan coast more quickly, decreasing the amount of time available for new ice to thicken or ridge prior to the melt season. Re-circulation reduces the growing season by transporting ice to warmer coastal waters, reducing the ice growth rate.

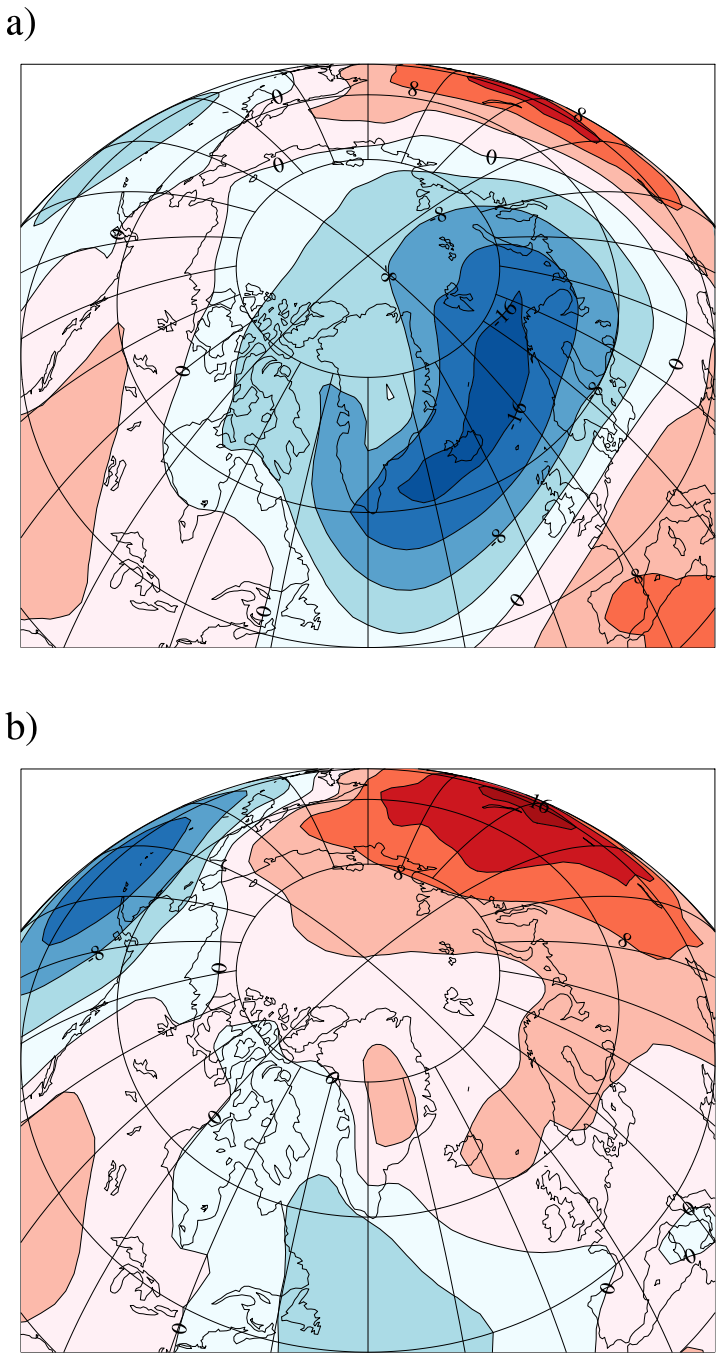

Figure 1.9: ARP a) positive and b) negative phases created by averaging winter (DJF) monthly sea level pressure field from NCEP/NCAR reanalysis for high (+1 STD) and low (-1 STD) index months for the period 1985-2009 from the timeseries from the International Arctic Research Center. Contour labels show sea level pressure anomalies in kPa.

Lindsay et al. (2009) suggested that although the loss of sea ice extent in 2007 was anomalous, the loss in total ice mass was not; rather, it was largely consistent with a steady ice thickness decrease that began in 1987. Both the areal coverage of thin ice at the beginning of the melt season and the total volume of ice lost in the summer had been steadily increasing before 2007 (Lindsay et al. 2009). The combined impact of trends in increasing thin ice coverage at the expense of thick multi-year ice, combined with the continuing reduction of ice volume in the Arctic, ultimately resulted in the pronounced 2007 minimum (Lindsay et al. 2009). These results agree with findings from other studies that suggest large ice reductions become common once a critical ice thickness is reached (North 1984; Gildor et al. 2001; Holland et al. 2008; Winton 2006).

1.6.2 Ice Albedo Feedback

Ice Albedo feedback is an important climatic process that has been recognized since at least the 19th century (Croll 1875). Changes in land and ocean ice or snow coverage alters the surface albedo. Ice and snow cover in the Arctic affects surface energy absorbance, reducing absorbance of incoming shortwave radiation and thereby cooling the surface. Thick multi-year ice reflects 55 to 75% of incoming solar radiation, first year ice reflects 30 to 60% and open sea water reflects 6 to 10% (Serreze et al. 2005). An increase in open water due to ice melt and/or replacement of multi-year ice with thinner first year ice therefore greatly increases solar absorption. Growth and overall thickness of sea ice is sensitive to sensible heat flux released to ice from the underlying ocean (Maykut et al. 1971). Sensible heat flux to the ice increases when the ocean is warmer. In this way, increases in open water initiate a positive ice albedo feedback, where open water causes additional energy absorption which leads to further ice melt.

Top and bottom ice melt rates are not equal and both melt rates exhibit inter-

annual variability (Perovich et al. 2003). The average annual surface melting rate between 1994-2007 was larger for the Beaufort Sea (0.64 m/yr) than near the North Pole region (0.26 m/yr) due to reduced intensity of incident solar radiation at higher latitudes (Perovich et al. 2008). In 2007, the bottom melt rate at the pole was similar to earlier years but the Beaufort region had significantly increased rates of bottom melt, six times the annual average of the 1990s and 2.5 times greater than in 2006 (Perovich et al. 2008). Bottom melt in the Beaufort sector occurred at a rate of near 4 cm per day for all of August and values as high as 11 cm per day in the last week of August (Perovich et al. 2008) compared to the region's characteristic average melt rate of 1 cm per day (Perovich et al. 2003). The increased fraction of open water was explained by ice albedo feedback and reduced cloud cover in the region by Kay et al. (2008) and provides an explanation for the 500% positive anomaly in solar heating of the upper ocean reported by Perovich et al. (2003).

1.6.3 Cloud Cover

Cloud cover reduces incoming solar radiation to the surface and enhances downwelling long wave radiation. Long periods of low solar radiation occur in the Polar Regions in winter, significantly reducing short wave radiation incident at the surface and causing significant surface cooling relative to summer. The Arctic summer is characterized by periods of 24 hours of daylight. The influence of cloud cover on the surface energy budget is different for the two seasons.

In winter with limited insolation, cloud cover has little impact on the short-wave energy budget. This implies that the net surface impact of winter clouds is considerable warming. Overland et al. (1991) estimated that 100% cloud cover in winter increases downwelling long wave radiation to the surface by 90 W/m^2. Cloud cover in winter has been associated with increases in surface snow temperature by

up to 15 degrees Celcius (Overland et al. 1991). The effects of summer cloud cover on long wave radiation is the same as winter, however due to enhanced insolation in summer, cloud cover also limits incident shortwave radiation at the surface. As such, summer clouds can act to cool or heat the surface depending on the surface energy balance.

Cloud cover variability near the sea ice margins has been strongly linked to the sea ice variability. Sea ice retreat is linked to a decrease in low-level cloud and a simultaneous increase in mid-levels clouds (Schweiger et al. 2008a). The change from ice covered to ice-free ocean changes the vertical temperature profile, increasing near-surface temperatures which decreases static stability and deepens the atmospheric boundary layer promoting the formation of higher level clouds (Schweiger et al. 2008a). The net surface energy balance impact of the change from low level to mid-level clouds is small as changes in temperature and humidity profiles compensate for the direct radiative impacts of the clouds themselves (Schweiger et al. 2008a). Schweiger et al. (2008b), conducted experiments with an ice-ocean model to investigate cloud anomalies over the Beaufort region in 2007. Findings were that the strong high pressure over the Beaufort Sea during summer was associated with a negative cloud anomaly, two standard deviations below the average from 1980-2007. However, they found that this negative cloud anomaly and increased down welling shortwave flux from June through August did not contribute substantially to the record sea ice extent minimum (Schweiger et al. 2008b).

Kay et al. (2008) found a 16% decrease in cloud cover over the Beaufort region between 2006 and 2007. They concluded that clearer skies led to increased radiative short wave fluxes and decreased long wave fluxes which would generate an additional 0.3 m top side ice thickness decrease or 2.4 K warming of the ocean surface which would cause bottom melt (Kay et al. 2008).

1.6.4 Surface Air Temperature

Increasing Arctic temperatures have been tied to reductions in sea ice concentration. Decreases in summer sea ice in the Pacific sector of the Arctic has been found to correlate with an Arctic-wide warming trend (Stroeve et al. 2007). Air temperatures at the 925 hPa level and principal components of sea ice concentrations have a correlation coefficients of 0.7 and 0.3 for September and March respectively (Stroeve et al. 2007).

Deser et al. (2000) found that the winter leading mode of ice variability is associated with large scale hemispheric surface air temperature anomalies: warming over the northern continents and cooling over the sub-polar oceans with largest SAT anomalies (+10 ^{o}C) coincident with changes in ice cover (Deser et al. 2000). However, it is unclear whether SAT increase is driving ice melt, or vice versa.

1.7 Potential relationships between variables and abrupt ice loss events

Several variables have been examined for a possible relationship to periods of abrupt sea ice loss such as critical ice thickness, cloud cover and ocean heat pulses.

Holland et al. (2008) examined CCSM3 model runs and found little evidence that arrival at a critical ice thickness leads to rapid ice loss events. They found that May ice thickness distribution over the Arctic basin was not similar between runs prior to rapid ice loss events, and mean ice conditions averaged over ice loss regions also vary considerably across the different events. Some of the events were preceded by large regions of ice cover reaching a critical thickness five years prior to ice free-conditions, but other runs only show a comparatively small area with the critical ice thickness reached.

Cloud cover in RILEs decreases in summer and increases in the fall in CCSM3 21st century CCSM3 model simulations (Vavrus et al. 2011). Cloud cover in the fall season is thought to produce an amplifying effect during autumn by reducing long-wave radiation losses, thereby leading to a later freeze-up (Vavrus et al. 2011). However, it is unclear whether increased cloud cover initiates reduction in ice extent or if ice extent reduction causes increased cloud cover (Vavrus et al. 2011). Holland et al. (2008) suggested that RILEs, result from natural variability in summer ice extent, which increases in the 21st century because of thinning ice cover due to anthropogenic forcing. Further research is necessary to investigate variables that may trigger RILEs. It has been inferred that RILEs may be associated with ocean heat pulses in the CCSM3 model simulations (Holland et al. 2006).

1.8 Gaps in Literature

There are many gaps in RILE research. In particular, there has been limited analysis of RILEs in models other than NCAR CCSM 3. Holland et al. (2006) stated that six of 15 models tested with the SRES A1B emissions forcing feature RILEs, as do seven of 11 SRES A2 models. However, only the dates of RILE periods in CCSM3 runs have been identified in publications. Cloud cover and critical ice thickness have been examined for their connection to RILEs in the CCSM3 model but not in additional models. Although general circulation models as a group share many features, and often feature common numerical schemes, their interpretation of climate and climate dynamics can diverge considerably. The presence of common phenomena (such as RILEs) in multiple models therefore suggests the phenomena are likely features of the true climate system; further, model intercomparisons have the potential to reveal useful insight into these phenomena.

There has yet to be an multi-model investigation into the relationship between RILEs and possible triggers of the reduction such as: tele-connection patterns, increases in atmospheric heat advection to the arctic, surface air temperature and the frequency of semi-permanent atmospheric features in rapid ice loss initiation. Research has also not be conducted to determine if rapid ice loss events are an artifact of model behaviour or could realistically occur in the 21st century, for example through a comparison of simulated RILEs and recent abrupt ice loss events.

1.9 Current Study

The current study examines relationships between atmospheric circulation and periods of rapid ice loss. The relationship between tele-connection indices, atmospheric features counts and rapid ice loss events will be examined. This will be accomplished by studying observed periods of rapid ice loss and simulated periods of rapid ice loss in models forced with SRES A1B and SRES A2 emissions scenarios. Analyses are framed around a synoptic climatology of pan-Arctic weather, using an approach that considers long-term mean climate anomalies as a summation of individual daily weather events. In contrast to analyses based on mean fields alone, the current approach can highlight the influence of high frequency variability obscured in long-term averages. Analyses will rely on synoptic typing of daily gridded data, using the method of self-organizing maps (SOMs), a technique from the family of neural networks (Kohonen 1990). Essentially a clustering technique, the SOM will be used to generalize high volumes of model output and observations by extracting key synoptic patterns. Variations in the frequency of these patterns will be used to compare data sets, assess the impacts of key teleconnection patterns, and analyse conditions surrounding ice loss events.

Models and observations are converging towards a seasonally ice free arctic by the end of the 21st century (Zhang et al. 2005). Removal of sea ice is expected to exert a pronounced influence on the Arctic, potentially acting to change atmospheric circulation, the depth and character of the boundary layer (Warshaw et al. 1973). The current study is intended to improve our understanding of how that change might proceed. The projection of ice free conditions in the Arctic by climate models and the associated potential climate changes emphasize the need for improved understanding of the relationship between sea ice and the atmosphere. An improved understanding could lead to the development of better climate models which will result in better predictions of the future climate and allow for better informed planning for northern communities and northern resource development.

Chapter 2

Methodology and Data Sources

This section contains a description of data sources and methodology used in this study. Methods of calculating sea ice extent from sea ice concentration, pre-processing of sea level pressure data, development of a synoptic climatology using self-organizing maps (SOMs) and the use of SOMs to investigate circulation changes during rapid ice loss events are described.

2.1 Data Sources

Gridded climate datasets sets, from model runs and atmospheric reanalysis, were obtained from various climate research agencies. Climate model output was obtained from the Program for Climate Diagnosis and Intercomparison's (PCMDI's) Coupled Model Intercomparison Project Phase 3 (CMIP3). Although a new iteration of CMIP (CMIP5) simulations is now available, this updated data was not used because a) it was not available when the current project was starting, and b) all available literature on rapid ice loss events (RILEs) at the time was completed using CMIP3 data, making CMIP3 a useful comparison point. Model runs obtained include 20^{th} century baseline simulations (20c3m) and two 21^{st} century climate change scenarios; a middle of the

road scenario (SRES A1B), and a high emissions scenario (SRES A2). 20th century climate model simulations were obtained for the purpose of validating climate models, accomplished by comparison between models and reanalysis datasets. Additional model runs of the National Center for Atmospheric Research's (NCAR) Community Climate System Model 3 (CCSM3) model forced with SRES A2 and SRES A1B emissions scenarios were obtained from the Earth System Grid Federation (ESGF). Although not included in the PCMDI database, these additional CCSM3 simulations feature several documented rapid ice loss events (Holland et al. 2006), making them useful data points in the current study.

The 20c3m simulations were produced by forcing general circulation models (GCMs) with greenhouse gases, sulfur, and aerosol concentration evolutions observed during the 20th century, as well as recorded timeseries of other external sources of climate variability such as solar variability (Meehl et al. 2007). These cover the complete 20th century, ending in the year 2000. In cases where multiple simulations from a single model were produced, the 20th century forcing was started from slightly differently initial model conditions; referred to as an ensemble simulation, this multi-run approach provides a better sense of simulated climate variability, and allows rough uncertainty estimates to be generated. 21st century simulations were generated by continuing 20c3m beyond year 2000 with evolving greenhouse gas concentrations prescribed by one of several greenhouse gas scenarios prepared for the Intergovernmental Panel on Climate Change (IPCC) Special Report on Emissions Scenarios (SRES) (Nakicenovic et al. 2000) (Meehl et al. 2007). SRES A1B simulations reflect a somewhat optimistic future, in which international cooperation, new technologies, multiple energy sources, and a global population peaking at 9 billion in 2050 lead to moderate rises in greenhouse gas forcing (Nakicenovic et al. 2000). SRES A2 simulations are forced with higher greenhouse gas concentrations, associated with limited interna-

tional cooperation, continuous population increase, and continued emphasis on energy from fossil fuels (Nakicenovic et al. 2000). RILEs have been identified in the NCAR CCSM3 when forced with these two scenarios (Holland et al. 2006).

Re-analysis data was obtained from the first National Center for Environmental Prediction (NCEP)/National Center for Atmospheric Research (NCAR) Reanalysis Project. The NCEP/NCAR reanalysis assimilates data from land surface, ship, raw-insonde, pibal, aircraft, satellite and other measurement sources with prior model forecasts to a uniform grid which covers the entire globe, using a static data assimilation and forecasting system to provide a complete, long-term (Kalnay et al. 1996). The reanalysis consists of two distinct data types: analysis fields, which incorporate direct observations, and forecast fields that are entirely a product of the weather model used in the reanalysis. The current study exclusively uses analysis fields, which can be considered a "best guess" of the atmospheric state given available observations for recorded times.

Daily mean sea level pressure data was obtained for 20c3m model simulations covering the period 1961 to 1999. Models for which data was obtained are listed in Table 2.1. This time period represents the longest common period between 20c3m model runs and the NCEP/NCAR reanalysis product. It is beneficial to use the longest period of common data to minimize the possibility that low frequency modes of variability (such as the Pacific Decadal Oscillation) will result in spurious disagreement between models and re-analysis product; as periods of comparison become longer, it becomes more likely that the full range of climate variability is respresented in each data set, providing a more realistic point of comparison. A concern with using this time period is that the early portion of the reanalysis includes a substantial period prior to widespread satellite observations of the Arctic; data prior to the late 1970s may therefore be poorly constrained by observations relative to later decades.

However, research on reanalysis products in the Arctic has shown that the reanalysis products are skilled at cyclone tracking before and after the introduction of satellite measurements, and the NCEP/NCAR reanalysis appears to be reliable back to 1958 (Bromwich et al. 2007).

A record of monthly sea ice extents was obtained from the National Snow and Ice Data Center (NSIDC) to accompany the reanalysis data set. NSIDC calculates sea ice extents, total ice-covered area, ice persistence and monthly climatologies from satellite measurements of sea ice concentrations on a 25 x 25 km grid. The data set begins October 1978, which marks the beginning of satellite observations in the Arctic, and is updated regularly with new observations. Sea ice extent data was used for the period of 1979 to 2010. Monthly gridded sea ice concentration data was obtained from the PCMDI and ESGF databases for all model runs of the SRES A1B and SRES A2 scenarios which had daily sea level pressure fields available.

Monthly values of tele-connection indices for the AO, NAO and PNA were obtained from the Center for Climate Prediction (CCP) of the National Weather Service (NWS) of the National Oceanic and Atmospheric Association (NOAA). Values for the Arctic Rapid Change Pattern (ARP) index were obtained from the International Arctic Research Center (IARC).

A monthly value of the Central Arctic Index was not available from any agency. Values of the Central Arctic Index at latitudes 80, 82 and 84 were calculated using monthly NCEP/NCAR sea level pressure data for the period of 1961-2010. The index is calculated as the pressure difference in units of millibars between longitudes 90 degrees west and 90 degrees east at latitude degrees 80, 82 and 84 as described by (Vihma et al. 2012).

2.2 Methods

2.2.1 Sea Ice Calculations

Sea ice concentration was used to calculate total areal Arctic sea ice extent, which was subsequently used to identify periods of rapid ice loss. Sea ice extent is one of two measures of the area of ocean covered by ice; the other measure is sea ice area. Sea ice extent is the summation of grid cell areas with a fraction of ice coverage greater than 0.15. Sea ice area is calculated as the sum of grid cell areas multiplied by the cell's ice fraction. Sea ice extents are larger than the sea ice areas, as it counts the marginal ice zone as being fully part of the Arctic sea ice pack. Extent is used in the current study to facilitate comparison with previous extent based ice loss research (e.g. Vavrus et al. 2011; Holland et al. 2006; Holland et al. 2008). The sea ice concentration field was also used to calculate sea ice extents which were used in work by Holland et al. 2006 to identify periods of rapid ice loss.

Grid cell areas corresponding to each sea ice concentration point observation were calculated for each model using the grid area function from the Climate Data Operators (CDO) software package (Schulzweida et al. 2004). The grid area function calculates grid cell area using the model's grid type and grid coordinates. The fraction of sea ice coverage for each cell was multiplied by the grid cell areas and the resulting array was summed to calculate the sea ice extent.

The annual minimum sea ice extent was determined by identifying the month of minimum ice extent in each year. A five year running average was taken of the annual minimum sea ice extents. The loss rate or derivative of the five year running average was determined as the change between the current year and the preceding year.

Rapid ice loss events were identified following the method of Holland et al. 2006. The algorithm searches the derivative of the five year running mean for years with

Table 2.1: Models included in the study for identification of Rapid Ice Loss Events (RILEs). Resolution is listed as degrees latitude by longitude. Models and re-analysis used in self-organizing map (SOM) training are indicated by a star after the model name.

Model	Governing Body	Country	Atmospheric Resolution	Ocean Resolution
BCCR BCM 2.0*	Bjerknes Centre for Climate Research, Univeristy of Bergen	Norway	1.85 x 1.85	0.5-1.5 x 1.5
CCSM 3.0*	National Center for Atmospheric Research	USA	1.4 x 1.4	0.27-1.0 x 1.125
CGCM 3.1*	Canadian Centre for Climate Modeling and Analysis	Canada	3.75 x 3.75	1.85 x 1.85
CGCM 3.1(T63)*	Canadian Centre for Climate Modeling and Analysis	Canada	1.85 x 1.85	0.9 x 1.4
CNRM CM3*	Centre National de Recherches Meteorologiques, Meteo France	France	1.85 x 1.85	152 x 182
CSIRO-Mk3.0	CSIRO Atmospheric Research	Australia	1.85 x 1.85	0.84 x 1.875
CSIRO-Mk3.5*	CSIRO Atmospheric Research	Australia	1.85 x 1.85	0.84 x 1.875
ECHAM5-MPI*	Max Planck Institute for Meteorology	Germany	1.85 x 1.85	1.5 x 1.5
GFDL CM2.0*	U.S. Department of Commerce/NOAA/Geophysical Fluid Dynamics Laboratory	USA	2.0 x 2.5	0.33-1.0 x 1.0
GFDL CM2.1*	U.S. Department of Commerce/NOAA/Geophysical Fluid Dynamics Laboratory	USA	2.0 x 2.5	0.33-1.0 x 1.0
GISS AOM	NASA Goddard Institue for Space Studies (NASA/GISS)	USA	3 x 4	3 x 4
GISS model e r	NASA Goddard Institute for Space Studies(NASA/GISS)	USA	4 x 5	4 x 5
HAD GEM 1	Hadley Centre for Climate Prediction and Research Met Office United Kingdom (UKMO)	UK	1.25 x 1.875	1.0 x 1.0
HADCM 3	Hadley Centre for Climate Prediction and Research Met Office United Kingdom (UKMO)	UK	2.75 x 3.75	1.25 x 1.25
IAP FGOALS 1.0 g	LASG, Institute of Atmospheric Physics (IAP), Chinese Academy of Sciences	China	2.8 x 2.8	1.0 x 1.0
INMCM 3.0	Institute of Numerical Mathematics, Russian Academy of Science	Russia	4 x 5	2 x 2.5
IPSL CM4*	Institut Pierre Simon Laplace	France	2.5 x 3.75	2 x 2[1]
MIROC 3.2(HIRES)	Center for Climate System Research (The University of Tokyo), National Institue for Environmental Studies, and Frontier Research Center for Global Change (JAMSTEC)	Japan	1.1 x 1.1	0.1875 x 0.28125
MIROC 3.2(MEDRES)*	Center for Climate System Research (The University of Tokyo), National Institue for Environmental Studies, and Frontier Research Center for Global Change (JAMSTEC)	Japan	2.8 x 2.8	0.5-1.4 x 1.4
MIUB ECHO-G	Meteorological Institute University of Bonn and Institue of KMA	Germany/Korea	3.75 x 3.75	2.8 x 2.8
MRI CGCM 2.3.2a	Meteorological Research Institute, Japan Meteorological Agency(JMA)	Japan	2.8 x 2.8	2.0 x 2.5
NCEP/NCAR Re-analysis*	National Center for Environmental Prediction/National Center for Atmospheric Research	USA	1.9 x 1.9	2.5 x 2.5

[1] 1.0 x 1.0 near equator, Mediterranean and Red Seas

a loss greater than 500 000 km^2/yr, with one or more years surrounding the period with a loss greater than 150 000 km^2. The identification of one rapid ice loss event in at least one run of a model was used as criteria for a model's inclusion in the training data set for the SOM. Models tested for rapid ice loss event criteria to model runs are listed in Table 2.1. In addition to the identification of periods of rapid ice loss, high ice loss years in model runs with RILEs were also identified, defined as years with ice loss greater than 0.450 Million km^2.

2.2.2 Data Pre-Processing

The sea-level pressure data required pre-processing prior to SOM analysis. This was necessary because climate model data and the NCEP/NCAR reanalysis were provided at different grid resolutions, from different map projections. The original grid cell sizes are shown in Table 2.1. SOM analysis of a geospatial field requires that elements of the data vectors correspond to the same geographical location, and that each training vector is the same length.

Equal area geographic grids are beneficial for SOM analysis; as all grid points represent an equal area, each has an equal geographical influence. As such,there is no need to introduce areal weighting to ensure that results are not disproportionately influenced by regions with higher observation density. A version of the National Snow and Ice Data Center's (NSIDC's) Equal-Area Scalable Earth (EASE) grid (Armstrong et al. 1995) centered over the North Pole was chosen as the common grid on which to interpolate the sea level pressure field for each model. A 200 km grid dimension size was selected as a balance between maintaining detail from high resolution climate models and limiting extrapolation from low resolution models.

Cressman interpolation (Cressman 1959) was used to interpolate sea level pressure data from the reanalysis and model grids to the EASE grid. The Cressman

Figure 2.1: Region of study. Includes all points north of 65^o

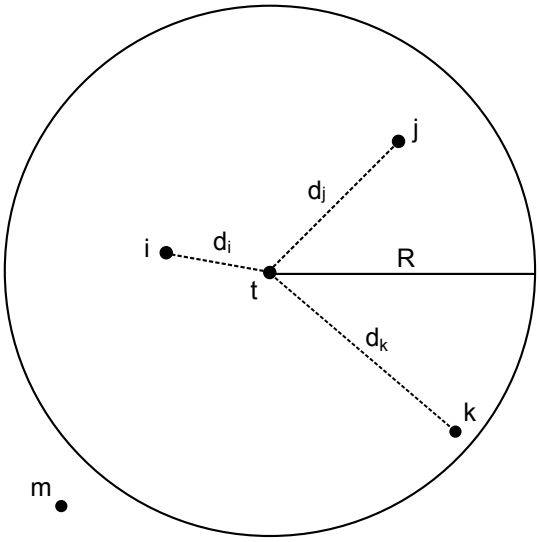

Figure 2.2: Cressman interpolation hypothetical distances between original data points (i, j, k and m) and a new grid point (t). Points i, j and k are within the critical radius R and are weighted inversely proportional to their distance from t. Point i will have the most influence on the value of t as d_i is the shortest distance and point k will have the least influence. Point m has no influence on t as it is outside the critical radius, R.

interpolation uses an inverse weighting function to interpolate data to a new geographical position. The value at the new coordinate is dependent on original values within a specified critical distance. The critical distance was selected to be 500 km after visual inspection of resulting interpolations from different critical distances. The 500 km adjustment radius preserved the size and shape of dominant features apparent in original data, from both high and low resolution models.

In the Cressman interpolation "weightings" are calculated to determine the amount of influence surrounding values have on the new value. The magnitude of the weighting is inversely proportional to the distance between the surrounding values and the new value. The weightings are determined using Equation 2.1 and the value of the new coordinate is calculated using Equation 2.2. Figure 2.2 shows the critical radius and distances between hypothetical points used in Cressman interpolation

calculations.

$$w_i = \frac{(R^2 - d_i^2)}{(R^2 + d_i^2)} \quad d_i \leq R \tag{2.1}$$

R is the critical update radius, and d_i is the distance between original values and the new coordinate. The interpolated value c_t is equal to the sum of the multiplication of each weighting by its point value within the critical radius, divided by the sum of all weightings. The calculation for the value at the new coordinate is shown in Equation 2.2.

$$c_t = \frac{\sum_{i=1}^{n} w_i c_i}{\sum_{i=1}^{n} w_i} \tag{2.2}$$

Interpolated values in the study region (shown in Figure 2.1) were converted to training vectors with a length of 593. The study region contains 593 grid cells and each training vector is therefore 593 points long. The training vectors were converted to sea level pressure anomalies by subtracting the vector's mean value. This emphasizes the circulation in the region, as circulation is dependent on the pressure gradient force. A further advantage of removing the mean of each training vector is that cyclonic and anti-cyclonic features are easier to identify when circulation is shown in terms of anomalies. Removing the mean of each training vector also serves to remove possible offset biases between models.

A dataset of winter training vectors was created by selecting training vectors within the months of December, January and February and a dataset of summer training vectors was created by selecting training vectors within the months of June, July and August. The winter and summer data subsets were used to create SOMs describing the Arctic synoptic climatology in these seasons.

2.2.3 Self-Organizing Maps

Self-organizing maps (SOMs) (Kohonen 1990) belong to the family of neural networks and provide a framework for assessing climate model performance on synoptic scales. Through an iterative training process, the SOM method approximates the distribution of an input data set using a relatively small number of "nodes", or archetypal patterns. The SOM can be used to categorize or summarize data sets, by identifying the node that provides the closest match to individual entries or vectors. The training process can be understood as a means of minimizing the sum of differences between the original data and the best matching nodes.

The algorithm treats the data as a continuum of states, with no assumptions regarding the underlying distribution. It is therefore well suited to climate data which is continuous and inherently non-linear. Nodes in the self-organizing map relate to one another through a rectangular two-dimensional grid. The training process can be interpreted as fitting a two dimensional surface to data distributed in a multi-dimensional space, always greater than one dimension and usually much larger.

The steps in the use of the SOM algorithm include: initialization, training and classification. Initialization is the placement of nodes in the data space. The nodes can be placed randomly, at specific locations, or systematically, e.g. using linear initialization. Linear initialization calculates the two principal eigenvectors of the data set and evenly spans the nodes along this space (Kohonen et al. 1996). The user specified dimensions of the SOM determines the amount of variability in the direction of the first and second principal component if linear initialization is used. An 8 by 6 SOM will have eight nodes spanning the direction of the first principal component and six spanning the direction of the second principal component.

In the training step, data vectors are sequentially shown to the map. In each step the nodes most similar to the training vector are adjusted to better match the

vector. The process for node adjustment is as follows: for the input vector $x \in \Re$, the Euclidean distance between the data vector and each node is calculated as $\parallel x - m_i \parallel$, where m is an array of all i nodes. The best matching node is determined as the node with the smallest Euclidean distance from the input data vector, described by $\parallel x - m_c \parallel = min\{\parallel x_n - m_i \parallel\}$, where m_c is the winning node. Additional nodes surrounding the winner are also adjusted if they are within the user selected update radius. The change in all nodes after exposure to the training vector is described in Equation 2.3.

$$m_i(t+1) = m_i(t) + h_{ci}(t)[(x(t) - m_i(t)] \tag{2.3}$$

Where t is the step number and $h_{ci}(t)$ is the neighbourhood kernel of adjustment rates which is dependent on the "learning rate", $\alpha(t)$, of the iterative process.

There are two types of neighborhood kernels in the SOM package, one based on the Gaussian function and the“bubble” type. The "bubble" type of neighborhood kernel was used in this study. In this type the neighborhood is a set of array points around node c, denoted as $N_c(t)$, as the neighborhood can vary with the step number. For nodes within the neighbourhood (i in the set of N_c) in a given time step, $h_{ci} = \alpha(t)$; $h_{ci} = 0$ for nodes outside the activated neighbourhood (i not in the set of N_c). The "learning rate' '$\alpha(t)$ is a monotonically decreasing function of time and varies between 0 and 1; a value of 1 sets the activated node to perfectly match the input training vector, while a value of 0 means the node is unchanged in a training step. Typically the learning rate decreases to 0 at the end of the training process.

The SOM algorithm operates with the assumption that data are continuous. Consequently, the algorithm may place nodes in discontinuous areas if they exist in the dataset; i.e. it may place nodes in regions that lack observations. This is due to the updating of un-activated nodes if neighbouring nodes are activated. This can

introduce problems if discontinuities exist for physical reasons (i.e. some states are impossible); however this is not an issue with this research, as atmospheric data is generally continuous and any implausible outcomes can be quickly identified as no data vectors will map to those nodes.

The states that are returned by SOM training relate to one another through the rectangular grid or "map", with similar states found nearest to each other and the most extreme states are typically located at the corners. The states at the ends of one diagonal are often similar to the positive and negative phases of the first principal component of the input data, with the second principal component often corresponding to the end of the other diagonal (Reusch et al. 2007). In atmospheric applications diagonally opposing nodes are rarely perfect inverses of one another, a consequence of nonlinearities in the climate system and asymmetry in teleconnection patterns. In this regard, SOM analysis presents additional, often complementary, information obscured in the more common empirical orthogonal function decomposition of that is often used to assess variability in large data sets.

After training is completed, the SOM is again compared to the training data vectors to assess the quality of the map, through calculation of the quantization error. The quantization error is the average mean squared error between the training vectors and the nodes to which they map. Lower quantization errors indicate the map better fits the distribution of the training data set. Quantization error is a useful tool for comparing multiple maps trained using different training parameters. The quantization error of the map together with its interpretability is used as the basis for selecting the best map for an application. Interpretability of maps can be evaluated using Sammon Maps (Sammon 1969).

Sammon mapping (Sammon 1969) is a method of representing relationships between high (n) dimensional data on a two dimensional plane, facilitating interpre-

tation. Each n dimensional node vector is converted to a 2 dimensional coordinate, the distances between the node coordinates is approximately equal to the Euclidean distance between the vectors. The Sammon map can be used as a tool for visual inspection of the relationship between nodes. Sammon maps are useful in identifying SOMs with a high degree of distortion; that is, SOMs in which separation of nodes on the two-dimensional node array does not lead to greater difference between nodes. This often produces a circular or twisted Sammon map. Distorted maps do not have less statistical significance, but may be more difficult to interpret than a "flat map", as neighbouring nodes are not necessarily most similar to one another.

Figures 2.3 shows an example of the self-organizing map algorithm applied to surface temperature data for three locations in Alaska (Fairbanks, Barrow and Anchorage). Using three locations was intentional as the x vector for each observation time is 3 dimensional and therefore the data can be represented in a three dimensional plot along with the resulting self-organizing maps after 1, 1000 and 25 000 training steps. The Sammon map corresponding to a 25 000 training step self-organizing map is shown in Figure 2.4. The example shows the impact of training on the 'shape' of the SOM, as it gradually adjusts to 'fit' the training data set. Initiallized as an evenly distributed grid in our 3D space, the final (trained) SOM instead places more nodes in regions with more observations. That is, it approximates the original distribution with fewer data points.

The final step in the use of SOMs is to compare training vectors and/or additional vectors to the map to type each vector. The occurrence frequency of nodes can be determined by tallying the number of vectors mapping to each node divided by the total number of vectors shown to the map. Climatology is established for each model by looking at the expected count of node occurrence in a year or the frequency of node occurrences for the whole data period. Deviations from climatology can be

observed as changes in the frequency of nodes or node counts in a year.

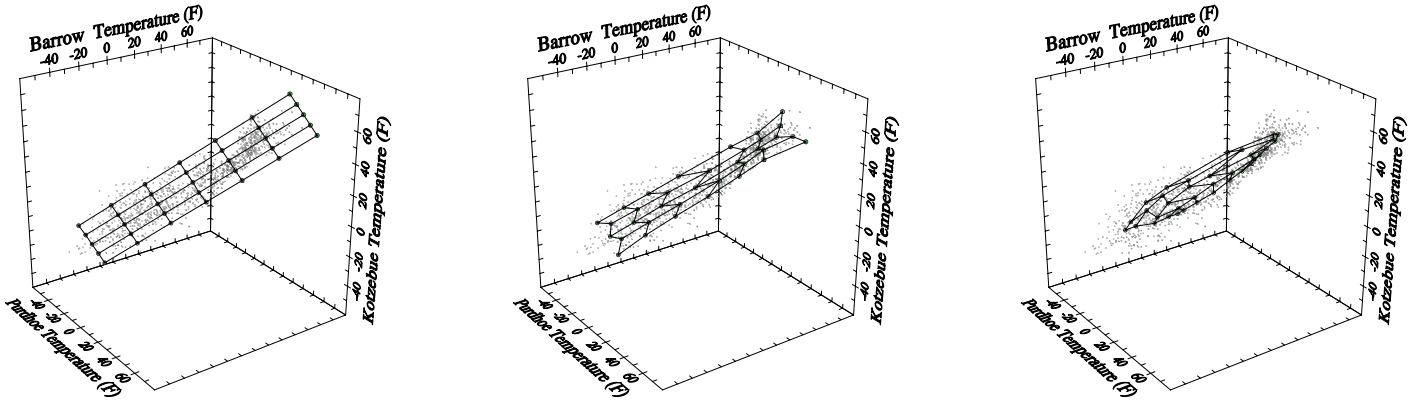

(a) 1 iteration (b) 1000 iterations (c) 25 000 iterations

Figure 2.3: A self-organizing map example using surface temperature data from three locations in Alaska (Fairbanks, Barrow and Anchorage). Each data point plotted is the temperatures at the three stations at a observation time. The three figures show the resulting self-organizing maps plotted onto the data distribution after 1 (a), 1000 (b) and 25 000 (c) training steps. The Sammon map corresponding to the 25 000 training step self-organizing map is shown in Figure 2.4.

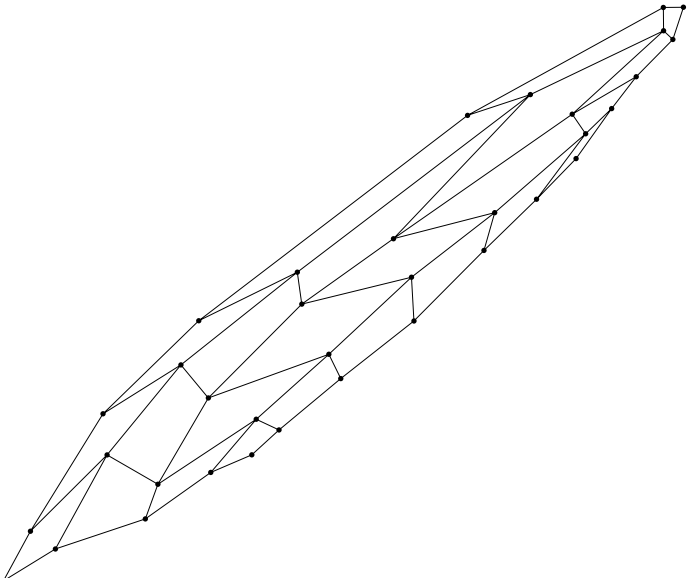

Figure 2.4: Sammon map for 25 000 training step self-organizing map example in Figure 2.3

2.2.4 Model Performance

SOMs with varying numbers and rectangular arrangements of nodes were trained and tested. Different learning rates and update radii were used. Maps trained for winter (DJF) and summer (JJA) periods were selected based on favorable state configuration and quantization errors, favouring maps with low quantization error and high interpretability. 48(8 x 6) node maps were selected as suitable arrangements for both winter and summer, providing a balance between describing circulation variability and providing enough generalization to allow for interpretation.

The map was trained with NCEP reanalysis and SRES A1B data from models marked with a star in Table 2.1. Only one ensemble run for each model, was used in order to provide equal training weight to all models. SRES A2 data was not used in the training as not all models used had daily sea level pressure data for runs forced with the SRES A2.

The 20^{th} century climatology for each climate model was determined by mapping 20^{th} century model data (1961-1999) and NCEP/NCAR reanalysis data (1961-2010) to the chosen SOMs for the appropriate seasons, and the frequency with which each SOM node occurs is calculated. In this way, a model's representation is summarized as vector (in this case, 48 points long) of occurrence frequencies. Models can then be compared to observations (e.g. renalyses) in terms of these frequencies. This similarity can be summarized as a correlation between the SOM node frequency vectors (Finnis 2008; Cassano et al. 2007). The correlation score was used to evaluate each model's skill in simulating the NCEP/NCAR node frequency climatology. The required value of the correlation score to be significantly different from zero is dependent on the selected confidence interval and the degrees of freedom of the matching pairs. The degrees of freedom is 2 less than the number of matching pairs; in this case two less than the number of nodes (N). For the forty-eight node SOM, we get a standard

error (sr) of correlation equal to 0.1474, and a 95% confidence interval (CI) of -0.29 to 0.29. That is, correlations with an absolute value greater than 0.29 are statistically significant.

Negative or insignificant correlations between models and the reanalysis could be attributed to an inability to accurately reproduce Arctic atmospheric dynamics. However, poor correlation scores could also result from model runs and observations being in different phases of a slow varying atmospheric mode such as the Pacific Decadal Oscillation. The use of a 39 years period of model output and 50 years of reanalysis reduces this possibility, but does not entirely preclude it.

2.2.5 Self-organizing map Applications

We have used trained SOMs as the basis for investigating connections between sea ice loss and atmospheric circulation. As a first step, we have identified key atmospheric features in SOM nodes, and tracked their occurrence in various data sets (models and reanalyses). Anomalous node or feature counts can then be compared to anomalous ice conditions. This process is outlined briefly here.

Feature counts were calculated for the winter and summer seasons in each year. The expected feature counts and standard deviations for each season were determined for each model run, calculated by averaging the occurrence rates, the count for the season divided by the number of days in the season, and multiplying this value by the number of days in the season. Significantly different values from average occurrence rates were determined using the 95 % CI; the bounds of the confidence interval are established by an interval around the average plus or minus the standard deviation multiplied by the z scores corresponding to the sample size and 95% CI. Statistically significant anomalies in feature occurrence can be determined by fitting a binomial distribution to annual feature counts, treating daily counts as a series of Bernoulli

(binary 'yes' or 'no') trials; in this case, testing whether the feature was or was not present in a given day. The fitted binomial distribution then describes the probability with which a particular feature (or node) can be expected to occur, and can be used to determine the likelihood of a given year's occurrence rate. In this distribution, the probability of each individual vector mapping to a particular node is p and the probability of the vector not mapping to the node is $1 - p$. p is the climatologically expected value. The expected number of days mapping to a node, E, for a given number of training vectors or days of data, n, is $E = pn$. In this study p for a particular node was calculated for each run, as the fraction of days (vectors) mapping to the particular node.

If n is large enough one can reasonably assume that the binomial distribution is approximately normal. However if the probability of occurrence is near 0 or 1 the assumption of normality is not valid. Normality can be assumed when $np(1 - p) > 5$ with the distribution becoming increasing normal with a value greater than 5 (Dunning 1993). This condition is met in the current study.

The distribution is calculated as:

$$\sigma = \sqrt{(p(1-p)n)} \tag{2.4}$$

The 95% CI is calculated by subtracting or adding the standard deviation multiplied by the z score 1.96 to the expectant value $E = np$ to define the interval. Values outside of this range are statistically significant at the 95% CI.

2.2.5.1 Teleconnection Indices

In order to facilitate intercomparison of different data sets, we have adopted a SOM-based means of quantifying the phase and strength of teleconnections. The approach

compares a given period to conditions expected during the positive and negative phases of a teleconnection; as such, it allows for asymmetry between opposing phases. This method is described below.

Monthly teleconnection index scores time series from various agencies listed in Section 2.1 were used to identify months in the historical record that were in the positive, negative or neutral phase of a given teleconnection. The criteria used to identify the phase associated with a given month were one standard deviation above the index average (positive), one standard deviation below (negative) and falling within plus or minus one standard deviation of the average score (neutral).

Positive and negative index months were grouped into two respective subsets, and the frequency with which NCEP/NCAR data mapped to SOM nodes was calculated for each subset. This gave a SOM-based "climatology" of negative and positive phases for each teleconnection examined. These were then converted to anomalies by subtracting the long-term climatological NCEP/NCAR node frequencies. Nodes with significant shifts at the 95% CI from the longterm NCEP/NCAR average were identified and all other nodes with insignificant shifts from climatology were masked with a value of zero. This gives a node anomaly vector that describes the statistically significant impacts of a given teleconnection phase; these will be referred to as teleconnection weighting vectors.

The state of a teleconnection over a given month or season is quantified as the dot product between i) SOM node anomalies for that month/season and ii) a teleconnection weighting vector. This gives two values for each teleconnection: one showing similarity to the positive phase, and another to the negative phase. Time series of these similarity measures were calculated for all model and reanalysis time series, and normalized to vary between -1 and 1. Seasons in which one of these dot product similarity scores met or exceeded one standard deviation were considered associated with

that teleconnection phase. This method shows good agreement between significant (above one standard deviation) seasonal teleconnection scores (created by averaging monthly tele-connection indices for each season) and significant dot products scores. The high and low threshold dot product scores established using the NCEP/NCAR reanalysis data were used as the bench mark for flagging years in model runs as low and/or high index seasons. Further discussion of our SOM-based teleconnections and their agreement with traditional indices is provided in the following chapter (section 3.6).

Chapter 3

Arctic Climatology

The following section presents the results of SOM training, and examines Arctic climatology in the context of this SOM output. This provides a basis for the ice/atmsophere analysis presented in subsequent chapters. The results of self-organizing map (SOM) training with the sea level pressure field for the Arctic winter (DJF) and summer (JJA) are shown in Figures 3.1 and 3.5 respectively. Each panel plot is a 48 node (8 x 6) SOM array which shows the prominent sea level pressure features of the region. Winter patterns have larger pressure gradients than summer; therefore different contour intervals were used for each plot to better emphasize the circulation of each season.

3.1 Winter Patterns

As was discussed in Chapter 2, the strength of the SOM methodology is that SOMs organize nodes in a manner that facilitates visual interpretation. This organization is apparent in the winter self-organizing map shown in Figure 3.1, with neighbouring nodes sharing similar weather features. Organization is further illustrated objectively using a Sammon map (Figure 3.2; Chapter 2). Using this property, nodes have been

subjectively grouped on the basis of weather features, facilitating the analysis of climatology and seasonal anomalies detailed in following chapters. A definition of key synoptic features present in the SOM follows, along with a list of the nodes these features occupy; this discussion is summarized in Table 3.1.

The most common features appearing in the winter SOM nodes are the Siberian, Central Arctic Ocean, and Beaufort Highs, along with low pressure systems in the North Atlantic (including Icelandic Lows and related systems near the Barents Sea) and North Pacific (Aleutian Lows). Most nodes feature clear, unambiguous representations of two or more of these features, and may include additional (if often weaker) representations of others. These weaker features are largely excluded from following analyses, as the degree to which the occurrence of these nodes reflects the presence of a weak feature is unclear. Visual inspection confirms individual observations mapping to a node often lack features represented weakly in that node. Instead, the nodes are typically activated by the presence of one or more of the dominant features.

The most prominent low pressure systems captured by the SOM analysis are centered over the North Atlantic. For the purposes of analysis, these have been subjectively separated between Icelandic lows (IL) and more easterly Barents lows (BAL). Strong IL events are found along the left side of the SOM [0:2 (column), 0:5 (row)], placing a deep low pressure system within the Greenland-Icelandic-Norwegian (GIN) Sea. Weaker IL events are found in the upper middle nodes ([3:4, 0:2]). BAL events shift the center of an Atlantic low eastwards relative to IL events, towards the Norwegian coast and Barents Sea; these occupy much of the lower center nodes [3:5, 3:5] and lower right [5:6, 2:5]. A small number of nodes in the lower right corner [7, 3:5] shift the BAL even further east over the Siberian coast (Eurasian Low, or EL). Additonal strong low pressure systems occur over the North Pacific and Alaska. Although the Aleutian Islands lie outside our SOM domain, these features can be

considered a limited representation of the climatological Aleutian Low (AL); we refer to these features as such to emphasize this connection. These AL features appear in the upper left [0:2, 0:2] and right [5:7, 0:2], with the center of the feature varying from the Bering Strait to the Alaskan interior and Yukon.

Of the anticyclonic features identified by the SOM, the strongest are located over Siberia (Siberian Highs; SH). Occupying the leftmost columns ([0, 1:5]; [1, 1:4]), SH demonstrate the greatest spatial extent of any SOM identified feature, covering the majority of northern Eurasia. Reading these SOM columns from top to bottom, the centre of the anticyclone shifts from western Siberia eastwards. Related nodes place an anticyclone further north, just off the Siberian coast; the most prominent of these are centered near the East Siberian Sea (East Siberian Sea Highs, or ESSH; [2, 3:4], [3, 3]), while others (generally weaker) are located over the Laptev Sea (e.g. [2, 0:2]). Highs located over and near the Beaufort Sea (Beaufort Highs, or BH; [3:4, 0:1], [1:2, 5], [3, 4:5]) vary considerably in strength, but occupy a large portion of the SOM's central nodes. In the current study, these are considered as distinct from similar anticyclones located closer to the pole (Central Arctic Highs, or CAH; [5:6, 0]). Other weak anticyclones are evident in the lower right quadrant of the SOM, including systems over Greenland (GH; [6:7, 1:3]) and the Canadian Arctic Archipelago (CAAH; [5:7, 4:5]), along with Eurasian Highs (EH; e.g. [6:7, 1]) that resemble weak, easterwardly displaced Siberian Highs.

The frequency distribution of NCEP/NCAR Reanalysis data from 1961-2010 is shown in Figure 3.3; that is, the relative frequency with which daily winter data maps to each SOM node. Nodes along the lefthand side of the SOM show relatively high occurrence frequencies, particularly near the center and lower left (e.g. [0, 2:4]); these nodes are dominated by strong Icelandic Lows and Siberian Highs. Other common winter features include Beaufort High events and Barents Lows, associated with nodes

Table 3.1: Atmospheric features captured in sub-regions of the winter SOM (Figure 3.1) and nodes in which they are found.

Feature Name	Abbreviation	SOM Nodes
Aleutian Low	AL	[0:2,0:2], [5:7,0:2]
Barents Low	BAL	[3:5,3:5], [5:6,2:5]
Beaufort High	BH	[3:4,0:1], [1:2,5], [3,4:5]
Canadian Arctic Archipelago High	CAAH	[5:7,4:5]
Central Arctic High	CAH	[3:4,2], [4,3], [5,1:2], [5:6,0]
East Siberian Sea High	ESSH	[2,3:4], [3,3]
Eurasian High	EH	[6:7,1], [7,0]
Eurasian Low	EL	[7,3:5]
Greenland High	GH	[6:7,1:3]
Icelandic Low	IL	[0:4,0:2], [0:2,3:5]
Siberian High	SH	[0:1,0:4], [0,5]

along the bottom of the SOM ([3:6, 4:5]); generally, these occur along with Canadian Archipelago Highs. The final highlighted region is a series of nodes oriented diagonally across the SOM's center ([5, 3], [4, 2], [3, 1]). These demonstrate generally weak features; it is likely that these are often triggered by days with weak circulation patterns, days in transition between stronger features, or days that do not fit neatly with other nodes.

Patterns which occur at relatively low frequencies include those that simultaneously feature a strong Aleutian Low, weaker examples of Icelandic Lows, and Siberian/Eurasian High features (upper left corner; [0:2, 0:2]); by contrast, the simpler patterns with a strong IL paired to a strong high in the eastern Arctic are much more common (lower left) . Patterns labelled Canadian Arctic Archipelago High [6:7, 0:1] and Central Arctic High [3:4, 0:1], East Siberian Sea High [3:5, 2:3] and Barents Low [5:7, 4:5] also occur at less than expected frequencies.

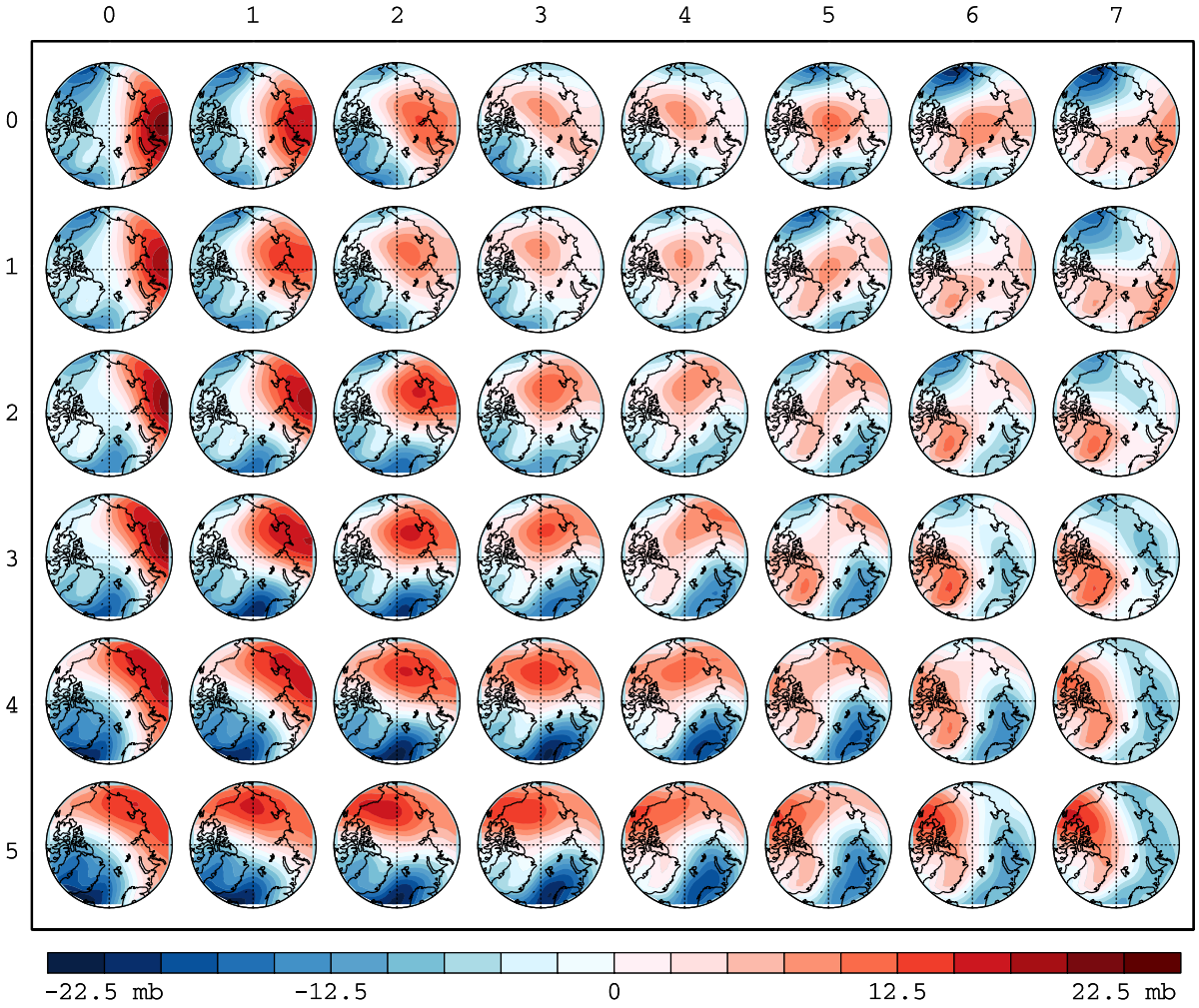

Figure 3.1: Winter(DJF) daily synoptic climatology patterns of the Arctic (above 65 degrees latitude) developed using SOM technique.

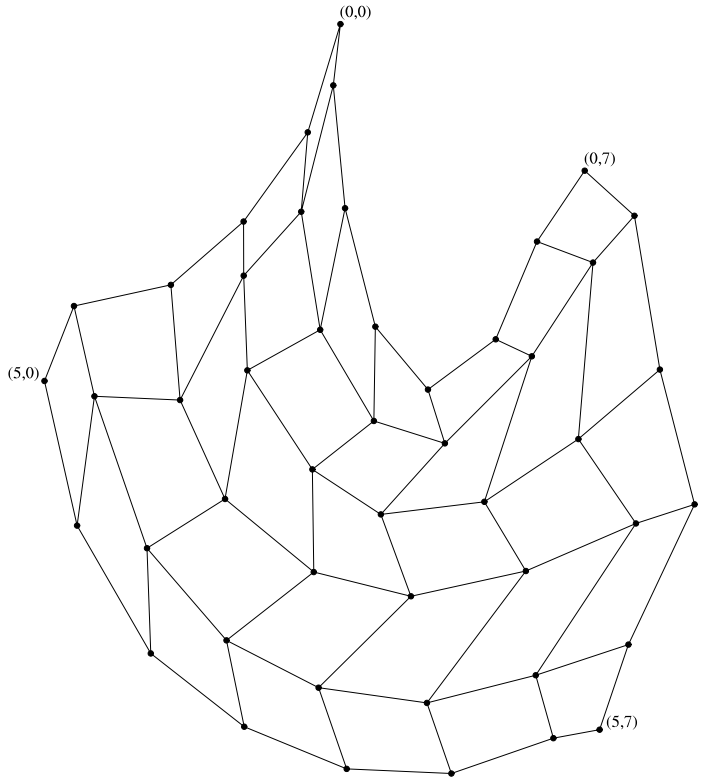

Figure 3.2: Sammon map corresponding to winter(DJF) self-organizing map of daily synoptic climatology of the Arctic (above 65 degrees latitude) shown in Figure 3.1.

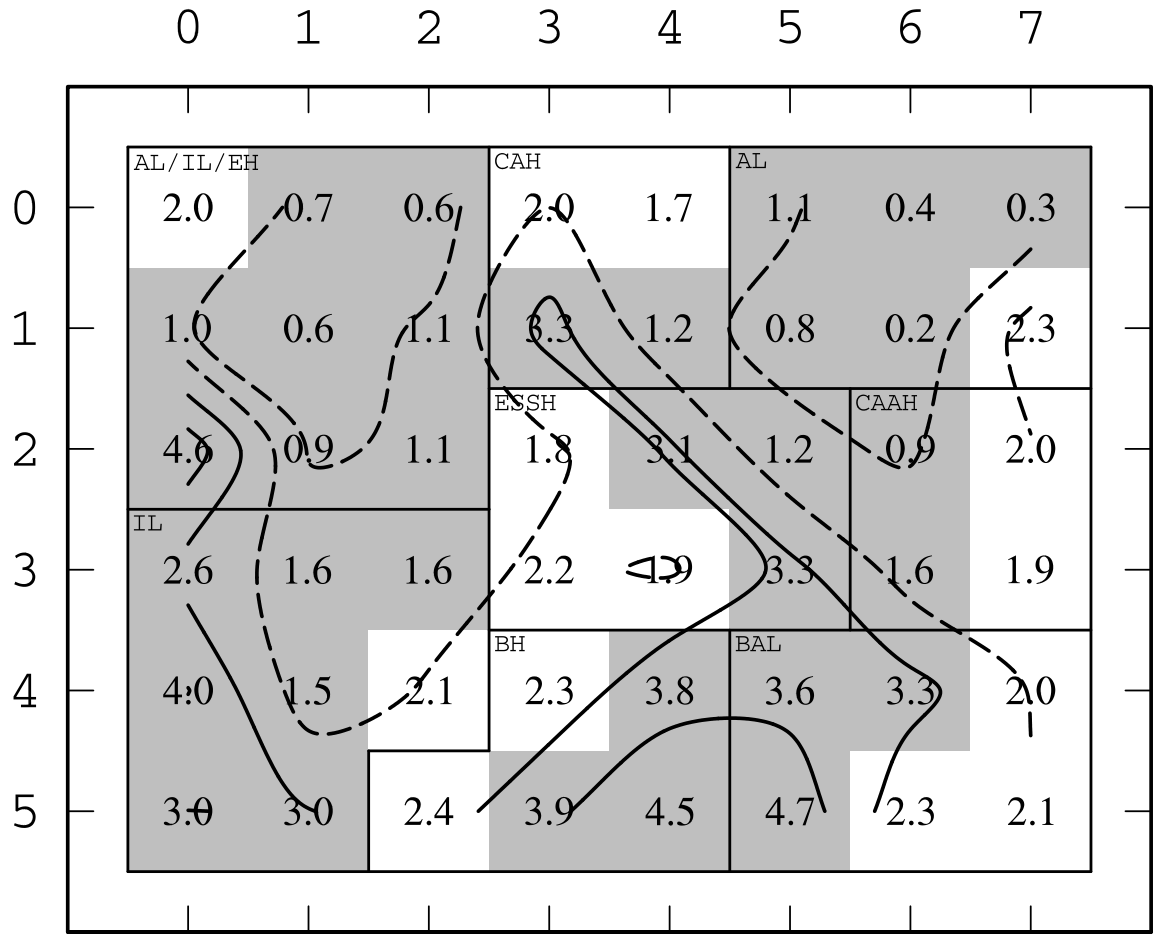

Figure 3.3: Occurence frequency of self-organizing nodes for winter (DJF) NCEP/NCAR reanalysis (1961-2010). Dashed contours are below the value that would be expected if days were evenly distributed between the 48 nodes (2.08%), and solid contours mark nodes with higher than expected frequency. Nodes which occur significantly (95% CI) above or below the expected value are shaded grey. To facilitate interpretation, the SOM has been separated into sections dominated by specific features; the dominant feature is labelled following the code given in Table 3.1.

3.1.1 Winter Model Performance

Model performance was evaluated by mapping each model's daily sea level pressure data to SOM nodes, and comparing each model's node frequency distribution to the NCEP/NCAR distribution. The degree of agreement between model output for the 1961-1999 period and NCEP/NCAR reanalysis for the 1961-2010 period was quantified as correlation between node frequencies. That is, correlations were calculated between 48 (6x8) point node frequency vectors associated with a) a specific model and b) NCEP/NCAR data. Resulting correlation scores are shown in Table 3.2. For a 48 point vector, correlations with an absolute value greater than 0.29 are statistically significant at the 95% confidence level.

Models which perform the best for the winter (DJF) are CGCM3.1 (T63) (higher resolution than CGCM3.1 (T43) model), ECHAM5/MPI-OM and NCAR CCSM3.0. A number of the models have negative correlations significant at the 95% CI; these are CSIRO-Mk3.5, GFDL-CM2.0, GFDL-CM2.1 and MIROC3.2 (MEDRES). This indicates that these models tend to reduce (increase) the frequency of nodes emphasized (under-emphasized) by the NCEP/NCAR reanalysis. In order to highlight common model biases, a composite node frequency distribution was calculated by averaging models showing negative correlations with NCEP/NCAR reanalysis (Figure 3.4). The composite favours the upper portion of the map, representing a relative increase in coincident Aleutian Low, Central Arctic High, and Icelandic Low patterns. . There is decreased frequency of East Siberian Sea High (ESSH), Barents Low (BAL), Beaufort High (BH) and Icelandic Low (IL) patterns in other nodes; the reduced frequency of BH is notable, and has been identified as a common bias in previous analyses of model performance (Bitz et al. 2002).

Models with significant correlation to the NCEP/NCAR data set vary in their node frequency distribution. The CGCM3.1 (T63) model has higher frequency of

the Barents Low pattern, Central Arctic High and East Siberian High patterns. ECHAM5/MPI-OM favors nodes with Icelandic Lows and Beaufort Highs. The NCAR CCSM3.0 favors nodes with Icelandic Lows, Beaufort Highs and the Barents Lows. Frequency distribution for these models are shown in Appendix A.

Table 3.2: Pearson correlation coefficients (r) between node frequencies in NCEP/NCAR (1961-1999) and models (1961-1999). Data from the 11 models and NCEP/NCAR reanalysis were used to train the SOM used to determine the node frequency distribution. Correlations are shown for JJA and DJF to the respective climatologies using the SOMs trained for those seasons.

Model	DJF	JJA
BCCR BCM 2.0	0.24	-0.64
NCAR CCSM 3.0	**0.65**	**0.65**
CGCM 3.1	0.24	-0.31
CGCM 3.1(T63)	**0.63**	**0.39**
CNRM CM3	0.18	-0.62
CSIRO-MK3.5	-0.65	**0.71**
ECHAM5-MPI	**0.45**	**0.46**
GFDL CM2.0	-0.29	-0.46
GFDL CM2.1	0.14	0.09
IPSL CM4	0.00	-0.13
MIROC 3.2(med)	-0.52	0.22

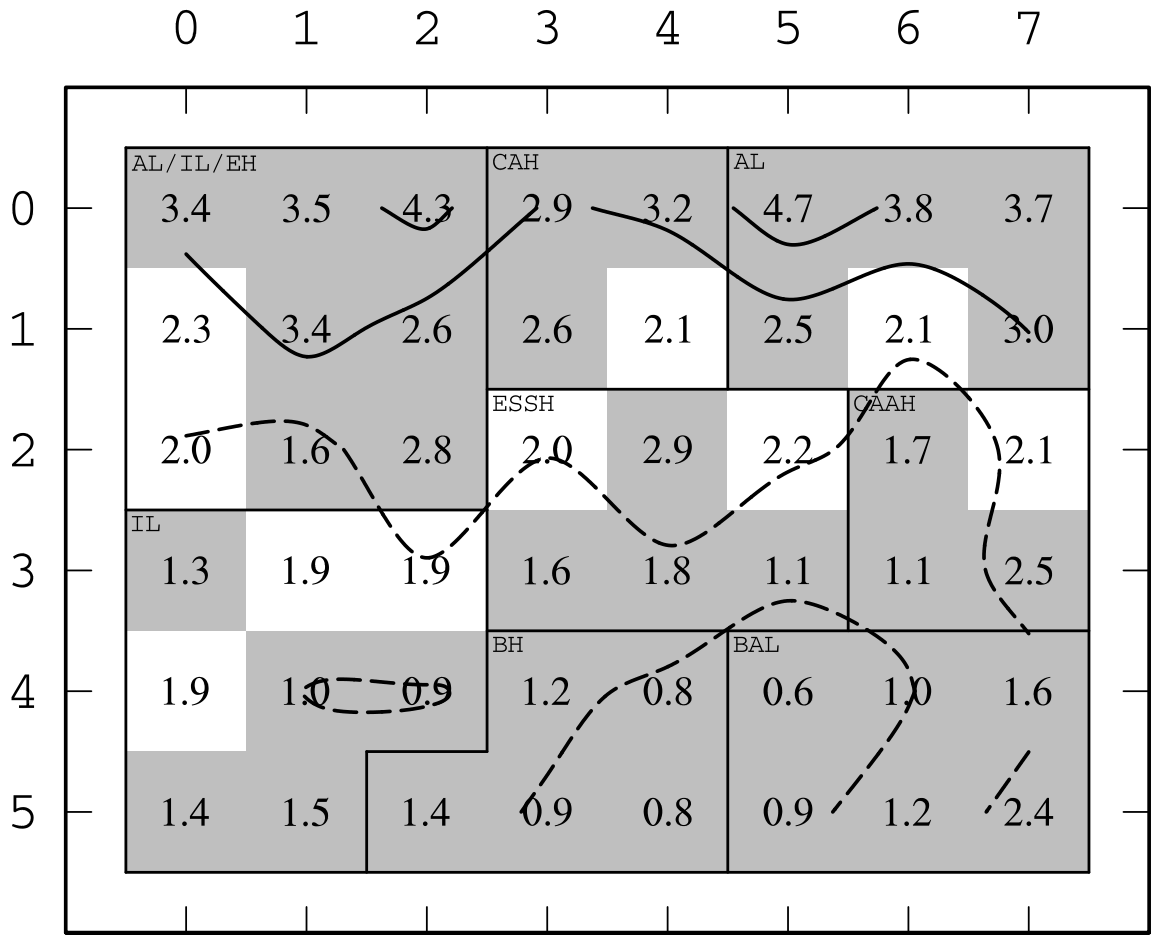

Figure 3.4: Frequency distribution of SOM nodes for models showing poor agreement with the NCEP/NCAR reanalysis (CSIRO MK 3.5, GFDL CM 2.0 and MIROC 3.2(med)); i.e.with signfiicant negative correlations (less than -0.29). Dashed contours are below the expected value of 2.08% and solid contours are above the expected value. Grey shaded nodes indicate that the frequency of occurence is significantly different from the expectant value (2.08%) at the 95% CI.

3.2 Summer Patterns

Self-organizing maps trained with daily data from summer months (June through August) feature many patterns broadly similar to those identified in the winter training, with several key differences. The most prominent is that features are generally weaker than winter, with reduced pressure gradients. For this reason, a different scale has

been used when plotting the summer results (Figure 3.5) in order to better distinguish feature differences in similar nodes. The map also dedicates a greater number of nodes to low pressures systems over Siberia/Eurasia and the central Arctic, at the expense of Icelandic and Aleutian lows, reflecting weakening and northwards shift of the Atlantic and Pacific storm tracks during this season. Preferred locations of highs shifts from Siberia/Eurasia towards the Arctic Ocean; particularly notable is the increase in nodes featuring a Beaufort High, given the identified association between this feature and sea ice cover (e.g. Bitz et al. (2002)).

As with winter, the dominant features in all SOM nodes have been identified and subjectively classifed; results are given in Table 3. Strong Eurasian and Siberian Lows (here "Siberian" Lows are located relatively further East than their 'Eurasian' counterparts) dominate the upper rows of the SOM, with the strongest in row 0 and intensity decreasing as row number increases. Moving down the right hand side of the SOM, the center of these lows shifts gradually westwards, first towards the Barents Sea (BL; [6:7,2:3]) then towards Iceland (IL, [6:7,4:5]). This displacement continues from right-to-left along the bottom nodes, which show considerably weaker lows near the Canadian Arctic Archipelago (CAAL; [3, 4:5]) and Greenland. In the lower left corner, these lows drift away from the coast towards the Central Arctic (CAL).

Similarly, prominent high pressure systems shift location and generaly decrease in mean intensity moving counterclockwise around the SOM from the upper left to lower left, although these adjustments are less clean than the gradual transitions of lows captured by the map. Intense highs centered between Greenland and Iceland in the upper left give way to highs over the Beaufort Sea (BH) along the centre columns of the upper rows, before migrating back East towards the archipelago (CAAH) in the upper right. Down the righthand side, highs return to the Beaufort Sea before finally moving towards the Siberian coast (ESSH; lower right). Coastal Siberian lows

Table 3.3: Atmospheric features captured in sub-regions of the summer(JJA) SOM.

Feature Name	Abbreviation	SOM Nodes
Barents High	BAH	[0:1,2], [2:3,3:5]
Barents Low	BAL	[6:7,2:3]
Beaufort High	BH	[2:4,0], [2,2], [2:3,1], [7,1], [7,2:3]
Beaufort Low	BL	[4:5,4:5]
Canadian Arctic Archipelago High	CAAH	[1,1], [4,1], [6:7,0], [6,1]
Canadian Arctic Archipelago Low	CAAL	[3,4:5]
Central Arctic High	CAH	[3:6,2:3]
Central Arctic Low	CAL	[0,3], [0:1,4:5]
Davis Strait Low	DSL	[2,3:5]
Eurasian Low	EL	[2:7,0:1], [2:5,2], [4:5,3]
East Siberian Sea high	ESSH	[6:7,4:5]
Greenland High	GH	[0,0:1], [1,0], [5,0:1]
Icelandic Low	IL	[6:7,4:5]
Siberian Low	SL	[0:1,0:2], [1,3]
Yukon High	YK	[0:1,4:5], [1,3]

continue to shift west into the Barents Sea (BAH) moving right-to-left along the bottom rows, eventually becoming paired with weak highs near the Yukon and Alaska (YH) that dominate in the lower left. Much of the SOM's center features high pressure over the central Arctic (CAH).

Figure 3.7 shows the result of node frequency analyses for the NCEP/NCAR reanalysis. As with the winter map, the map is separated on the basis of dominant features to ease interpretation; however, the separations are somewhat less clear for this SOM, due to the increased number of features present (e.g. Table 3.1 vs. 3.3). Results emphasize the high frequency of nodes in the lower left corner, highlighting cyclone maxima over the central Arctic during summer (Serreze et al. 2008). Most nodes occur at below-expected frequencies, particularly the intense patterns along the SOM's upper rows. Notably uncommon are the dipole-like patterns in the upper-center to upper right.

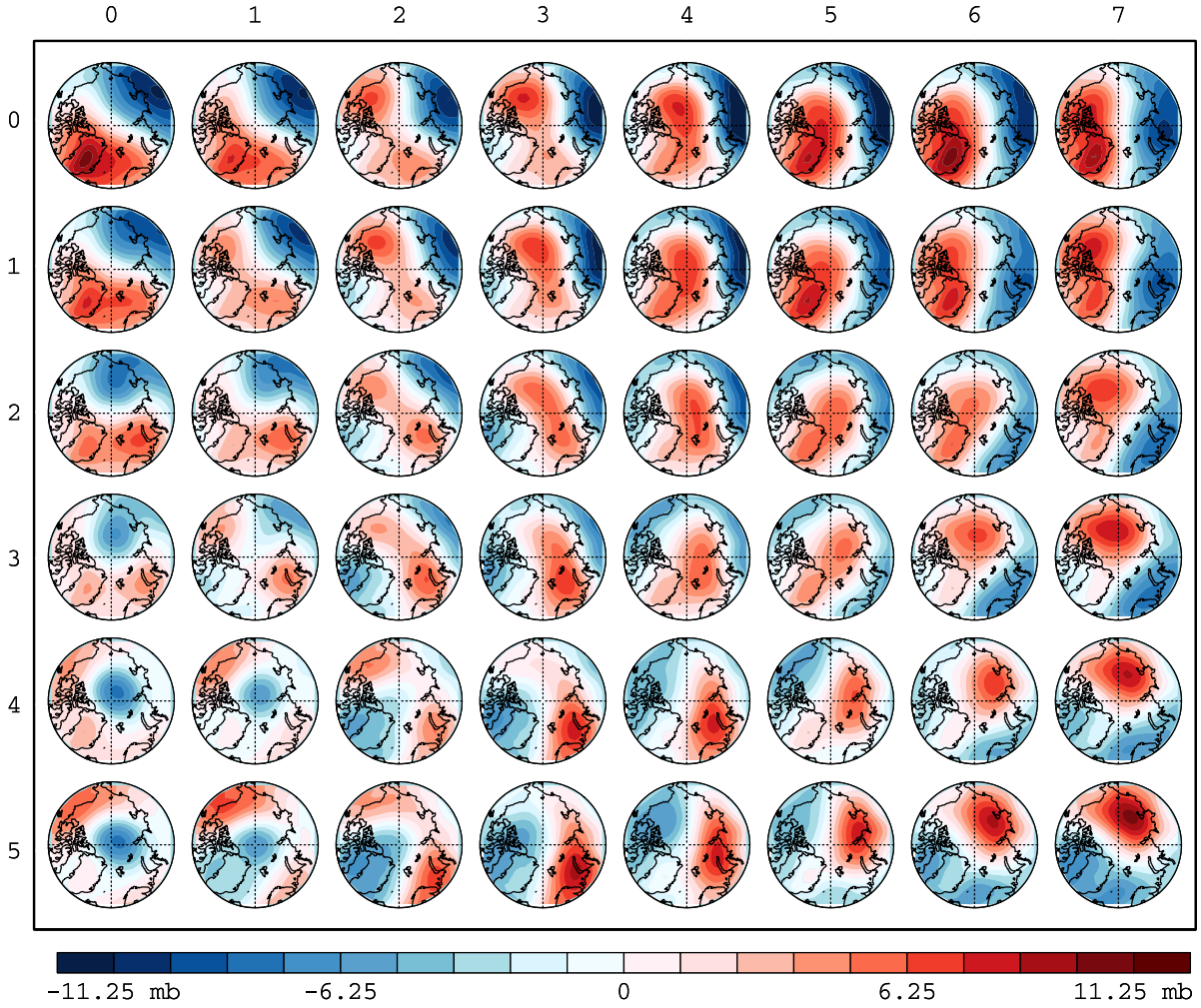

Figure 3.5: Daily summer (JJA) synoptic climatology of the Arctic (above 65 degrees latitude) developed using SOM technique.

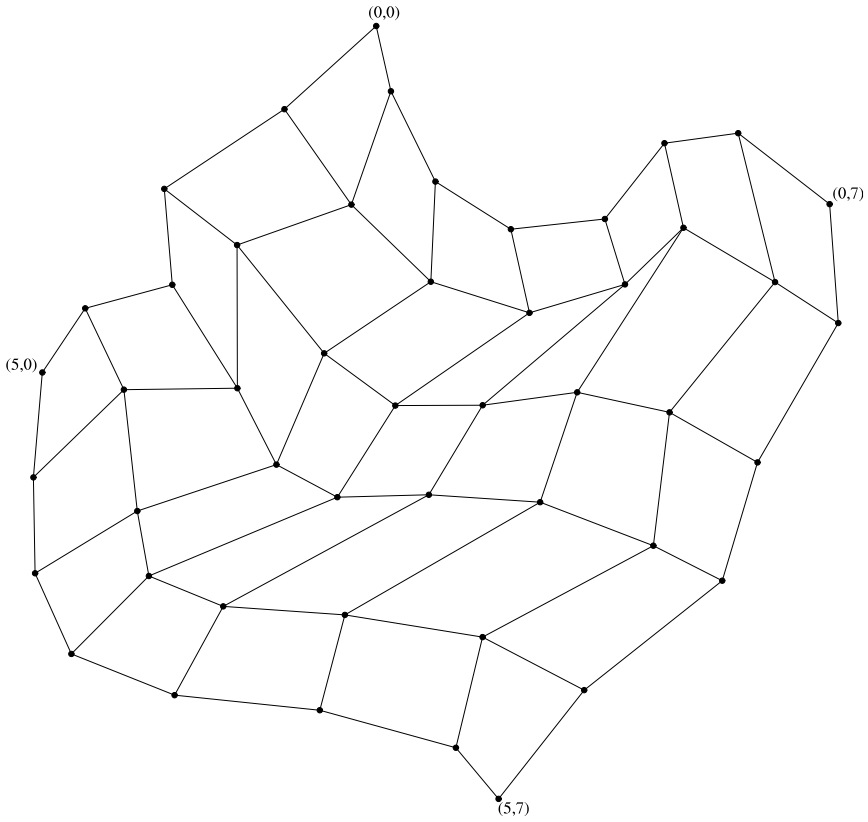

Figure 3.6: Sammon map for summer (JJA) SOM.

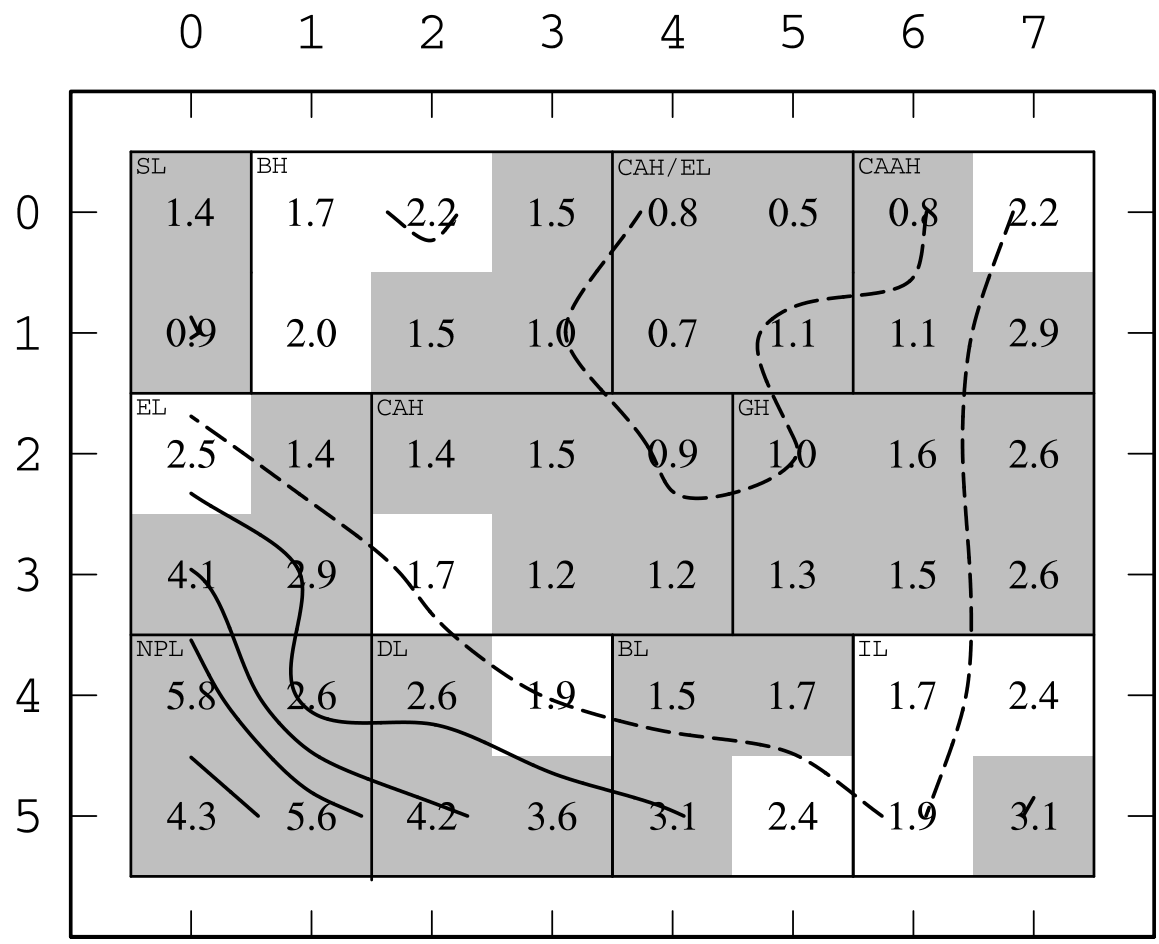

Figure 3.7: NCEP/NCAR reanalysis frequency distribution of synoptic types in summer for period 1961-2010. Dashed contours are below the expected value of 2.08% and solid contours are above the expected value. Shaded nodes are significantly different than the expected value 2.08% at the 95% CI.

3.2.1 Model Performance

The performance of models in summer was again evaluated by comparing the models' ability to replicate the frequencies of synoptic types (self-organizing map nodes) demonstrated by the NCEP/NCAR reanalysis (1961-2010), using correlation between node frequency. Table 3.2 gives results. The best performing models are CGCM3.1 (T63), CSIRO-Mk3.5, ECHAM5/MPI-OM and NCAR CCSM3.0, which give summer correlations on the order 0.6-0.71 (36%-50% aggreement).

BCCR-CM2.0, CGCM3.1, CNRM-CM3 and GFDL-CM2.0 have significantly negative correlations (above the 95% CI). Composite node frequencies of these models are shown in Figure 3.8, in order to highlight common biases. Pronounced differences from NCEP/NCAR include increased occurrence of Central Arctic Highs (CAH/EL), Siberian Lows, and Canadian Arctic Archipelago Highs. These tend to replace nodes showing cyclonic activity in the Arctic Basin, particularly Siberian Sea Lows (SSL), Central Arctic Lows (CAL), and Beaufort Lows (BL). There are also lower than expected frequencies of Canadian Arctic Archipelago High and Yukon/Alaskan High patterns.

Taken together, analyses of winter and summer Global Climate Model (GCM) performance suggests that CCSM 3.0, CGCM3.1 (T63) and ECHAM5-MPI perform particularly well in the Arctic, and most closely capture the synoptic climatology of the Arctic as represented by the SOMs used. For this reason, further analyses will pay particular attention to these models.

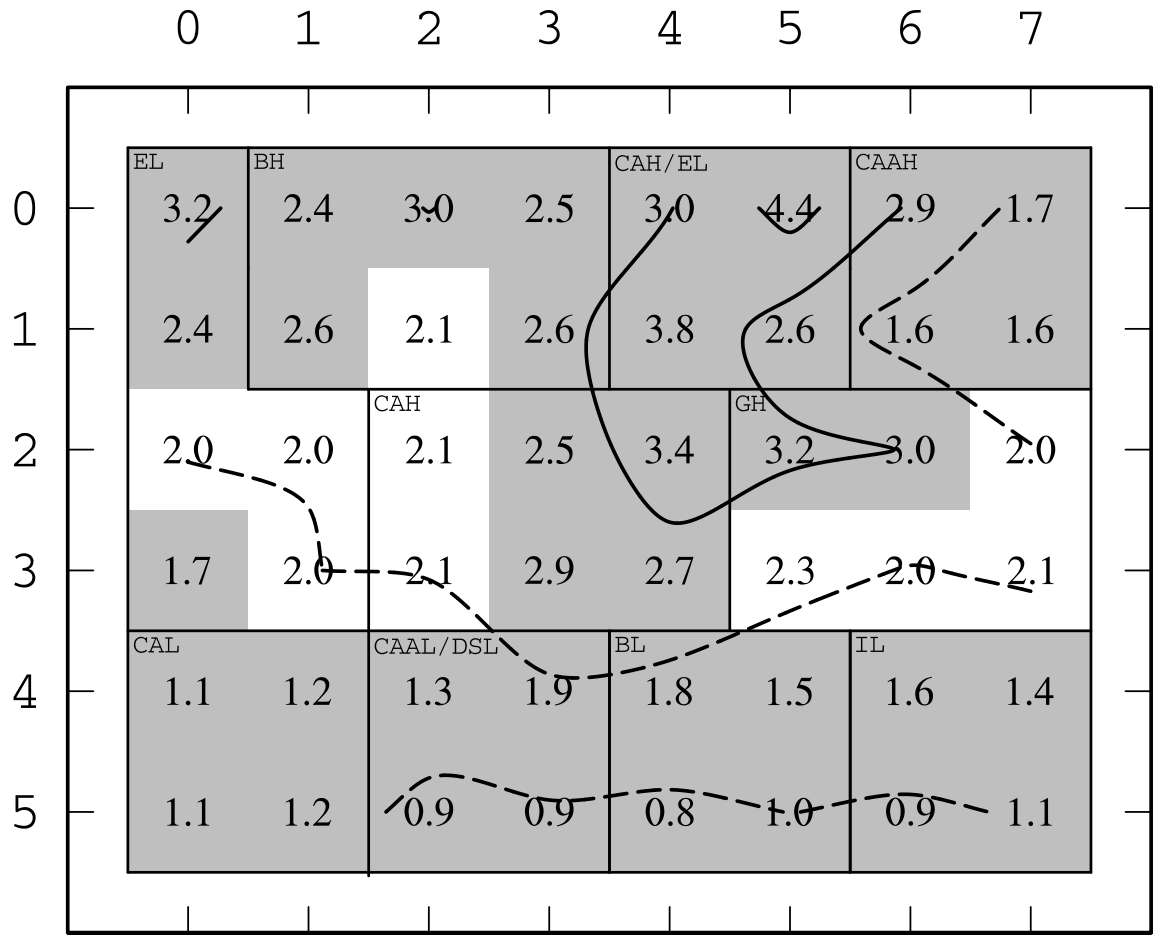

Figure 3.8: Frequency distribution of synoptic types in summer for models showing poor agreement with the NCEP/NCAR reanalysis (BCCR BCM 2.0, CGCM 3.1, CNRM CM3 and GFDL CM 2.0). Dashed contours are below the expected value of 2.08% and solid contours are above the expected value.

3.3 Tele-connection Indices

Studies of observed ice loss frequently rely on established teleconnection patterns as a means of summarizing atmospheric conditions. As representations of large-scale atmospheric oscillations, teleconnections provide a convenient means of categorizing atmospheric circulation anomalies on monthly to interannual timescales, and can often facilitate the comparison of related events. They can also provide insight into possible

atmospheric drivers of ice loss through wind-forcing of ice (Wang et al. 2009a; Rigor et al. 2002; Maslanik et al. 2007), effects on radiative forcing (L'Heureux et al. 2008), or ocean heat transport into the Arctic (Zhang et al. 2004). Although various methods have been used to identify and define these patterns, many teleconnections are now defined using some variant of principal component analysis (PCA), a statistical decomposition technique that isolates prominent patterns of variability. Many operational centers use an adjusted form of PCA with relaxed orthogonality contraints to define key teleconnection patterns, commonly referred to as rotated PCA (Barnston et al. 1987). For example, the National Oceanic and Atmospheric Administration Climate Prediction Center uses this approach to produce long-term monthly and daily time series of most teleconnections examined in the current study.

Reliance on teleconnections as a means of interpreting atmospheric circulation anomalies presents several challenges. The first concern reflects the fact that teleconnections defined using PCA oscillate in a linear fashion; i.e. the positive phase is the inverse of the negative phase. This appears to be an oversimplification, and many teleconnections demonstrate asymmetry masked in their PCA-based definition (Cassou et al. 2004). The second concern reflects the fact that the high frequency variability underlying a Principal Component (PC) is often difficult to infer from the spatial pattern of the PC itself (Tremblay 2001; Reusch et al. 2007), potentially leading to misinterpretations in the relationship of the teleconnection to other phenomena (e.g. sea ice loss).

Other concerns relate to the use of teleconnections in data set intercomparison efforts. While teleconnections are useful in the comparison of related events in a single data set, applying them across data sets (e.g. separate climate models) is a nontrivial exercise. Many models display modes of variability broadly similar to observed teleconnections, suggesting that the models capture aspects of underlying climatic

processes driving the teleconnections. However, the spatial structure and temporal variability can vary considerably from observations and across models (Stoner et al. 2009; Schoof et al. 2006), emphasizing differences in the physical manifestation of teleconnections and persistence of teleconnection anomalies.

In the context of the current study, biases in the spatial structure of simulated teleconnections present a particular problem, as it becomes unclear whether a) it is suitable to interpret GCM-simulated variability in terms of teleconnections defined using reanalysis data, and b) if the spatial structure of simulated teleconnections influence sea ice in a manner comparable to observed teleconnections. This can be illustrated by considering the influence of the North Atlantic Oscillation (NAO) on Arctic sea ice. Observations suggest the NAO is related to sea ice export from the Arctic, and contributed to long-term thinning of ice cover (Maslanik et al. 2007; Rigor et al. 2002). To assess whether the NAO is responsible for ice loss in GCM simulations, a user must either use the observed NAO structure to infer a teleconnection time series for the GCM simulation, or instead use the (inevitably biased) structure of NAO-like variability produced by the GCM. The first option risks underestimating the influence of the teleconnection on simulated ice loss, due to differences in the model's interpretation of the NAO structure. The second option also presents problems, as the simulated structure of the teleconnection pattern may exert a considerably different influence on Arctic Sea ice; e.g. a simulated NAO with a weaker or displaced Icelandic Low center of action would have a different impact on the transpolar drift than the observed NAO, and may consequently have a different impact on sea ice export.

SOMs allow an alternative means of interpreting teleconnections, which avoids these complications and facilitates data intercomparison. Here, observed teleconnection patterns are interpreted within the context of the trained Arctic SOMs. The influence of teleconnection patterns has been summarized using NCEP/NCAR node

frequency composites, produced by averaging months during strongly positive or negative incidences of a given teleconnection; respectively, these were defined as months in which a teleconnection index was one standard deviation above or below zero. This approach emphasizes the teleconnection's relationship with daily weather patterns, and facilitates visualization of the actual daily circulation anomalies associated with positive and negative phases of the index. By assessing positive and negative phases separately, the approach also accommodates asymmetry in teleconnections. Furthermore, the resulting anomalies can be used to interpret different data sets on roughly equal footing; if a model-simulated period features SOM-node frequency anomalies consistent with an observed teleconnection, then the simulation has effectively experienced that teleconnection. The use of an Arctic-centered SOM further focuses interpretation on a region influenced by sea ice, filtering out aspects of a teleconnection that cannot exert a direct influence on ice movement and melt. For example, our SOM-based analysis will consider the NAO in terms of the Icelandic center of action alone, without influence from the Azores center.

SOM-based interpretations of teleconnections used in the current study are outlined below, followed by an evaluation of the method's performance with respect to identifying observed teleconnection anomalies using NCEP/NCAR data.

3.4 Winter tele-connection indices

Synoptic climatology of negative and positive composities of teleconnection indices were determined using the winter self-organizing map (SOM) and represented as node frequency anomalies relative to the full NCEP/NCAR climatology. Nodes which show a frequency anomaly significantly greater than zero (95% confidence level, assuming a Poisson distribution for the likelihood that a node is activated) are given in grey

shading.

3.4.1 Arctic Oscillation (AO)

Frequency distributions of months with strong positive and negative AO conditions are shown in Figure 3.9. In AO positive months there is an increase in the frequency of patterns in the lower left of the map corresponding to increased frequency of strong Icelandic Lows, and associated cyclonic systems in a region extending north-eastward from Iceland into the Arctic Ocean via the Barents Sea (IL and BAL). There is a decrease in patterns in the upper left that couple a strong Aleutian Low, a strong central Eurasian high, and a relatively weak IL. Other de-emphasized nodes include several in the center of the SOM that share a prominent Central Arctic High, and row 2 of the rightmost column, which places high pressures over Greenland. Together, these suggest decreased central Arctic and North Atlantic pressures, roughly consistent with the structure of the AO pattern.. The negative phase of the AO is associated with a decrease in the Icelandic-through-Barents Sea lows emphasized in the positive phase. However, the influence of the negative phase on high pressure systems is less ambiguous than the positive phase, with a strong preference indicated for the Canadian Arctic Archipelago, Central Arctic, and Greenland Highs captured in the upper right corner of the SOM.

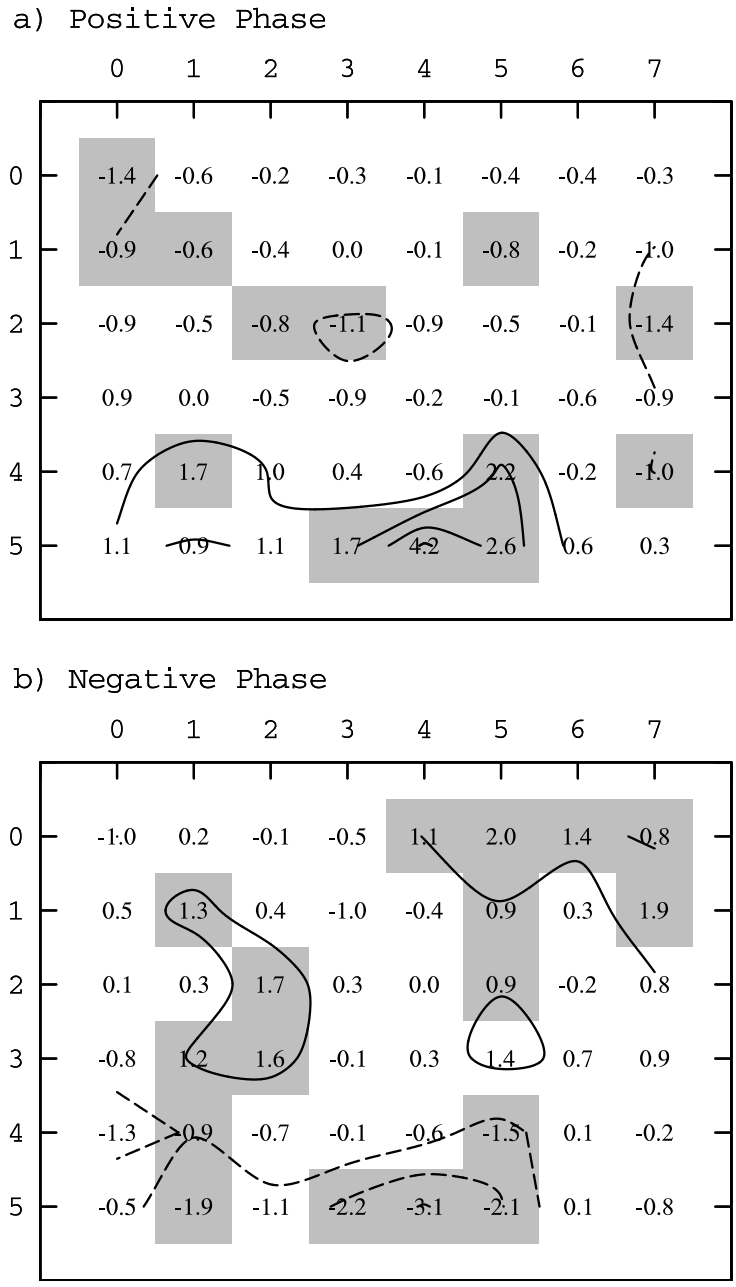

Figure 3.9: Arctic Oscillation frequency deviations from climatology of winter months with a) positive and b) negative AO indexes (defined as one standard deviation above and below average respectively). Boxes shaded grey are values that are significantly different from climatology significant at the 95% CI. Dashed contour lines are negative anomalies and solid lines are positive anomalies.

3.4.2 North Atlantic Oscillation (NAO)

The frequency anomalies relative to climatology for the NAO are shown in Figure 3.10. The positive phase of the index is similar to the result from AO positive months, with an increase in frequency of Icelandic Low patterns in the lower left and center of the SOM. The result from the NAO positive composite differs from the AO positive composite in that there is a more marked increase in patterns with cyclonic circulation near Iceland relative to the Barents Sea, and greater emphasis on anti-cyclonic circulation over the eastern Arctic (Eurasia and Siberia) (e.g. nodes near the lower left end of the SOM). The NAO positive composite has decreased frequency of patterns in the lower right of the map; these nodes are characterized by anti-cyclonic circulation in the Canadian Arctic Archipelago and Greenland region and cyclonic circulation overover Eurasia. The negative phase of the NAO shows decreased frequency in the Icelandic Lows in the lower left of the SOM. There is increased frequency in nodes in the upper right portion of the map, showing high pressure over Greenland and Canadian Arctic Archipelago.

The nodes favoured by the positive and negative phase of the NAO pattern are as expected, as the positive phase of the NAO is characterized by lower pressure over Iceland and the negative phase emphasizes patterns with higher than normal pressure over Iceland. Relative to the AO, the NAO shows greater influence on Icelandic Lows and less influence on Barents Lows. Both show an asymmetry through strong impacts on the upper right end of the SOM in the negative phase only.

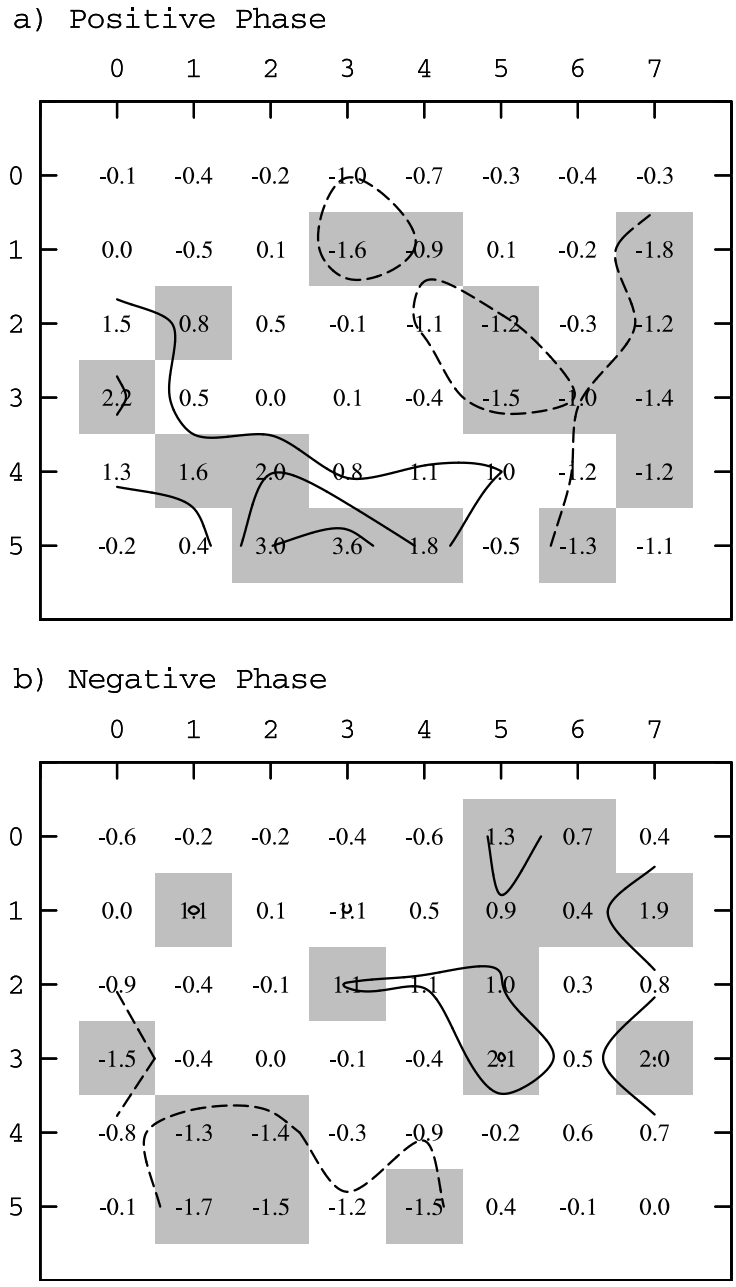

Figure 3.10: NAO deviations from climatology of winter months with positive and negative NAO index (defined as one standard deviation above and below average respectively). Grey shading shows values which are significantly different from climatology at the 95% CI. Dashed lines are negative anomalies values and solid lines are positive anomalies.

3.4.3 Pacific North-America Pattern (PNA)

The PNA positive and negative composites do not have as many significant shifts from climatology as other teleconnections considered here (Figure 3.11), although the positive phase produces more consistent anomalies than the negative phase. The positive phase has an increased occurrence of patterns near the upper right of the SOM that simultaneously depict Icelandic Lows, Aleutian lows, and strong Siberian Highs. There is a decrease in patterns in the lower left of the self-organizing map, which show Icelandic Lows and Siberian Highs, but lack the Aleutian feature. Most of these decreased nodes extend the Siberian High across the Atlantic towards Alaska and the Yukon, inconsistent with a strong Aleutian Low. These results suggest the SOM interpretation of a positive PNA is focused on decreased Aleutian/Alaskan pressures, through both an increase in regional lows and a decrease in highs.The negative phase has only three nodes with significant frequency shifts from climatology. There is no apparent consistency in the weather features emphasized in these nodes, suggesting the negative phase has little coherent impact on the region that can be captured by this specific SOM.

The limited impact of the PNA on SOM node anomalies can be understood in terms of the PNA's physical structure. The only PNA center of action that would be visible on the self-organizing map is located in the North Pacific region, which has minimal representation in our SOM domain. Circulation in this center of action must be inferred by extending isobars from the study region southwards into the North Pacific; the positive PNA composite can be interepreted as a strengthening of this feature. In short, the signal of the PNA in this Arctic-centered SOM is not very clear, pointing to either a) the PNA having little impact on Arctic circulation, or b) the unsuitability of the current SOM as a means of diagnosing the PNA's Arctic influence. Regardless of the reason, the PNA pattern will not be considered extensively in the

investigation of RILEs for the winter season.

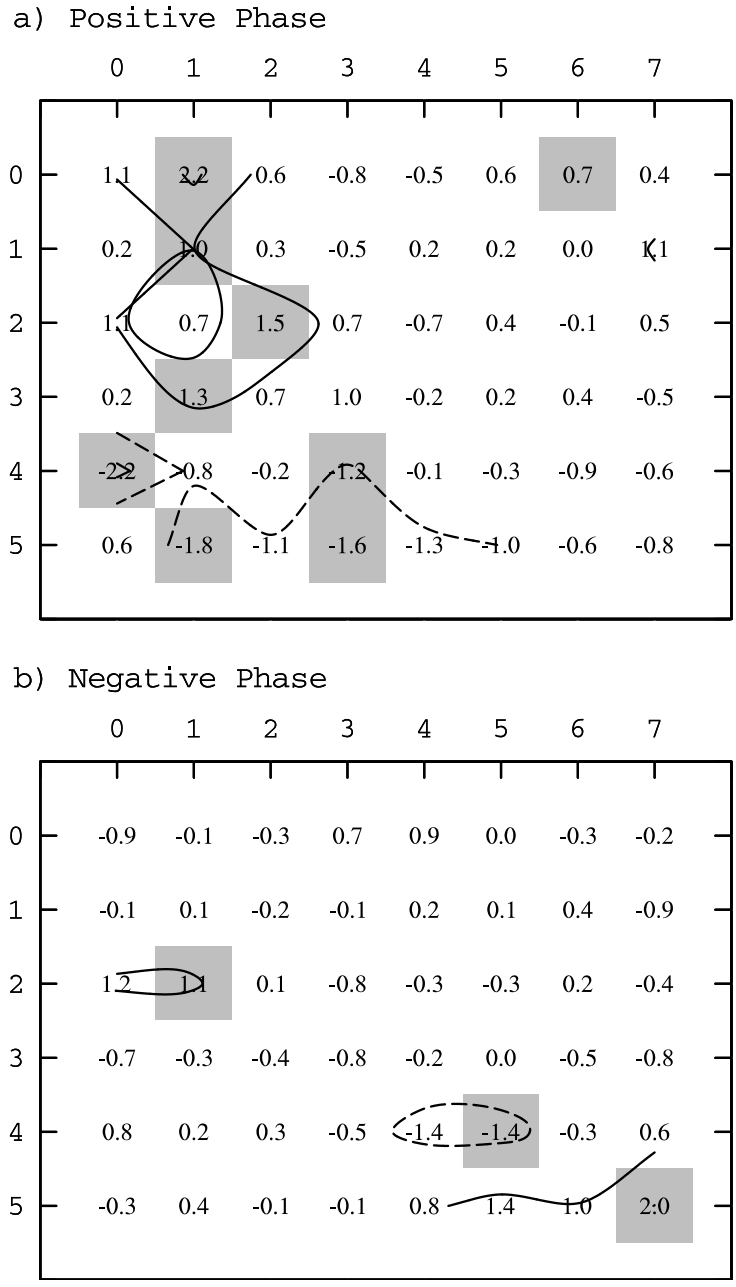

Figure 3.11: PNA frequency deviations from climatology of winter months with high PNA indexes (defined as 1 standard deviation above average). Grey shading indicates values which are significantly different from climatology at the 95% CI. Dashed lines are contours of negative anomalies and solid lines are contours of positive anomalies.

3.4.4 Arctic Rapid Change Pattern (ARP)

The positive phase of the ARP has an increase in patterns in the lower central regions of the map, as shown in Figure 3.12. These nodes feature patterns with cyclonic circulation over the Barents Sea and Norway, and high pressure over the Canadian Arctic Archipelago; although broadly similar to the AO and NAO, the ARP shows less influence on Icelandic Lows. There is a significant decrease in frequency of nodes [7,1:2], which have higher pressures near Greenland and a cyclonic system extending from Alaska/Yukon across the Arctic basin to Eurasia. The negative phase of the ARP emphasizes patterns that share a strong Aleutian low, strong Siberian/Eurasian high, and a moderately strong Icelandic Low (in the upper left of the map). Other emphasized nodes are located on the mid-left of the map, highlighting Siberian Highs (again with moderately strong Icelandic Lows), and the mid-right showing Aleutian lows with Greenland Highs. There is a decrease in nodes at the bottom of the self-organizing map which show the migration of an Icelandic low towards the Barents sea. Together, these suggest the negative phase of the ARP is associated with a) reduced cyclone activity and/or strength near Iceland, increased cyclone activity in the Northeastern Pacific and nearby Arctic Seas, and high pressures over Siberia/Eurasia. Emphasis on Alaska/Yukon/Aleutians and nearby seas distinguish the negative ARP from the negative NAO and AO.

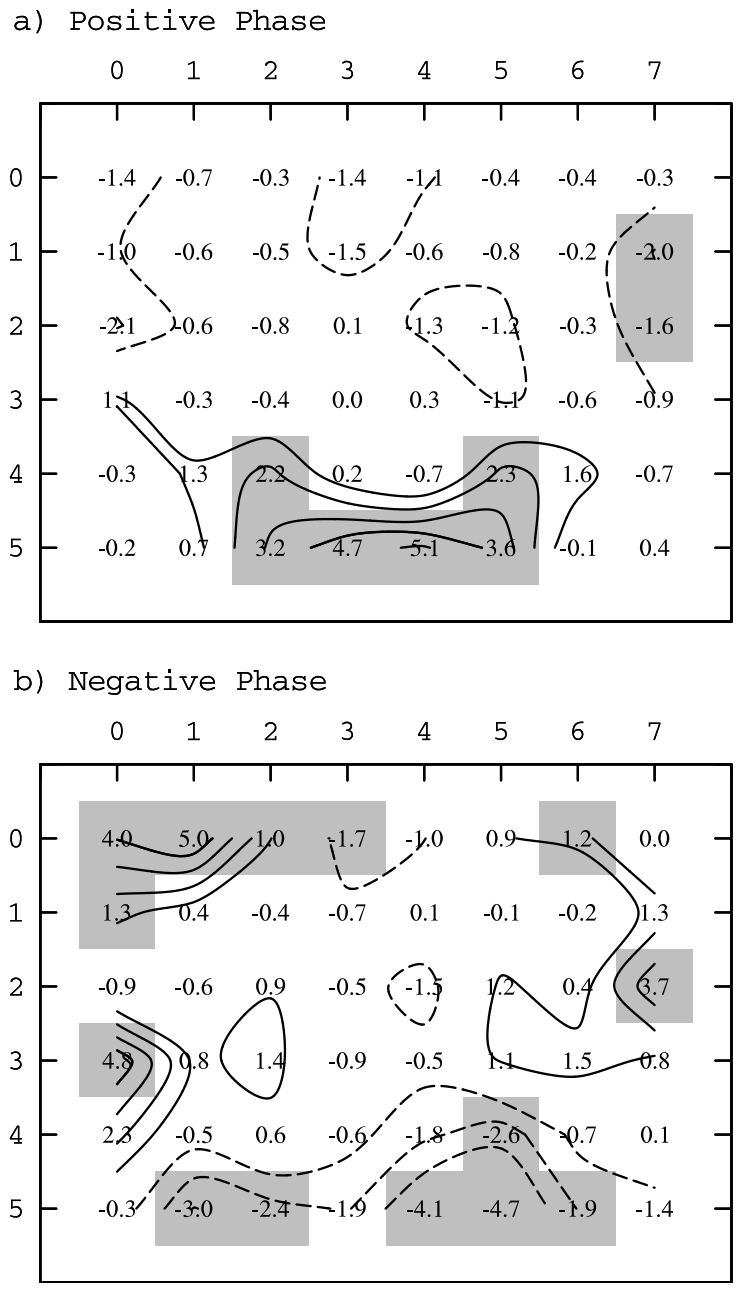

Figure 3.12: ARP index positive and negative phase of the winter ARP deviations from climatology Grey shading indicates values which are significantly different from climatology above the 95% CI. Dashed lines are negative values and solid lines are positive anomalies.

3.4.5 Central Arctic Index (CAI)

Results for the CAI-80, CAI-82 and CAI-84 indexes are broadly similar; for this reason, we only present results for CAI-80 in Figure 3.13. The positive phase of the index favours patterns in the lower right of the map with cyclonic circulation over the eastern Arctic and higher pressure over the western Arctic. There is decreased frequency of nodes in the low- to mid-left of the map, showing the more typical winter combination of an eastern Arctic high with a western Arctic or North Atlantic low.

The CAI negative phase composite inverts the positive anomalies, raising frequency along the left of the SOM and decreasing the frequency of lower right nodes, effectively reversing the positive phase dipole.

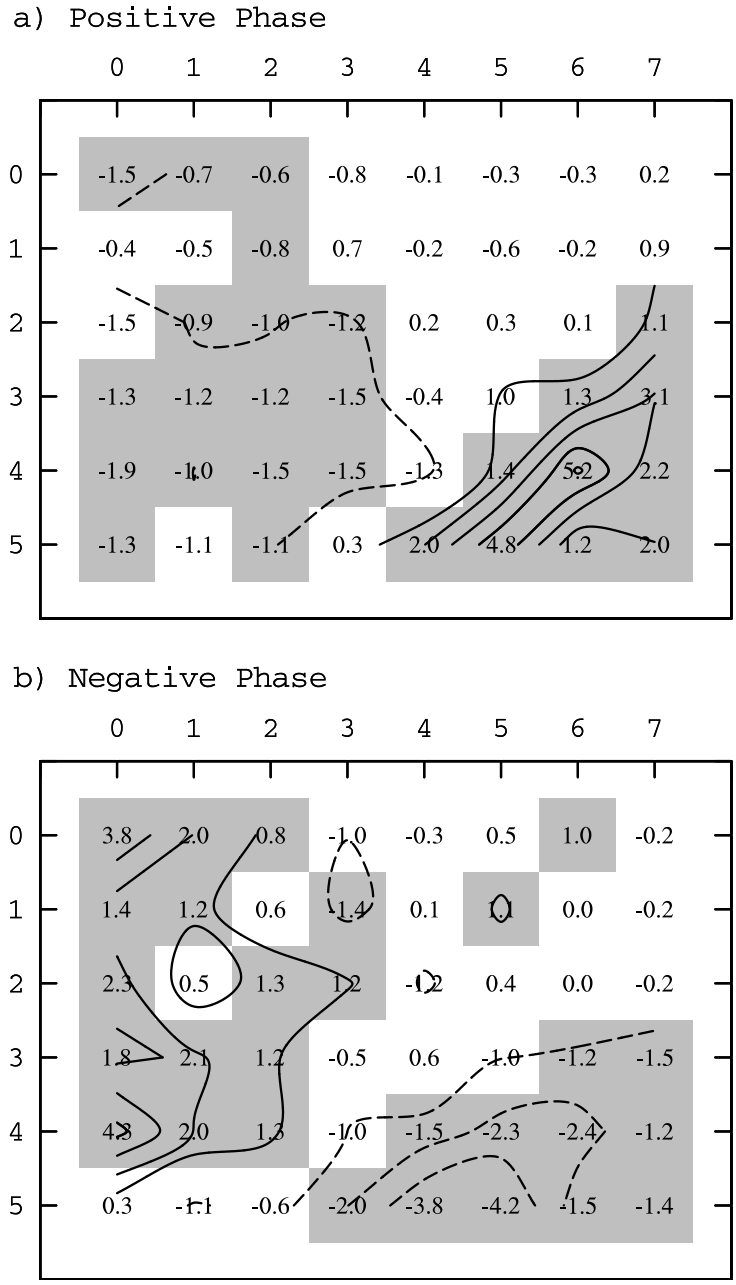

Figure 3.13: Central Arctic Index (CAI) 80 winter composite deviations from climatology of positive and negative phases of the index. Composites are mappings of days in months that are either one standard deviation above the average index for positive phase or one standard deviation below average for the negative phase. Grey shading indicates nodes with shifts in frequency significantly different from climatology at the 95% CI. Dashed lines are contours of negative anomalies and solid lines of positive anomalies.

3.5 Summer Tele-connection Patterns

3.5.1 Arctic Oscillation (AO)

The composites for the summer AO are shown in Figure 3.14, again as node frequency anomalies relative to the full NCEP/NCAR climatology. The positive phase (a) shows increased frequency of patterns in the lower left of the map, characterized by cyclonic circulation over the Central Arctic Ocean. A cluster of lower node frequencies near the upper right suggest this is complemented by decreases in the number of anticyclones near the central Arctic and Beaufort/Chukchi Seas. The negative phase broadly inverts these patterns, but through an emphasis on nodes that suggest subtle deviations from a perfectly linear oscillation; while the positive phase sees the greatest decrease in highs near the North American end of the Arctic, the negative phase emphasizes a greater increase in highs closer to the North Atlantic through Central Arctic (center of the SOM). Similarly, the negative phase places additional emphasis on decreasing cyclones near Greenland and the Canadian Archipelago, while the positive phase focuses on central Arctic systems.

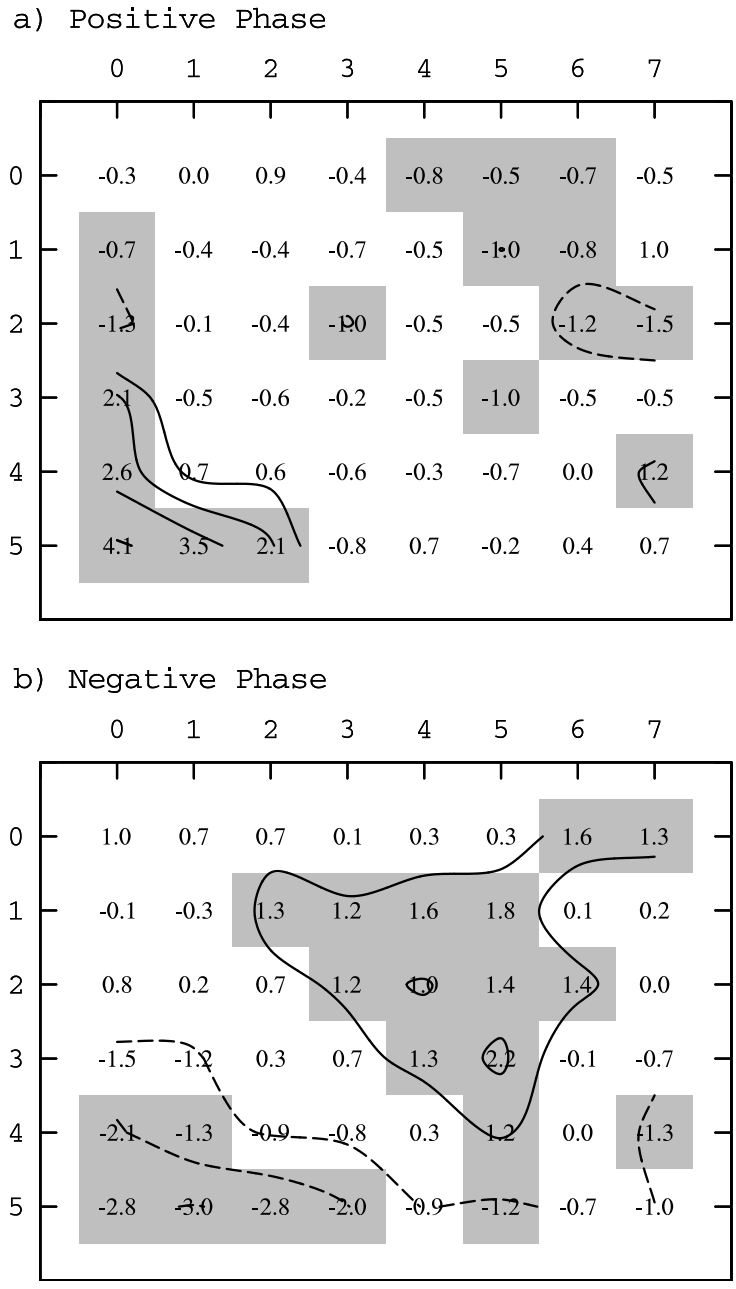

Figure 3.14: Summer AO positive and negative phase composites frequency deviations from climatology. Grey shaded nodes highlight nodes significantly different from climatology at the 95% CI. Dashed lines are negative values and solid lines are positive anomalies.

3.5.2 North Atlantic Oscillation (NAO)

NAO positive and negative composite frequency anomalies from climatology are shown in Figure 3.15. In the positive phase there is an increase in patterns with cyclonic circulation over the central Arctic Ocean (lower left) and near Iceland/the Barents Sea (lower right), with a decrease in patterns showing anti-cyclonic circulation over the Arctic Ocean (upper and centre right). The negative phase shows a decrease in most lows along the bottom row; these include cyclones spanning the central Arctic through the Barents Sea. In addition to emphasing similar anticyclones as the negative AO (mostly North American sector), the negative NAO also emphasizes nodes in the upper left corner associated with high pressures extending from Greenland through to the Barents Sea.

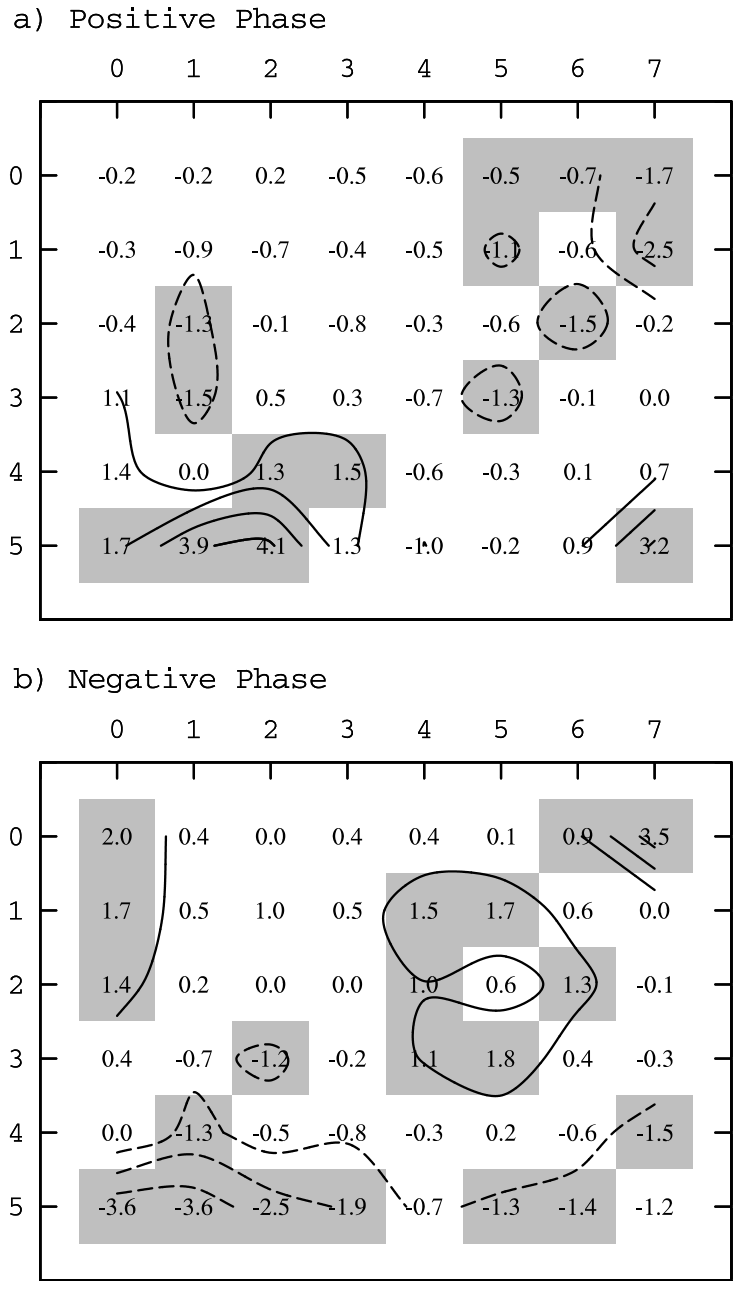

Figure 3.15: NAO JJA positive and negative phase composite frequency anomalies from climatology. Grey shading indicates nodes which have significantly different frequencies from climatology at the 95% CI. Dashed lines are contours of negative anomaliesand solid lines indicate positive anomalies.

3.5.3 Pacific North-America Pattern (PNA)

The PNA negative and positive phases have more nodes with a significant shift from climatology in the summer composites (Figure 3.16) than winter (Figure 3.11). However, the number remains low relative to other teleconnections. The positive phase of the PNA emphasizes nodes with significant shifts scattered over the map, again indicating either a) little relevance of the pattern to Arctic circulation, or b) inadequacies in the SOM's ability to detect these influences. Although no clear similarities exist between these nodes, there are broadly decreased counts of nodes with cyclonic circulation over the central Arctic Ocean (lower left nodes [0,5]) and decreased incidence of nodes with a Beaufort Low pattern ([5,4:5]). There is an increase in nodes with Beaufort High patterns nodes ([1,1], and [7,2]). The negative phase composite shows increased frequency of patterns with cyclonic circulation ([0, 2:4]) over the Arctic Ocean and decreased frequency of highs over the Canadian Arctic Archipelago and Beaufort Sea(nodes [7,0:3]).

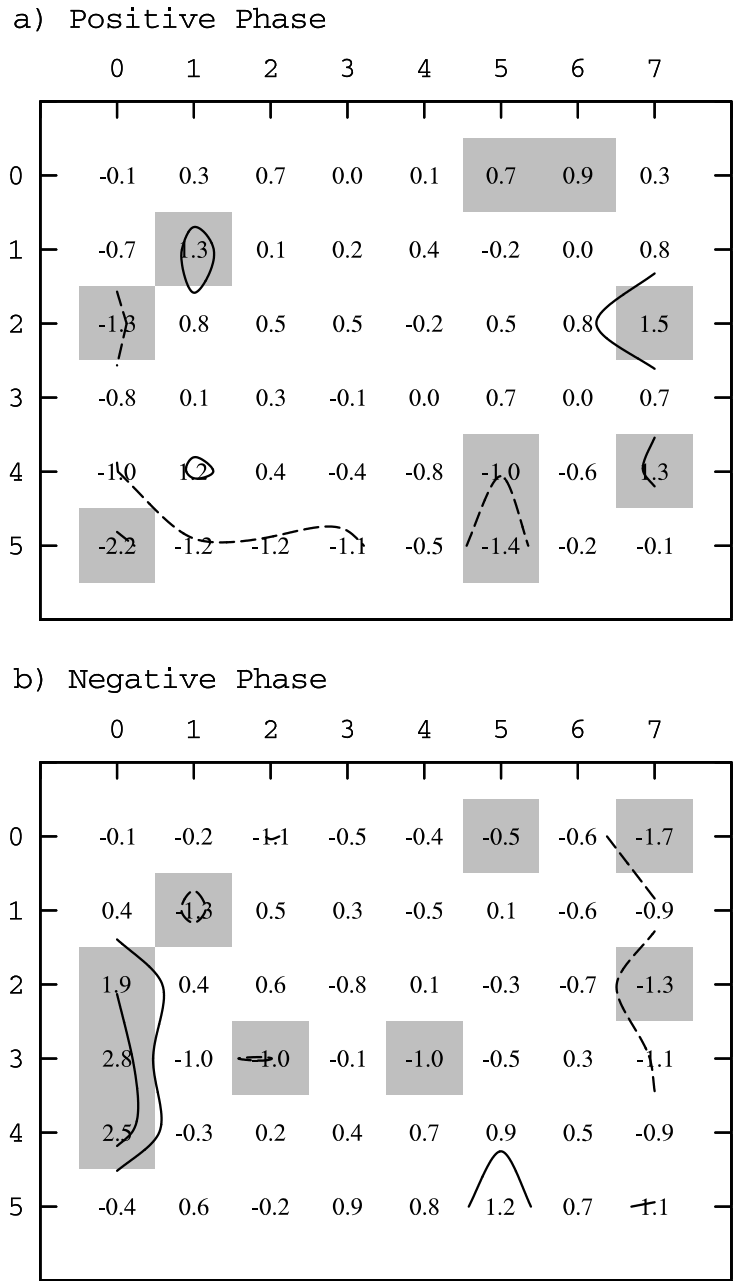

Figure 3.16: PNA JJA positive and negative phase summer composite deviations from climatology. Grey shading indicates nodes which are significantly different from climatology at the 95% CI. Dashed lines are contours of negative anomalies and solid lines are contours of positive anomalies.

3.5.4 Arctic Rapid Change Pattern (ARP)

The summer ARP positive and negative phase anomalies are shown in Figure 3.12. The positive phase emphasize upper right nodes ([7, 0:1] and [6,1]) with a strong Canadian Arctic Archipelago anticyclone/Eurasian cyclone dipole. There is also a significant increase in upper left nodes showing a broadly similar dipole, although these patterns are weaker and shift the cyclone center east towards Siberia and the anticyclone west towards the Beaufort region. The few nodes that show strong decreases generally feature central Arctic lows, or invert the preferred dipole with an Eastern Arctic High/Western Arctic Low. This associates the positive ARP with a strong winds along the transpolar drift, promoting ice flux out of the Arctic.

The negative phase of the ARP strengthens this interpretation, increasing the incidence of Western Arctic lows and Eastern Arctic highs (e.g. along the center bottom of the SOM), or Atlantic sector highs with central Arctic lows (center left nodes).

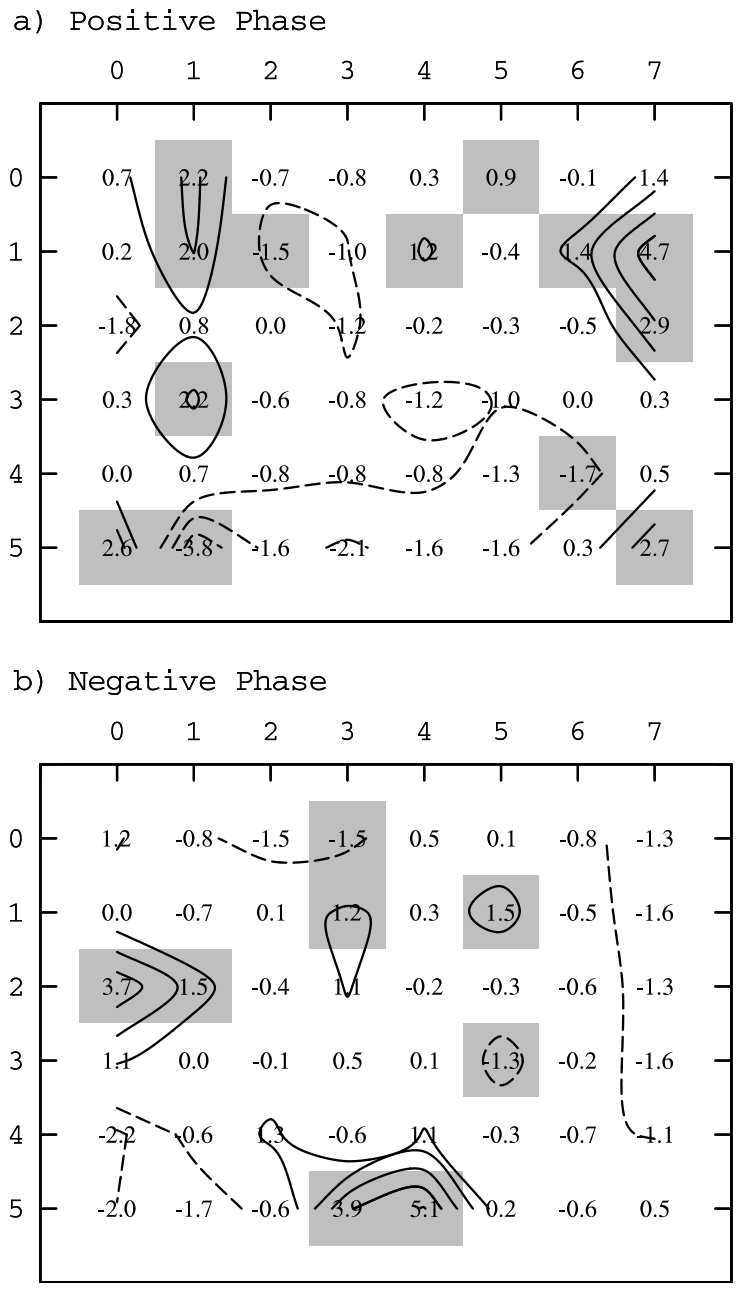

Figure 3.17: JJA ARP positive and negative phase month composites deviations from climatology Grey shaded nodes indicates values which are significantly different from climatology at the 95% CI. Dashed lines are contours of negative anomalies and solid lines are contours of positive anomalies.

3.5.5 Central Arctic Index (CAI)

As with winter, CAI-80, 82, and 84 all show very similar SOM node preferences; CAI-80 is shown in Figure 3.18 for reference. Summer CAI composites are similar to, though much more clear, than the ARP. This reflects the relative simplicity and regional focus of the CAI, which provides a measure of winds across the Fram Strait. The positive phase favours nodes with a strong East Arctic low/West Arctic high dipole promoting along transpolar drift winds (upper right nodes [0,4:5]). Also emphasized are nodes in the lower left, with anti-cyclonic flow over the North American continent and cyclones over the Arctic Ocean; these can be interpreted as later stages of the upper right nodes, as Eurasina/Siberian cyclones migrate into the Arctic (Serreze et al. 2008). Nodes with decreased frequencies (bottom rows) reverse this dipole, promoting winds blowing against the transpolar drift. Other de-emphasized nodes shift the western Arctic cyclones in this de-emphasized dipole north, again suggesting a later stage in the cyclone's trajectory. The negative CAI inverts these patterns, reflecting increased incidence of southerly winds across Fram Strait.

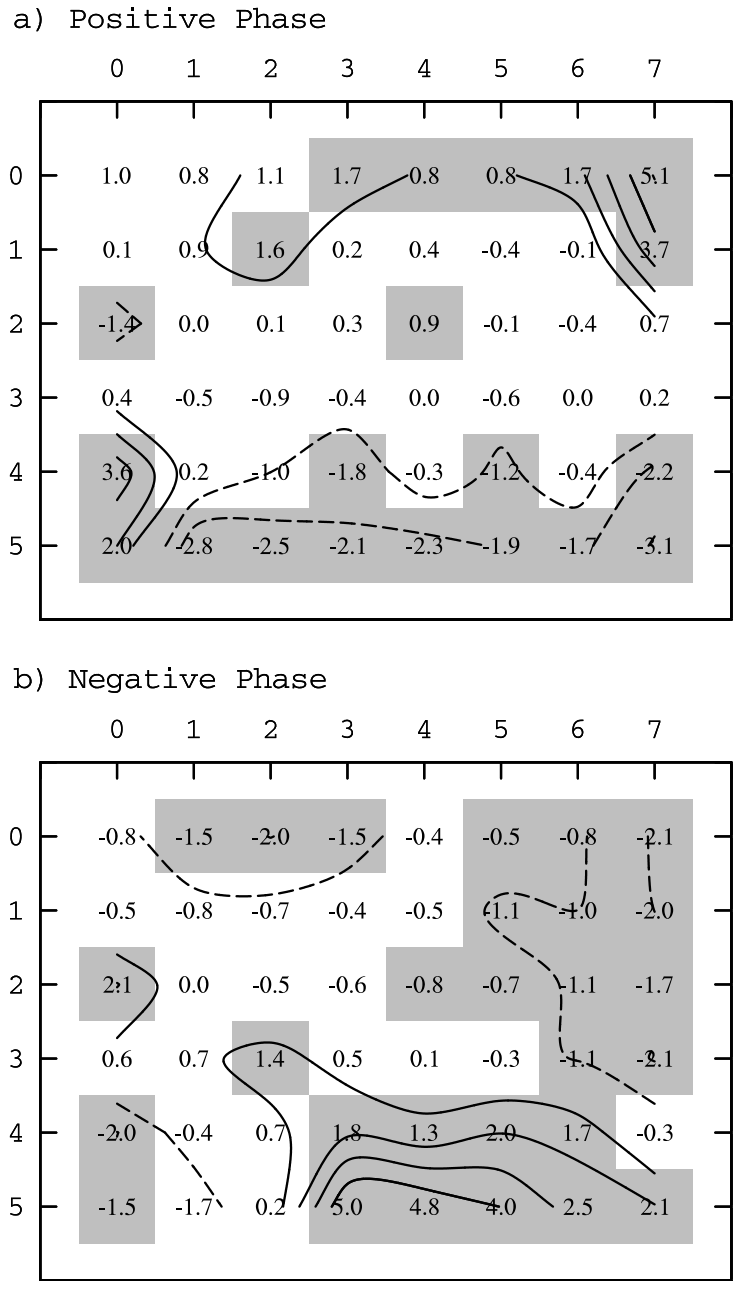

Figure 3.18: CAI-80 deviations from climatology of summer months with high CAI 80 indexes (defined as 1 STD deviation above average). Grey shading indicates values which are significantly different from climatology at the 95% CI. Dashed lines are negative values and solid lines are positive anomalies.

3.6 Standard Teleconnection Indices vs. SOM-based Alternatives

Comparing time series of traditional teleconnection indices and SOM-derived analogues supports the validity of a SOM-based approach to quantifying the amplitude and phase of teleconnections. Here, the seasonal teleconnection values are calculated as the dot product between i) node frequency anomaly vectors calculated for a specific teleconnection phase (discussed in the previous section) and ii) node frequency anomalies over the season being examined. This provides a measure of similarity between a given season's node frequencies and those found in teleconnection composites. To strengthen the signal, the dot products were calculated using the subset of SOM nodes that show statistically significant deviations from climatology in the teleconnection's composite anomaly (shaded gray in diagrams previous diagrams). For example, the winter positive AO strength is calculated using a 13-point vector, while the negative AO uses a 17-point vector (see Figure 9). Several quantitative comparisons of these time series follow, focusing on the NAO, AO, and PNA in winter. These teleconnections were chosen because i) these are well-known teleconnections many readers will be familiar with, and ii) they highlight important aspects of the SOM-based approach to teleconnection analysis. Winter was chosen because the influence of teleconnections

Table 3.4: Pearson correlation between the negative and positive winter time series for each teleconnection examined. The seasonally averaged time series used were derived from a SOM-based dot-product approach. Statistically significant ($p > 0.1$) are given in bold type.

Index	Correlation
AO	**-0.89**
NAO	**-0.84**
PNA	0.14
ARP	**-0.71**
CAI	**-0.84**

Table 3.5: Pearson correlations between SOM-derived teleconnection time series and the standard teleconnection indices. Results are given separately for the positive and negative SOM-derived data. Statistically significant ($p > 0.1$) correlations are given in bold type. Note: ARP was excluded, due to it's shorter observed time series.

	Positive Phase	Negative Phase
AO	**0.660**	**-0.689**
NAO	**0.668**	**-0.752**
PNA	0.309	-0.056
CAI	**0.852**	**-0.778**

Table 3.6: Accuracy and Heidke Skill Scores showing agreement between categorical teleconnection classifications based on SOM-based analysis and the standard telecconection indices.

	Accuracy	Heidke Skill Score
AO	0.63	0.43
NAO	0.73	0.59
PNA	0.53	0.29
CAI	0.59	0.39
ARP	0.84	0.73

on weather patterns is most apparent during this season.

Pearson correlation values between the positive and negative phase dot-product time series confirms a strong inverse relationship in most cases (Table 3.4); e.g. the positive phase AO time series varies inversely with the negative phase (r = -0.89, indicating 70% shared variability). Strong negative correlation coefficients confirm that the SOM-based positive/negative time series pairs reflect a common phenomenon, with changes in weather patterns connected to one phase occurring less frequently during the opposing phase. Remaining unexplained variability is due to i) asymmetry in the spatial structures of positive and negative index phases, ii) the impact of additional phenomena (e.g. other teleconnections) on the signal, and iii) the limitations of the SOM-based approach to teleconnection analysis. The latter arises from the limited number of SOM-extracted patterns, and the spatial domain used in SOM training. The PNA presents an extreme example of SOM limitations in this regard; as discussed previously, the PNA does not exert a strong influence within the Arctic region, and consequently produces relatively minor frequency anomalies in the current SOMs. This increases the chance the PNA-related SOM frequency anomalies are the result of random noise, and decreases the chance that the positive and negative PNA time series reflect an identifiable phenomenon.

Table 3.5 gives Pearson correlation coefficients between standard teleconnection indices and the positive/negative phase SOM-based alternatives. The degree of agreement varies considerably by index and phase, although all but the negative PNA are statistically significant at the p = 0.1 level or above. Results suggest that the SOM-based approach adequately reflects most of the standard indices, capturing a large portion of teleconnection variability (r = 0.66 or higher in most cases, implying 43% agreement). The modest correlations identified for the AO and NAO are understandable, given that this approach allows for asymmetry between the negative/positive

phases, and the focus is on the Arctic rather than North Atlantic (NAO) or larger Northern Hemisphere (AO); as a result, only some teleconnection centers of action contribute to our SOM-based time series. It is interesting to note that the NAO negative phase demonstrates higher agreement with the standard index than the positive phase (r =-0.752, relative to r = 0.668 for the positive phase). This suggests the negative NAO may exert a stronger or more predictable influence on the Arctic than the positive NAO. Similarly, the positive PNA shows significant correlations while the negative PNA does not; in this case, it is largely because the negative PNA does not produce many significant node frequency anomalies in the study domain, while the positive PNA is better represented.

In addition to comparing continuous teleconnection time series, it is useful to compare categorical time series in which teleconnections are either in a neutral state (category 1), positive phase (category 2), or negative phase (category 3). Ultimately, the greatest interest is whether the SOM-based approach accurately separates these three categories. For the purposes of comparison, these three categories have been subjectively defined as follows:

Positive Phase: The standard index is one or more standard deviations above zero (standard category). Using the SOM-based index (SOM-based category), a positive phase is identified if the positive dot product is greater than or equal to 0.55.

Negative Phase: The standard index is one or more standard deviations below zero; the SOM-based negative index is greater than or equal to 0.55.

Neutral Phase: The standard index is within one standard deviation of zero. Neither or both the negative and positive SOM-based indices are greater than 0.55.

These definitions were selected to roughly split individual years evenly into each category.

Two skill scores are presented (Table 3.4) for winter categorical time series: i)

accuracy, which simply reports the fraction of SOM-based categories that agree with the standard index categories, and ii) the Heidke skill score (Table 3.6), which is accuracy after the impact of random chance is removed (e.g. Doswell et al. (1990)). Both scores return a value of one for perfect agreement, and zero for no agreement. Results confirm that SOM-based teleconnection data captures these semi-objective categories, with accuracies all larger than 0.5 (50% correct). Heidke scores confirm that in many cases these are considerably higher than random chance, with the NAO (0.59) and ARP (0.74) giving particularly high scores. The PNA again emerges as a low scoring outlier, but SOM-based PNA categories still show greater agreement with standard categories than would be expected by random chance (Heidke score of 0.29).

In summary, the SOM-based approach to quantifying the state of teleconnection indices is appropriate for those indices exerting a strong influence on the geographical region on which a particular SOM focuses. Agreement between these SOM-derived indices and more traditional (continuous) indices will not be perfect; however the SOM-based approach is suitable for identifying periods when synoptic conditions in the study region reflect those associated with a given teleconnection. This approach is also likely to identify periods when local conditions resemble one phase of a teleconnection even when regions outside the Arctic do not; e.g. situations in which a strong Icelandic Low occurs (captured by the SOM) in conjunction with a weak Azores High (not captured). In such a situation, the traditional NAO index would remain neutral, while the SOM-based index would indicate a positive NAO event. Assuming the local manifestation of the index is most important to local phenomena (e.g. sea ice loss in the current study), the SOM-based index is likely preferable.

Tables in Appendix A give all teleconnection time series (SOM dot products and traditional indices) for winter and summer respectively.

Chapter 4

Rapid Arctic Sea Ice Loss in 21st Century Model Simulations

Having introduced a SOM-based Arctic circulation framework in Chapter 3, we now use this framework to compare rapid ice loss events (RILEs) across CMIP models and scenarios. The goal is to identify common atmospheric conditions (either as seasonal anomalies in SOM node frequencies or SOM-based teleconnection indices) coincident with periods of rapid ice loss. We begin by summarizing all RILEs identified in SRES A1B and SRES A2 simulations provided through the CMIP archive, using the definition of Holland et al. (2006), then proceed through seasonal (Winter and Summer) circulation analyses. Circulation anomalies are summarized both for i) RILE periods ii) and composites of all years with marked September ice loss. Results presented here focus on a small subset of GCMs that demonstrate reasonable capacity to simulate observed climatology, as measured in the previous chapter. This was done to increase the likelihood that results could be reliably interpreted in the context of observed atmospheric circulation. This criteria, combined with greater availability of daily data and an apparent susceptibility to RILEs, has led to an emphasis on results

from the Community Climate System Model (CCSM3). Of the RILEs examined in two climate change scenarios, thirteen of seventeen occur in CCSM 3.0 simulations, with the remaining four taken from CGCM 3.1 (T63), CSIRO MK 3.5, and ECHAM5-MPI. Consequently, the results should be viewed as a detailed analysis of rapid ice loss in one GCM, with a handful of additional simulations providing context.

4.1 Results

4.1.1 Periods of Rapid Arctic Sea Ice Loss

Using the criteria described by Holland et al. (2006) periods of rapid ice loss (RILEs) were found in 21^{st} model projections, forced with SRES A1B and SRES A2 emission scenarios. Tables 4.1 and 4.2 show identified periods of rapid ice loss for model runs of the SRES A1B and SRES A2 emission scenarios respectively. Eleven of the nineteen models forced with the SRES A1B scenario produced RILEs in at least one ensemble member, as do ten of the fifteen SRES A2 models. These events are very common in some models, with all SRES A1B runs featuring an RILE (BCCR BCM2.0, NCAR CCSM3.0, CNRM CM3, IPSL CM4 and MIROC 3.2 (medres)). Several of these models (BCCR BCM2.0, CNRM CM3 and IPSL CM4) also feature an RILE in every SRES A2 run available. Other models appear less susceptible to these events, either only producing an RILE in only the more aggressive SRES A2 scenario (CSIRO-Mk3.0, CSIRO-Mk3.5, CGCM3.1 and GFDL CM2.0), or producing no RILEs at all (INMCM 3.0, MRI CGCM 2.3.2a and GISS Model e r). GISS AOM has one RILE in SRES A1B run 1 ; however, this event occurs at the end of the century, and may simply be an artifact of averaging over a shorter period at the end of the study period. RILEs that are only two years long often do not contain the years of greatest ice loss; ie. ECHAM5. The timing of RILEs differs between models, greenhouse gas scenarios,

and individual runs from a given model. The majority occur in the second half of the 21^{st} century, although several models place events prior to 2050. It is notable that these early RILEs are mostly found in the middle-of-the-road SRES A1B climate scenario; however, this is likely due to the greater availability of SRES A1B runs compared to SRES A2 rather than an indication that early RILEs are more likely in a slower-warming scenario. This interpretation is reinforced by NCAR CCSM3, which produces early RILEs under both scenarios due to an apparent susceptibility to these events and the large number of runs available under each scenario.

Table 4.1: Identified periods of rapid ice loss in SRES A1B models runs. Bolded events have a RILE within available daily sea level pressure data. The ice loss trend for each event is shown in the right most column.

Model	Run	Years	Length, years	Trend, 10^6 km^2/year
BCCR BCM 2.0	Run 1	**2064-2068**	5	-0.33
	Run 1	**2094-2095**	2	-0.60
CCSM 3.0	Run 1	**2024-2033**	10	-0.38
	Run 2	**2034-2041**	8	-0.43
	Run 2	**2047-2050**	4	-0.39
	Run 3	**2025-2029**	5	-0.45
	Run 4	**2030-2034**	5	-0.40
	Run 5	**2027-2034**	8	-0.35
	Run 6	**2030-2034**	5	-0.52
	Run 6	**2042-2045**	4	-0.37
	Run 7	**2012-2016**	5	-0.44
	Run 7	**2043-2047**	5	-0.39
	Run 8	**2045-2049**	5	-0.47
CGCM 3.1	Run 1	-	-	-
CGCM 3.1(T63)	Run 1	2057-2059	3	-0.32
	Run 1	**2095-2096**	2	-0.44
CNRM CM3	Run 1	2035-2042	8	-0.43
CSIRO-Mk3.0	Run 1	-	-	-
CSIRO-Mk3.5	Run 1	-	-	-
ECHAM5-MPI	Run 1	2078-2082	5	-0.40
	Run 2	2071-2073	3	-0.43
	Run 2	**2081-2082**	2	-0.38
	Run 2	**2097-2098**	2	-0.59
GFDL CM2.0	Run 1	-	-	-
GFDL CM2.1	Run 1	2040-2044	5	-0.39
GISS AOM	Run 1	**2097-2098**	2	-0.45
	Run 2	-	-	-
GISS model e r	Run 1	-	-	-
	Run 2	-	-	-
	Run 3	-	-	-
	Run 4	-	-	-
	Run 5	-	-	-
IAP FGOALS 1.0 g	Run 1	-	-	-
	Run 2	2002-2005	4	-0.40
	Run 3	-	-	-
INMCM 3.0	Run 1	-	-	-
IPSL CM4	Run 1	2001-2002	2	-0.40
	Run 1	**2061-2065**	5	-0.42
	Run 1	2071-2075	5	-0.39
	Run 1	**2096-2098**	3	-0.46
MIROC 3.2(hi)	Run 1	-	-	-
MIROC 3.2(med)	Run 1	2067-2072	6	-0.40
	Run 2	**2059-2065**	7	-0.30
	Run 3	**2063-2068**	6	-0.43
MIUB ECHO-G	Run 1	-	-	-
MRI CGCM 2.3.2a	Run 2	2072-2078	7	-0.44
	Run 3	-	-	-

Table 4.2: Identified periods of rapid ice loss (RILEs) in runs of tested models forced with the SRES A2 scenario. Years that are bold have at least one year within a RILE with daily sea level pressure data. The ice loss trend for each event is shown in the right most column.

Model	Run	Years	Length, years	Trend, 10^6 km^2/year
BCCR BCM 2.0	Run 1	**2082-2091**	10	-0.34
CCSM 3.0	Run 1	**2033-2035**	3	-0.41
	Run 2	**-**	-	-
	Run 3	**-**	-	-
	Run 4	**-**	-	-
	Run 5	**2025-2027**	3	-0.36
CGCM 3.1	Run 1	**-**	-	-
	Run 2	**-**	-	-
	Run 3	**-**	-	-
	Run 4	**-**	-	-
	Run 5	**2085-2086**	3	-0.42
CNRM CM3	Run 1	**2048-2054**	7	-0.50
CSIRO-Mk3.0	Run 1	**2086-2092**	7	-0.33
CSIRO-Mk3.5	Run 1	**2080-2085**	6	-0.38
ECHAM5-MPI	Run 1	-	-	-
GFDL CM2.0	Run 1	2070-2075	6	-0.34
	Run 1	**2096-2099**	4	-0.49
GFDL CM2.1	Run 1	-	-	-
GISS model e r	Run 1	-	-	-
INMCM 3.0	Run 1	-	-	-
IPSL CM4	Run 1	2068-2070	3	-0.54
MIROC 3.2(med)	Run 1	2067-2073	7	-0.50
MIUB ECHO-G	Run 1	**2063-2067**	5	-0.37
	Run 2	**-**	-	-
	Run 3	**2062-2063**	2	-0.60
MRI CGCM 2.3.2a	Run 1	-	-	-
	Run 2	-	-	-
	Run 3	-	-	-
	Run 4	-	-	-
	Run 5	-	-	-

4.1.2 Atmospheric feature counts and SOM-derived teleconnection indices

Results of SOM-based analyses are presented in detail in tables provided in Appendix B, and summarized as a series of images here. The initial analyses focused on a comparison of Arctic circulation a) over a complete 21^{st} century model simulation and b) RILEs within the run. Here circulation anomalies are measured as occurrence counts of key circulation features found in the SOM nodes (e.g. cyclones/anticyclones in specific geographical locations; see previous chapter for a list of features, and their description). Each RILE (of sixteen analyzed) is treated as an individual event, and the range of anomalies across all RILEs are summarized with boxplots. These show the median (a solid black line), 25^{th} and 75^{th} percentiles (edges of the 'box'), and the 5^{th} and 95^{th} percentiles (whiskers). Values shown are standardized difference of population mean test scores:

$$z = \frac{(u_1 - u_2)}{\sqrt{\frac{s_1^2}{n_1} + \frac{s_2^2}{n_2}}}$$

where u_{i}, s_{i}, and n_{i} are respectively the mean, standard deviation, and number of observations in population i. This allows results to be compared across models and individual runs, all with differing climatologies. All figures highlight the area in which the null hypothesis (that the two populations have the same mean) is accepted at the $\alpha = 0.1$ level (z=-1.64 to 1.64).

Anomalies in the SOM feature counts over RILEs are summarized for winter in Figure 4.1 and for summer in Figure 4.2. The winter results show no strong relationship between feature counts and RILEs, with median anomalies statistically indistinguishable from zero. The 25^{th} to 75^{th} quartiles all straddle the z = 0 (no anomaly) line, indicating at least 25% of RILE-averaged anomalies are positive and at least 25% are negative. Only Beaufort Highs (BH) show a somewhat compelling

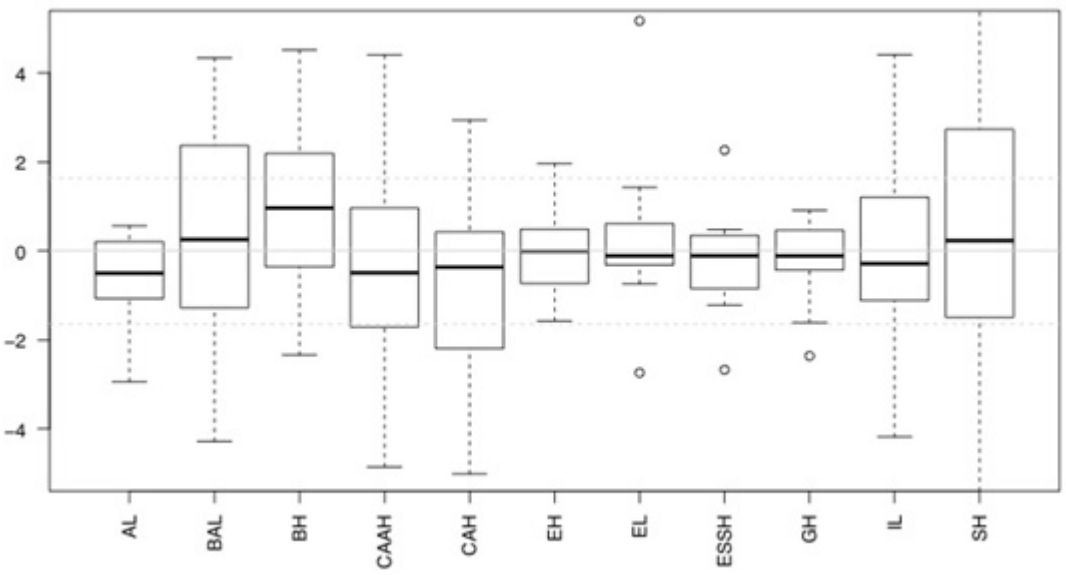

Figure 4.1: Deviations of winter SOM feature counts during RILEs from mean simulated climatology. Results are presented as difference of population mean tests (z-scores) between a full model run and embedded RILEs. Boxplots show the range of results over the 15 examined ice loss events.

case for a consistent winter anomaly, with a median significantly above zero (~1). Still, less than half of the analysed RILEs show a statistically significant difference from the long-term mean.

Summer results (Figure 4.2) also show few common anomalies, with the possible exception of fewer lows in the Barents Sea (BAL). Although several RILEs give weak positive anomalies, just under half of the RILEs give a statistically significant negative BAL anomaly.

To better identify circulation anomalies associated with rapid ice loss, a second analysis was performed on years with ice loss greater than 0.45 million km^2. This highlights anomalies associated with year-on-year ice loss, whether or not they occur within a longer period of pronounced loss (a RILE). Here, means over all high ice

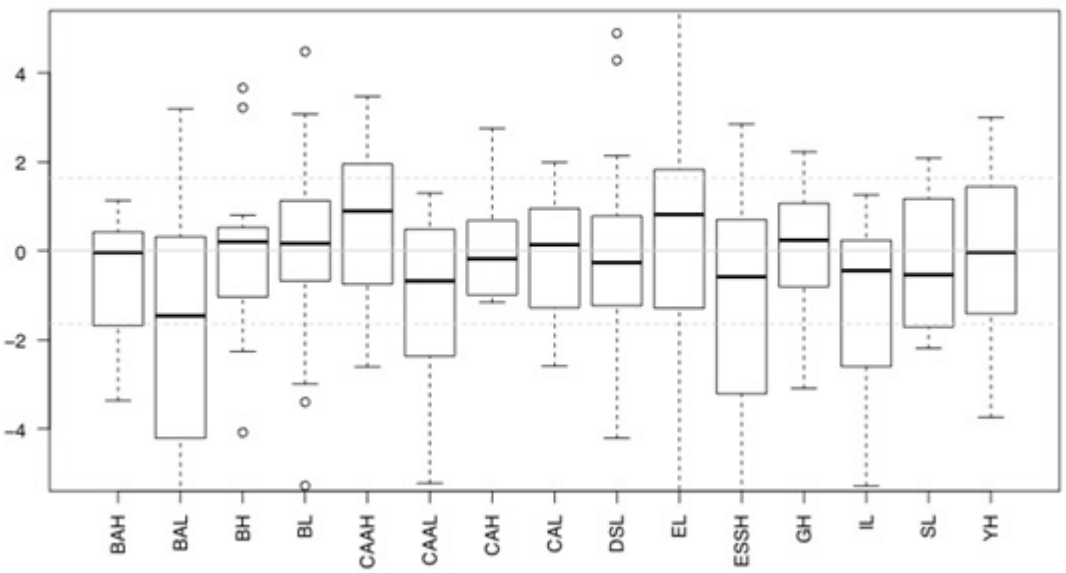

Figure 4.2: Deviations of RILE summer SOM feature counts from simulated climatology. Results are presented as difference of population mean tests (z-scores) between a full model run and embedded RILEs; boxplots show the range of results over the 15 examined ice loss events.

loss years in a given run were compared to the climatology of the full run. Thirteen runs were examined; the ten SRES A1B scenarios and three SRES A2 scenarios containing analyzed RILEs. Results for winter are shown in Figure 4.3. The figure shows greater agreement than the RILE-based calculations, with many feature count anomalies showing a consistent sign across all runs. For example, Aleutian lows are almost entirely decreased during high ice loss averages, while Beaufort Highs mostly increase. However, very few of the large ice loss anomalies are statistically significant.

Summer anomalies for large ice loss years similarly show greater coherence than the related RILE-based analysis (Figure 4.4). While the number of statistically significant differences from mean climatology remains low, there is generally greater cross-run agreement and stronger differences than in winter. In particular, the median and

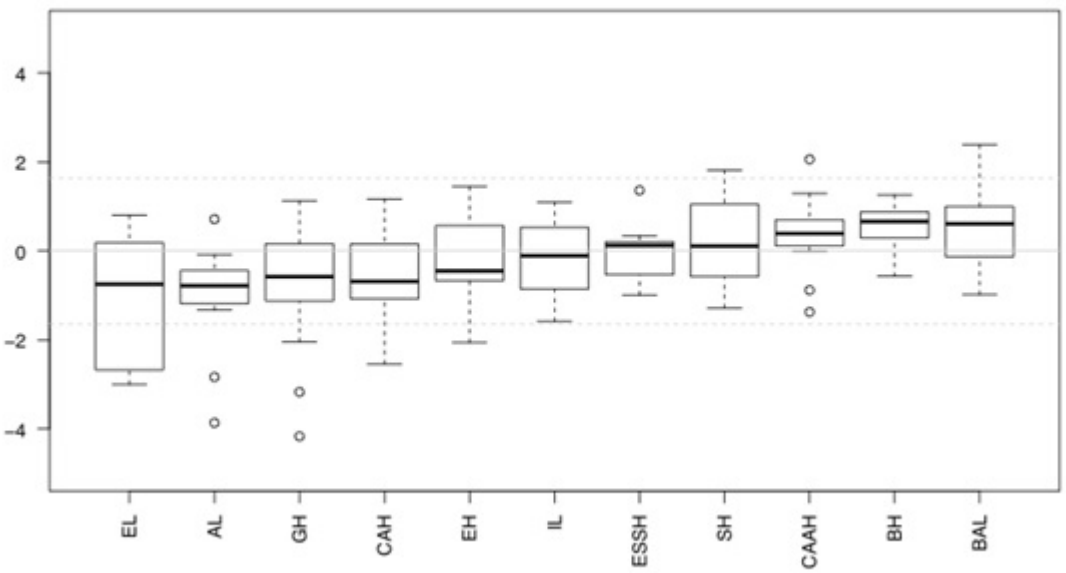

Figure 4.3: Deviations of winter SOM feature counts averaged over large ice loss years relative to simulated climatology. Results are presented as difference of population mean tests (z-scores) between i) the subset of high ice loss years in a model run containing an RILE and ii) the remaining model run. Boxplots show the range of results across the 13 runs examined. Features here have been ordered on the basis of the mean test score over all examined runs, to ease interpretation.

25^{th} percentiles of Canadian Arctic Archipelago Lows (CAAL) and Barents Sea Highs (BAH) are negative and relatively significant; more than a quarter of anomalies for these features are statistically significant, and more than 75% are negative. Other features showing a tendency to decrease are Beaufort Sea Lows (BL), Central Arctic Lows (CAL) and Yukon Highs (YH); all show decreases in more than 75% of runs. Similarly, highs over the Central Arctic (CAH), Canadian Arctic Archipelago (CAAH), Greenland (GH), and the Beaufort Sea (BH) all tend to increase in frequency, along with Eurasian (EL) and Barents Sea Lows (BAL).

Figures 4.5 through 4.8 show results of SOM-based teleconnection anomalies relative to mean climatology, again calculated as averages over individual RILEs (Figures

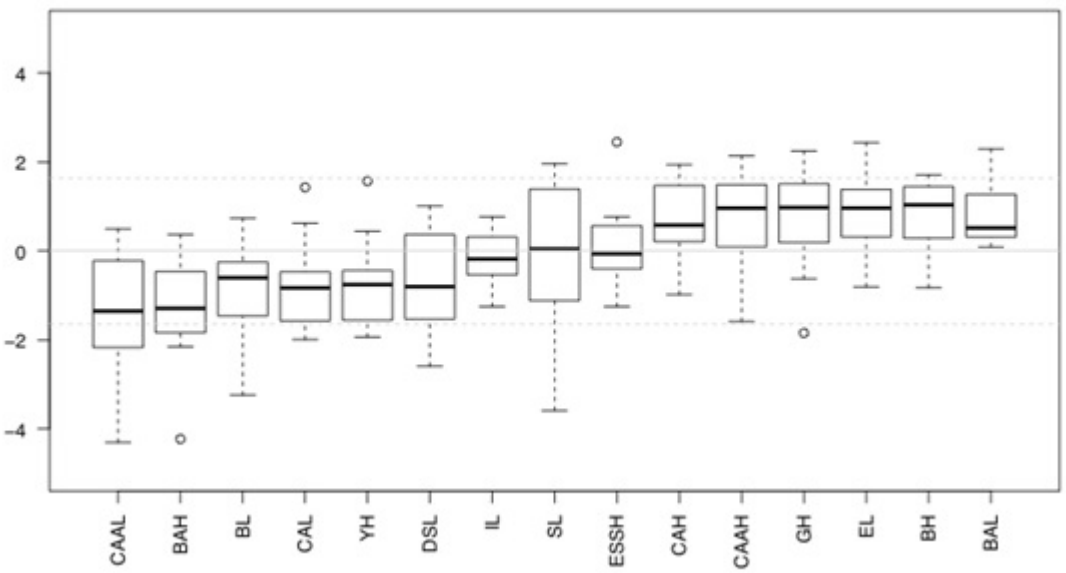

Figure 4.4: Deviations of summer SOM feature counts averaged over large ice loss years from simulated climatology. Results are presented as difference of population mean tests (z-scores) between i) the subset of high ice loss years in a model run containing an RILE and ii) the remaining model run. Boxplots show the range of results across 13 runs examined. Features here have been ordered on the basis of the mean test score over all examined runs, to ease interpretation.

4.5 and 4.6) and high ice loss years within runs (Figures 4.7 and 4.8).

Teleconnection anomalies across all RILEs show no clear agreement. In winter the median scores are near zero for both phases of all indices. Median results for summer show greater deviation from zero, but statistically significant anomalies remain rare. Results for both winters and summers of RILEs show no clear preference for the negative or positive phase of any index.

Anomalies over large ice loss years show clear preference for certain phases of teleconnection indices (Figure 4.7). The positive phase of the ARP appears to be common during ice loss years, with all but one run producing a positive anomaly. The positive phase of the AO, and to a slightly lesser extent the NAO, is also emphasized.

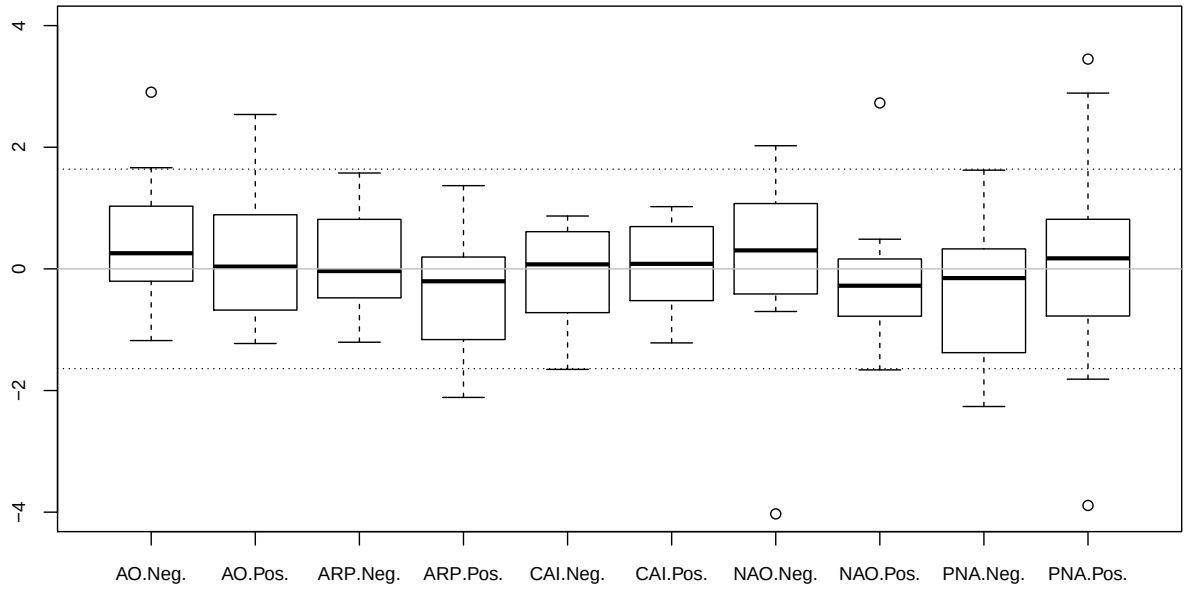

Figure 4.5: Deviations of winter teleconnections scores averaged over RILEs from simulated climatology. Results are presented as difference of population mean tests (z-scores) between a full run and embedded RILEs; boxplots show the range of results over the 15 examined ice loss events.

There are some weak indications that the PNA has a connection to high ice loss, although the results are somewhat contradictory; most (75%) of runs show a decrease in the positive phase of the PNA, but roughly half also show a decrease in the PNA negative phase.

Large ice loss analysis for the summer again shows more variation in teleconnection scores with larger interquartile range. However the negative phases of the AO and NAO are associated with ice loss, with both favoring positive anomalies (>75% and >50% of runs, respectively). The positive phase of the CAI occurs in more than 75% of runs and the positive phase of the PNA is favored in more than 50%.

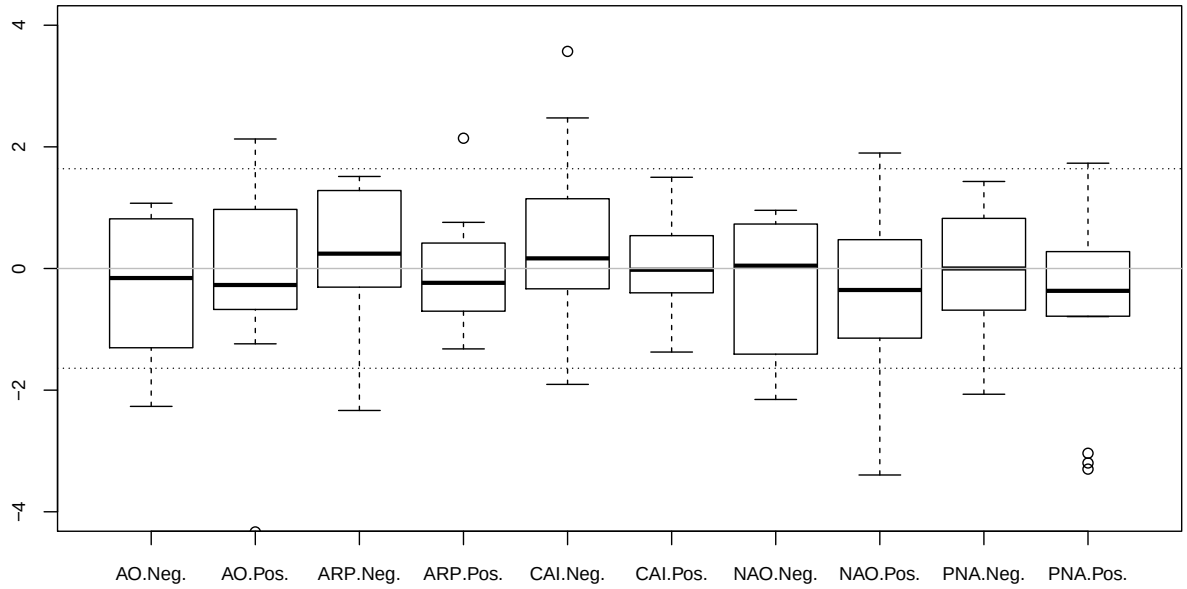

Figure 4.6: Deviations of summer teleconnections scores averaged over RILEs from simulated climatology. Results are presented as difference of population mean tests (z-scores) between a full run and embedded RILEs; boxplots show the range of results over the 15 examined ice loss events.

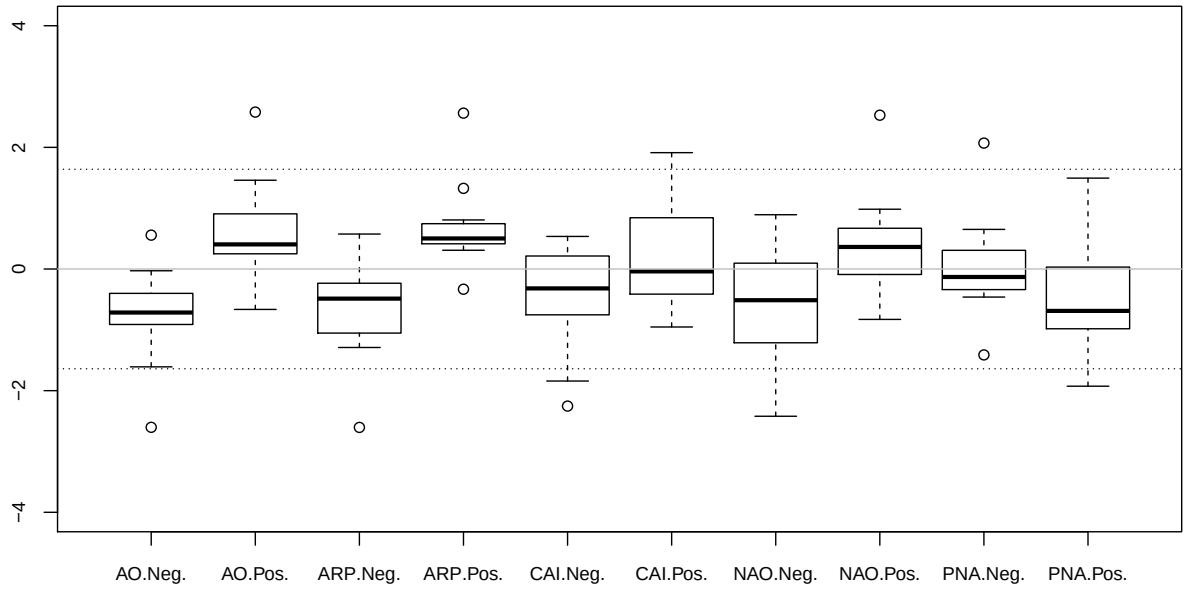

Figure 4.7: Deviations of winter teleconnections scores averaged over large ice loss years from simulated climatology. Results are presented as difference of population mean tests (z-scores) between i) the subset of large ice loss years in a model run containing an RILE and ii) the climatology of the model run.

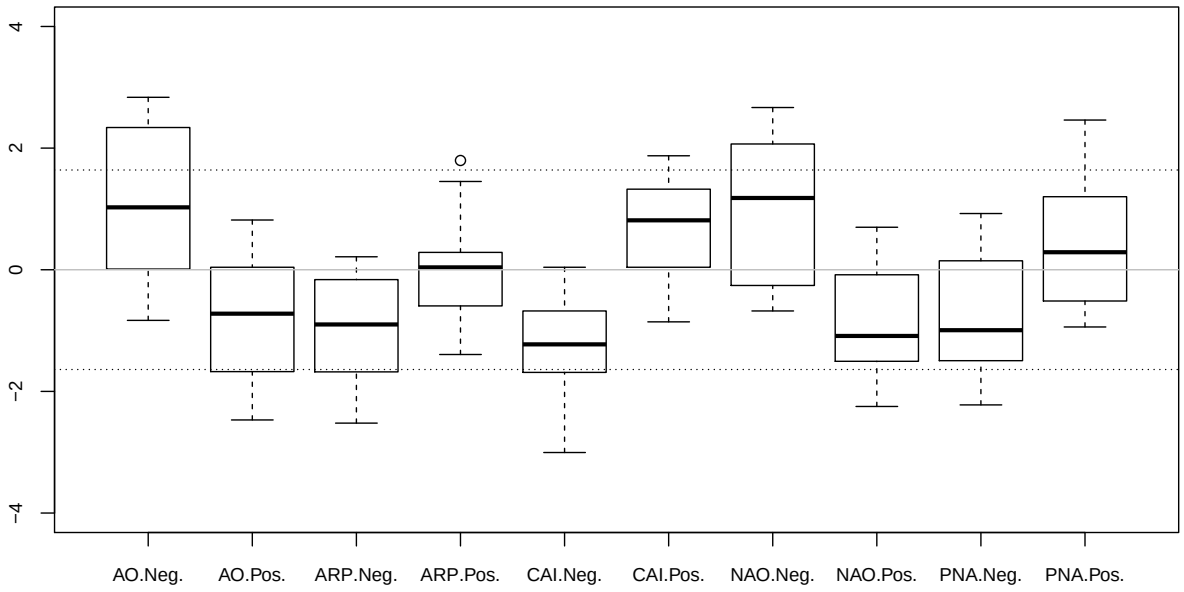

Figure 4.8: Deviations of summer teleconnection scores averaged over years with large ice loss years from climatology. Results are presented as difference of population mean tests (z-scores) between i) the subset of large ice loss years in a model run and ii) the remaining model run.

4.2 Discussion

Cursory analysis of simulated RILEs fails to identify any common atmospheric circulation anomalies that could explain enhanced ice loss. Although individual RILEs were associated with statistically significant feature-count anomalies, few affected more than a quarter to a third of the identified events. In winter, all circulation features examined also show a significant chance of producing either positive or negative anomalies over the course of an RILE. In summer, there is weak evidence that a decrease in Barents Lows (BAL) contributes to many RILEs, with a modest number of RILEs showing a statistically significant BAL decrease. However, most Barents Low anomalies remain statistically insignificant and several RILEs are characterized by the inverse (positive) anomaly. This suggests reduced Barents Lows may promote extended periods of enhanced ice loss, but is not required for this to occur.

RILEs produce very few statistically significant teleconnection anomalies. Similar to feature counts, the summers produce stronger results with larger absolute median scores. However, the results demonstrate no connection between teleconnection scores and RILEs.

The limited agreement and weak significance identified in these results may be related to the RILE definition used. Because this definition is based on five year running means in ice coverage change, individual RILEs can include years with instantaneous (single year) ice growth. Some years within RILEs were found to have ice gains greater than one million km^2 from the preceding year. Also, since a five year running average is used to identify the events, shorter RILEs do not always contain the largest single year of reduction in a given run. It is expected that ice growth years would be less likely to demonstrate atmospheric anomalies associated with rapid ice loss, and including them in SOM-based analyses may weaken or obscure the impact of these anomalies in averages over a full RILE period. This was addressed by examining

circulation anomalies during years with significant instantaneous ice loss only, highlighting similarities between the high ice loss years that ultimately drive an individual RILE.

Results based on large ice loss years alone show greater agreement than across full RILE periods with greater consistency in the sign of feature count anomalies. While the number of statistically significant anomalies remains low, a few features in summer show a relatively high proportion of significant anomalies (~50% of runs): a decrease in Barents Highs and Central Arctic Lows. Focusing on high ice loss years also strengthens the mean strength and consistency of teleconnection responses; winter responses have less variance and have clear preference for phases of some indices. This suggests ice loss may be connected to the positive phases of the ARP, the AO, and NAO. Summer shows greater differences across model runs, but suggests ice loss is connected to the negative phases of the AO and NAO, and perhaps the positive phases of the CAI and PNA.

Taken as a whole, these results suggest very limited agreement across simulated RILEs. Large ice loss years demonstrate greater agreement; with winter favoring positive phase of the Arctic Rapid Change Pattern and positive phases of the Arctic and North Atlantic Oscillation. The lack of common winter feature anomalies suggests that teleconnection anomalies can arise from variability in several weather systems contributing to related centers of action. In summer the situation reverses, with feature counts showing the strongest agreement. This likely reflects the influence of large-scale (synoptic-scale) influences on weather in winter, and the shift to regional (mesocale) influences in summer. In other words, common conditions promoting winter ice loss likely involve multiple centers of action and several circulation features, while summer loss is best explained by specific centers.

Recalling that the SOM-based (and Arctic-specific) approach to measuring tele-

connections differs considerably from traditional teleconnection definitions, it is useful to compare the results to teleconnections proposed as drivers of observed ice loss. As a whole, anomalies during large ice loss favor enhanced winds along the transpolar ice drift, corresponding to increased ice flux out of the Arctic. In winter, this appears as a strong preference for the positive phase of the Arctic Rapid Change Pattern (ARP; (Zhang et al. 2008)). The ARP is associated with a dipole over the Arctic that promotes winds along the Transpolar Drift, encouraging ice flux out of the Arctic through the Fram Strait. Weak tendencies for lows to increase to the east of the drift (in the Barents Sea; BAL) with a corresponding increase in highs to the west (near the Canadian Arctic Archipelago; CAAH) further suggest a tendency towards enhanced drift. The same tendency is observed in summer, with increases in lows over the Barents Sea (BAL) and highs over Greenland (GH), the Canadian Arctic (CAAH) and the central Arctic (CAH) acting to enhance along-drift winds. At the same time, features that would weaken the drift typically decrease; e.g. lows to the west of the drift (Davis Strait, DSL; Canadian Arctic, CAAL; Central Arctic, CAL), and highs over the Barents Sea (BAH). This last change can also be interpreted as a contribution to an Arctic Dipole, similar to that discussed in several studies of observed ice loss (Wu et al. 2006; Overland et al. 2005; Wang et al. 2009a). This is particularly true of cases where the Barents High reduction accompanies an increase in highs over the Canadian Arctic Archipelago (CAAH; 46% of runs) and/or a reduction in the number of lows in the same region (CAAL; 54% of runs). A decrease in central Arctic lows (CAL; 54% of runs) may further enhance this dipole character, as these features resemble more northerly CAAL events; the combination of decreased CAAL and CAL events may also reflect the tendency of CAAL lows to subsequently move towards the central Arctic (Serreze et al. 2008). These features do not result in a strong Central Arctic Index (CAI; Vihma et al. (2012)) anomaly (dipole centered near Fram Strait).

The CAI quantifies the pressure gradient approximately perpendicular to the mean orientation of the transpolar drift and qualitatively resembles a dipole anomaly, although with more direct alignment to the outflow of transpolar drift than the ARP. The results suggest that the direct forcing of a CAI-like dipole is less representative of ice loss than the ARP.

The preference for both a positive NAO and positive AO in the winter of large ice loss years agrees with findings by (Deser et al. 2000), Omstedt et al. (2001), Hu et al. (2002), and Maslanik et al. (2007) that have all shown that winters with a strong positive NAO historically precede summer reductions in sea ice extent. The connection between a positive AO in winter proceeding ice loss has been discussed by Stroeve et al. (2008), Deser et al. (2008), Overland et al. (2005), Lindsay et al. (2005), and Rigor et al. (2002). The similar results for the AO and NAO is consistent with the high correlation of these two indices (Ambaum et al. 2001). The Barents Low (BAL) is the feature with the most significant increase in winter large ice loss years and is a characteristic feature of the positive phase of the NAO and AO regimes. It can be interpreted as increased penetration of the Atlantic storm track into the Arctic Ocean. The above results suggest an association with wind forcing of the transpolar drift and increased penetration of the Atlantic storm track into the Arctic Ocean.

Results do not show a clear connection with Beaufort Gyre forcing. While past studies have suggested weakened Beaufort Highs can explain anomalies in simulated ice climatology (DeWeaver et al. 2006) or drive observed ice loss (L'Heureux et al. 2008), the SOM-based analysis suggests a weak tendency for Beaufort Highs to increase during high ice loss years (46% of runs). This may be slightly offset by a reduction in weaker Beaufort Highs in other SOM nodes; for example, some nodes dominated by Barents Highs feature a more muted Beaufort High. It may be that the identified Barents High decrease reflects a reduction in Beaufort High activity.

However, it is unlikely that these SOM nodes strongly reflect Beaufort High activity, as they are dominated by other (stronger) features. Consequently, inferences based on the stronger Barents Highs, and the nearby transpolar drift seem more reliable.

It is worthwhile repeating that the analysis focuses largely on NCAR CCSM3.0 simulations, and the interpretation presented here may not apply to other models. It is also important to reiterate that these anomalies are (with rare exception) statistically weak and vary considerably across individual model runs. However, their suggestion of an enhanced transpolar drift is in broad agreement with several observational studies (Stroeve et al. 2012b). It is clear, however, that this enhancement is not necessary for a simulated large ice loss year to occur, nor for rapid ice loss period. Other factors, including those unrelated to atmospheric forcing, are needed to explain enhanced ice loss in NCAR CCSM3.0 and the other models considered here.

Chapter 5

Observed Periods of Rapid Ice Loss

Having examined ice loss events simulated by a range of General Circulation Models (GCMs), we now turn our attention to the observational record. The sharp decline in minimum ice extent since 2000 has received a good deal of attention, and in many ways resembles GCM-predicted RILEs (e.g. Stroeve et al. (2007)). Here, we examine large loss years using the same SOM-based methodology applied to simulated RILEs. Similar to Chapter 4, these are defined as single year ice loss of 0.45 Million km^2 or more. The goal is to determine whether significant single year decreases between 1980 and 2010 share common atmospheric circulation anomalies. We further examine a seven year period of accelerated ice retreat (2002-2008); although not technically a RILE according to the criteria of Holland et al. (2006), it does share many characteristics with these events, and is here treated as their observational analogue. This analysis provides an opportunity to compare our SOM-based circulation analyses with previous work focusing on more traditional teleconnection definitions, as well as a basis for comparing observed loss to the weak trends identified in Chapter 4.

5.1 Results

Following the approach of the last chapter, we compare mean SOM feature counts and SOM-based teleconnection scores averaged over i) all large ice loss years and ii) 2002-2008 to the mean climatology of 1980-2010. Differences are again reported as a difference of population mean test statistic:

$$z = \frac{(u_1 - u_2)}{\sqrt{\frac{s_1^2}{n_1} + \frac{s_2^2}{n_2}}} \tag{5.1}$$

in which u, s, and n are respectively the mean, standard deviation, and size of a sample. Results are presented for winter (DJF) and summer (JJA) averages separately.

5.1.1 Winter

In winter the "RILE like" period demonstrates no consistent anomalies, either in counts of SOM-extracted SLP features (see Figure 5.2). However, the composite of large ice loss years has significantly lower (90% CI) than expected counts of the Aleutian Low and Central Arctic High and strong (though not statistically significant) increase in the Barents Low (see Figure 5.1).

Figures 5.3 and 5.4 show SOM-derived teleconnection winter anomalies, averaged over large loss years and the 2002-2008 period respectively. Again, the 2002-2008 period shows no significant similarities, while large ice loss years as a whole show some agreement. These years show a statistically significant preference for the positive phases of the Arctic Oscillation (AO), North Atlantic Oscillation (NAO) and Arctic Rapid Change Pattern (ARP).

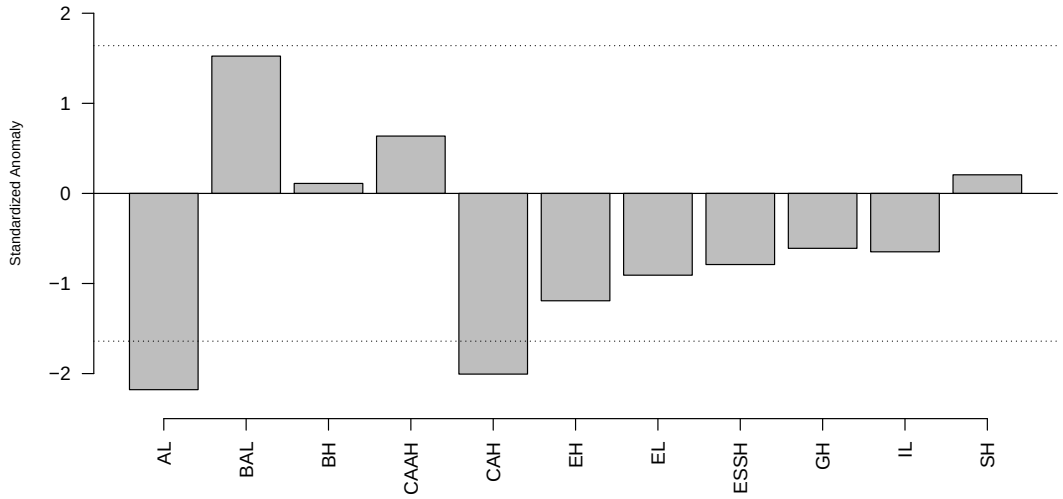

Figure 5.1: Difference between the mean winter feature counts averaged over i) large ice loss years and ii) 1980-2010 of feature count anomalies. Results are given a normally distributed, standardized test statistic ('z' score). Values outside the range (-1.64, 1.64) are statistically significant at the $\alpha = 0.1$ level (marked with dashed lines).

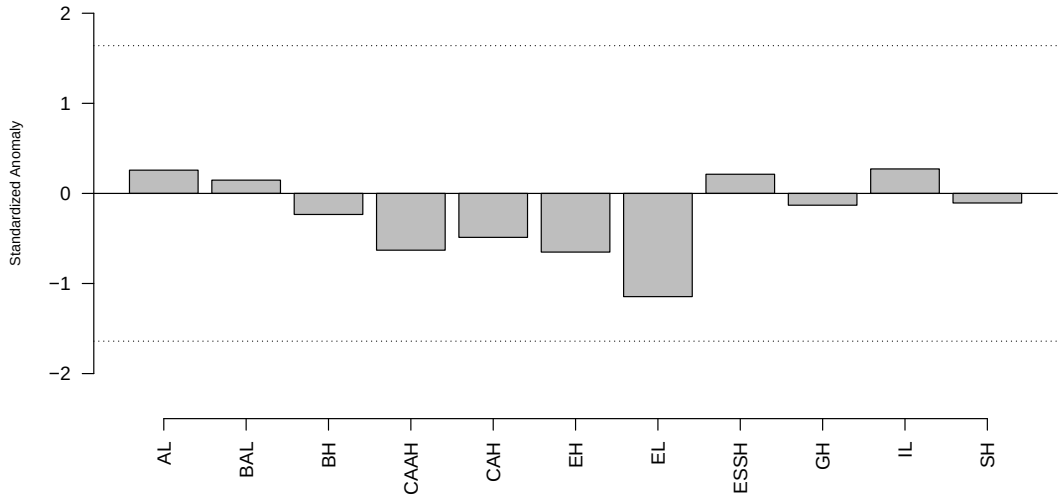

Figure 5.2: Difference between the mean winter feature counts averaged over i) the 2002-2008 advanced ice loss period and ii) 1980-2010 of feature count anomalies. Results are given a normally distributed, standardized test statistic ('z' score). Values outside the range (-1.64, 1.64) are statistically significant at the $\alpha = 0.1$ level (marked with dashed lines).

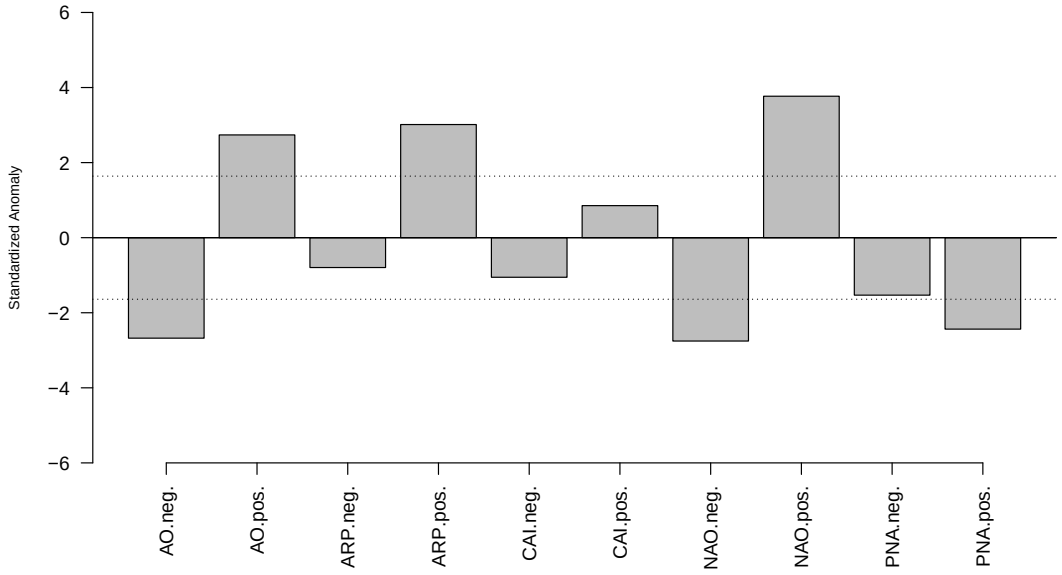

Figure 5.3: Difference between the mean winter teleconnection scores averaged over i) large ice loss years and ii) 1980-2010. Results are given a normally distributed, standardized test statistic ('z' score). Values outside the range (-1.64, 1.64) are statistically significant at the $\alpha = 0.1$ level (marked with dashed lines).

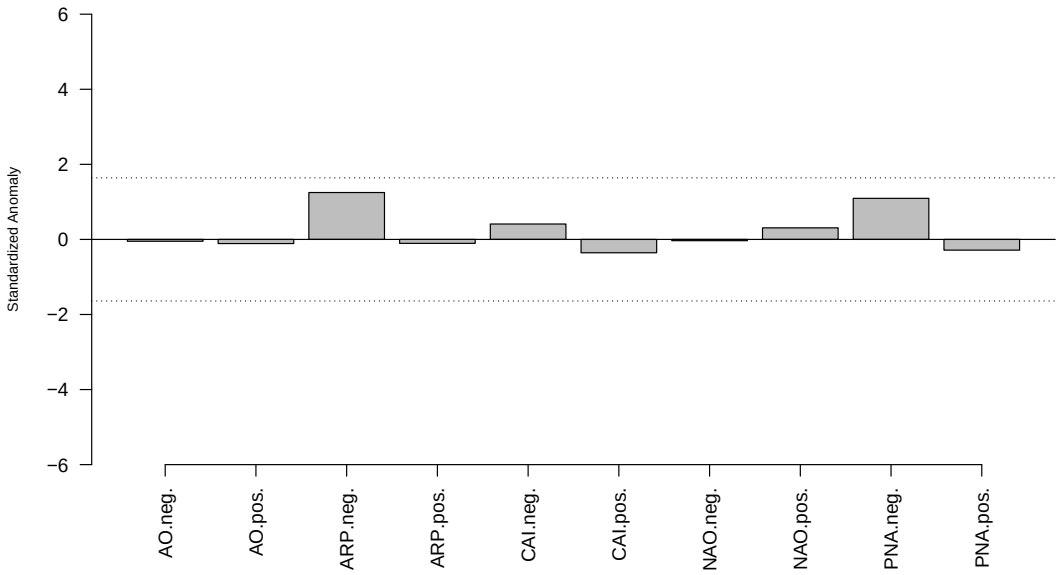

Figure 5.4: Difference between the mean winter teleconnection scores averaged over i) the 2002-2008 advanced ice loss period and ii) 1980-2010. Results are given a normally distributed, standardized test statistic ('z' score). Values outside the range (-1.64, 1.64) are statistically significant at the $\alpha = 0.1$ level (marked with dashed lines).

5.1.2 Summer

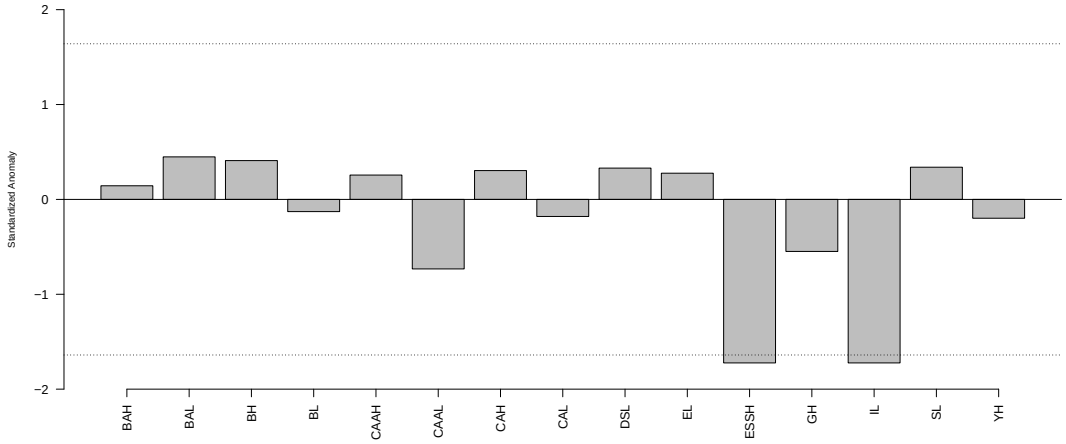

Figure 5.5: Difference between the mean summer feature counts averaged over i) large ice loss years and ii) 1980-2010 of feature count anomalies. Results are given a normally distributed, standardized test statistic ('z' score). Values outside the range (-1.64, 1.64) are statistically significant at the $\alpha = 0.1$ level (marked with dashed lines).

Feature count anomalies for summer averaged over large ice loss years (Fig. 5.5) and the 2002-2008 advanced ice loss period (Fig. 5.6) show several statistically significant differences. Notably, both show a large decrease in Icelandic Lows (IL) and East Siberian Sea Highs (ESSH); the 2002-2008 also saw a decrease in Davis Strait Lows (DSL). However, it is worth noting that all of these features are relatively rare during the summer, with mean occurrences of seven or eight days in a ninety day summer. As such, the statistically significant decreases are unlikely to exert a significant impact on ice circulation.

Teleconnection anomalies averaged over summer large ice loss years (Fig. 5.7) and the 2002-2008 period (Fig. 5.8) show no statistically significant anomalies. Although some individual years in these two subsamples show strong negative or positive teleconnection phases, no universal trend can be seen.

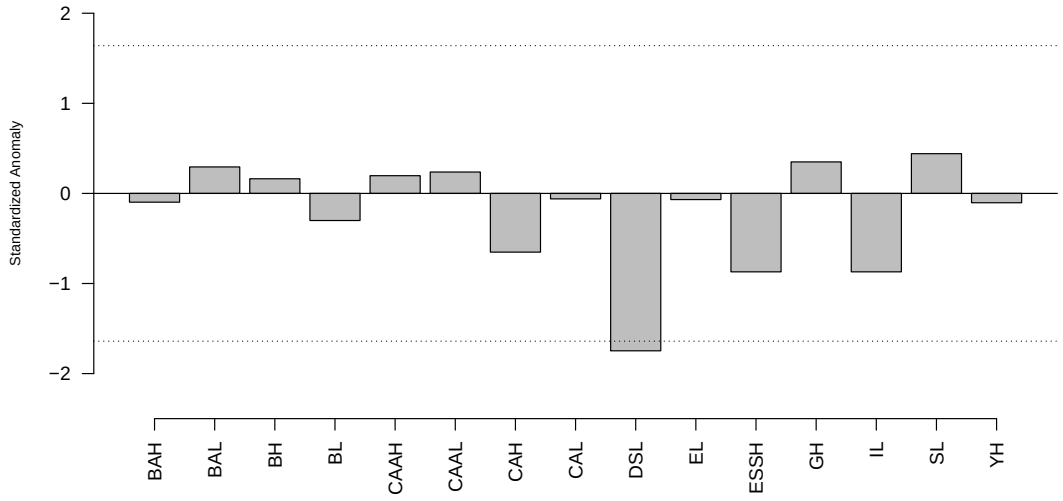

Figure 5.6: Difference between the mean summer feature counts averaged over i) the 2002-2008 advanced ice loss period and ii) 1980-2010 of feature count anomalies. Results are given a normally distributed, standardized test statistic ('z' score). Values outside the range (-1.64, 1.64) are statistically significant at the $\alpha = 0.1$ level (marked with dashed lines).

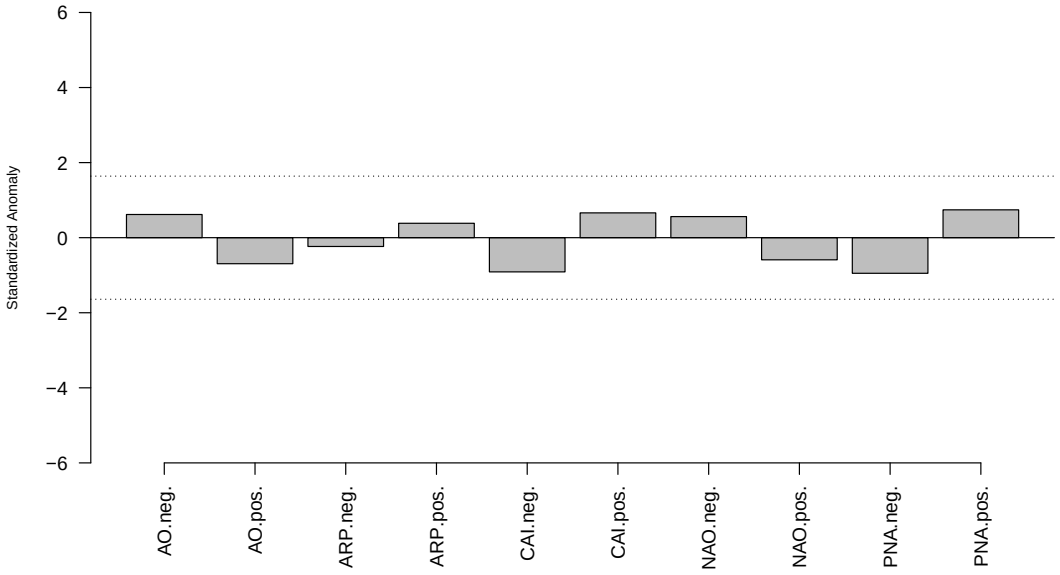

Figure 5.7: Difference between the mean summer teleconnection scores averaged over i) large ice loss years and ii) 1980-2010 . Results are given a normally distributed, standardized test statistic ('z' score). Values outside the range (-1.64, 1.64) are statistically significant at the $\alpha = 0.1$ level (marked with dashed lines).

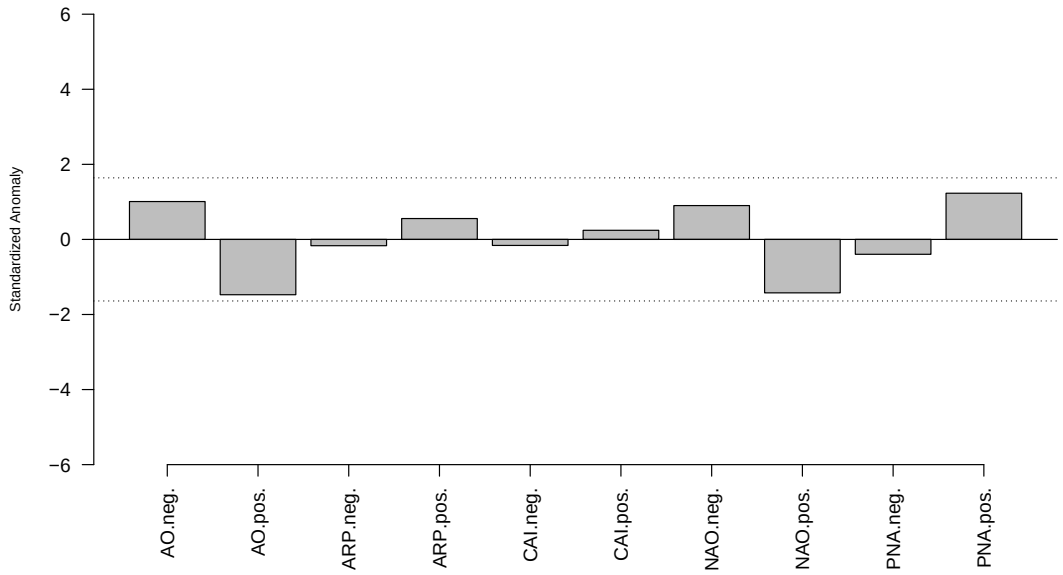

Figure 5.8: Difference between the mean summer teleconnection scores averaged over i) the 2002-2008 advanced ice loss period and ii) 1980-2010. Results are given a normally distributed, standardized test statistic ('z' score). Values outside the range (-1.64, 1.64) are statistically significant at the $\alpha = 0.1$ level (marked with dashed lines).

5.2 Discussion

Findings of this study agree with work of Deser et al. (2000), Omstedt et al. (2001), Hu et al. (2002), and Hu et al. (2002) all of whom show that winters with a strong positive NAO historically precede summer reductions in sea ice extent. Others have discussed this loss in terms of positive winter AO events (Stroeve et al. 2008; Deser et al. 2008; Overland et al. 2005; Lindsay et al. 2005; Rigor et al. 2002); this is supported by a significantly positive AO in large ice loss years of the results. The association of ice loss with both the AO and NAO is consistent with the high correlation of these two indices (Ambaum et al. 2001). The weaker agreement between the AO and ice loss is consistent with the hypothesis that the AO and ice loss decoupled sometime in the mid 1990s (Wu et al. 2006). The AO index was found to be positive during large ice loss years in the early record, the same relationship is absent in later years (see Appendix C). Wu et al. (2006) speculated that this decoupling was due to other atmospheric circulation regimes being more important drivers of ice loss and pointed to the dipole anomaly as a more important index in the prediction of ice loss. Subsequent work by Maslanik et al. (2007) suggest that ice loss is better connected to an "NAO-like" circulation pattern, with low pressure in the Icelandic region, a "central Arctic" pattern with cyclonic circulation over the Arctic Ocean basin, and a dipole pattern with high pressures in the North-American Arctic and low pressures in the Eurasian Arctic. The south-to-north winds encouraged by these patterns (and the 'NAO-like' pattern in particular) have persisted since the late 1980s while the AO index conversely has switched from positive to negative for the same period. These changes are consistent with the identified increase in Barents Lows (BAL) in large ice loss years, a characteristic of positive NAO and AO regimes that can be interpreted as increased penetration of the Atlantic storm track into the Arctic Ocean.

The other emphasized teleconnection pattern in the large ice loss average is the

Arctic Rapid Change Pattern (ARP; Zhang et al. (2008)). The ARP is associated with a dipole over the Arctic that promotes winds along the Transpolar Drift, encouraging ice flux out of the Arctic through the Fram Strait. This is consistent with increases in Barents Lows while counts of the Beaufort High and Canadian Arctic Archipelago High (CAAH) remain normal. It is also supported by the statistically significant decrease in SOM nodes with Aleutian Lows, as these resemble an inverted Dipole Anomaly (following Wu et al. (2006); Wang et al. (2009a)). As a whole, the combination of these feature counts and ARP anomalies could be interpreted as resembling the dipole-like anomaly of Maslanik et al. (2007), the dipole anomaly of Wu et al. (2006), and/or the ARP (Zhang et al. (2008)). However, they do not result in a strong Central Arctic Index (CAI;Vihma et al. (2012)) anomaly (dipole centered near Fram Strait). The CAI quantifies the pressure gradient approximately perpendicular to the mean orientation of the transpolar drift and qualitatively resembles a dipole anomaly, although with more direct alignment to the outflow of transpolar drift than the ARP. Our results suggest that the direct forcing of a CAI-like dipole is less representative of ice loss than the ARP.

It is interesting to note that although there are no statistically significant anomalies associated with the 2002-2008 composite, the NAO, AO, and ARP anomalies are all reversed relative to the large ice loss composite. To the extent that atmospheric forcing is a strong driver of ice loss over this period, this suggests that forcing during individual years (when teleconnections agree with the large ice loss composite average) are more important to ice reduction than the average over an RILE. This is broadly consistent with the findings in GCM analysis.

Summer composites show no consistent teleconnection anomalies. Several significant feature count anomalies are identified (East Siberian Sea Highs; Icelandic Lows; Davis Strait Lows). However, these are all relatively uncommon events, observed on

average seven or eight days in a ninety-day summer. As such, the observed decreases are unlikely to exert a significant impact on ice loss.

Although not the focus of the current study, analysis of single year ice loss event also corroborate prior studies. For example, several studies proposed a connection between the 2007 abrupt ice loss and anomalous anticyclonic circulation over the central Arctic, promoting clear skies and increasing incident solar radiation (Stroeve et al. 2008; Kay et al. 2008). Our results express a similar anomaly as increased frequency of Beaufort and Canadian Arctic Archipelago Highs. Other research suggest the 2007 loss was assisted by unusually high sea level pressure over the Beaufort Sea/Canada Basin and lower pressure over eastern Siberia, promoting warm southerly winds in the Chukchi and East Siberian seas (Kay et al. 2008; L'Heureux et al. 2008; Stroeve et al. 2008; Perovich et al. 2008; Schweiger et al. 2008b; Ogi et al. 2007) that favor melt and transport of ice towards the pole (Ogi et al. 2007; Wang et al. 2009a). In the results, this appears as a 2007 increase in Siberian Lows and Beaufort/Canadian Archipelago Highs.

Although the agreement in these year-specific results suggests that the methodology captures key anomalies on an annual basis, detailed treatment of these individual large loss years is beyond the scope of the current project. Instead, the focus here is on identifying common anomalies across multiple large loss events; results suggest that the most plausible common explanations for observed ice loss are centered in winter. These appear to best explained as positive phases of the NAO and ARP, associated with increased cyclonic activity near the Barents Sea, and a decrease in nodes in the upper left corner of the SOM (identified with Aleutian Lows, and showing a strong, inverted dipole-like anomaly).

The ARP, NAO and the AO are spatially similar patterns: the AO and NAO have been found to have a correlation of 0.95 in daily data (Ambaum et al. 2001)

and the ARP has been described as a north-east shift of the Icelandic center of the NAO pattern (Zhang et al. 2008). The three indexes also had similar results with large ice loss years with higher than expected (above 90% CI) scores for the positive phases of the AO, ARP and NAO indexes. Self-organizing map significant frequency anomalies of the positive phases of the three indices have significant (95% CI) positive correlations to one another (See Table A.10), and the negative phases have significant correlations (95% CI) between the AO and ARP, and NAO and ARP (See Table A.9). The similar anomalies for the positive phases of the patterns are increased frequency of days with cyclonic activity over Iceland and the Barents Sea region in the lower left and lower center of the self-organizing map at the expense of nodes in the upper left of the map. It could be argued that the similarity of these patterns justifies focusing on only one; e.g. the NAO alone. However, although the indices are significantly correlated, the actual explained variance between the three indices (as represented through our SOMs) is small (between 16 and 60%). Given this, it remains reasonable to assume that some of the unexplained variance may be important to understanding ice loss. For this reason, all were included in our analyses.

Chapter 6

Conclusion

Observed and simulated ice loss was studied using a framework for atmospheric analysis based on self-organizing maps (SOMs). The original focus of this research were Rapid Ice Loss Events (RILEs) defined by Holland et al. (2006); however, additional analysis was conducted on subsets of years with large ice loss. In both cases, model simulations and observations were examined in an effort to identify Arctic circulation anomalies common to periods of notable sea ice loss. Atmospheric circulation is quantified here using SOM analyses of sea level pressure (SLP) over the Arctic. Key SLP features were identified in resulting SOM nodes, and anomalies are expressed as anomalous counts of these features relative to climatology. The same Arctic-centered SOM was used to quantify the strength and phase of prominent teleconnection patterns, in order to explore links between these teleconnections and ice loss.

The approach to quantifying teleconnections used here is believed to be novel. In an effort to ease comparison across multiple GCMs and reanalyses, emphasize impacts on the Arctic, and accommodate asymmetry in opposing phases, teleconnections were represented in terms of their net impact on SOM node frequency. Using traditional teleconnection indices, months associated with either i) a strong positive or

ii) a strong negative phase of a particular teleconnection were identified. SOM node frequencies were then calculated for each of these negative and positive composites in reanalysis data, and significant (α=0.05) frequency anomalies relative to climatology were identified. A teleconnection 'weighting vector' was then defined for each phase, consisting of these statistically significant SOM node frequency anomalies. Taking the dot product between i) a teleconnection weighting vector and ii) anomalies in the same SOM nodes from a period of interest gives a quantitative measure of similarity to a teleconnection. Different phases are assigned their own weighting vector, allowing structural asymmetries to be highlighted. The validity of this SOM-based approach to quantifying the amplitude and phase of teleconnections is supported by several tests between traditional indices and SOM-derived indices with the following results: i) Pearson correlations for three-category (positive, neutral and negative) time series of all indices with the exception of the Pacific North American pattern were significant (above α=0.10), ii) accuracy scores for all indices were greater than 50%, and iii) Heidke Skill scores, which remove random chance, exceeded 50% for the North Atlantic Oscillation (NAO) and Arctic Rapid Change pattern (ARP). Complete agreement between these SOM-derived indices and more traditional (continuous) indices was not expected, as one or more teleconnection center of action is located outside the study region. The results show that the SOM-based approach is suitable for identifying periods when synoptic conditions in the study region reflect those associated with a given teleconnection.

Results from analysis of RILEs show a range of circulation patterns that appear to have some potential connection to accelerated ice loss, but no single pattern can explain all loss. Some RILEs have significant (alpha=0.10) anomalies in feature counts and teleconnection phases, but overall the events show near equal chance of producing positive or negative anomalies. The "RILE like" event in observations shows no

significant anomalies in winter with only a single significant anomaly in summer. The variance in atmospheric anomalies in simulated RILEs is likely due to the definition of the RILE period. Since a five year running average is used to calculate events, RILEs include years with instantaneous (single year) ice growth and shorter RILEs do not always contain the largest single year of reduction in a given event.

Averages over individual years with significant ice loss was conducted in an attempt to better emphasize likely links between the atmosphere and ice loss. Composites over these years alone produce different results than RILEs, suggesting that long-term and short-term periods of ice loss driven by different processes. Although high ice loss averages show fewer significant circulation anomalies than RILE averages, the sign of anomalies is more consistent. Stronger agreement over high ice loss averages than RILEs suggests any atmospheric drivers of ice loss are better understood over short time scales (a year) rather than longer periods of high average loss (years to decades). Although results for high loss averages show broad agreement, the limited statistical significance and high variability in results across model runs does not support a strong, simple connection between atmospheric circulation and ice loss. Rather, results emphasize that atmosphere/sea ice connections are complex and varied. The failure of this study to identify common anomalies associated with RILEs and high loss years reflects the complexity of interactions between the ocean, atmosphere and sea ice. Overall, our results suggest that RILEs are not a suitable time unit for the study of atmospheric drivers of ice loss, and that no single atmospheric pattern is required for significant ice loss to occur.

Although significant, consistent atmospheric drivers could not be identified, a careful reading of the results suggests enhanced wind-driven flux through Fram Strait is the most likely atmospheric factor driving ice loss. This can manifest itself in a variety of SOM node and teleconnection anomalies, leading to weak quantitative

results in this analysis. Enhanced cross-Fram winds are a feature of the positive phases of the AO, NAO,and ARP, common features in simulated and observed winter results. In simulated summer results, the effect seems best explained in terms of the CAI. Feature count anomalies reflect across-Fram winds most prominently as an increase in lows over the Barents Sea, an anomaly common to winter results in simulations and observations, and in simulated summer results. In simulations, this is further enhanced by increases in winter highs over the Canadian Arctic Archipelago and in summer as increased Eurasian Lows and Beaufort Highs. Summer simulated results in particular suggest a connection between a dipole-like pattern, with lower pressure over the Barents Sea and Eurasia and higher pressure over Beaufort Sea and Canadian Arctic Archipelago. Observed winter patterns suggest a somewhat similar dipole, with a weaker Barents anomaly and shift from Canadian to Central Arctic highs. Although its' statistical significance is often relatively low, the Barents low anomaly emerges as the most consistent anomaly across seasons, models, and observations, suggesting it has a robust relationship to ice loss. It is also a common feature in nodes included in the SOM-based ARP, NAO, AO, and CAI definitions, and a strong contribution to the emergence of these teleconnections in the results.

The key findings of the analyses can be summarized as follows: i) RILEs are an unsuitable framework for the study atmospheric contributions to Arctic ice loss, ii) winds are the most consistent atmospheric feature associated with periods of ice loss, both in model simulations and observations, iii) these winds are connected to the positive phase of the AO, ARP and NAO in observations and model simulations in winter for years with large ice loss, as well as increased frequency of strong Barents Lows and Beaufort Highs. It is important to reiterate that the lack of significant anomalies in large ice loss years shows that neither anomalous feature counts nor strong teleconnection scores are necessary for instantaneous ice loss to occur, and other variables

may be more closely tied to large sea ice losses. Also, because RILEs were the initial motivation for the current study, and these events are largely found in NCAR CCSM3 model output, the analysis was focused primarily on this model. Consequently, they may not reflect ice loss in the full range of available GCMs. However, Fram winds (albeit in a variety of forms) remains the best available atmospheric driver of ice loss identified in the observations and other GCMs we examined.

Future work could examine RILEs found in additional years of observational data and additional model runs. However, current results show little agreement between RILEs and years of instantaneous ice loss, suggesting it is unlikely that additional analysis of further RILEs will give different results. Greater agreement in individual ice loss years suggests efforts are better spent focusing on shorter periods of loss; just as yearly analyses show greater agreement than multi-year (RILE) analyses, monthly analyses may show greater agreement than seasonal. However, it is not clear that SOM-based methods are appropriate for analyses over such short periods, and delayed response of ice extent to atmospheric forcing could complicate interpretation. The results further suggest that a smaller study domain is warranted. While the Pan-Arctic results did not identify strong common patterns, they did identify specific regions worth exploring; specifically the Barents Sea, Beaufort Sea, and Fram Strait. While the Beaufort and Fram regions have been identified as likely areas of concern by many prior studies, the Barents emphasis is somewhat more novel (although reminiscent of Skeie (2000) discussion of a 'Barents Oscillation' or Wang et al. (2009a) discussion of a dipole anomaly). A greater focus on these regions could better highlight any associations with ice loss while allowing a more detailed consideration of atmospheric anomalies, using SOMs trained with multiple variables (SLP, atmospheric heat flux, etc) or the analysis of node-averaged composites of additional variables. This would, for example, allow a comparison of the relative impacts of

cross-Fram winds to increased atmospheric heat transport from Barents Sea storms.

As a final note, it is worth highlighting the potential of the approach to quantifying the strength and phase of teleconnections used in this study. Although not the primary focus of the current research, it is believed to have the potential to better highlight regional impacts of large scale teleconnections, as well as variability in their structure and behaviour, and has potential value in other research. The SOM-based approach to quantifying the state of teleconnection indices is appropriate for indices exerting a strong influence on the geographical region. The approach is likely to identify periods when local conditions resemble one phase of a teleconnection even when regions outside the region of study do not. Assuming the local manifestation of a teleconnection is most important to local phenomena, the SOM-based index is likely preferable. The method also accommodates asymmetry between positive and negative phases and allows easy comparison between different climate models, where changes in location of teleconnection centers otherwise make inter-comparison difficult. We feel this method combines flexibility with specificity in a manner that makes it a potentially powerful way to reassess local-to-regional impacts of teleconnections.

Bibliography

Aagaard, K. and E. Carmack (1989). "The role of sea ice and other fresh water in the Arctic circulation". In: *Journal of Geophysical Research: Oceans* 94.C10, pp. 14485–14498.

Aagaard, K., L. Coachman, and E. Carmack (1981). "On the halocline of the Arctic Ocean". In: *Deep Sea Research Part A. Oceanographic Research Papers* 28.6, pp. 529–545.

Ambaum, M. H., B. J. Hoskins, and D. B. Stephenson (2001). "Arctic oscillation or North Atlantic oscillation?" In: *Journal of Climate* 14.16, pp. 3495–3507.

Arctic sea ice extent settles at record seasonal minimum (2016). National Snow and Ice Data Center. URL: `http://nsidc.org/arcticseaicenews/2012/09/arctic-sea-ice-extent-settles-at-record-seasonal-minimum/` (visited on 07/25/2016).

Armstrong, R. and M. Brodzik (1995). "An earth-gridded SSM/I data set for cryospheric studies and global change monitoring". In: *Advances in Space Research* 16.10, pp. 155–163.

Arzel, O., T. Fichefet, and H. Goosse (2006). "Sea ice evolution over the 20th and 21st centuries as simulated by current AOGCMs". In: *Ocean Modelling* 12.3, pp. 401–415.

Barnston, A. and R. Livezey (1987). "Classification, seasonality and persistence of low-frequency atmospheric circulation patterns". In: *Monthly weather review* 115.6, pp. 1083–1126.

Bitz, C., R. Moritz, and J. Yin (2002). "Understanding Controls On Mid-and High-latitude Atmospheric Circulation Using High-resolution Gcms". In: *EGS General Assembly Conference Abstracts*. Vol. 27, p. 5099.

Bromwich, D., R. Fogt, K. Hodges, and J. Walsh (2007). "A tropospheric assessment of the ERA-40, NCEP, and JRA-25 global reanalyses in the polar regions". In: *Journal of Geophysical Research: Atmospheres* 112.D10.

Budyko, M. (1962). "Polyarnye l'dy i klimat". In: *Izvestiya Akademii Nauk SSSR: Seriya Geograficheskaya* 6, pp. 3–10.

Cassano, J., P. Uotila, A. Lynch, and E. Cassano (2007). "Predicted changes in synoptic forcing of net precipitation in large Arctic river basins during the 21st century". In: *Journal of Geophysical Research: Biogeosciences* 112.G4.

Cassou, C., L. Terray, J. Hurrell, and C. Deser (2004). "North Atlantic winter climate regimes: Spatial asymmetry, stationarity with time, and oceanic forcing". In: *Journal of Climate* 17.5, pp. 1055–1068.

Coachman, L. and K. Aagaard (1974). *Physical oceanography of Arctic and Subarctic seas*. Springer.

Cressman, G. P. (1959). "An operational objective analysis system". In: *Mon. Wea. Rev* 87.10, pp. 367–374.

Croll, J. (1875). "Climate and time in their geological relations: a theory of secular changes of the Earth's climate, Edward Stanford". In: *London.–1875.–577 p.*

Deser, C. and H. Teng (2008). "Evolution of Arctic sea ice concentration trends and the role of atmospheric circulation forcing, 1979–2007". In: *Geophysical Research Letters* 35.2.

Deser, C., J. Walsh, and M. Timlin (2000). "Arctic sea ice variability in the context of recent atmospheric circulation trends". In: *Journal of Climate* 13.3, pp. 617–633.

Devasthale, A., J. Sedlar, T. Koenigk, and E. Fetzer (2013). "The thermodynamic state of the Arctic atmosphere observed by AIRS: comparisons during the record minimum sea ice extents of 2007 and 2012". In: *Atmospheric Chemistry and Physics* 13.15, pp. 7441–7450.

DeWeaver, E. and C. M. Bitz (2006). "Atmospheric Circulation and Its Effect on Arctic Sea Ice in CCSM3 Simulations at Medium and High Resolution*". In: *Journal of Climate* 19.11, pp. 2415–2436.

Dickson, R., T. Osborn, J. Hurrell, J. Meincke, J. Blindheim, B. Adlandsvik, T. Vinje, G. Alekseev, and W. Maslowski (2000). "The Arctic ocean response to the North Atlantic oscillation". In: *Journal of Climate* 13.15, pp. 2671–2696.

Doswell, C., R. Davies-Jones, and D. Keller (1990). "On summary measures of skill in rare event forecasting based on contingency tables". In: *Weather and Forecasting* 5.4, pp. 576–585.

Dunning, T. (1993). "Accurate methods for the statistics of surprise and coincidence". In: *Computational linguistics* 19.1, pp. 61–74.

Eisenman, I. and J. Wettlaufer (2009). "Nonlinear threshold behavior during the loss of Arctic sea ice". In: *Proceedings of the National Academy of Sciences* 106.1, pp. 28–32.

Finnis, J. (2008). "Perspectives on Arctic hydroclimatology from general circulation models". PhD thesis. UNIVERSITY OF COLORADO AT BOULDER.

Finnis, J., W. W. Hsieh, H. Lin, and W. J. Merryfield (2012). "Non-Linear Post-Processing of Numerical Seasonal Climate Forecasts". In: *Atmosphere-Ocean* 50.2, pp. 207–218.

Fletcher, J. O. (1965). "The heat budget of the Arctic Basin and its relation to climate". In: *Rand Corporation*.

Gildor, H. and E. Tziperman (2001). "A sea ice climate switch mechanism for the 100-kyr glacial cycles". In: *Journal of Geophysical Research: Oceans* 106.C5, pp. 9117–9133.

Gillett, N., H. Graf, and T. Osborn (2003). "Climate change and the North Atlantic oscillation". In: *The North Atlantic oscillation: climatic significance and environmental impact*, pp. 193–209.

Griggs, D. J. and M. Noguer (2002). "Climate change 2001: the scientific basis. Contribution of working group I to the third assessment report of the intergovernmental panel on climate change". In: *Weather* 57.8, pp. 267–269.

Hakkinen, S., A. Proshutinsky, and I. Ashik (2008). "Sea ice drift in the Arctic since the 1950s". In: *Geophysical Research Letters* 35.19.

Hilmer, M. and T. Jung (2000). "Evidence for a recent change in the link between the North Atlantic Oscillation and Arctic sea ice export". In: *Geophysical Research Letters* 27.7, pp. 989–992.

Holland, M. M. and C. M. Bitz (2003). "Polar amplification of climate change in coupled models". In: *Climate Dynamics* 21.3-4, pp. 221–232.

Holland, M., C. Bitz, and B. Tremblay (2006). "Future abrupt reductions in the summer Arctic sea ice". In: *Geophysical Research Letters* 33.23.

Holland, M., C. Bitz, L. Tremblay, D. Bailey, et al. (2008). "The role of natural versus forced change in future rapid summer Arctic ice loss". In: *Arctic sea ice decline: observations, projections, mechanisms, and implications*, pp. 133–150.

Hu, A., C. Rooth, R. Bleck, and C. Deser (2002). "NAO influence on sea ice extent in the Eurasian coastal region". In: *Geophysical Research Letters* 29.22.

Kalnay, E., M. Kanamitsu, R. Kistler, W. Collins, D. Deaven, L. Gandin, M. Iredell, S. Saha, G. White, J. Woollen, et al. (1996). "The NCEP/NCAR 40-year reanalysis project". In: *Bulletin of the American meteorological Society* 77.3, pp. 437–471.

Kay, J. E., T. L'Ecuyer, A. Gettelman, G. Stephens, and C. O'Dell (2008). "The contribution of cloud and radiation anomalies to the 2007 Arctic sea ice extent minimum". In: *Geophysical Research Letters* 35.8.

Keegan, T. J. (1958). "Arctic synoptic activity in winter". In: *Journal of Meteorology* 15.6, pp. 513–521.

Kohonen, T. (1990). "The self-organizing map". In: *Proceedings of the IEEE* 78.9, pp. 1464–1480.

Kohonen, T., J. Hynninen, J. Kangas, and J. Laaksonen (1996). "Som pak: The self-organizing map program package". In: *Report A31, Helsinki University of Technology, Laboratory of Computer and Information Science*.

Kwok, R., G. Cunningham, M. Wensnahan, I. Rigor, H. Zwally, and D. Yi (2009a). "Thinning and volume loss of the Arctic Ocean sea ice cover: 2003–2008". In: *Journal of Geophysical Research: Oceans* 114.C7.

Kwok, R. and D. Rothrock (1999). "Variability of Fram Strait ice flux and North Atlantic oscillation". In: *Journal of Geophysical Research: Oceans* 104.C3, pp. 5177–5189.

— (2009b). "Decline in Arctic sea ice thickness from submarine and ICESat records: 1958–2008". In: *Geophysical Research Letters* 36.15.

Lawrence, D. M., A. Slater, R. Tomas, M. Holland, and C. Deser (2008). "Accelerated Arctic land warming and permafrost degradation during rapid sea ice loss". In: *Geophysical Research Letters* 35.11.

L'Heureux, M. L., A. Kumar, G. D. Bell, M. S. Halpert, and R. W. Higgins (2008). "Role of the Pacific-North American (PNA) pattern in the 2007 Arctic sea ice decline". In: *Geophysical Research Letters* 35.20.

Lindsay, R. and J. Zhang (2005). "The thinning of Arctic sea ice, 1988-2003: Have we passed a tipping point?" In: *Journal of Climate* 18.22, pp. 4879–4894.

Lindsay, R., J. Zhang, A. Schweiger, M. Steele, and H. Stern (2009). "Arctic sea ice retreat in 2007 follows thinning trend". In: *Journal of Climate* 22.1, pp. 165–176.

Livina, V. N. and T. M. Lenton (2012). "A recent tipping point in the Arctic sea-ice cover: abrupt and persistent increase in the seasonal cycle since 2007". In: *arXiv preprint arXiv:1204.5445*.

Maslanik, J., S. Drobot, C. Fowler, W. Emery, and R. Barry (2007). "On the Arctic climate paradox and the continuing role of atmospheric circulation in affecting sea ice conditions". In: *Geophysical Research Letters* 34.3.

Maykut, G. A. and N. Untersteiner (1971). "Some results from a time-dependent thermodynamic model of sea ice". In: *Journal of Geophysical Research* 76.6, pp. 1550–1575.

Meehl, G., C. Covey, K. Taylor, T. Delworth, R. Stouffer, M. Latif, B. McAvaney, and J. Mitchell (2007). "The WCRP CMIP3 multimodel dataset: A new era in climate change research". In: *Bulletin of the American Meteorological Society* 88.9, pp. 1383–1394.

Morison, J., M. Steele, and R. Andersen (1998). "Hydrography of the upper Arctic Ocean measured from the nuclear submarine USS Pargo". In: *Deep Sea Research Part I: Oceanographic Research Papers* 45.1, pp. 15–38.

Nakicenovic, N. and R. Swart (2000). "Special report on emissions scenarios". In: *Special Report on Emissions Scenarios, Edited by Nebojsa Nakicenovic and Robert*

Swart, pp. 612. ISBN 0521804930. Cambridge, UK: Cambridge University Press, July 2000. 1.

North, G. (1984). "The small ice cap instability in diffusive climate models". In: *Journal of the atmospheric sciences* 41.23, pp. 3390–3395.

Ogi, M. and J. Wallace (2007). "Summer minimum Arctic sea ice extent and the associated summer atmospheric circulation". In: *Geophysical Research Letters* 34.12.

Omstedt, A. and D. Chen (2001). "Influence of atmospheric circulation on the maximum ice extent in the Baltic Sea". In: *Journal of Geophysical Research: Oceans* 106.C3, pp. 4493–4500.

Overland, J. and M. Wang (2005). "The Arctic climate paradox: The recent decrease of the Arctic Oscillation". In: *Geophysical Research Letters* 32.6.

Overland, J. E. and P. S. Guest (1991). "The Arctic snow and air temperature budget over sea ice during winter". In: *Journal of Geophysical Research: Oceans* 96.C3, pp. 4651–4662.

Perovich, D. K., T. C. Grenfell, J. A. Richter-Menge, B. Light, W. B. Tucker, and H. Eicken (2003). "Thin and thinner: Sea ice mass balance measurements during SHEBA". In: *Journal of Geophysical Research: Oceans* 108.C3.

Perovich, D. K., J. A. Richter-Menge, K. F. Jones, and B. Light (2008). "Sunlight, water, and ice: Extreme Arctic sea ice melt during the summer of 2007". In: *Geophysical Research Letters* 35.11.

Putnins, P. (1970). "The climate of Greenland". In: *Climates of the Polar Regions. World Survey of Climatology* 14, pp. 3–128.

Rampal, P., J. Weiss, and D. Marsan (2009). "Positive trend in the mean speed and deformation rate of Arctic sea ice, 1979–2007". In: *Journal of Geophysical Research: Oceans* 114.C5.

Reusch, D., R. Alley, and B. Hewitson (2007). "North Atlantic climate variability from a self-organizing map perspective". In: *Journal of Geophysical Research* 112.D02104, pp. 1–20.

Rigor, I., J. Wallace, and R. Colony (2002). "Response of sea ice to the Arctic oscillation". In: *Journal of Climate* 15.18, pp. 2648–2663.

Rigor, I. G. and J. M. Wallace (2004). "Variations in the age of Arctic sea-ice and summer sea-ice extent". In: *Geophysical Research Letters* 31.9.

Rudels, B., N. Kuzmina, U. Schauer, T. Stipa, and V. Zhurbas (2009). "Double-diffusive convection and interleaving in the Arctic Ocean—Distribution and importance". In: *Geophysica* 45.1-2, pp. 199–213.

Sammon, J. W. (1969). "A nonlinear mapping for data structure analysis". In: *IEEE Transactions on computers* 18.5, pp. 401–409.

Schoof, J. T. and S. Pryor (2006). "An evaluation of two GCMs: Simulation of North American teleconnection indices and synoptic phenomena". In: *International Journal of Climatology* 26.2, pp. 267–282.

Schulzweida, U., L. Kornblueh, and R. Quast (2004). "Climate data operators". In: *Max-Planck-Institute for Meteorology, Hamburg and http://www. mpimet. mpg. de/˜ cdo*.

Schweiger, A., R. Lindsay, S. Vavrus, and J. Francis (2008a). "Relationships between Arctic Sea Ice and Clouds during Autumn". In: *Journal of Climate* 21.18, p. 4799.

Schweiger, A., J. Zhang, R. Lindsay, and M. Steele (2008b). "Did unusually sunny skies help drive the record sea ice minimum of 2007?" In: *Geophysical Research Letters* 35.L10503, p. 1.

Serreze, M. C. and A. P. Barrett (2008). "The summer cyclone maximum over the central Arctic Ocean". In: *Journal of Climate* 21.5, pp. 1048–1065.

Serreze, M. C., A. P. Barrett, A. G. Slater, R. A. Woodgate, K. Aagaard, R. B. Lammers, M. Steele, R. Moritz, M. Meredith, and C. M. Lee (2006). "The large-scale freshwater cycle of the Arctic". In: *Journal of geophysical research.JGR.Atmospheres* 111.10.1029.

Serreze, M. C. and R. G. Barry (1988). "Synoptic activity in the Arctic Basin, 1979-85". In: *Journal of Climate* 1.12, pp. 1276–1295.

— (2011a). "Processes and impacts of Arctic amplification: A research synthesis". In: *Global and Planetary Change* 77.1, pp. 85–96.

Serreze, M. C., R. G. Barry, and A. S. McLaren (1989). "Seasonal variations in sea ice motion and effects on sea ice concentration in the Canada Basin". In: *Journal of Geophysical Research: Oceans* 94.C8, pp. 10955–10970.

Serreze, M. and A. Barrett (2011b). "Characteristics of the Beaufort Sea High". In: *Journal of Climate* 24.1, pp. 159–182.

Serreze, M. and R. Barry (2005). *The Arctic Climate System*. 1st ed. Cambridge, England: Cambridge University Press.

Serreze, M., J. Box, R. Barry, and J. Walsh (1993). "Characteristics of Arctic synoptic activity, 1952-1989". In: *Meteorology and atmospheric physics* 51.3-4, pp. 147–164.

Skeie, P. (2000). "Meridional flow variability over the Nordic seas in the Arctic Oscillation framework". In: *Geophysical Research Letters* 27.16, pp. 2569–2572.

Spreen, G., R. Kwork, and D. Menemenlis (2011). "Trends in Arctic sea ice drift and role of wind forcing: 1992-2009". In: *Geophysical Research Letters* 38.19.

Steele, M. and T. Boyd (1998). "Retreat of the cold halocline layer in the Arctic Ocean". In: *Journal of Geophysical Research: Oceans* 103.C5, pp. 10419–10435.

Stoner, A., K. Hayhoe, and D. Wuebbles (2009). "Assessing general circulation model simulations of atmospheric teleconnection patterns". In: *Journal of Climate* 22.16, pp. 4348–4372.

Stroeve, J. and W. Meier (1999 updated 2012). *Ice Trends and Climatologies from SMMR and SSM/I-SSMIS, 1978-2010*.

Stroeve, J. C., V. Kattsov, A. Barrett, M. Serreze, T. Pavlova, M. Holland, and W. N. Meier (2012a). "Trends in Arctic sea ice extent from CMIP5, CMIP3 and observations". In: *Geophysical Research Letters* 39.16.

Stroeve, J. C., M. C. Serreze, M. M. Holland, J. E. Kay, J. Malanik, and A. P. Barrett (2012b). "The Arctic's rapidly shrinking sea ice cover: a research synthesis". In: *Climatic Change* 110.3-4, pp. 1005–1027.

Stroeve, J., M. M. Holland, W. Meier, T. Scambos, and M. Serreze (2007). "Arctic sea ice decline: Faster than forecast". In: *Geophysical research letters* 34.9.

Stroeve, J., M. Serreze, S. Drobot, S. Gearheard, M. Holland, J. Maslanik, W. Meier, and T. Scambos (2008). "Arctic sea ice extent plummets in 2007". In: *Eos* 89.2, p. 13.

Thompson, D. W., J. M. Wallace, and G. C. Hegerl (2000). "Annular modes in the extratropical circulation. Part II: Trends". In: *Journal of Climate* 13.5, pp. 1018–1036.

Thompson, D. and J. Wallace (1998). "The Arctic Oscillation signature in the wintertime geopotential height and temperature fields". In: *Geophysical Research Letters* 25.9, p. 1297.

Tietsche, S., D. Notz, J. Jungclaus, and J. Marotzke (2011). "Recovery mechanisms of Arctic summer sea ice". In: *Geophysical Research Letters* 38.2.

Tremblay, L. (2001). "Can we consider the Arctic Oscillation independently from the Barents Oscillation?" In: *Geophysical Research Letters* 28.22, pp. 4227–4230.

Trenberth, K. and J. Caron (2001). "Estimates of Meridional Atmosphere and Ocean Heat Transports". In: *Journal of Climate* 14.16, pp. 3433–3443.

Treshnikov, A. F. and G. I. Baranov (1972). "Circulation Structure of the Arctic Basin Waters (in Russian)". In: *Hydrometeoizdat, Leningrad*, p. 158.

Treshnikov, A. et al. (1985). "Arctic atlas". In: *Arkt Antarkt, Moscow: Nauchno Issled, Inst*, pp. 1–204.

Treshnikov, A. and R. Colony (1982). "Sea ice motion in response to geostrophic winds". In: *Journal of Geophysical Research: Oceans* 87.C8, pp. 5845–5852.

vanLoon, H. and J. C. Rogers (1978). "The seesaw in winter temperatures between Greenland and northern Europe. Part I: General description". In: *Monthly Weather Review* 106.3, pp. 296–310.

Vavrus, S., M. Holland, and D. Bailey (2011). "Changes in Arctic clouds during intervals of rapid sea ice loss". In: *Climate Dynamics* 36.7-8, pp. 1475–1489.

Vihma, T., P. Tisler, and P. Uotila (2012). "Atmospheric forcing on the drift of Arctic sea ice in 1989–2009". In: *Geophysical Research Letters* 39.2, p. L02501.

Vinje, T., N. Nordlund, and A. Kvambekk (1998). "Monitoring ice thickness in Fram Strait". In: *Journal of geophysical research* 103.c5, pp. 10437–10449.

Walker, G. and E. Bliss (1932). "World Weather V". In: *Mem. Roy. Meteor. Soc.* 4.36, pp. 53–84.

Wallace, J. M. and D. S. Gutzler (1981). "Teleconnections in the geopotential height field during the Northern Hemisphere winter". In: *Monthly Weather Review* 109.4, pp. 784–812.

Wang, J., J. Zhang, E. Watanabe, M. Ikeda, K. Mizobata, J. Walsh, X. Bai, and B. Wu (2009a). "Is the Dipole Anomaly a major driver to record lows in Arctic summer sea ice extent?" In: *Geophysical Research Letters* 36.5.

Wang, M. and J. Overland (2009b). "A sea ice free summer Arctic within 30 years?" In: *Geophysical Research Letters* 36.

Warshaw, M. and R. Rapp (1973). "An Experiment on the Sensitivity of a Global Circulation Model". In: *Journal of applied meteorology (1962)* 12.1, pp. 43–49.

Winton, M. (2006). "Does the Arctic sea ice have a tipping point". In: *Geophysical Research Letters* 33, p. L23504.

Wu, B., J. Wang, and J. Walsh (2006). "Dipole Anomaly in the Winter Arctic Atmosphere and Its Association with Sea Ice Motion". In: *Journal of Climate* 19.2, pp. 210–225.

Zhang, J., M. Steele, D. Rothrock, and R. Lindsay (2004). "Increasing exchanges at Greenland[U+2010]Scotland Ridge and their links with the North Atlantic Oscillation and Arctic sea ice". In: *Geophysical Research Letters* 31.9.

Zhang, X., A. Sorteberg, J. Zhang, R. Gerdes, and J. Comiso (2008). "Recent radical shifts of atmospheric circulations and rapid changes in Arctic climate system". In: *Geophysical Research Letters* 35.22, p. L22701.

Zhang, X. and J. Walsh (2005). "Towards a Seasonally Ice-Covered Arctic Ocean: Scenarios from the IPCC AR4 Model Simulations". In: *Journal of Climate* 19.9, p. 1730.

Appendices

Appendix A

First appendix

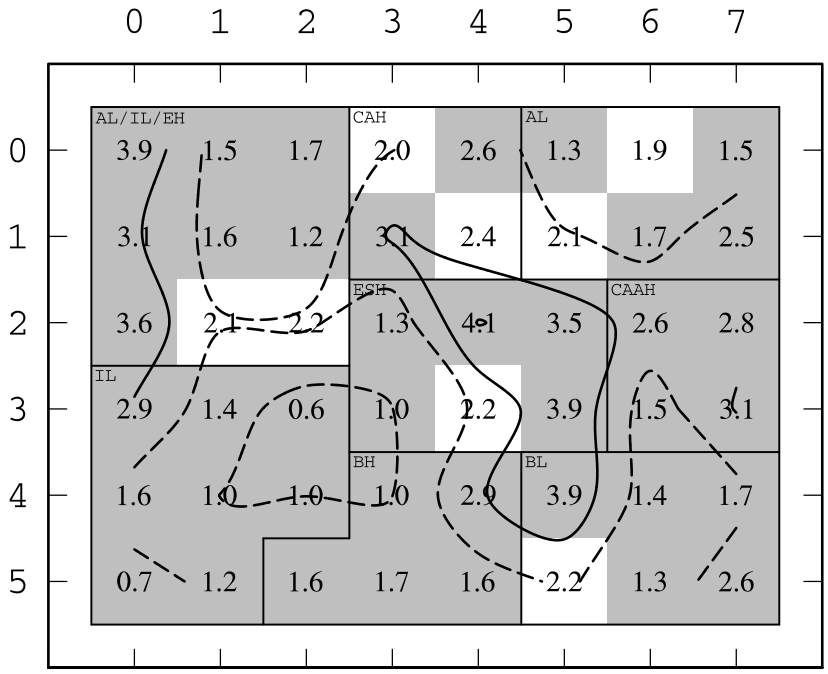

Figure A.1: Winter Frequency distribution of SOM nodes for CCCMA CGCM3.1 T63. Dashed contours are below the expected value of 2.08% and solid contours are above the expected value. Grey shaded nodes indicate that the frequency of occurence is significantly different from the expectant value (2.08%) at the 95% CI.

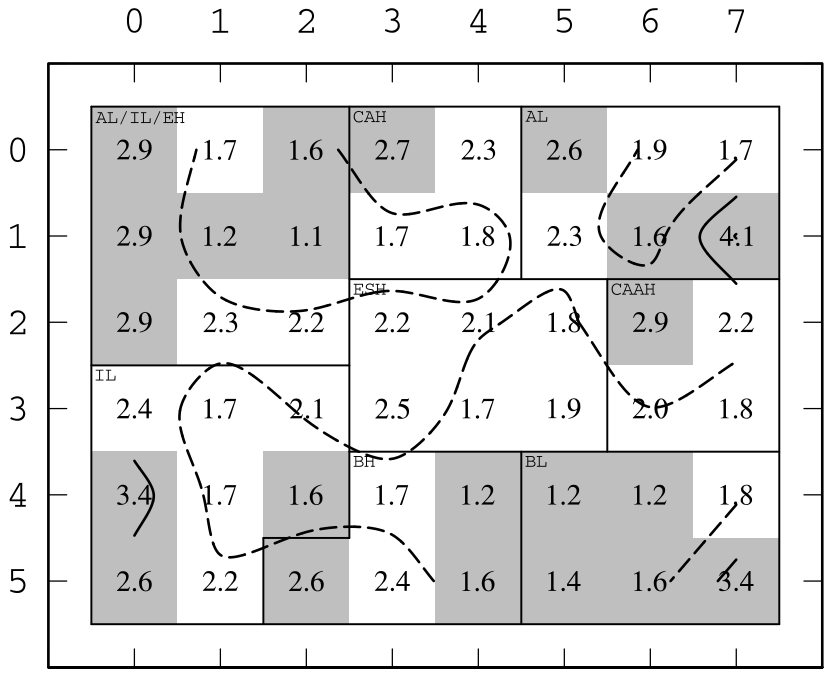

Figure A.2: Winter Frequency distribution of SOM nodes for ECHAM5/MPI-OM. Dashed contours are below the expected value of 2.08% and solid contours are above the expected value. Grey shaded nodes indicate that the frequency of occurence is significantly different from the expectant value (2.08%) at the 95% CI.

Table A.1: Winter (DJF) average seasonal teleconnection index calculated by averaging the monthly teleconnection scores for the season. Dot product scores of season's projection onto significant node shifts from climatology of the frequency distribution of winter negative and positive composite months.

	AO			ARP			NAO			PNA		
YYYY	Index	Projection		Index	Projection		Index	Projection		Index	Projection	
		Neg.	Pos.		Neg.	Pos.		Neg.	Pos.		Neg.	Pos.
1962	-0.13	-0.54	**0.66**		-0.77	**0.53**	-0.36	0.05	-0.10	-0.51	-0.33	-0.21
1963	**-1.91**	-0.38	-0.05		-0.29	-0.26	**-1.94**	**0.44**	-0.49	0.27	-0.96	-0.07
1964	-0.46	-0.11	-0.15		0.19	-0.26	**-1.85**	**0.44**	-0.52	0.37	-0.90	0.03
1965	-1.13	0.06	0.09		-0.18	0.10	-1.03	-0.12	0.34	-0.74	0.56	-0.42
1966	**-1.50**	**0.55**	-0.37		-0.10	-0.75	**-1.13**	**0.53**	-0.34	**-1.11**	0.54	**0.52**
1967	-0.27	0.36	-0.52		**0.52**	-0.74	-0.40	0.01	-0.28	-0.66	-0.82	-0.12
1968	-0.97	-0.13	0.02		0.05	0.18	-0.93	0.00	-0.01	-0.09	-0.58	-0.20
1969	**-2.29**	**0.61**	-0.68		**0.60**	-0.76	**-1.69**	**0.39**	-0.29	**-1.84**	**0.88**	**0.61**
1970	**-1.86**	**0.49**	-0.38		0.32	-0.46	-0.78	0.16	-0.07	0.06	0.35	-0.05
1971	-0.49	-0.38	**0.48**		-0.19	**0.67**	-1.06	-0.42	**0.63**	-0.59	-0.58	-0.25
1972	0.26	-0.41	0.42		-0.42	0.39	0.07	-0.56	0.27	**-1.03**	0.26	-0.57
1973	**1.09**	-0.29	0.42		-0.44	**0.52**	0.05	-0.21	0.22	-0.41	-0.04	-0.58
1974	-0.15	0.29	-0.06		0.15	-0.29	0.22	-0.23	-0.03	**-1.13**	-0.99	0.09
1975	0.78	-0.59	**0.51**		-0.04	**0.53**	0.11	-0.47	**0.63**	-0.41	-0.24	-0.39
1976	**0.99**	-0.52	**0.79**		-0.44	**0.68**	-0.09	-0.40	0.41	-0.57	-0.90	-0.36
1977	**-2.62**	**0.65**	-0.56		**0.65**	-0.46	**-1.43**	**0.31**	0.31	**0.75**	0.29	**0.60**
1978	-1.20	-0.36	**0.50**		-0.68	0.33	**-1.23**	**0.32**	-0.43	**0.62**	-0.26	0.14
1979	-1.30	**0.49**	-0.51		0.20	-0.30	**-1.62**	**0.38**	-0.17	**-1.33**	0.44	0.15
1980	-0.57	0.45	-0.28		-0.43	-0.41	-0.31	0.27	-0.28	0.40	0.46	**0.36**
1981	-0.17	-0.52	**0.55**		-0.44	**0.53**	0.38	-0.43	**0.53**	0.50	-0.78	-0.73
1982	-0.38	-0.08	-0.33		0.15	-0.33	-0.27	-0.26	-0.18	**-1.52**	**0.80**	-0.34
1983	0.17	-0.49	**0.77**		-0.56	**0.69**	**0.62**	-0.17	0.41	**0.78**	-0.01	-0.50
1984	0.26	-0.45	0.14		-0.01	**0.56**	**0.66**	-0.67	**0.54**	0.12	0.41	-0.63
1985	-1.27	**0.74**	-0.64	**-1.48**	**0.60**	-0.74	**-1.16**	**0.32**	-0.13	0.17	0.44	-0.37
1986	**-1.81**	**0.74**	-0.70	**-0.95**	**0.49**	-0.70	-0.23	**0.45**	-0.38	0.32	0.09	**0.46**
1987	-0.85	**0.73**	-0.70	-0.56	**0.59**	-0.89	-0.76	**0.49**	-0.57	**0.87**	-0.09	**0.68**
1988	-0.45	0.29	-0.49	-0.06	**0.75**	-0.40	0.44	0.13	0.08	**0.87**	**0.79**	**0.46**
1989	**2.69**	-0.80	**0.82**	**1.97**	-0.72	**0.85**	**1.05**	-0.45	**0.51**	-0.84	-0.60	-0.53
1990	**1.25**	-0.21	0.39	0.51	0.10	**0.52**	0.24	-0.81	**0.80**	**-1.27**	0.03	-0.25
1991	0.37	-0.01	-0.72	-0.09	-0.07	-0.16	0.45	-0.38	0.13	0.23	**0.80**	-0.52
1992	**1.09**	-0.53	**0.50**	0.75	-0.52	**0.71**	0.15	-0.35	**0.66**	**1.02**	-0.09	0.04
1993	**1.77**	-0.72	**0.92**	**1.53**	-0.58	**0.89**	**0.61**	-0.50	**0.56**	-0.23	-0.01	-0.22
1994	-0.42	0.19	-0.29	-0.03	-0.03	-0.24	**0.71**	-0.19	0.21	**-1.01**	**0.60**	-0.37
1995	0.72	-0.42	**0.48**	0.59	0.13	**0.62**	**1.07**	-0.56	**0.68**	**0.74**	-0.42	-0.17
1996	-1.05	0.32	-0.64	-0.49	-0.04	-0.88	-0.94	**0.37**	-0.56	-0.23	-0.73	-0.22
1997	-0.10	-0.37	0.05	0.48	-0.45	0.27	-0.33	-0.30	0.21	-0.07	-0.23	-0.32
1998	-0.78	0.33	-0.67	-0.21	0.24	-0.73	-0.53	-0.04	-0.34	0.48	-0.04	0.26
1999	0.65	0.17	-0.17	0.19	0.03	0.14	0.33	-0.15	0.47	-0.52	**0.70**	-0.40
2000	**1.13**	0.12	0.09	0.33	-0.15	0.15	**1.02**	-0.46	**0.52**	-0.48	-0.82	**0.50**
2001	-1.31	**0.74**	-0.54	-0.74	**0.80**	-0.67	-0.26	-0.12	0.06	0.00	-0.03	**0.74**
2002	0.45	0.21	-0.29	0.51	**0.67**	-0.27	-0.02	-0.19	0.29	-0.12	0.33	-0.53
2003	-0.65	-0.35	0.12	-0.39	0.28	0.01	-0.34	-0.02	-0.17	**1.10**	0.55	0.23
2004	-0.98	0.20	-0.29	0.31	-0.33	0.01	-0.32	0.22	-0.08	0.44	**0.72**	0.07
2005	0.11	-0.16	-0.01	-0.61	0.39	0.22	**0.59**	-0.65	**0.66**	-0.16	0.09	-0.43
2006	-0.81	**0.61**	-0.54	**-1.62**	**0.72**	-0.83	-0.18	-0.03	-0.07	-0.42	**0.71**	0.24
2007	**1.00**	0.02	0.09	**0.93**	0.12	0.23	-0.03	0.05	0.37	0.39	0.57	0.03
2008	0.86	-0.30	0.09	0.33	-0.05	0.20	0.38	-0.30	0.36	-0.14	-0.50	-0.52
2009	0.26	-0.34	0.01	-0.09	-0.39	0.25	-0.42	-0.36	0.05	**-0.97**	0.46	-0.35
2010	**-3.42**	**0.74**	-0.53		0.24	-0.68	**-2.12**	**0.63**	-0.28	0.21	0.09	**0.39**

Table A.2: Winter (DJF) average seasonal teleconnection index calculated by averaging the monthly teleconnection scores for the season. Dot product scores of season's projection onto significant node shifts from climatology of the frequency distribution of winter negative and positive composite months.

	CAI-80			CAI-82			CAI-84		
YYYY	Index	Projection		Index	Projection		Index	Projection	
		Neg.	Pos.		Neg.	Pos.		Neg.	Pos.
1962	**6.66**	-0.60	**0.30**	**6.40**	-0.58	**0.35**	**4.98**	-0.60	0.21
1963	**6.87**	-0.50	**0.50**	5.74	-0.45	**0.39**	3.62	-0.39	**0.39**
1964	5.70	0.21	0.04	**6.43**	0.20	0.07	**5.34**	0.16	0.11
1965	**-3.84**	0.21	-0.44	**-3.03**	0.26	-0.47	**-2.89**	0.23	-0.44
1966	0.51	-0.09	0.21	0.21	-0.04	0.23	-0.38	0.04	0.15
1967	4.02	0.41	-0.12	4.58	0.35	-0.12	3.72	0.27	-0.10
1968	**7.56**	0.00	**0.23**	**7.54**	-0.16	0.14	**6.20**	-0.31	**0.37**
1969	1.42	0.35	-0.09	2.48	0.34	-0.15	2.54	0.25	-0.14
1970	-0.08	0.27	-0.68	0.65	0.28	-0.75	0.46	0.40	-0.76
1971	2.96	-0.02	0.08	3.11	-0.06	0.20	2.23	-0.07	0.20
1972	0.14	0.14	-0.21	-0.17	0.11	-0.15	-0.81	0.13	-0.25
1973	5.48	-0.33	0.15	4.46	-0.36	**0.29**	2.73	-0.28	0.02
1974	**-3.42**	**0.47**	-0.51	**-2.87**	**0.51**	-0.51	**-2.85**	**0.60**	-0.52
1975	3.53	0.04	-0.13	4.67	-0.08	-0.05	4.41	-0.34	0.12
1976	4.32	-0.15	0.05	4.10	-0.23	0.10	2.63	-0.21	0.09
1977	**-7.94**	**0.58**	-0.66	**-6.49**	**0.58**	-0.60	**-5.22**	**0.63**	-0.61
1978	**9.25**	-0.63	**0.61**	**8.52**	-0.59	**0.70**	**6.42**	-0.55	**0.58**
1979	1.92	0.00	-0.05	1.53	-0.04	-0.15	0.66	0.01	-0.11
1980	1.84	-0.07	-0.21	3.00	-0.04	-0.13	2.70	0.11	-0.24
1981	**6.10**	-0.10	-0.02	**6.20**	-0.17	0.10	**4.83**	-0.31	0.01
1982	**10.25**	-0.36	**0.44**	**10.37**	-0.41	**0.41**	**8.57**	-0.36	**0.39**
1983	2.31	-0.39	-0.23	2.15	-0.41	-0.24	1.23	-0.33	-0.31
1984	4.24	0.24	-0.22	4.56	0.18	-0.29	3.59	0.19	-0.33
1985	**-3.42**	**0.73**	-0.64	**-2.57**	**0.68**	-0.61	**-2.03**	**0.79**	-0.63
1986	-1.26	0.32	-0.44	-1.34	0.39	-0.50	**-1.88**	**0.57**	-0.49
1987	**-3.37**	**0.44**	-0.31	**-3.60**	**0.50**	-0.36	**-3.80**	**0.60**	-0.39
1988	3.14	0.20	-0.19	3.11	0.21	-0.28	2.28	0.19	-0.26
1989	**11.55**	-0.61	**0.70**	**10.59**	-0.67	**0.78**	**8.13**	-0.68	**0.75**
1990	**-5.98**	0.39	-0.52	**-4.95**	0.28	-0.48	**-4.24**	0.39	-0.50
1991	**-3.27**	0.32	-0.35	**-1.85**	0.34	-0.32	-1.19	**0.50**	-0.34
1992	2.76	-0.23	-0.03	3.32	-0.24	0.07	2.86	-0.19	0.03
1993	**7.05**	-0.63	**0.54**	**6.09**	-0.68	**0.60**	4.42	-0.68	**0.50**
1994	-0.06	0.06	-0.34	0.68	0.00	-0.37	0.53	0.07	-0.43
1995	4.47	-0.21	-0.04	4.05	-0.43	-0.10	2.73	-0.54	-0.02
1996	4.75	-0.12	**0.35**	3.86	-0.13	**0.46**	2.34	-0.05	0.20
1997	0.79	-0.30	-0.11	0.76	-0.43	-0.02	0.23	-0.37	-0.03
1998	3.19	0.11	-0.17	3.28	0.20	-0.19	2.30	0.41	-0.27
1999	0.30	**0.47**	-0.57	1.01	**0.48**	-0.56	0.84	**0.53**	-0.54
2000	-2.16	0.27	-0.53	-1.02	0.38	-0.54	-0.71	0.42	-0.49
2001	**-3.48**	**0.60**	-0.66	**-2.05**	**0.61**	-0.71	-1.50	**0.68**	-0.66
2002	2.22	0.30	-0.15	3.46	0.24	-0.14	3.53	0.34	-0.19
2003	2.23	-0.26	0.11	2.52	-0.22	0.17	1.51	-0.13	0.07
2004	2.77	-0.18	0.05	2.15	-0.15	0.10	1.24	-0.10	0.11
2005	-1.42	**0.51**	-0.44	0.35	**0.49**	-0.46	0.64	0.44	-0.50
2006	**-3.92**	**0.72**	-0.38	**-1.93**	**0.70**	-0.36	-1.14	**0.63**	-0.34
2007	1.28	-0.10	-0.30	1.98	-0.08	-0.39	1.83	-0.03	-0.27
2008	3.60	0.02	-0.32	4.07	-0.06	-0.25	3.29	-0.04	-0.31
2009	1.24	-0.08	0.15	1.26	-0.11	0.24	0.58	-0.03	0.20
2010	**-2.99**	**0.48**	-0.46	**-2.54**	**0.49**	-0.44	**-2.73**	**0.56**	-0.38

Table A.3: Summer (JJA) average seasonal teleconnection index calculated by averaging the monthly teleconnection scores for the season. Dot product scores of season's projection onto significant node shifts from climatology of the frequency distribution of winter negative and positive composite months.

	AO			ARP			NAO			PNA		
YYYY	Index	Projection		Index	Projection		Index	Projection		Index	Projection	
		Neg.	Pos.		Neg.	Pos.		Neg.	Pos.		Neg.	Pos.
1961	0.25	**0.52**	-0.47		-0.40	0.21	0.61	0.11	-0.23	**0.60**	-0.50	**0.44**
1962	-0.16	**0.38**	-0.15		-0.65	0.25	**-0.64**	0.30	-0.71	-0.25	0.23	-0.41
1963	**-0.50**	**0.62**	-0.58		-0.27	-0.21	**-0.61**	**0.53**	-0.47	-0.54	-0.15	-0.14
1964	-0.11	0.02	0.19		-0.71	-0.64	0.38	-0.01	0.37	0.43	0.27	**0.43**
1965	-0.24	**0.48**	-0.44		-0.94	-0.10	0.47	0.24	-0.57	0.32	-0.72	**0.54**
1966	-0.18	0.36	-0.25		-0.67	0.30	-0.22	**0.47**	0.09	0.06	-0.64	-0.18
1967	0.20	-0.58	0.10		**0.84**	-0.27	**1.30**	-0.35	**0.66**	-0.64	**0.61**	-0.14
1968	-0.36	0.20	-0.21		-0.30	**0.58**	-0.37	0.11	-0.37	0.39	-0.23	-0.20
1969	-0.24	0.29	-0.45		0.13	-0.61	-0.18	0.19	-0.10	**0.64**	0.01	-0.20
1970	0.25	-0.46	**0.49**		0.08	-0.07	0.67	-0.35	0.28	0.12	**0.49**	-0.51
1971	-0.14	0.12	-0.07		-0.15	0.15	0.29	0.06	0.13	-0.68	-0.46	**0.75**
1972	-0.23	-0.15	0.06		0.08	0.30	**0.99**	-0.30	0.16	-0.44	0.15	-0.75
1973	**0.37**	-0.33	0.34		**0.52**	**0.45**	0.37	-0.31	-0.42	-0.07	**0.58**	-0.26
1974	-0.06	0.10	-0.33		0.27	0.12	-0.50	0.20	-0.26	-0.18	-0.42	-0.10
1975	0.05	-0.12	0.30		0.07	-0.21	0.19	-0.20	0.37	**-0.98**	**0.72**	-0.36
1976	0.19	-0.41	**0.44**		-0.55	-0.35	**1.05**	-0.36	**0.46**	-0.69	-0.15	0.11
1977	**-0.71**	**0.45**	-0.42		-0.78	0.09	-0.39	**0.40**	-0.51	**0.58**	-0.76	0.22
1978	-0.11	0.24	-0.31		0.32	-0.46	0.43	-0.09	0.04	**-1.11**	-0.10	-0.56
1979	0.10	0.17	-0.55		0.07	-0.55	**1.30**	0.03	-0.18	-0.15	-0.34	0.22
1980	-0.03	-0.15	0.30		**0.56**	**0.43**	**-1.16**	0.10	-0.22	**-1.22**	0.26	-0.04
1981	-0.04	0.03	-0.38		**0.78**	-0.17	0.10	0.05	-0.14	**-0.89**	-0.05	0.21
1982	-0.27	-0.26	**0.36**		-0.26	0.05	0.02	-0.43	0.21	**0.99**	-0.27	-0.13
1983	**0.51**	-0.61	**0.37**		0.04	-0.08	**1.49**	-0.49	**0.54**	**1.14**	0.04	-0.20
1984	0.16	-0.20	-0.08		**0.69**	-0.55	0.40	-0.42	**0.55**	**-1.37**	-0.58	-0.43
1985	-0.25	0.22	-0.37	-0.23	0.17	0.21	0.00	-0.09	0.15	0.19	-0.67	0.26
1986	-0.10	-0.25	0.05	-0.36	**0.67**	-0.40	0.05	0.03	0.16	-0.48	**0.56**	-0.33
1987	**-0.67**	**0.39**	-0.16	-0.32	-0.54	0.04	**-0.72**	0.31	0.00	0.29	-0.72	0.25
1988	0.06	-0.03	-0.44	-0.25	**0.46**	-0.10	0.27	-0.10	-0.27	**0.76**	-0.02	-0.22
1989	**0.59**	-0.70	**0.92**	-0.06	-0.68	0.11	0.31	-0.53	0.39	-0.47	**0.61**	-0.33
1990	-0.06	-0.20	-0.09	-0.33	**0.47**	-0.24	0.66	-0.20	**0.43**	0.04	0.03	-0.31
1991	0.16	-0.44	**0.67**	-0.20	-0.16	-0.44	0.16	-0.45	**0.78**	-0.31	**0.74**	-0.86
1992	0.14	-0.44	**0.58**	-0.10	-0.29	-0.37	0.56	-0.37	0.38	0.46	0.33	0.31
1993	**-0.47**	0.30	-0.18	**-0.47**	**0.59**	-0.16	**-1.13**	**0.51**	-0.39	0.07	0.07	0.05
1994	**0.93**	-0.61	**0.74**	**0.17**	-0.51	0.19	**1.18**	-0.55	**0.72**	**-0.93**	**0.77**	-0.46
1995	0.07	-0.15	0.01	**0.11**	-0.63	**0.86**	0.34	-0.25	0.10	-0.06	-0.62	0.35
1996	**0.45**	-0.52	**0.52**	-0.37	**0.62**	-0.04	**0.92**	-0.52	0.15	-0.64	**0.69**	-0.10
1997	-0.37	0.11	0.01	-0.28	-0.81	-0.47	0.05	0.29	0.25	-0.23	-0.22	**0.52**
1998	-0.09	0.26	0.02	-0.35	0.16	-0.30	**-1.01**	0.23	-0.35	0.39	0.11	-0.84
1999	0.01	0.05	0.11	-0.01	-0.75	-0.28	0.32	-0.26	0.35	0.49	-0.67	**0.65**
2000	0.03	0.17	-0.08	-0.08	-0.32	0.13	-0.41	**0.38**	0.22	**-1.42**	**0.52**	-0.50
2001	0.16	-0.01	0.15	-0.06	-0.58	0.29	-0.11	-0.11	-0.12	-0.46	-0.36	-0.51
2002	0.22	0.18	-0.09	-0.19	**0.62**	0.28	0.57	0.19	-0.55	0.36	0.13	-0.60
2003	-0.10	-0.18	-0.07	**-0.45**	**0.73**	**0.38**	0.06	0.04	-0.49	-0.04	0.28	0.28
2004	**-0.39**	-0.14	-0.48	**-0.39**	0.39	**0.36**	-0.06	-0.13	-0.21	0.30	-0.75	**0.78**
2005	-0.13	0.03	-0.20	-0.06	-0.50	-0.46	0.04	-0.31	0.22	0.36	-0.45	0.32
2006	**0.30**	-0.34	**0.49**	-0.13	-0.66	-0.76	-0.09	-0.30	**0.48**	-0.39	**0.74**	0.11
2007	-0.33	**0.65**	-0.76	**0.31**	-0.75	**0.67**	**-0.62**	**0.68**	-0.88	**1.10**	-0.68	**0.63**
2008	-0.22	**0.57**	-0.51	**0.04**	-0.48	0.23	**-1.32**	**0.79**	-0.32	-0.46	0.09	0.01
2009	**-0.92**	**0.58**	-0.59		-0.18	0.07	**-1.13**	**0.69**	-0.66	**0.61**	-0.27	0.36
2010	0.10	0.19	-0.23		-0.33	0.05	**-0.87**	**0.37**	-0.67	**0.62**	0.34	**0.41**

Table A.4: Summer (JJA) average seasonal teleconnection index and dot product scores of season's projection onto significant node shifts from climatology of the frequency distribution of winter negative and positive composite months.

	CAI-80			CAI-82			CAI-84		
YYYY	Index	Projection		Index	Projection		Index	Projection	
		Neg.	Pos.		Neg.	Pos.		Neg.	Pos.
1961	**-5.21**	**0.33**	-0.30	**-4.91**	0.30	-0.30	**-4.24**	**0.35**	-0.27
1962	0.93	-0.24	**0.36**	0.76	-0.23	**0.37**	0.51	-0.17	**0.34**
1963	-1.39	0.20	-0.07	-1.54	0.17	-0.06	-1.44	0.24	-0.05
1964	-1.78	-0.16	-0.38	**-2.50**	-0.21	-0.36	**-2.82**	-0.16	-0.31
1965	0.85	-0.23	0.02	0.00	-0.27	0.05	-0.63	-0.22	0.13
1966	2.03	-0.17	0.00	1.45	-0.16	0.02	0.66	-0.17	0.03
1967	**-3.87**	**0.72**	-0.69	**-3.04**	**0.72**	-0.71	**-2.23**	**0.70**	-0.69
1968	**7.65**	-0.56	**0.57**	**7.33**	-0.55	**0.58**	**6.05**	-0.64	**0.63**
1969	-1.55	**0.41**	-0.38	-1.47	**0.37**	-0.38	-1.17	**0.34**	-0.41
1970	0.26	0.09	0.09	0.57	0.15	0.06	0.68	0.14	0.02
1971	2.41	-0.20	-0.01	1.79	-0.18	0.05	1.25	-0.16	0.13
1972	-0.42	0.30	-0.20	0.12	**0.41**	-0.23	0.21	**0.43**	-0.35
1973	2.67	0.05	0.26	2.40	0.04	0.21	1.79	0.02	0.19
1974	2.06	0.04	0.10	1.62	-0.02	0.06	0.99	0.00	0.05
1975	**-3.15**	-0.03	-0.02	**-3.43**	0.03	0.02	**-3.09**	-0.01	0.00
1976	1.45	-0.22	-0.08	1.60	-0.25	-0.06	1.42	-0.18	-0.10
1977	3.13	-0.56	**0.41**	3.04	-0.57	**0.44**	2.31	-0.54	**0.44**
1978	-2.26	0.17	-0.17	-2.05	0.18	-0.10	-1.69	0.15	-0.18
1979	**-4.04**	0.30	-0.17	**-3.56**	0.27	-0.16	**-2.77**	**0.34**	-0.12
1980	2.35	-0.01	**0.35**	1.90	0.02	**0.31**	1.63	0.02	0.24
1981	**-2.76**	**0.52**	-0.34	-1.92	**0.52**	-0.37	-1.20	**0.47**	-0.29
1982	2.05	-0.16	0.07	2.18	-0.11	0.07	1.97	-0.10	0.09
1983	2.18	-0.09	0.01	2.61	-0.03	-0.08	2.33	-0.04	-0.11
1984	**-3.85**	**0.71**	-0.58	**-3.26**	**0.70**	-0.61	**-2.56**	**0.73**	-0.58
1985	-1.92	0.29	-0.37	-2.15	0.31	-0.35	-1.94	**0.40**	-0.33
1986	**-2.75**	0.29	-0.14	**-2.42**	0.26	-0.19	**-2.04**	0.17	-0.21
1987	3.14	-0.50	0.18	**3.44**	-0.49	0.23	**2.96**	-0.45	0.24
1988	-0.80	**0.42**	-0.23	-0.79	**0.43**	-0.22	-0.74	**0.45**	-0.26
1989	2.40	-0.46	**0.34**	2.38	-0.47	0.29	1.97	-0.47	0.21
1990	-1.94	0.21	-0.32	-1.46	0.21	-0.34	-1.12	0.12	-0.35
1991	-0.69	-0.08	-0.29	-0.58	-0.01	-0.28	-0.69	-0.07	-0.35
1992	2.68	-0.32	0.15	2.36	-0.32	0.17	1.73	-0.32	0.18
1993	0.44	0.05	0.27	-0.45	0.02	**0.31**	-1.43	-0.08	**0.32**
1994	-0.85	-0.09	0.05	-0.23	-0.04	0.02	-0.13	-0.01	-0.05
1995	**3.55**	-0.36	0.12	**3.33**	-0.32	0.11	**2.73**	-0.29	0.21
1996	**-4.03**	**0.51**	-0.35	**-4.48**	**0.53**	-0.37	**-4.32**	**0.54**	-0.41
1997	0.47	-0.60	**0.33**	0.42	-0.68	**0.35**	0.35	-0.69	**0.34**
1998	-1.47	0.31	0.06	-0.50	0.29	0.07	0.05	0.26	-0.01
1999	2.06	-0.36	-0.25	1.65	-0.35	-0.21	0.89	-0.30	-0.19
2000	2.16	-0.04	-0.25	2.58	-0.06	-0.21	2.23	-0.07	-0.19
2001	0.72	-0.02	0.15	1.15	0.03	0.15	1.10	0.10	0.09
2002	-0.10	0.06	0.10	-0.06	0.09	0.12	-0.28	0.04	0.09
2003	-0.30	**0.38**	-0.07	0.55	**0.39**	-0.08	0.89	**0.38**	-0.11
2004	**-2.63**	0.31	-0.38	**-2.25**	0.32	-0.38	-1.85	**0.38**	-0.33
2005	0.17	-0.11	-0.20	1.25	-0.11	-0.14	1.52	-0.10	-0.19
2006	1.57	-0.14	0.13	1.99	-0.16	0.11	1.94	-0.17	0.08
2007	**4.43**	-0.52	**0.41**	**4.56**	-0.55	**0.44**	**4.02**	-0.53	**0.54**
2008	2.11	-0.27	**0.31**	2.81	-0.37	0.29	**2.85**	-0.39	**0.38**
2009	**5.20**	-0.21	**0.53**	**5.27**	-0.26	**0.56**	**4.42**	-0.26	**0.53**
2010	**6.20**	-0.33	**0.66**	**6.00**	-0.38	**0.64**	**5.09**	-0.39	**0.71**

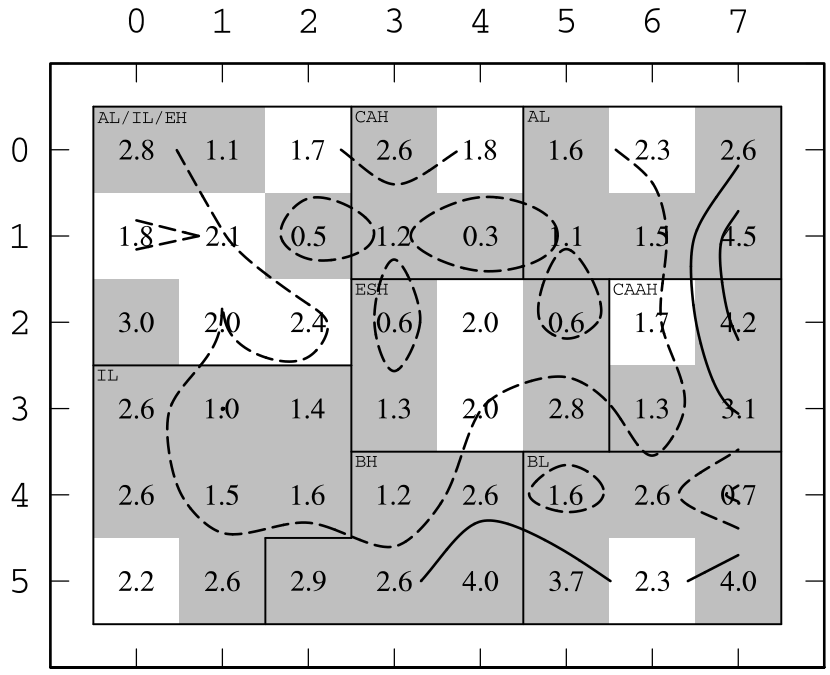

Figure A.3: Winter Frequency distribution of SOM nodes for CCSM3.0. Dashed contours are below the expected value of 2.08% and solid contours are above the expected value. Grey shaded nodes indicate that the frequency of occurence is significantly different from the expectant value (2.08%) at the 95% CI.

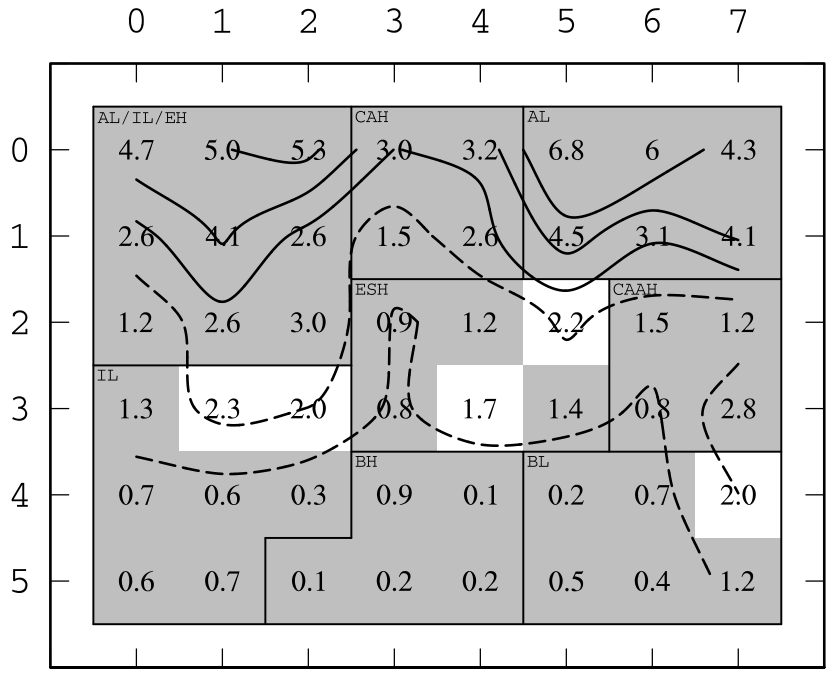

Figure A.4: Winter Frequency distribution of SOM nodes for ECHAM5/MPI-OM. Dashed contours are below the expected value of 2.08% and solid contours are above the expected value. Grey shaded nodes indicate that the frequency of occurence is significantly different from the expectant value (2.08%) at the 95% CI.

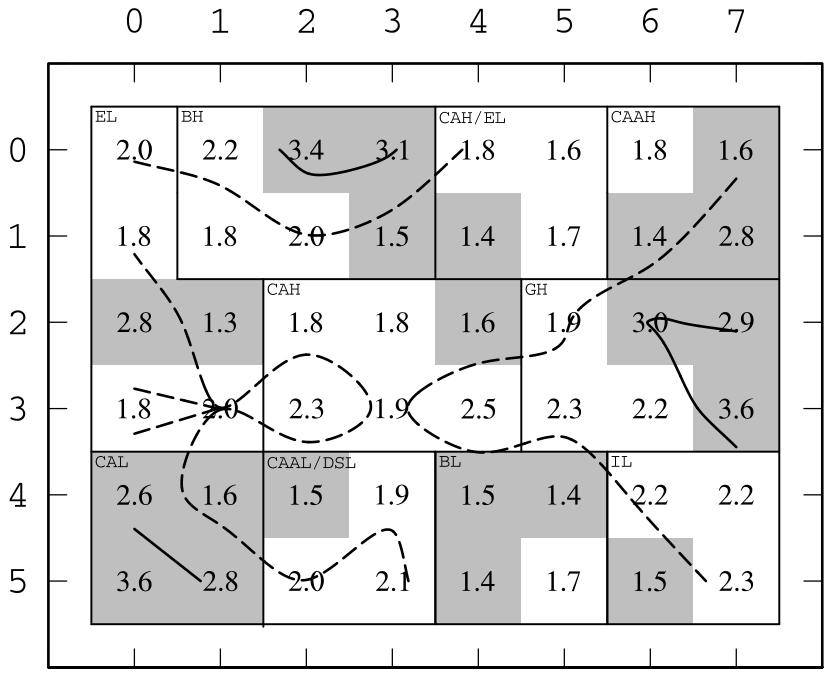

Figure A.5: Summer Frequency distribution of SOM nodes for CCCMA CGCM3.1 T63. Dashed contours are below the expected value of 2.08% and solid contours are above the expected value. Grey shaded nodes indicate that the frequency of occurence is significantly different from the expectant value (2.08%) at the 95% CI.

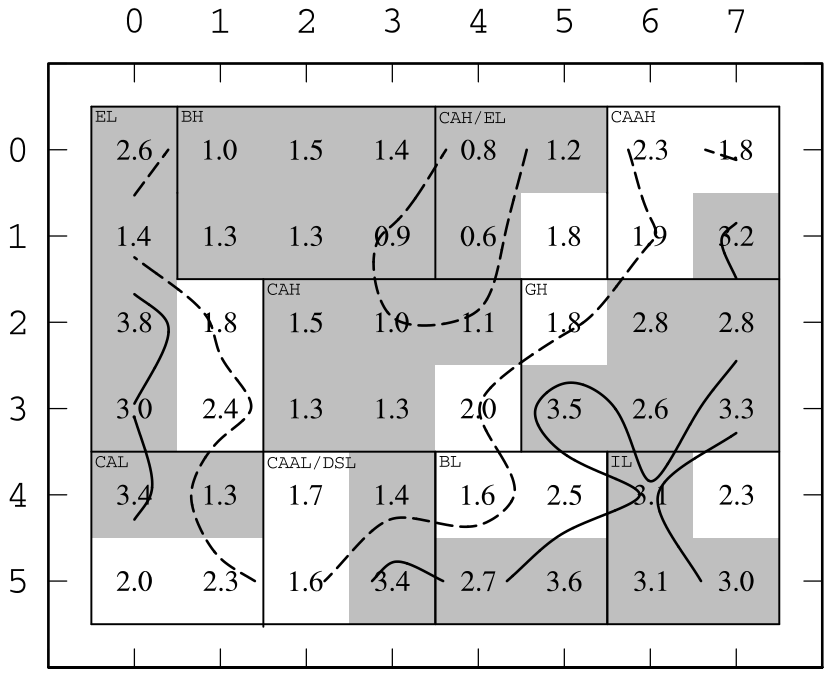

Figure A.6: Summer Frequency distribution of SOM nodes for ECHAM5/MPI-OM. Dashed contours are below the expected value of 2.08% and solid contours are above the expected value. Grey shaded nodes indicate that the frequency of occurence is significantly different from the expectant value (2.08%) at the 95% CI.

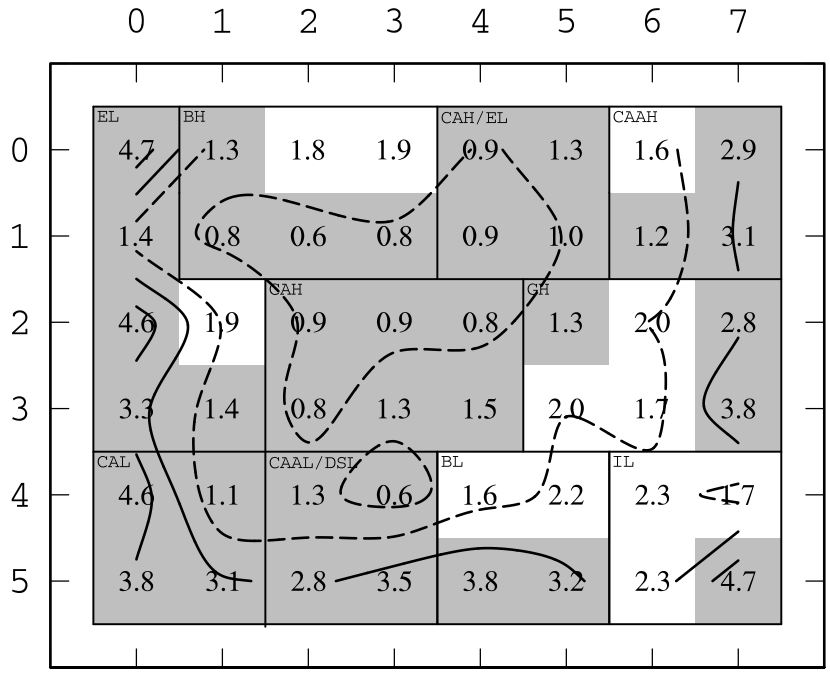

Figure A.7: Summer Frequency distribution of SOM nodes for CCSM3.0. Dashed contours are below the expected value of 2.08% and solid contours are above the expected value. Grey shaded nodes indicate that the frequency of occurence is significantly different from the expectant value (2.08%) at the 95% CI.

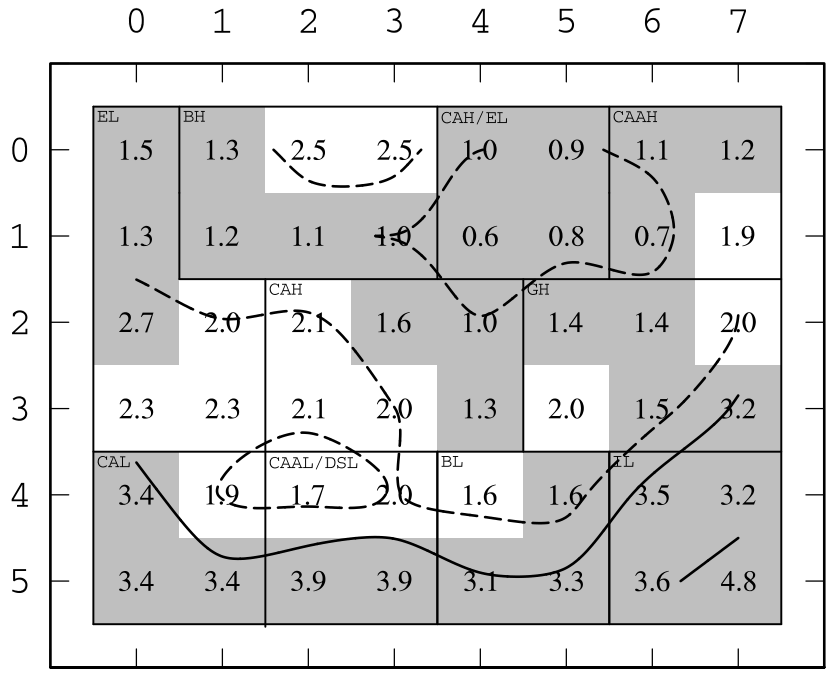

Figure A.8: Summer Frequency distribution of SOM nodes for CSIRO MK5. Dashed contours are below the expected value of 2.08% and solid contours are above the expected value. Grey shaded nodes indicate that the frequency of occurence is significantly different from the expectant value (2.08%) at the 95% CI.

Table A.5: Winter (DJF) average seasonal teleconnection index calculated by averaging the monthly teleconnection scores for the season. Dot product scores of season's projection onto significant node shifts from climatology of the frequency distribution of winter negative and positive composite months.

	AO			ARP			NAO			PNA		
YYYY	Index	Projection		Index	Projection		Index	Projection		Index	Projection	
		Neg.	Pos.		Neg.	Pos.		Neg.	Pos.		Neg.	Pos.
1962	-0.13	-0.54	**0.66**		-0.77	**0.53**	-0.36	0.05	-0.10	-0.51	-0.33	-0.21
1963	**-1.91**	-0.38	-0.05		-0.29	-0.26	**-1.94**	**0.44**	-0.49	0.27	-0.96	-0.07
1964	-0.46	-0.11	-0.15		0.19	-0.26	**-1.85**	**0.44**	-0.52	0.37	-0.90	0.03
1965	-1.13	0.06	0.09		-0.18	0.10	-1.03	-0.12	0.34	-0.74	0.56	-0.42
1966	**-1.50**	**0.55**	-0.37		-0.10	-0.75	**-1.13**	**0.53**	-0.34	**-1.11**	0.54	**0.52**
1967	-0.27	0.36	-0.52		**0.52**	-0.74	-0.40	0.01	-0.28	-0.66	-0.82	-0.12
1968	-0.97	-0.13	0.02		0.05	0.18	-0.93	0.00	-0.01	-0.09	-0.58	-0.20
1969	**-2.29**	**0.61**	-0.68		**0.60**	-0.76	**-1.69**	**0.39**	-0.29	**-1.84**	**0.88**	**0.61**
1970	**-1.86**	**0.49**	-0.38		0.32	-0.46	-0.78	0.16	-0.07	0.06	0.35	-0.05
1971	-0.49	-0.38	**0.48**		-0.19	**0.67**	-1.06	-0.42	**0.63**	-0.59	-0.58	-0.25
1972	0.26	-0.41	0.42		-0.42	0.39	0.07	-0.56	0.27	**-1.03**	0.26	-0.57
1973	**1.09**	-0.29	0.42		-0.44	**0.52**	0.05	-0.21	0.22	-0.41	-0.04	-0.58
1974	-0.15	0.29	-0.06		0.15	-0.29	0.22	-0.23	-0.03	**-1.13**	-0.99	0.09
1975	0.78	-0.59	**0.51**		-0.04	**0.53**	0.11	-0.47	**0.63**	-0.41	-0.24	-0.39
1976	**0.99**	-0.52	**0.79**		-0.44	**0.68**	-0.09	-0.40	0.41	-0.57	-0.90	-0.36
1977	**-2.62**	**0.65**	-0.56		**0.65**	-0.46	**-1.43**	**0.31**	0.31	**0.75**	0.29	**0.60**
1978	-1.20	-0.36	**0.50**		-0.68	0.33	**-1.23**	**0.32**	-0.43	**0.62**	-0.26	0.14
1979	-1.30	**0.49**	-0.51		0.20	-0.30	**-1.62**	**0.38**	-0.17	**-1.33**	0.44	0.15
1980	-0.57	0.45	-0.28		-0.43	-0.41	-0.31	0.27	-0.28	0.40	0.46	**0.36**
1981	-0.17	-0.52	**0.55**		-0.44	**0.53**	0.38	-0.43	**0.53**	0.50	-0.78	-0.73
1982	-0.38	-0.08	-0.33		0.15	-0.33	-0.27	-0.26	-0.18	**-1.52**	**0.80**	-0.34
1983	0.17	-0.49	**0.77**		-0.56	**0.69**	**0.62**	-0.17	0.41	**0.78**	-0.01	-0.50
1984	0.26	-0.45	0.14		-0.01	**0.56**	**0.66**	-0.67	**0.54**	0.12	0.41	-0.63
1985	-1.27	**0.74**	-0.64	**-1.48**	**0.60**	-0.74	**-1.16**	**0.32**	-0.13	0.17	0.44	-0.37
1986	**-1.81**	**0.74**	-0.70	**-0.95**	**0.49**	-0.70	-0.23	**0.45**	-0.38	0.32	0.09	**0.46**
1987	-0.85	**0.73**	-0.70	-0.56	**0.59**	-0.89	-0.76	**0.49**	-0.57	**0.87**	-0.09	**0.68**
1988	-0.45	0.29	-0.49	-0.06	**0.75**	-0.40	0.44	0.13	0.08	**0.87**	**0.79**	**0.46**
1989	**2.69**	-0.80	**0.82**	**1.97**	-0.72	**0.85**	**1.05**	-0.45	**0.51**	-0.84	-0.60	-0.53
1990	**1.25**	-0.21	0.39	0.51	0.10	**0.52**	0.24	-0.81	**0.80**	**-1.27**	0.03	-0.25
1991	0.37	-0.01	-0.72	-0.09	-0.07	-0.16	0.45	-0.38	0.13	0.23	**0.80**	-0.52
1992	**1.09**	-0.53	**0.50**	0.75	-0.52	**0.71**	0.15	-0.35	**0.66**	**1.02**	-0.09	0.04
1993	**1.77**	-0.72	**0.92**	**1.53**	-0.58	**0.89**	**0.61**	-0.50	**0.56**	-0.23	-0.01	-0.22
1994	-0.42	0.19	-0.29	-0.03	-0.03	-0.24	**0.71**	-0.19	0.21	**-1.01**	**0.60**	-0.37
1995	0.72	-0.42	**0.48**	0.59	0.13	**0.62**	**1.07**	-0.56	**0.68**	**0.74**	-0.42	-0.17
1996	-1.05	0.32	-0.64	-0.49	-0.04	-0.88	-0.94	**0.37**	-0.56	-0.23	-0.73	-0.22
1997	-0.10	-0.37	0.05	0.48	-0.45	0.27	-0.33	-0.30	0.21	-0.07	-0.23	-0.32
1998	-0.78	0.33	-0.67	-0.21	0.24	-0.73	-0.53	-0.04	-0.34	0.48	-0.04	0.26
1999	0.65	0.17	-0.17	0.19	0.03	0.14	0.33	-0.15	0.47	-0.52	**0.70**	-0.40
2000	**1.13**	0.12	0.09	0.33	-0.15	0.15	**1.02**	-0.46	**0.52**	-0.48	-0.82	**0.50**
2001	-1.31	**0.74**	-0.54	-0.74	**0.80**	-0.67	-0.26	-0.12	0.06	0.00	-0.03	**0.74**
2002	0.45	0.21	-0.29	0.51	**0.67**	-0.27	-0.02	-0.19	0.29	-0.12	0.33	-0.53
2003	-0.65	-0.35	0.12	-0.39	0.28	0.01	-0.34	-0.02	-0.17	**1.10**	0.55	0.23
2004	-0.98	0.20	-0.29	0.31	-0.33	0.01	-0.32	0.22	-0.08	0.44	**0.72**	0.07
2005	0.11	-0.16	-0.01	-0.61	0.39	0.22	**0.59**	-0.65	**0.66**	-0.16	0.09	-0.43
2006	-0.81	**0.61**	-0.54	**-1.62**	**0.72**	-0.83	-0.18	-0.03	-0.07	-0.42	**0.71**	0.24
2007	**1.00**	0.02	0.09	**0.93**	0.12	0.23	-0.03	0.05	0.37	0.39	0.57	0.03
2008	0.86	-0.30	0.09	0.33	-0.05	0.20	0.38	-0.30	0.36	-0.14	-0.50	-0.52
2009	0.26	-0.34	0.01	-0.09	-0.39	0.25	-0.42	-0.36	0.05	**-0.97**	0.46	-0.35
2010	**-3.42**	**0.74**	-0.53		0.24	-0.68	**-2.12**	**0.63**	-0.28	0.21	0.09	**0.39**

Table A.6: Winter (DJF) average seasonal teleconnection index calculated by averaging the monthly teleconnection scores for the season. Dot product scores of season's projection onto significant node shifts from climatology of the frequency distribution of winter negative and positive composite months.

	CAI-80			CAI-82			CAI-84		
YYYY	Index	Projection		Index	Projection		Index	Projection	
		Neg.	Pos.		Neg.	Pos.		Neg.	Pos.
1962	**6.66**	-0.60	**0.30**	**6.40**	-0.58	**0.35**	**4.98**	-0.60	0.21
1963	**6.87**	-0.50	**0.50**	5.74	-0.45	**0.39**	3.62	-0.39	**0.39**
1964	5.70	0.21	0.04	**6.43**	0.20	0.07	**5.34**	0.16	0.11
1965	**-3.84**	0.21	-0.44	**-3.03**	0.26	-0.47	**-2.89**	0.23	-0.44
1966	0.51	-0.09	0.21	0.21	-0.04	0.23	-0.38	0.04	0.15
1967	4.02	0.41	-0.12	4.58	0.35	-0.12	3.72	0.27	-0.10
1968	**7.56**	0.00	**0.23**	**7.54**	-0.16	0.14	**6.20**	-0.31	**0.37**
1969	1.42	0.35	-0.09	2.48	0.34	-0.15	2.54	0.25	-0.14
1970	-0.08	0.27	-0.68	0.65	0.28	-0.75	0.46	0.40	-0.76
1971	2.96	-0.02	0.08	3.11	-0.06	0.20	2.23	-0.07	0.20
1972	0.14	0.14	-0.21	-0.17	0.11	-0.15	-0.81	0.13	-0.25
1973	5.48	-0.33	0.15	4.46	-0.36	**0.29**	2.73	-0.28	0.02
1974	**-3.42**	**0.47**	-0.51	**-2.87**	**0.51**	-0.51	**-2.85**	**0.60**	-0.52
1975	3.53	0.04	-0.13	4.67	-0.08	-0.05	4.41	-0.34	0.12
1976	4.32	-0.15	0.05	4.10	-0.23	0.10	2.63	-0.21	0.09
1977	**-7.94**	**0.58**	-0.66	**-6.49**	**0.58**	-0.60	**-5.22**	**0.63**	-0.61
1978	**9.25**	-0.63	**0.61**	**8.52**	-0.59	**0.70**	**6.42**	-0.55	**0.58**
1979	1.92	0.00	-0.05	1.53	-0.04	-0.15	0.66	0.01	-0.11
1980	1.84	-0.07	-0.21	3.00	-0.04	-0.13	2.70	0.11	-0.24
1981	**6.10**	-0.10	-0.02	**6.20**	-0.17	0.10	**4.83**	-0.31	0.01
1982	**10.25**	-0.36	**0.44**	**10.37**	-0.41	**0.41**	**8.57**	-0.36	**0.39**
1983	2.31	-0.39	-0.23	2.15	-0.41	-0.24	1.23	-0.33	-0.31
1984	4.24	0.24	-0.22	4.56	0.18	-0.29	3.59	0.19	-0.33
1985	**-3.42**	**0.73**	-0.64	**-2.57**	**0.68**	-0.61	**-2.03**	**0.79**	-0.63
1986	-1.26	0.32	-0.44	-1.34	0.39	-0.50	**-1.88**	**0.57**	-0.49
1987	**-3.37**	**0.44**	-0.31	**-3.60**	**0.50**	-0.36	**-3.80**	**0.60**	-0.39
1988	3.14	0.20	-0.19	3.11	0.21	-0.28	2.28	0.19	-0.26
1989	**11.55**	-0.61	**0.70**	**10.59**	-0.67	**0.78**	**8.13**	-0.68	**0.75**
1990	**-5.98**	0.39	-0.52	**-4.95**	0.28	-0.48	**-4.24**	0.39	-0.50
1991	**-3.27**	0.32	-0.35	**-1.85**	0.34	-0.32	-1.19	**0.50**	-0.34
1992	2.76	-0.23	-0.03	3.32	-0.24	0.07	2.86	-0.19	0.03
1993	**7.05**	-0.63	**0.54**	**6.09**	-0.68	**0.60**	4.42	-0.68	**0.50**
1994	-0.06	0.06	-0.34	0.68	0.00	-0.37	0.53	0.07	-0.43
1995	4.47	-0.21	-0.04	4.05	-0.43	-0.10	2.73	-0.54	-0.02
1996	4.75	-0.12	**0.35**	3.86	-0.13	**0.46**	2.34	-0.05	0.20
1997	0.79	-0.30	-0.11	0.76	-0.43	-0.02	0.23	-0.37	-0.03
1998	3.19	0.11	-0.17	3.28	0.20	-0.19	2.30	0.41	-0.27
1999	0.30	**0.47**	-0.57	1.01	**0.48**	-0.56	0.84	**0.53**	-0.54
2000	-2.16	0.27	-0.53	-1.02	0.38	-0.54	-0.71	0.42	-0.49
2001	**-3.48**	**0.60**	-0.66	**-2.05**	**0.61**	-0.71	-1.50	**0.68**	-0.66
2002	2.22	0.30	-0.15	3.46	0.24	-0.14	3.53	0.34	-0.19
2003	2.23	-0.26	0.11	2.52	-0.22	0.17	1.51	-0.13	0.07
2004	2.77	-0.18	0.05	2.15	-0.15	0.10	1.24	-0.10	0.11
2005	-1.42	**0.51**	-0.44	0.35	**0.49**	-0.46	0.64	0.44	-0.50
2006	**-3.92**	**0.72**	-0.38	**-1.93**	**0.70**	-0.36	-1.14	**0.63**	-0.34
2007	1.28	-0.10	-0.30	1.98	-0.08	-0.39	1.83	-0.03	-0.27
2008	3.60	0.02	-0.32	4.07	-0.06	-0.25	3.29	-0.04	-0.31
2009	1.24	-0.08	0.15	1.26	-0.11	0.24	0.58	-0.03	0.20
2010	**-2.99**	**0.48**	-0.46	**-2.54**	**0.49**	-0.44	**-2.73**	**0.56**	-0.38

Table A.7: Summer (JJA) average seasonal teleconnection index calculated by averaging the monthly teleconnection scores for the season. Dot product scores of season's projection onto significant node shifts from climatology of the frequency distribution of winter negative and positive composite months.

	AO			ARP			NAO			PNA		
YYYY	Index	Projection		Index	Projection		Index	Projection		Index	Projection	
		Neg.	Pos.		Neg.	Pos.		Neg.	Pos.		Neg.	Pos.
1961	0.25	**0.52**	-0.47		-0.40	0.21	0.61	0.11	-0.23	**0.60**	-0.50	**0.44**
1962	-0.16	**0.38**	-0.15		-0.65	0.25	**-0.64**	0.30	-0.71	-0.25	0.23	-0.41
1963	**-0.50**	**0.62**	-0.58		-0.27	-0.21	**-0.61**	**0.53**	-0.47	-0.54	-0.15	-0.14
1964	-0.11	0.02	0.19		-0.71	-0.64	0.38	-0.01	0.37	0.43	0.27	**0.43**
1965	-0.24	**0.48**	-0.44		-0.94	-0.10	0.47	0.24	-0.57	0.32	-0.72	**0.54**
1966	-0.18	0.36	-0.25		-0.67	0.30	-0.22	**0.47**	0.09	0.06	-0.64	-0.18
1967	0.20	-0.58	0.10		**0.84**	-0.27	**1.30**	-0.35	**0.66**	-0.64	**0.61**	-0.14
1968	-0.36	0.20	-0.21		-0.30	**0.58**	-0.37	0.11	-0.37	0.39	-0.23	-0.20
1969	-0.24	0.29	-0.45		0.13	-0.61	-0.18	0.19	-0.10	**0.64**	0.01	-0.20
1970	0.25	-0.46	**0.49**		0.08	-0.07	0.67	-0.35	0.28	0.12	**0.49**	-0.51
1971	-0.14	0.12	-0.07		-0.15	0.15	0.29	0.06	0.13	-0.68	-0.46	**0.75**
1972	-0.23	-0.15	0.06		0.08	0.30	**0.99**	-0.30	0.16	-0.44	0.15	-0.75
1973	**0.37**	-0.33	0.34		**0.52**	**0.45**	0.37	-0.31	-0.42	-0.07	**0.58**	-0.26
1974	-0.06	0.10	-0.33		0.27	0.12	-0.50	0.20	-0.26	-0.18	-0.42	-0.10
1975	0.05	-0.12	0.30		0.07	-0.21	0.19	-0.20	0.37	**-0.98**	**0.72**	-0.36
1976	0.19	-0.41	**0.44**		-0.55	-0.35	**1.05**	-0.36	**0.46**	-0.69	-0.15	0.11
1977	**-0.71**	**0.45**	-0.42		-0.78	0.09	-0.39	**0.40**	-0.51	**0.58**	-0.76	0.22
1978	-0.11	0.24	-0.31		0.32	-0.46	0.43	-0.09	0.04	**-1.11**	-0.10	-0.56
1979	0.10	0.17	-0.55		0.07	-0.55	**1.30**	0.03	-0.18	-0.15	-0.34	0.22
1980	-0.03	-0.15	0.30		**0.56**	**0.43**	**-1.16**	0.10	-0.22	**-1.22**	0.26	-0.04
1981	-0.04	0.03	-0.38		**0.78**	-0.17	0.10	0.05	-0.14	**-0.89**	-0.05	0.21
1982	-0.27	-0.26	**0.36**		-0.26	0.05	0.02	-0.43	0.21	**0.99**	-0.27	-0.13
1983	**0.51**	-0.61	**0.37**		0.04	-0.08	**1.49**	-0.49	**0.54**	**1.14**	0.04	-0.20
1984	0.16	-0.20	-0.08		**0.69**	-0.55	0.40	-0.42	**0.55**	**-1.37**	-0.58	-0.43
1985	-0.25	0.22	-0.37	-0.23	0.17	0.21	0.00	-0.09	0.15	0.19	-0.67	0.26
1986	-0.10	-0.25	0.05	-0.36	**0.67**	-0.40	0.05	0.03	0.16	-0.48	**0.56**	-0.33
1987	**-0.67**	**0.39**	-0.16	-0.32	-0.54	0.04	**-0.72**	0.31	0.00	0.29	-0.72	0.25
1988	0.06	-0.03	-0.44	-0.25	**0.46**	-0.10	0.27	-0.10	-0.27	**0.76**	-0.02	-0.22
1989	**0.59**	-0.70	**0.92**	-0.06	-0.68	0.11	0.31	-0.53	0.39	-0.47	**0.61**	-0.33
1990	-0.06	-0.20	-0.09	-0.33	**0.47**	-0.24	0.66	-0.20	**0.43**	0.04	0.03	-0.31
1991	0.16	-0.44	**0.67**	-0.20	-0.16	-0.44	0.16	-0.45	**0.78**	-0.31	**0.74**	-0.86
1992	0.14	-0.44	**0.58**	-0.10	-0.29	-0.37	0.56	-0.37	0.38	0.46	0.33	0.31
1993	**-0.47**	0.30	-0.18	**-0.47**	**0.59**	-0.16	**-1.13**	**0.51**	-0.39	0.07	0.07	0.05
1994	**0.93**	-0.61	**0.74**	**0.17**	-0.51	0.19	**1.18**	-0.55	**0.72**	**-0.93**	**0.77**	-0.46
1995	0.07	-0.15	0.01	**0.11**	-0.63	**0.86**	0.34	-0.25	0.10	-0.06	-0.62	0.35
1996	**0.45**	-0.52	**0.52**	-0.37	**0.62**	-0.04	**0.92**	-0.52	0.15	-0.64	**0.69**	-0.10
1997	-0.37	0.11	0.01	-0.28	-0.81	-0.47	0.05	0.29	0.25	-0.23	-0.22	**0.52**
1998	-0.09	0.26	0.02	-0.35	0.16	-0.30	**-1.01**	0.23	-0.35	0.39	0.11	-0.84
1999	0.01	0.05	0.11	-0.01	-0.75	-0.28	0.32	-0.26	0.35	0.49	-0.67	**0.65**
2000	0.03	0.17	-0.08	-0.08	-0.32	0.13	-0.41	**0.38**	0.22	**-1.42**	**0.52**	-0.50
2001	0.16	-0.01	0.15	-0.06	-0.58	0.29	-0.11	-0.11	-0.12	-0.46	-0.36	-0.51
2002	0.22	0.18	-0.09	-0.19	**0.62**	0.28	0.57	0.19	-0.55	0.36	0.13	-0.60
2003	-0.10	-0.18	-0.07	**-0.45**	**0.73**	**0.38**	0.06	0.04	-0.49	-0.04	0.28	0.28
2004	**-0.39**	-0.14	-0.48	**-0.39**	0.39	**0.36**	-0.06	-0.13	-0.21	0.30	-0.75	**0.78**
2005	-0.13	0.03	-0.20	-0.06	-0.50	-0.46	0.04	-0.31	0.22	0.36	-0.45	0.32
2006	**0.30**	-0.34	**0.49**	-0.13	-0.66	-0.76	-0.09	-0.30	**0.48**	-0.39	**0.74**	0.11
2007	-0.33	**0.65**	-0.76	**0.31**	-0.75	**0.67**	**-0.62**	**0.68**	-0.88	**1.10**	-0.68	**0.63**
2008	-0.22	**0.57**	-0.51	**0.04**	-0.48	0.23	**-1.32**	**0.79**	-0.32	-0.46	0.09	0.01
2009	**-0.92**	**0.58**	-0.59		-0.18	0.07	**-1.13**	**0.69**	-0.66	**0.61**	-0.27	0.36
2010	0.10	0.19	-0.23		-0.33	0.05	**-0.87**	**0.37**	-0.67	**0.62**	0.34	**0.41**

Table A.8: Summer (JJA) average seasonal teleconnection index and dot product scores of season's projection onto significant node shifts from climatology of the frequency distribution of winter negative and positive composite months.

	CAI-80			CAI-82			CAI-84		
YYYY	Index	Projection		Index	Projection		Index	Projection	
		Neg.	Pos.		Neg.	Pos.		Neg.	Pos.
1961	**-5.21**	**0.33**	-0.30	**-4.91**	0.30	-0.30	**-4.24**	**0.35**	-0.27
1962	0.93	-0.24	**0.36**	0.76	-0.23	**0.37**	0.51	-0.17	**0.34**
1963	-1.39	0.20	-0.07	-1.54	0.17	-0.06	-1.44	0.24	-0.05
1964	-1.78	-0.16	-0.38	**-2.50**	-0.21	-0.36	**-2.82**	-0.16	-0.31
1965	0.85	-0.23	0.02	0.00	-0.27	0.05	-0.63	-0.22	0.13
1966	2.03	-0.17	0.00	1.45	-0.16	0.02	0.66	-0.17	0.03
1967	**-3.87**	**0.72**	-0.69	**-3.04**	**0.72**	-0.71	**-2.23**	**0.70**	-0.69
1968	**7.65**	-0.56	**0.57**	**7.33**	-0.55	**0.58**	**6.05**	-0.64	**0.63**
1969	-1.55	**0.41**	-0.38	-1.47	**0.37**	-0.38	-1.17	**0.34**	-0.41
1970	0.26	0.09	0.09	0.57	0.15	0.06	0.68	0.14	0.02
1971	2.41	-0.20	-0.01	1.79	-0.18	0.05	1.25	-0.16	0.13
1972	-0.42	0.30	-0.20	0.12	**0.41**	-0.23	0.21	**0.43**	-0.35
1973	2.67	0.05	0.26	2.40	0.04	0.21	1.79	0.02	0.19
1974	2.06	0.04	0.10	1.62	-0.02	0.06	0.99	0.00	0.05
1975	**-3.15**	-0.03	-0.02	**-3.43**	0.03	0.02	**-3.09**	-0.01	0.00
1976	1.45	-0.22	-0.08	1.60	-0.25	-0.06	1.42	-0.18	-0.10
1977	3.13	-0.56	**0.41**	3.04	-0.57	**0.44**	2.31	-0.54	**0.44**
1978	-2.26	0.17	-0.17	-2.05	0.18	-0.10	-1.69	0.15	-0.18
1979	**-4.04**	0.30	-0.17	**-3.56**	0.27	-0.16	**-2.77**	**0.34**	-0.12
1980	2.35	-0.01	**0.35**	1.90	0.02	**0.31**	1.63	0.02	0.24
1981	**-2.76**	**0.52**	-0.34	-1.92	**0.52**	-0.37	-1.20	**0.47**	-0.29
1982	2.05	-0.16	0.07	2.18	-0.11	0.07	1.97	-0.10	0.09
1983	2.18	-0.09	0.01	2.61	-0.03	-0.08	2.33	-0.04	-0.11
1984	**-3.85**	**0.71**	-0.58	**-3.26**	**0.70**	-0.61	**-2.56**	**0.73**	-0.58
1985	-1.92	0.29	-0.37	-2.15	0.31	-0.35	-1.94	**0.40**	-0.33
1986	**-2.75**	0.29	-0.14	**-2.42**	0.26	-0.19	**-2.04**	0.17	-0.21
1987	3.14	-0.50	0.18	**3.44**	-0.49	0.23	**2.96**	-0.45	0.24
1988	-0.80	**0.42**	-0.23	-0.79	**0.43**	-0.22	-0.74	**0.45**	-0.26
1989	2.40	-0.46	**0.34**	2.38	-0.47	0.29	1.97	-0.47	0.21
1990	-1.94	0.21	-0.32	-1.46	0.21	-0.34	-1.12	0.12	-0.35
1991	-0.69	-0.08	-0.29	-0.58	-0.01	-0.28	-0.69	-0.07	-0.35
1992	2.68	-0.32	0.15	2.36	-0.32	0.17	1.73	-0.32	0.18
1993	0.44	0.05	0.27	-0.45	0.02	**0.31**	-1.43	-0.08	**0.32**
1994	-0.85	-0.09	0.05	-0.23	-0.04	0.02	-0.13	-0.01	-0.05
1995	**3.55**	-0.36	0.12	**3.33**	-0.32	0.11	**2.73**	-0.29	0.21
1996	**-4.03**	**0.51**	-0.35	**-4.48**	**0.53**	-0.37	**-4.32**	**0.54**	-0.41
1997	0.47	-0.60	**0.33**	0.42	-0.68	**0.35**	0.35	-0.69	**0.34**
1998	-1.47	0.31	0.06	-0.50	0.29	0.07	0.05	0.26	-0.01
1999	2.06	-0.36	-0.25	1.65	-0.35	-0.21	0.89	-0.30	-0.19
2000	2.16	-0.04	-0.25	2.58	-0.06	-0.21	2.23	-0.07	-0.19
2001	0.72	-0.02	0.15	1.15	0.03	0.15	1.10	0.10	0.09
2002	-0.10	0.06	0.10	-0.06	0.09	0.12	-0.28	0.04	0.09
2003	-0.30	**0.38**	-0.07	0.55	**0.39**	-0.08	0.89	**0.38**	-0.11
2004	**-2.63**	0.31	-0.38	**-2.25**	0.32	-0.38	-1.85	**0.38**	-0.33
2005	0.17	-0.11	-0.20	1.25	-0.11	-0.14	1.52	-0.10	-0.19
2006	1.57	-0.14	0.13	1.99	-0.16	0.11	1.94	-0.17	0.08
2007	**4.43**	-0.52	**0.41**	**4.56**	-0.55	**0.44**	**4.02**	-0.53	**0.54**
2008	2.11	-0.27	**0.31**	2.81	-0.37	0.29	**2.85**	-0.39	**0.38**
2009	**5.20**	-0.21	**0.53**	**5.27**	-0.26	**0.56**	**4.42**	-0.26	**0.53**
2010	**6.20**	-0.33	**0.66**	**6.00**	-0.38	**0.64**	**5.09**	-0.39	**0.71**

Table A.9: Correlations between winter (DJF) negative phase AO, NAO and ARP self-organizing map node frequencies significant anomalies (insignificant shifts masked with zeros). Significant correlations are less than -0.29 or greater than 0.29 shown in bolded font.

	AO	ARP	NAO
AO	1	**0.41**	**0.55**
ARP	**0.41**	1	0.23
NAO	**0.55**	0.23	1

Table A.10: Correlations between winter (DJF) positive phase AO, NAO and ARP self-organizing map node frequencies significant anomalies (insignificant shifts masked by zeros). Significant correlations are less than -0.29 or greater than 0.29 shown in bolded font.

	AO	ARP	NAO
AO	1	**0.77**	**0.39**
ARP	**0.77**	1	**0.67**
NAO	**0.39**	**0.67**	1

Appendix B

Second appendix

Table B.1: Days mapping to each feature during RILEs for Winter (DJF) season for SRES A1B runs examined. Ice area change for each year and RILE period are shown in the right most column. High features counts significant at the 95% CI are bolded and black and low feature counts significant at the 95% CI are bolded and red.

Model Run	YYYY	AL	BAL	BH	CAAH	CAH	EH	EL	ESSH	GH	IL	SH	Ice Area (M km^2)
CCSM3	2024	**48**	**13**	12	9	3	**16**	7	5	**19**	49	8	0.245
Run 1	2025	28	21	22	13	12	**12**	5	6	12	42	15	1.081
	2026	**6**	21	**37**	17	3	**0**	7	2	**0**	**61**	**28**	-1.903
	2027	**43**	**8**	**10**	6	5	9	2	**0**	9	**65**	**25**	-0.716
	2028	**15**	33	**30**	7	**1**	**1**	**0**	7	**1**	**56**	13	0.018
	2029	**43**	31	**9**	15	9	9	3	4	15	37	6	-0.729
	2030	27	28	18	**19**	9	7	**13**	1	11	**35**	**4**	0.253
	2031	**18**	**38**	20	13	7	2	9	2	**19**	**35**	14	-0.119
	2032	20	26	22	13	**2**	2	10	1	14	49	16	-0.897
	2033	**15**	**37**	**28**	11	4	2	**15**	3	**24**	**32**	12	-1.737
	2024-2033	263	256	208	123	55	60	71	31	124	461	**141**	-4.503
CCSM3	2034	33	19	**10**	12	**24**	7	11	5	9	41	6	-0.398
Run 2	2035	22	28	20	19	3	6	11	5	11	41	**3**	-0.988
	2036	27	**50**	**8**	**25**	6	3	8	3	7	**25**	**2**	0.917
	2037	**42**	**16**	17	**4**	8	6	5	5	7	**60**	13	-0.075
	2038	30	27	15	**6**	4	4	2	6	**3**	52	9	0.007
	2039	**13**	35	**29**	15	**0**	1	4	2	**2**	49	17	-0.907
	2040	20	**40**	**9**	**24**	5	4	11	2	**16**	**31**	**4**	0.392
	2041	**18**	**40**	**26**	18	6	2	2	1	**3**	43	7	-0.401
	2034-2041	205	**255**	134	123	56	33	54	29	**58**	**342**	**61**	-1.454
	2047	**39**	**10**	12	8	3	**9**	4	2	13	**61**	18	0.104
	2048	29	32	24	18	10	1	8	2	**2**	44	9	-1.141
	2049	30	26	18	18	**1**	4	7	0	10	48	12	0.064
	2050	**16**	29	21	18	6	5	9	3	9	43	15	-0.595
	2047-2050	114	97	75	62	20	19	28	**7**	34	196	54	-1.568
CCSM3	2025	**44**	18	12	**5**	9	8	4	1	16	50	10	1.168
Run 3	2026	**10**	**34**	**34**	16	5	1	5	5	**3**	46	14	0.039
	2027	**14**	30	12	**24**	9	2	**21**	1	14	**31**	10	-2.202
	2028	33	32	12	14	**13**	5	9	**8**	**19**	**28**	**2**	-0.546
	2029	31	23	21	10	11	**10**	5	6	13	46	6	-0.040
	2025-2029	132	137	91	69	47	26	44	21	**65**	**201**	42	-1.581

Table B.2: Days mapping to each feature during RILEs for Winter (DJF) season for SRES A2 runs examined. Ice area change for each year and for the RILE period are shown in the right most column. High features counts significant at the 95% CI are bolded and black and low feature counts significant at the 95% CI are bolded and red.

Model Run	YYYY	AL	BAL	BH	CAAH	CAH	EH	EL	ESSH	GH	IL	SH	Ice Area (M km^2)
CCSM3	2030	**37**	**14**	17	8	6	**1**	5	4	**2**	**66**	14	0.215
Run 4	2031	20	**40**	15	9	**1**	**1**	**0**	3	9	47	17	-0.130
	2032	25	**34**	22	12	5	**0**	**1**	2	**4**	52	16	-1.630
	2033	**14**	24	22	**23**	6	5	**14**	0	**3**	45	15	0.460
	2034	31	**42**	**9**	**25**	7	**10**	**13**	0	**24**	**16**	**4**	-0.885
	2030-2034	127	**154**	85	**77**	25	**17**	33	**9**	42	226	66	-1.970
CCSM3	2027	22	27	11	9	6	4	4	2	8	53	**23**	-0.649
Run 5	2028	29	**36**	**27**	7	6	8	4	1	11	**38**	11	0.233
	2029	30	26	23	10	2	3	5	3	**4**	54	12	-0.723
	2030	28	29	**35**	**3**	3	8	3	0	15	43	11	0.478
	2031	21	22	19	**18**	4	2	**23**	1	**17**	**37**	11	-0.116
	2032	**18**	23	**33**	9	4	3	7	**10**	9	54	13	-0.988
	2033	**10**	**38**	21	14	**1**	2	6	2	14	41	**23**	0.262
	2034	**8**	**39**	**27**	17	6	2	3	1	5	44	**22**	-0.733
	2027-2034	***166***	**240**	**196**	87	***32***	32	55	20	83	364	**126**	-2.236
CCSM3	2030	25	**17**	16	**23**	4	**10**	**19**	5	14	39	13	-1.078
Run 6	2031	25	27	17	**25**	**14**	**0**	**14**	5	5	**36**	7	0.118
	2032	**14**	**49**	21	11	9	**0**	3	1	**4**	**36**	**5**	-0.684
	2033	**7**	**54**	**32**	**25**	2	**0**	11	5	13	**21**	**2**	-0.352
	2034	**36**	21	11	**4**	6	7	3	3	9	55	**19**	-0.099
	2030-2034	**107**	**168**	97	**88**	35	17	**50**	19	45	**187**	**46**	-2.094
	2042	35	25	13	8	**13**	5	7	4	**18**	43	7	-0.347
	2043	**18**	29	**26**	15	3	4	10	5	9	44	13	-0.494
	2044	30	**37**	**27**	**0**	10	5	**0**	**14**	5	43	**6**	-0.791
	2045	**9**	29	23	17	**0**	**0**	9	**8**	7	51	**22**	0.271
	2042-2045	92	120	**89**	40	26	14	26	**31**	39	181	48	-1.631

Table B.3: Days mapping to each feature during RILEs for Winter (DJF) season for SRES A1B runs examined. Ice area change for each year and for the RILE period are shown in the right most column. High features counts significant at the 95% CI are bolded and black and low feature counts significant at the 95% CI are bolded and red.

Model Run	YYYY	AL	BAL	BH	CAAH	CAH	EH	EL	ESSH	GH	IL	SH	Ice Area (M km^2)
CCSM3	2012	35	**9**	**26**	11	**0**	3	4	4	**4**	**73**	17	0.082
Run 7	2013	**20**	**37**	18	**27**	3	**10**	7	0	11	**34**	14	-0.763
	2014	30	**13**	24	**4**	**0**	**10**	**1**	**8**	12	**65**	15	-1.129
	2015	**43**	**13**	**9**	**1**	4	5	**0**	3	**19**	**63**	**27**	-0.734
	2016	**14**	28	16	13	**12**	**0**	**19**	3	13	**33**	14	-0.218
	2012-2016	142	**100**	93	56	**19**	28	31	18	59	**268**	**87**	-2.763
	2043	21	**37**	22	**19**	3	8	4	1	11	39	17	0.343
	2044	21	28	13	15	2	4	5	5	14	47	19	-0.427
	2045	29	23	21	**4**	7	**1**	**0**	6	**0**	**63**	10	-1.633
	2046	**46**	**6**	**10**	**0**	7	**14**	**0**	**11**	13	**64**	19	0.425
	2047	31	28	**7**	17	8	4	8	1	12	44	11	-0.051
	2043-2047	148	122	73	55	27	31	**17**	24	50	257	76	-1.342
CCSM3	2045	**37**	**14**	**6**	**2**	**18**	2	**0**	4	**3**	**68**	14	0.051
|Run 8	2046	**17**	**36**	16	**31**	**1**	8	**23**	1	**23**	**18**	7	-0.140
	2047	19	30	18	**23**	5	6	9	6	12	40	7	-0.429
	2048	20	32	**40**	6	2	**13**	4	**0**	12	40	10	-0.157
	2049	**64**	**9**	**4**	**1**	**15**	**20**	5	6	**19**	47	**0**	-0.075
	2045-2049	**157**	121	84	63	41	**49**	**41**	17	**69**	**213**	**38**	-0.750
CGCM3.1 (T63)	2057	**46**	**20**	15	**4**	**24**	8	**0**	5	**7**	**47**	4	-0.041
Run 1	2058	**55**	38	11	**1**	**26**	**11**	**2**	3	**26**	29	**0**	0.064
	2059	**19**	33	**29**	11	20	2	**16**	**0**	17	35	4	-0.645
	2057-2059	**120**	91	**55**	**16**	**70**	21	18	8	50	111	**8**	-0.622
	2095	28	26	16	13	**6**	7	11	**8**	17	41	8	-1.071
	2096	**46**	22	10	14	**22**	5	10	1	11	36	2	0.731
	2095-2096	74	48	26	27	28	12	21	9	28	77	10	-0.341
ECHAM 5-MPI	2097	**17**	20	**39**	**14**	**2**	3	**14**	**0**	11	51	16	-0.920
Run 2	2098	**60**	**12**	**11**	**1**	**4**	**15**	2	**9**	11	58	7	0.337
	2097-2098	77	32	50	15	**6**	18	16	9	22	109	23	-0.583

Table B.4: Days mapping to each feature during RILEs for Winter (DJF) season for SRES A2 runs examined. Ice area change for each year and for the RILE period are shown in the right most column. High features counts significant at the 95% CI are bolded and black and low feature counts significant at the 95% CI are bolded and red.

Model Run	YYYY	AL	BAL	BH	CAAH	CAH	EH	EL	ESSH	GH	IL	SH	Ice Loss (M km^2)
CCSM3	2033	29	25	12	**21**	4	**10**	**13**	4	16	**34**	13	-1.404
Run 1	2034	**13**	**38**	**27**	13	**20**	**0**	4	7	**2**	45	12	-0.005
	2035	22	25	**7**	**24**	**14**	5	**26**	1	**19**	**24**	6	-2.058
	2033-2035	**64**	88	46	**58**	**38**	15	**43**	12	37	**103**	31	-3.467
CCSM3	2025	**45**	**10**	24	**2**	**23**	5	2	2	**2**	54	7	-0.343
Run 5	2026	**41**	19	14	9	4	4	2	2	11	**57**	14	0.421
	2027	**13**	33	**41**	12	**0**	6	**1**	5	5	50	18	-1.340
	2025-2027	99	62	**79**	**23**	27	15	**5**	9	**18**	**161**	39	-1.262
CSIRO MK(3.5)	2082	**82**	**3**	**2**	0	24	**24**	3	0	17	**33**	1	-1.858
Run 1	2083	**44**	**23**	7	9	20	8	9	4	16	**33**	2	-0.287
	2084	**66**	**3**	11	2	16	**27**	**12**	0	**26**	**32**	1	0.512
	2085	**72**	**3**	4	2	**12**	**35**	4	1	6	37	0	-0.921
	2082-2085	**264**	32	**24**	13	72	94	**28**	5	**65**	135	4	-2.553

Table B.5: Days mapping to each feature for winter season all high loss years for the SRES A1B emission scenario in a run. Significantly high values at the 95% CI are bolded and significantly low values at 95% CI are bolded and red.

Model	Run	AL	BAL	BH	CAAH	CAH	EH	EL	ESSH	GH	IL	SH
CCSM 3	1	602	586	**482**	276	136	102	150	76	**222**	**1123**	**314**
	2	**402**	**647**	**417**	**334**	116	**56**	151	67	**140**	**876**	255
	3	**491**	476	347	254	131	99	146	56	190	**804**	195
	4	526	**515**	331	**270**	104	111	135	73	**239**	**868**	222
	5	**324**	**421**	293	197	92	**55**	84	**71**	**122**	733	252
	6	486	**546**	317	203	128	79	91	73	177	830	208
	7	**533**	495	368	250	106	97	118	75	**173**	1004	**309**
	8	298	298	201	135	70	50	67	43	112	522	139
CGCM 3.1(T63)	1	415	404	**184**	170	190	68	97	53	178	499	**89**
ECHAM5-MPI	2	**271**	**216**	195	77	**113**	**23**	41	40	56	459	87

Table B.6: Days mapping to each feature for winter season all high loss years in a run for SRES A2 emission scenario. Significantly high values at the 95% CI are bolded and significantly low values at 95% CI are bolded and red.

Model	Run	AL	BAL	BH	CAAH	CAH	EH	EL	ESSH	GH	IL	SH
CCSM 3	1	544	501	375	**306**	148	**77**	**198**	73	**192**	902	**198**
	5	**524**	566	**469**	252	**99**	111	128	**50**	206	997	**277**
CSIRO MK 3.5	1	**468**	**102**	**74**	41	161	107	47	**32**	100	**320**	15

Table B.7: Z-scores as compared to climatology for SOM-derived teleconnection indices during RILEs for Winter (DJF) season for SRES A1B runs examined. Ice area change for each year and RILE period are shown in the right most column. Values significantly different from climatology above 90% CI are bold and black for positive and bold and red for negative.

Model	Run	Length	YYYY	AO		ARP		CAI-80		NAO		PNA	
				Neg.	Pos.	Neg.	Pos.	Neg.	Pos.	Neg.	Pos.	Neg.	Pos.
NCAR CCSM3	1	10	2024-2033	-0.33	0.11	-0.41	0.20	-0.32	0.36	-0.04	-0.31	0.11	-0.43
	2	8	2034-2041	-0.62	1.61	-1.21	1.37	-1.09	1.01	-0.42	0.49	-0.79	0.92
		4	2047-2050	0.60	-1.23	1.58	-1.22	0.84	-0.22	1.21	-0.81	1.62	-1.21
	3	5	2025-2029	0.22	1.06	-0.66	0.05	-0.85	1.02	0.94	-0.74	**-1.88**	0.50
	4	5	2030-2034	-1.18	0.72	-0.05	0.14	0.06	0.29	-0.41	0.19	0.40	**-1.81**
	5	8	2027-2034	**-4.82**	**2.44**	-1.10	**4.45**	**-1.65**	-0.13	**-4.03**	**2.73**	0.26	**-3.89**
	6	5	2030-2034	-0.08	0.36	-0.41	0.28	-0.72	0.72	0.32	0.25	-0.29	0.59
		4	2042-2045	0.29	-0.25	-0.02	0.04	0.17	-0.15	-0.45	0.13	1.09	-0.74
	7	5	2012-2016	1.02	-1.02	0.76	**-2.11**	0.87	-0.72	-0.70	-0.01	0.77	-0.81
		5	2043-2047	0.31	-0.08	0.87	-1.17	0.22	-0.33	0.17	-0.92	**-2.26**	0.92
	8	5	2045-2049	1.04	0.03	0.45	-0.49	-0.18	0.38	1.54	-0.66	-0.87	0.71
CCCMA CGCM(	1	2	2097-2098	**1.66**	-1.15	-0.45	-0.86	0.09	-0.77	**2.02**	**-1.65**	-0.01	0.42
MPI_ECHAM5	2	2	2097-2098	**8.81**	**-4.95**	1.00	-1.16	**7.14**	-0.89	0.45	-0.24	-0.55	**3.45**

Table B.8: Z-scores as compared to climatology for SOM-derived teleconnection indices during RILEs for Winter (DJF) season for SRES A2 runs examined. Ice area change for each year and RILE period are shown in the right most column. Values significantly different from climatology above 90% CI are bold and black for positive and bold and red for negative.

Model	Run	Length	YYYY	AO		ARP		CAI-80		NAO		PNA	
				Neg.	Pos.	Neg.	Pos.	Neg.	Pos.	Neg.	Pos.	Neg.	Pos.
CSIRO Mk_5	1	4	2082-2085	-0.07	0.04	-0.50	0.19	-0.72	0.68	0.72	-0.41	0.16	-0.41
NCAR CCSM3	1	3	2033-2035	0.21	-0.34	0.15	-0.45	0.41	-1.22	0.29	-0.21	**-1.92**	-0.08
NCAR CCSM3	5	3	2025-2027	**2.91**	**2.54**	**5.95**	**-4.75**	0.81	**5.35**	**11.00**	**-1.66**	**-4.85**	**2.89**

Table B.9: Zscores as compared to climatology for SOM-derived teleconnection indices during large ice loss years of runs for Winter (DJF) season for SRES A1B. Ice area change for each year and RILE period are shown in the right most column. Values significantly different from climatology 90% CI are bold and black for positive and bold and red for negative.

Model	Run	AO		ARP		CAI-80		NAO		PNA	
		Neg.	Pos.	Neg.	Pos.	Neg.	Pos.	Neg.	Pos.	Neg.	Pos.
NCAR CCSM3	1	-0.67	0.27	-0.23	0.59	0.31	-0.41	-0.40	0.73	-0.46	0.05
	2	**-2.60**	**2.58**	**-2.60**	**2.56**	**-2.25**	1.03	**-2.42**	**2.53**	-0.13	-0.75
	3	-1.22	1.46	-1.25	0.75	-1.24	0.70	-0.51	0.31	-0.29	-1.34
	4	-0.45	0.58	-0.24	0.41	-0.48	1.21	0.17	-0.29	-0.10	0.03
	5	-1.61	1.44	-1.29	1.33	-0.18	-0.27	**-1.70**	0.42	-0.34	**-1.93**
	6	-0.03	0.25	-0.17	0.31	0.26	-0.46	0.04	-0.09	0.65	-1.16
	7	-0.76	-0.31	0.09	0.48	0.54	-0.49	-1.27	0.67	0.15	-0.98
	8	-0.40	0.40	-1.05	0.50	**-1.84**	**1.91**	0.50	-0.83	0.53	1.49
CCCMA CGCM(T63)	1	-0.86	0.27	-0.49	0.48	0.03	-0.95	-0.52	0.36	-1.41	-0.69
ECHAM/MPI	2	-0.91	0.72	-0.33	0.41	-0.48	0.84	-1.21	0.08	-0.43	-0.40

Table B.10: Zscores for SOM-derived teleconnection indices during large ice loss years of runs for Winter (DJF) season for SRES A2. Ice area change for each year and RILE period are shown in the right most column. Values significantly different from climatology at 90% CI are bold and black for positive and bold and red for negative.

Model	Run	AO		ARP		CAI-80		NAO		PNA	
		Neg.	Pos.	Neg.	Pos.	Neg.	Pos.	Neg.	Pos.	Neg.	Pos.
CSIRO MK5	1	-0.395131	-0.664457	0.5749714	-0.331838	0.2138713	-0.073661	0.0961109	-0.3939	-0.216778	-0.779348
NCAR CCSM3	2	0.5573209	-0.558165	-0.796728	0.7257585	-0.753042	0.8350958	0.8924104	0.6579401	**2.0706197**	0.549484
NCAR CCSM3	5	-0.715531	0.9071379	-0.509636	0.8067718	-0.318917	-0.038962	-0.637557	0.9829933	0.3071228	-0.392798

Table B.11: Days mapping to each feature during RILEs for Summer (JJA) season for SRES A1B runs examined. Ice area change for each year and RILE period are shown in the right most column. High features counts significant at the 95% CI are bolded and black and low feature counts significant at the 95% CI are bolded and red.

Model Run	YYYY	BAH	BAL	BH	BL	CAAH	CAAL	CAH	CAL	DSL	EL	ESSH	GH	IL	SL	YH	Ice Change (M km^2)
CCSM3	2024	23	5	19	11	11	13	**0**	**9**	6	35	11	6	11	13	9	0.245
Run 1	2025	23	5	11	13	5	4	**20**	13	4	40	3	8	3	19	**8**	1.081
	2026	23	**1**	8	12	**1**	**14**	**1**	**30**	3	**20**	5	**12**	5	18	**24**	-1.903
	2027	20	5	**21**	5	6	8	10	16	**11**	36	6	4	6	10	17	-0.716
	2028	27	2	7	**24**	3	**14**	4	20	4	34	5	2	5	13	15	0.018
	2029	**6**	**16**	13	5	10	**2**	15	15	4	31	**21**	6	**21**	**3**	16	-0.729
	2030	21	6	11	10	3	10	15	20	4	31	8	4	8	11	19	0.253
	2031	26	3	15	9	8	12	5	20	5	31	4	5	4	14	21	-0.119
	2032	13	9	13	14	5	**0**	**16**	18	2	36	10	6	10	14	16	-0.897
	2033	16	9	14	8	11	**2**	10	12	3	38	8	**13**	8	20	11	-1.737
	2024-2033	198	61	132	111	63	79	96	173	46	332	81	66	81	135	156	-4.503
CCSM3	2034	24	**16**	**5**	7	3	7	**29**	15	**0**	**20**	14	3	14	12	8	-0.398
Run 2	2035	12	**17**	16	9	2	**0**	**23**	**7**	**0**	39	**4**	**20**	**4**	**23**	8	-0.988
	2036	24	**3**	8	15	4	5	9	20	**10**	29	8	6	8	14	19	0.917
	2037	**3**	**23**	**26**	7	6	**0**	8	**4**	2	28	**19**	**18**	**19**	16	**5**	-0.075
	2038	**8**	5	10	13	**11**	2	**22**	**2**	5	**57**	**18**	7	**18**	**3**	**3**	0.007
	2039	15	13	17	9	2	8	9	12	5	24	**27**	**1**	**27**	**3**	11	-0.907
	2040	17	**1**	**4**	11	3	2	**1**	**47**	6	**18**	8	**1**	8	10	**41**	0.392
	2041	**2**	**16**	**24**	14	2	**0**	**16**	**6**	2	**45**	**21**	7	**21**	**2**	**5**	-0.401
	2034-2041	**105**	**94**	110	85	**33**	**24**	**117**	**113**	**30**	260	**119**	63	**119**	**83**	**100**	-1.454
	2047	21	**0**	**6**	**4**	7	8	**0**	**39**	6	**17**	7	7	7	15	**34**	0.104
	2048	15	5	**5**	**20**	8	9	12	**4**	5	**41**	**21**	6	**21**	**7**	**3**	-1.141
	2049	17	**17**	17	9	7	4	**20**	13	2	27	6	7	6	19	13	0.064
	2050	13	9	11	17	3	3	4	**26**	5	28	15	3	15	**6**	21	-0.595
	2047-2050	66	31	**39**	50	25	24	36	**82**	18	113	49	23	49	47	**71**	-1.568

Table B.12: Days mapping to each feature during RILEs for Summer (JJA) season for SRES A1B runs examined. Ice area change for each year and RILE period are shown in the right most column. High features counts significant at the 95% CI are bolded and black and low feature counts significant at the 95% CI are bolded and red.

Model Run	YYYY	BAH	BAL	BH	BL	CAAH	CAAL	CAH	CAL	DSL	EL	ESSH	GH	IL	SL	YH	Ice Change (M km^2)
CCSM3	2025	**28**	**1**	7	14	2	8	3	13	7	25	**18**	7	**18**	20	11	1.168
Run 3	2026	25	6	19	**5**	4	7	5	22	10	33	**3**	10	**3**	10	17	0.039
	2027	12	9	8	9	4	6	**16**	22	2	28	12	9	12	11	11	-2.202
	2028	22	**1**	9	18	**12**	**13**	5	**4**	2	**46**	8	**14**	8	17	**4**	-0.546
	2029	14	**0**	8	**30**	**1**	4	**2**	20	2	40	13	5	13	12	15	-0.040
	2025-2029	101	**17**	51	**76**	23	38	31	81	23	172	54	45	54	70	58	-1.581
CCSM3	2030	**25**	**1**	12	**19**	8	**11**	9	**4**	3	**53**	**3**	**17**	**3**	11	**3**	0.215
Run 4	2031	**9**	**17**	15	7	3	**1**	**23**	20	4	36	9	5	9	**5**	**21**	-0.130
	2032	19	**0**	**8**	9	**16**	5	9	16	9	35	9	7	9	17	10	-1.630
	2033	15	12	**23**	7	4	6	**17**	18	5	40	5	4	5	**5**	14	0.460
	2034	**29**	**2**	9	15	2	**19**	12	15	3	38	**3**	7	**3**	12	14	-0.885
	2030-2034	97	32	67	57	33	**42**	**70**	73	24	**202**	**29**	40	**29**	**50**	62	-1.970
CCSM3	2027	12	11	19	**4**	4	**1**	15	**6**	2	31	**21**	8	**21**	19	10	-0.649
Run 5	2028	**27**	**2**	**2**	13	8	4	7	**7**	4	26	**18**	9	**18**	**31**	**6**	0.233
	2029	21	**3**	**1**	**29**	6	8	9	**3**	5	**42**	7	**16**	7	**22**	**5**	-0.723
	2030	**6**	10	19	**18**	5	**0**	**17**	**8**	1	**47**	**17**	3	**17**	8	**4**	0.478
	2031	12	6	11	10	**13**	3	5	9	**0**	35	10	**22**	10	**29**	8	-0.116
	2032	**2**	12	**39**	5	**14**	**0**	7	**8**	2	**59**	**4**	**13**	**4**	7	**7**	-0.988
	2033	**8**	11	17	6	9	**0**	11	**28**	**0**	36	**3**	8	**3**	14	**25**	0.262
	2034	20	**1**	11	**20**	5	2	10	**4**	3	**45**	7	**14**	7	**29**	**3**	-0.733
	2027-2034	**108**	56	119	105	64	**18**	81	**73**	**17**	**321**	87	**93**	87	**159**	**68**	-2.236

Table B.13: Days mapping to each feature during RILEs for Summer (JJA) season for SRES A1B runs examined. Ice area change for each year and RILE period are shown in the right most column. High features counts significant at the 95% CI are bolded and black and low feature counts significant at the 95% CI are bolded and red.

Model Run	YYYY	BAH	BAL	BH	BL	CAAH	CAAL	CAH	CAL	DSL	EL	ESSH	GH	IL	SL	YH	Ice Change (M km^2)
CCSM3	2030	**5**	7	8	11	**13**	**1**	**21**	**8**	**0**	**51**	**3**	**23**	**3**	**22**	8	-1.078
Run 6	2031	**6**	**15**	**25**	9	5	3	15	17	1	**45**	**4**	11	**4**	7	17	0.118
	2032	25	11	9	6	4	5	12	11	3	**22**	12	12	12	**28**	10	-0.684
	2033	14	4	18	**25**	8	3	10	**6**	6	**51**	14	**0**	14	**4**	**7**	-0.352
	2034	14	4	11	**2**	8	8	**1**	23	5	**18**	17	**15**	17	17	**22**	-0.099
	2030-2034	**64**	41	71	53	**38**	**20**	59	**65**	15	**187**	50	**61**	50	78	64	-2.094
	2042	**26**	**0**	**1**	13	9	**18**	**3**	**25**	3	29	**4**	10	**4**	13	21	-0.347
	2043	21	**1**	8	6	3	7	**2**	**40**	**13**	**17**	**2**	11	**2**	11	**37**	-0.494
	2044	22	3	8	**34**	**0**	7	6	**9**	2	**44**	7	6	7	19	8	-0.791
	2045	16	10	**5**	15	4	9	14	21	7	29	14	**1**	14	**2**	**23**	0.271
	2042-2045	85	**14**	**22**	**68**	16	**41**	**25**	**95**	**25**	119	**27**	28	**27**	45	**89**	-1.360
CCSM3	2012	16	6	**24**	15	9	3	5	9	6	**45**	**3**	9	**3**	20	9	0.082
Run 7	2013	9	11	**29**	**2**	**11**	4	7	**25**	2	39	5	4	5	**6**	**23**	-0.763
	2014	17	**25**	**32**	5	7	7	8	**2**	2	26	7	13	7	**23**	**2**	-1.129
	2015	9	**17**	20	11	**15**	4	14	**4**	2	40	6	**15**	6	17	**4**	-0.734
	2016	14	12	20	4	7	9	6	13	4	23	16	12	16	14	14	-0.218
	2012-2016	65	**71**	**125**	37	**49**	27	40	**53**	16	173	**37**	53	**37**	80	**52**	-2.763
	2043	**31**	**1**	**8**	5	**0**	**12**	8	18	**9**	**20**	10	11	10	**22**	14	0.343
	2044	10	**4**	11	6	4	2	5	**43**	6	**18**	14	**1**	14	**3**	**39**	-0.427
	2045	**29**	7	9	5	6	5	13	10	4	23	13	7	13	**29**	**4**	-1.633
	2046	12	**0**	**8**	15	4	**0**	5	**24**	4	31	9	**18**	9	21	15	0.425
	2047	17	12	20	5	**1**	3	**4**	**27**	6	**18**	12	4	12	14	**25**	-0.051
	2043-2047	**99**	**24**	**56**	36	**15**	22	**35**	**122**	**29**	**110**	58	41	58	89	**97**	-1.342
CCSM3	2045	22	7	16	17	6	**15**	10	**3**	4	37	11	8	11	14	**3**	0.051
Run 8	2046	20	**0**	**3**	**20**	7	**10**	14	16	4	41	**4**	11	**4**	14	14	-0.140
	2047	20	8	16	10	2	7	4	17	8	**23**	**18**	4	**18**	10	12	-0.429
	2048	16	9	18	17	**1**	4	**3**	21	1	30	10	3	10	17	**23**	-0.157
	2049	19	**0**	**5**	**18**	8	9	5	9	7	36	**22**	6	**22**	9	9	-0.075
	2045-2049	97	**24**	58	**82**	24	**45**	36	66	24	167	65	32	65	64	61	-0.750

Table B.14: Days mapping to each feature during RILEs for Summer (JJA) season for SRES A1B runs examined. Ice area change for each year and RILE period are shown in the right most column. High features counts significant at the 95% CI are bolded and black and low feature counts significant at the 95% CI are bolded and red.

Model Run	YYYY	BAH	BAL	BH	BL	CAAH	CAAL	CAH	CAL	DSL	EL	ESSH	GH	IL	SL	YH	Ice Change (M km^2)
ECHAM5-MPI	2081	12	7	16	**17**	5	3	**22**	9	**1**	**50**	8	7	8	8	**4**	0.393
Run 2	2082	16	6	24	3	11	3	**2**	**24**	8	30	7	5	7	13	**22**	-0.216
	2081-2082	28	**13**	40	**20**	16	6	24	**33**	9	80	15	12	15	21	26	0.177
	2097	**29**	9	18	**0**	10	**10**	10	6	**13**	**27**	13	6	13	12	8	-0.920
	2098	13	15	**31**	5	**13**	2	**21**	**1**	4	**52**	10	4	10	**2**	**1**	0.337
	2097-2098	**42**	24	49	**5**	**23**	12	31	**7**	17	79	23	10	23	14	**9**	-0.583
CGCM3.1 (T63)	2057	14	**0**	16	10	7	**0**	**3**	**21**	6	36	8	7	8	**20**	**24**	-0.041
Run 1	2058	**7**	6	24	**17**	8	**0**	9	10	2	**54**	8	8	8	12	6	0.064
	2059	**25**	11	21	5	8	**9**	**23**	**1**	9	42	7	3	7	8	5	-0.645
	2057-2059	46	**17**	61	**32**	23	9	35	32	17	**132**	**23**	18	**23**	**40**	35	-0.622
	2095	16	**0**	28	3	8	**0**	**6**	15	8	43	11	7	11	12	16	-1.071
	2096	11	8	25	2	**15**	4	**3**	14	7	34	16	5	16	9	14	0.731
	2095-2096	27	**8**	53	**5**	**23**	4	**9**	29	15	77	27	12	27	21	**30**	-0.341

Table B.15: Days mapping to each feature during RILEs for Summer (JJA) season for SRES A2 runs examined. Ice area change for each year and RILE period are shown in the right most column. High features counts significant at the 95% CI are bolded and black and low feature counts significant at the 95% CI are bolded and red.

Model Run	YYYY	BAH	BAL	BH	BL	CAAH	CAAL	CAH	CAL	DSL	EL	ESSH	GH	IL	SL	YH	Ice Change (M km^2)
CCSM3	2033	**11**	5	19	**24**	5	2	9	**7**	6	**46**	8	4	8	16	12	-1.404
Run 1	2034	18	12	15	**4**	**14**	7	9	19	3	29	7	7	7	14	18	-0.005
	2035	15	8	14	**5**	8	6	8	**7**	3	29	**18**	**17**	**18**	20	**6**	-2.058
	2033-2035	44	25	48	33	**27**	15	26	**33**	12	104	33	28	33	50	36	-3.467
CCSM3	2025	23	**0**	**4**	**28**	4	5	**3**	**10**	**11**	38	9	12	9	18	10	-0.343
Run 5	2026	10	**1**	10	8	7	**0**	**1**	**42**	3	24	7	5	7	15	**43**	0.421
	2027	**26**	7	10	**1**	7	**11**	**0**	**38**	**15**	**11**	8	**1**	8	**2**	**37**	-1.340
	2025-2027	59	**8**	**24**	37	18	16	**4**	**90**	**29**	**73**	24	18	24	35	**90**	-1.262
CSIRO MK(3.5)	2046	11	10	**24**	5	**0**	6	**19**	19	3	36	15	**0**	15	**1**	20	-0.772
Run 1	2081	17	4	13	**16**	5	5	8	16	11	**39**	11	7	11	5	12	1.790
	2082	9	12	17	11	2	4	5	17	5	23	**28**	**0**	**28**	3	20	-1.858
	2083	**3**	10	**24**	**0**	9	**0**	7	**29**	**1**	31	13	3	13	8	**30**	-0.287
	2084	**31**	6	**7**	12	1	**15**	7	17	11	**17**	12	5	12	10	20	0.512
	2085	18	11	22	7	7	4	6	**8**	**14**	33	15	3	15	7	14	-0.921
	2081-2085	78	43	83	46	24	28	**33**	87	42	143	79	18	79	33	**96**	-0.762

Table B.16: Days mapping to each feature for summer season all high loss years in a run. Significantly high values at the 95% CI are bolded and significantly low values at 95% CI are bolded and red.

Model	Run	BAH	BAL	BH	BL	CAAH	CAAL	CAH	CAL	DSL	EL	ESSH	GH	IL	SL	YH
CCSM 3	1	384	181	319	263	163	147	**183**	390	120	733	238	170	238	286	342
	2	**344**	190	**261**	268	**124**	**92**	**264**	**288**	**78**	**735**	**240**	**226**	**240**	379	**257**
	3	**331**	**239**	**353**	**220**	**170**	**91**	**228**	**262**	111	742	244	**207**	244	321	**240**
	4	346	178	**349**	207	**92**	109	163	313	**130**	633	231	142	231	234	285
	5	**231**	134	216	168	**130**	**67**	**186**	**219**	**56**	**575**	160	**159**	160	**243**	210
	6	**291**	159	230	210	118	**90**	**217**	**278**	**61**	622	201	**211**	201	**319**	**240**
	7	**303**	**289**	**414**	**152**	**195**	108	231	307	**68**	721	**199**	220	199	313	288
	8	**208**	131	221	178	**114**	**43**	154	208	63	**542**	159	133	159	217	191
CGCM 3.1(T63)	1	207	160	**323**	**64**	88	59	178	118	85	490	152	79	152	**103**	116
ECHAM5-MPI	2	150	117	237	56	78	41	143	**76**	71	386	134	62	134	**73**	**79**

Table B.17: Days mapping to each feature for winter season all high loss years in a run for SRES A2 emissions scenario. Significantly high values at the 95% CI are bolded and significantly low values at 95% CI are bolded and red.

Model	Run	BAH	BAL	BH	BL	CAAH	CAAL	CAH	CAL	DSL	EL	ESSH	GH	IL	SL	YH
CCSM 3	1	**314**	170	**305**	206	**152**	**94**	188	**245**	**64**	**690**	213	206	213	**348**	235
	5	**273**	**217**	**333**	203	**139**	**81**	172	425	107	638	237	**126**	237	220	395
CSIRO MK3.5	1	225	123	228	115	53	71	142	**153**	107	396	**227**	49	**227**	101	**162**

Table B.18: Zscores as compared to climatology for SOM-derived teleconnection indices during RILEs for Summer (JJA) season for SRES A1B runs examined. Ice area change for each year and RILE period are shown in the right most column. Values significantly different from climatology above 90% CIare bold and black for positive and bold and red for negative.

Model	Run	Length	YYYY	AO		ARP		CAI-80		NAO		PNA	
				Neg.	Pos.	Neg.	Pos.	Neg.	Pos.	Neg.	Pos.	Neg.	Pos.
NCAR CCSM3	1	10	2024-2033	-0.18	0.30	1.08	-0.63	0.64	0.26	-0.93	-0.29	-0.06	-0.39
	2	8	2034-2041	0.57	-0.46	-1.37	-1.32	-0.55	-0.32	0.18	0.08	-0.40	0.56
		4	2047-2050	-0.70	0.83	0.78	-0.06	0.18	-0.16	-1.39	-0.42	0.49	-0.34
	3	5	2025-2029	-0.28	-0.13	1.41	-0.21	1.26	-0.84	-0.08	0.16	1.43	0.00
	4	5	2030-2034	0.96	-0.30	0.12	-0.02	-0.14	1.23	0.67	-1.25	0.80	-0.79
	5	8	2027-2034	**5.52**	**-4.33**	0.13	0.72	-0.14	0.28	**6.26**	**-3.39**	0.06	1.39
	6	5	2030-2034	1.07	-0.77	-1.28	-0.26	-1.24	1.39	0.96	**-1.94**	**-1.76**	1.21
		4	2042-2045	-1.22	1.43	1.20	-0.78	1.03	-0.05	-1.42	0.41	1.15	**-3.20**
	7	5	2012-2016	0.66	-0.97	**-2.33**	**2.14**	**-1.91**	1.50	0.74	-0.82	**-2.07**	**1.73**
		5	2043-2047	-1.39	**1.79**	0.03	-1.01	0.61	0.00	-0.86	0.77	**5.56**	**-3.04**
	8	5	2045-2049	-1.42	-0.24	1.51	0.76	**3.57**	-1.37	**-2.15**	0.54	-0.28	-0.50
CCCMA CGCM(t63)	1	2	2097-2098	0.71	-0.30	1.36	0.56	**2.48**	0.10	0.72	-1.04	0.85	-0.64
MPI_ECHAM5	2	2	2097-2098	-0.14	-1.24	**6.11**	-0.60	**2.10**	-0.41	0.35	**-4.44**	0.06	-0.03

Table B.19: Zscores as compared to climatology for SOM-derived teleconnection indices during RILEs for Summer (JJA) season for SRES A2 runs examined. Ice area change for each year and RILE period are shown in the right most column. Values significantly different from climatology at 90% CI are bold and black for positive and bold and red for negative.

Model	Run	Length	YYYY	AO		ARP		CAI-80		NAO		PNA	
				Neg.	Pos.	Neg.	Pos.	Neg.	Pos.	Neg.	Pos.	Neg.	Pos.
CSIRO Mk_5	1	4	2081-2085	0.93	-0.58	-0.64	0.28	-0.52	0.80	0.80	-0.79	-0.80	-0.02
NCAR CCSM3	1	3	2033-2035	**-2.27**	1.11	0.21	-1.32	-0.07	-0.39	**-4.76**	**4.85**	-0.64	**-3.30**
NCAR CCSM3	5	3	2025-2027	-1.60	**2.13**	0.28	-0.59	0.16	-0.64	**-1.96**	**1.90**	-0.73	-0.78

Table B.20: Zscores as compared to climatology for SOM-derived teleconnection indices during large ice loss years of runs for Summer (JJA) season for SRES A1B. Ice area change for each year and RILE period are shown in the right most column. Values significantly different from climatology at 90% CI are bold and black for positive and bold and red for negative.

Model	Run	AO		ARP		CAI-80		NAO		PNA	
		Neg.	Pos.	Neg.	Pos.	Neg.	Pos.	Neg.	Pos.	Neg.	Pos.
NCAR CCSM 3	1	0.76	-0.37	**-2.52**	0.04	**-1.77**	0.81	0.18	-0.55	-1.57	0.41
	2	1.59	-1.44	-0.04	-1.39	0.01	0.00	1.63	0.04	0.41	-0.10
	3	**2.74**	**-2.11**	**-1.76**	1.11	**-1.69**	0.79	**2.07**	-1.58	**-2.22**	**1.97**
	4	-0.83	0.57	0.21	-0.35	0.00	-0.86	-0.64	0.70	0.15	-0.51
	5	**2.47**	**-1.68**	**-1.68**	0.29	-1.24	1.35	**2.52**	**-2.25**	-1.55	0.35
	6	**2.34**	**-1.67**	-1.37	-0.10	-1.41	0.43	**2.26**	-1.25	-1.07	0.29
	7	1.18	-0.83	-1.07	-0.59	**-1.85**	**1.87**	1.18	-1.50	-1.28	**2.46**
	8	1.03	-0.72	-0.90	1.45	-1.18	1.28	1.39	-1.09	0.28	-0.85
CCCMA CGCM (t63)	1	0.04	0.04	0.04	0.04	0.04	0.04	0.04	0.04	0.04	0.04
MPI ECHAM 5	2	-0.68	-0.68	-0.68	-0.68	-0.68	-0.68	-0.68	-0.68	-0.68	-0.68

Table B.21: Zscores as compared to climatology for SOM-derived teleconnection indices during large ice loss years of runs for Summer (JJA) season for SRES A2. Ice area change for each year and RILE period are shown in the right most column. Values significantly different from climatology at 90% CI are bold and black for positive and bold and red for negative.

Model	Run	AO		ARP		CAI-80		NAO		PNA	
		Neg.	Pos.	Neg.	Pos.	Neg.	Pos.	Neg.	Pos.	Neg.	Pos.
CSIRO MK5	1	-0.56	0.82	-0.36	-0.74	-0.76	1.10	-0.26	-0.08	0.92	-0.94
NCAR CCSM 3	1	-0.73	**-2.47**	-0.16	0.24	-1.23	1.33	**2.67**	**-1.97**	-1.49	**1.74**
NCAR CCSM 3	5	0.01	0.42	**-2.20**	**1.80**	**-3.00**	**1.87**	-0.56	-1.10	-0.99	1.20

Appendix C

Third appendix

Table C.1: Winter traditional teleconnection indices and SOM-derived teleconnection scores for winter seasons of large ice loss years significant (90% CI) positive anomalies from climatology are black and significantly (90% CI) negative anomalies are red and bold.

Year	AO			ARP			CAI-80			NAO			PNA			Loss Rate
	Index	Projection		Index	Projection		Index	Projection		Index	Projection		Index	Projection		(M km^2/yr)
		Neg.	Pos.		Neg.	Pos.		Neg.	Pos.		Neg.	Pos.		Neg.	Pos.	
1981	-0.17	-0.52	**0.55**		-0.44	**0.53**	**6.10**	-0.10	-0.02	0.38	-0.43	**0.53**	0.50	-0.78	-0.73	-0.462
1989	**2.69**	-0.80	**0.82**	**1.97**	-0.72	**0.85**	**11.55**	-0.61	**0.70**	**1.05**	-0.45	**0.51**	-0.84	-0.60	-0.53	-0.482
1991	0.37	-0.01	-0.72	-0.09	-0.07	-0.16	**-3.27**	0.32	-0.35	0.45	-0.38	0.13	0.23	**0.80**	-0.52	-0.863
1993	**1.77**	-0.72	**0.92**	**1.53**	-0.58	**0.89**	**7.05**	-0.63	**0.54**	**0.61**	-0.50	**0.56**	-0.23	-0.01	-0.22	-1.102
1995	0.72	-0.42	**0.48**	0.59	0.13	**0.62**	4.47	-0.21	-0.04	**1.07**	-0.56	**0.68**	**0.74**	-0.42	-0.17	-1.241
1997	-0.10	-0.37	0.05	0.48	-0.45	0.27	0.79	-0.30	-0.11	-0.33	-0.30	0.21	-0.07	-0.23	-0.32	-1.130
2002	0.45	0.21	-0.29	0.51	**0.67**	-0.27	2.22	0.30	-0.15	-0.02	-0.19	0.29	-0.12	0.33	-0.53	-0.710
2005	0.11	-0.16	-0.01	-0.61	0.39	0.22	-1.42	**0.51**	-0.44	**0.59**	-0.65	**0.66**	-0.16	0.09	-0.43	-0.599
2007	**1.00**	0.02	0.09	**0.93**	0.12	0.23	1.28	-0.10	-0.30	-0.03	0.05	0.37	0.39	0.57	0.03	-1.826

Table C.2: Summer traditional teleconnection indices and SOM-derived teleconnection scores for winter seasons of large ice loss years significant (90% CI) positive anomalies from climatology are black and significantly (90% CI) negative anomalies are red and bold.

Year	AO			ARP			CAI-80			NAO			PNA			Loss Rate
	Index	Projection		Index	Projection		Index	Projection		Index	Projection		Index	Projection		(M km^2/yr)
		Neg.	Pos.		Neg.	Pos.		Neg.	Pos.		Neg.	Pos.		Neg.	Pos.	
1981	-0.04	0.03	-0.38		**0.78**	-0.17	**-2.76**	**0.52**	-0.34	0.10	0.05	-0.14	**-0.89**	-0.05	0.21	-0.462
1989	**0.59**	-0.70	**0.92**	-0.06	-0.68	0.11	2.40	-0.46	**0.34**	0.31	-0.53	0.39	-0.47	**0.61**	-0.33	-0.482
1991	0.16	-0.44	**0.67**	-0.20	-0.16	-0.44	-0.69	-0.08	-0.29	0.16	-0.45	**0.78**	-0.31	**0.74**	-0.86	-0.863
1993	**-0.47**	0.30	-0.18	**-0.47**	**0.59**	-0.16	0.44	0.05	0.27	**-1.13**	**0.51**	-0.39	0.07	0.07	0.05	-1.102
1995	0.07	-0.15	0.01	**0.11**	-0.63	**0.86**	**3.55**	-0.36	0.12	0.34	-0.25	0.10	-0.06	-0.62	0.35	-1.241
1997	-0.37	0.11	0.01	-0.28	-0.81	-0.47	0.47	-0.60	**0.33**	0.05	0.29	0.25	-0.23	-0.22	**0.52**	-1.130
2002	0.22	0.18	-0.09	-0.19	**0.62**	0.28	-0.10	0.06	0.10	0.57	0.19	-0.55	0.36	0.13	-0.60	-0.710
2005	-0.13	0.03	-0.20	-0.06	-0.50	-0.46	0.17	-0.11	-0.20	0.04	-0.31	0.22	0.36	-0.45	0.32	-0.599
2007	-0.33	**0.65**	-0.76	**0.31**	-0.75	**0.67**	**4.43**	-0.52	**0.41**	**-0.62**	**0.68**	-0.88	**1.10**	-0.68	**0.63**	-1.826